

DYNAMICS AND OBSERVATIONAL APPEARANCE OF CIRCUMSTELLAR DISKS

by
Andrew Frederick Nelson

A Dissertation Submitted to the Faculty of the
DEPARTMENT OF PHYSICS
In Partial Fulfillment of the Requirements
For the Degree of
DOCTOR OF PHILOSOPHY
In the Graduate College
THE UNIVERSITY OF ARIZONA

THE UNIVERSITY OF ARIZONA •
GRADUATE COLLEGE

As members of the Final Examination Committee, we certify that we have
read the dissertation prepared by Andrew Frederick Nelson
entitled Dynamics and Observational Appearance of Circumstellar Disks

and recommend that it be accepted as fulfilling the dissertation
requirement for the Degree of Doctor of Philosophy

W. Benz

Willy Benz

8/31/98

Date

Roger Angel

8/31/98

Date

David Arnett

David Arnett

8/31/98

Date

Adam Burrows

Adam Burrows

8/31/98

Date

Mike Shupe

Mike Shupe

8/31/98

Date

Final approval and acceptance of this dissertation is contingent upon
the candidate's submission of the final copy of the dissertation to the
Graduate College.

I hereby certify that I have read this dissertation prepared under my
direction and recommend that it be accepted as fulfilling the dissertation
requirement.

W. Benz

Dissertation Director Willy Benz

8/31/98

Date

STATEMENT BY AUTHOR

This dissertation has been submitted in partial fulfillment of requirements for an advanced degree at The University of Arizona and is deposited in the University Library to be made available to borrowers under rules of the Library.

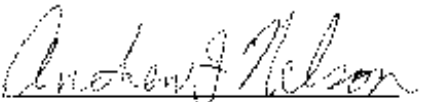
Brief quotations from this dissertation are allowable without special permission, provided that accurate acknowledgment of source is made. Requests for permission for extended quotation from or reproduction of this manuscript in whole or in part may be granted by the head of the major department or the Dean of the Graduate College when in his or her judgment the proposed use of the material is in the interests of scholarship. In all other instances, however, permission must be obtained from the author.

SIGNED: See next page

CORRECTED STATEMENT BY AUTHOR

Contrary to statements on the previous page (which are required by the microfilm folks and the graduate college for this manuscript to be accepted), chapters two and six have been previously published in *The Astrophysical Journal* (specifically, in volumes 500 and 502 respectively as noted in the abstract) and their copyrights are held by The American Astronomical Society. The right to republish such journal articles is explicitly granted to the authors by the AAS, as is their republication in electronic form. The rights to grant permission for extended quotations and reproduction of those chapters are held by The American Astronomical Society and the authors, not the major department head or the Dean of the Graduate college.

As first author on both of the copyrighted chapters, I hereby grant myself permission to republish them as part of my dissertation. Further, I also grant permission to various document archives (including but not limited to the Los Alamos preprint server and the Astrophysical Data System in whatever incarnations they may appear in the future) to electronically archive this entire document and to make single copies available to interested parties on my behalf, so long as the cost for such availability does not exceed the cost to physically print out the thesis (in other words no profit is to be made on this printing). Brief quotations from this dissertation are allowable without special permission, provided that accurate acknowledgment of source is made. In all other instances, however, permission must be obtained from the author, the major department head, the Dean of the Graduate College or, in the case of chapters two and six, The American Astronomical Society.

SIGNED 

ACKNOWLEDGMENTS

When someone submits a PhD thesis, there are always lots of people who have contributed directly and indirectly to its completion. On this page I'll say a few words about some of the more important ones who've helped in one way or another. Most of the people who might ever read this page will know some of these people. The rest of you ought to.

It goes without saying that a thesis committee is necessary for getting 'out'. Beyond the necessary, mine was just all around great. As my thesis advisor, Willy Benz provided direction, funding, humor and ideas to me on many occasions over the past years. It was a real privilege to work with Roger Angel and to see how a good idea evolves over time into something that becomes an important contribution to What We Know. Dave Arnett provided a wry perspective about how things work in astronomy and many sage comments over the years. Adam Burrows, with his voracious appetite for knowledge, provided advice and intelligent criticism of my work. Fulvio Melia was always ready with a friendly smile and a kind word. Mike Shupe and John Rutherford, while not directly involved in my thesis work, provided me an opportunity to explore other fields before deciding on astrophysics and an outsider's perspective once I did decide on astrophysics.

Over the years, my office mates have been great sounding boards all sorts of crack pot ideas, bad jokes, puns and silly songs with the words rearranged to fit the circumstances. They also proved willing (or at least gullible enough) to take all the pennies that filled up my pockets over the years. Every time I had too many I'd give some to them. The original members of the old Parker room office are: Crystal Martin, Chad Engelbracht, Chris Fryer, Paul Harding and me. Later additions from next door include Aimee and Audra and Dave and Jennifer. I'm very glad to have been in such good company for so many years.

No one can be happy just doing one thing. I'm no exception. Three important areas in my life outside of astrophysics are music, karate and family. I'll note people in the first two areas here but acknowledge my family in the dedication which follows.

For several years now, karate has provided me an outlet for all the frustrations that built up when things weren't going right or when I just needed someplace else to go. My teachers and fellow students at Ko Sho Karate have provided learning and friendship and more emotional support than I ever expected when I first signed up. Johnny Linebarger, who I can't think of as anyone but 'Sensei', Kim Linebarger, Elaine, Ralph, Norma and all the rest of the gang: you'll always have a place in my heart and memory.

Finally, there are several people in music who influenced me in fundamentally important ways. John Grossman and Dorothy Walker taught me a quiet dedication to and surpassing love of music. Crispin Campbell taught me how to learn: not just how to learn how to play the cello but how to learn anything. All the wonderful vocalists at St. Olaf taught me everything I know about choral music and, here in Arizona, Grayson Hirst taught me most of what I know about how to sing.

DEDICATION

Probably the most important part of my life is my family.

My parents, Jim and Judy Nelson.

My sister Margot and her husband Jeff.

And my brother, Charlie.

Hopefully someday soon there will be other additions.

I want to sincerely thank them all for past, present
and future support in every endeavor I've been a part of.

TABLE OF CONTENTS

LIST OF FIGURES	10
LIST OF TABLES	13
ABSTRACT	14
1 How We Got to This Point and Where We're Going	16
2 Dynamics of Circumstellar Disks	22
2.1 The Codes	23
2.1.1 Solving the Hydrodynamic Equations	23
2.1.2 Viscosity in the Codes	24
2.2 Physical Assumptions and Constraints	25
2.2.1 Circumstellar Disk Initial Conditions	25
2.2.2 The Construction of Circumstellar Accretion Disks, Boundary Conditions and Numerical Resolution	27
2.2.3 The Equation of State and Energy Considerations	30
2.3 Results of Simulations	30
2.3.1 General Observations and Morphology	32
2.3.2 The Effects of Temperature	33
2.3.3 Spiral Pattern Growth	35
2.3.4 Clump Formation and Characteristics	44
2.4 Conclusions	46
3 Interlude One	75
4 Heating and Cooling In Circumstellar Disks: Dynamics of Circumstellar Disks II	77
4.1 Physical Assumptions	78
4.1.1 Initial Conditions	78
4.1.2 The Equation of State	79

TABLE OF CONTENTS — *Continued*

4.2	Thermal Energy Generation and Dissipation	80
4.2.1	Thermal Energy Generation	80
4.2.2	Thermal Energy Dissipation and the Vertical Structure of Accretion Disks	82
4.2.3	Synthesizing Observations	84
4.2.4	Units: The Physical Scale of the System	84
4.3	The Simulations	84
4.3.1	Morphology and Spectral Energy Distributions	85
4.3.2	An Attempt to Improve the Cooling Prescription	87
4.3.3	Morphology and SED's using modified opacities	90
4.3.4	Variation of the SED's with time	91
4.3.5	Variation of the Dissipation with Resolution	92
4.3.6	The Origin of Thermal Energy Generation	93
4.3.7	Density, Temperature and Scale Height Structure	95
4.4	Comparison to other work	97
4.5	Concluding Remarks	98
5	Interlude Two	122
6	The range of masses and periods explored by radial velocity searches for planetary companions	124
6.1	Analysis Technique	125
6.1.1	Probability of a given velocity amplitude being exceeded by chance	126
6.2	Monte Carlo Analysis	128
6.2.1	Confirmation of the Analytical Results	128
6.2.2	Loss of Sensitivity at Long Periods	129
6.2.3	Limits of Sparse Data	130
6.2.4	Windowing	130
6.3	Comparison to Periodogram Techniques	131
6.4	Application to Real Data	132

TABLE OF CONTENTS — *Continued*

6.4.1	Determining the Measurement Uncertainty	133
6.4.2	Detecting Large Amplitude and Large Eccentricity Signals	133
6.4.3	Masses from Best Fit Velocities of the Walker et al. Sample, and Analysis of Significance	135
6.4.4	A Check by Monte Carlo Analysis	136
6.4.5	Sensitivity to Short Period Planets	137
6.5	Strategies for Large Radial Velocity Surveys	138
7	Concluding remarks and where we ought to go from here	158
7.1	Taking Inventory: What is Possible Using Various Detection Techniques	159
7.2	Disk Formation	160
7.3	The Transport and Evolution of Dust in the Disk: Effects on Energy Transport . .	161
7.4	Migration of Jovian Planets	163
	REFERENCES	164

LIST OF FIGURES

2.1	Disk initial conditions for PPM simulations	51
2.2	Disk initial conditions for SPH simulations	52
2.3	Gravitational potential near the star for disks and tori	53
2.4	High mass disk SPH simulation	54
2.5	High mass disk PPM simulation	55
2.6	Low mass disk SPH simulation	56
2.7	Low mass disk PPM simulation	57
2.8	SPH simulations with identical mass disks but varying initial Q_{\min}	58
2.9	Mass accretion and the star motion for a high Q_{\min} SPH simulation	59
2.10	PPM simulations with identical mass disks but varying initial Q_{\min}	60
2.11	Initial conditions for Tori	61
2.12	Comparison of the morphology of SPH and PPM simulations of tori	62
2.13	Amplitudes and best fits for the $m = 3$ spiral pattern of tori	63
2.14	Growth rates for the $m = 1 - 4$ spiral patterns derived from the PPM simulations	64
2.15	Growth rates for the $m = 1 - 4$ spiral patterns derived from the SPH simulations .	65
2.16	Later time comparison between SPH and PPM simulations of tori	66
2.17	Amplitudes and fits for the $m = 2$ and $m = 3$ patterns of the simulation in figure 2.5	67
2.18	Growth rates and pattern speeds for the simulation in figure 2.5 as a function of radius	68
2.19	Growth rates and pattern speeds for the simulation in figure 2.7 as a function of radius	69
2.20	Amplitude of the $m = 1$ and $m = 2$ patterns at various locations in the disk simulation <i>pqm5</i>	70
2.21	Growth rates for the $m = 2$ pattern as a function of disk mass	71
2.22	Pattern speed for the $m = 2$ pattern as a function of time for the disk shown in figure 2.5	72
2.23	Over density and minimum Q of low and high mass disks derived from SPH simulations	73
2.24	Radius at which clumps formed in the SPH simulations for each of the series varying disk mass	74

LIST OF FIGURES — *Continued*

4.1	Density and temperature structure for several conditions typical of the disks studies in our simulations	101
4.2	SPH simulation of a low mass disk with our ‘a’ cooling prescription	102
4.3	Spectral energy distribution’s for the simulation shown in figure 4.2	103
4.4	Amplitude of the $m = 4$ spiral pattern at several distances from the star from cooled and isothermally evolved simulations as a function of time.	104
4.5	Amplitude of several spiral patterns from simulations evolved under the ‘a’ cooling prescription as a function of radius. ($R_D = 50$ AU)	105
4.6	Amplitude of several spiral patterns from isothermally evolved simulations as a function of radius. ($R_D = 50$ AU)	106
4.7	Amplitude of several spiral patterns from simulations evolved under the ‘a’ cooling prescription as a function of radius ($R_D = 100$ AU).	107
4.8	Cartoon of conditions in the inner disk where dust may be destroyed	108
4.9	Grain size distribution at different altitudes above the midplane	109
4.10	Synthesized SED’s of simulations with varying modifications in grain opacity . . .	110
4.11	SPH simulation of a disk using our ‘b’ cooling prescription	111
4.12	Spectral energy distribution’s for the simulation shown in figure 4.11	112
4.13	Amplitude of several spiral patterns from simulations evolved under the ‘b’ cooling prescription as a function of radius. ($R_D = 50$ AU)	113
4.14	Disk flux in various wavelength bands and total luminosity as a function of time. .	114
4.15	Time expanded disk flux in various wavelength bands and total luminosity as a function of time.	115
4.16	Approximate magnitude of the local dissipation in the disk in terms of the well known ‘ α ’ parameter for viscous disks	116
4.17	Disk flux in various wavelength bands and total luminosity as a function of time. .	117
4.18	Azimuth averaged temperature structure of the disks shown in figures 4.2 and 4.11	118
4.19	Temperature power law index at the midplane and the disk photosphere of the simulations shown in 4.2 and 4.11	119
4.20	Azimuth averaged surface density of the disks.	120
4.21	Azimuth averaged scale height of the disk	121
6.1	Results of Monte Carlo simulations of fitted velocity amplitudes	144
6.2	Best fits for the long period sensitivity fall off parameters	145
6.3	Results of sparse data Monte Carlo simulations with a 6 year time baseline	146

LIST OF FIGURES — *Continued*

6.4	Results of sparse data Monte Carlo simulations with a 2 year time baseline	147
6.5	Best fit reflex velocities for the star 51 Pegasi derived from two radial velocity programs	148
6.6	Best fit reflex velocities for the star HD 110833 derived from the data of Mayor and Queloz	149
6.7	Best fit reflex velocities for the subset of data from HD 110833 with 5 measurements removed	150
6.8	Best fit companion masses and limits for a subset of 14 stars studied by Walker <i>et al.</i>	151
6.8-continued	152
6.8-continued	153
6.9	Best fits for the long period sensitivity fall off parameters derived from the Walker <i>et al.</i> sample	154
6.10	Radial velocities measurements for the stars 36 UMa and β Vir from the Walker <i>et al.</i> sample	155
6.10b	156
6.11	Companion mass limits possible for data of a given quality	157

LIST OF TABLES

2.1	Disk Parameters For SPH Simulations	48
2.2	Disk Parameters for PPM Simulations	49
2.3	Tori and Disk Results in SPH and PPM	50
4.1	Initial Parameters For Simulations	100
6.1	Period Ranges	141
6.2	The Subset of 14 Stars Included in our Analysis	142
6.3	Detection of Significant Periodicities	143

ABSTRACT

In my thesis I present a study of the dynamics and observational characteristics of massive circumstellar disks in two dimensions (r, ϕ) using two complimentary hydrodynamic codes: a ‘Smoothed Particle Hydrodynamic’ (SPH) code and a ‘Piecewise Parabolic Method’ (PPM) code. I also study the detection limits available to radial velocity searches for low mass companions to main sequence stars. This thesis is organized as a series of published or submitted papers, connected by introductory and concluding material. I strongly recommend that readers of this abstract obtain the published versions of each of these papers.

I first outline the progress which has been made in the modeling of the structure and origins of the solar system, then in chapter 2 (*The Astrophysical Journal* v502, p342, with W. Benz, F. Adams and D. Arnett), I proceed with numerical simulations of circumstellar disks using both hydrodynamic codes assuming a ‘locally isothermal’ equation of state. The disks studied range in mass from $0.05M_*$ to $1.0M_*$ and in initial minimum Toomre Q value from 1.1 to 3.0. Massive disks ($M_D > 0.2M_*$) tend to form grand design spiral structure with 1–3 arms, while low mass disks ($M_D \leq 0.2M_*$) tend to form filamentary, >4 armed spiral structures. Disks with minimum Toomre stability $Q \lesssim 2.0$ are dynamically active and structures within each disk become distorted, break apart and reform on orbital time scales. Spiral arms in disks with $Q \lesssim 1.5$ frequently collapse into clumps. I perform a detailed comparison of the two numerical techniques employed and conclude that SPH is unable to follow the linear instability regime of the disk systems due to noise inherent in the method.

In chapter 4 (submitted to *The Astrophysical Journal* with W. Benz and T. Ruzmaikina), I relax the assumption the locally isothermal evolution assumption and instead include simple heating and cooling prescriptions for the system. Under these physical conditions, the spiral arm growth is suppressed in the inner 1/3 of the disks relative to the isothermal evolution and in the remainder, changes character to more diffuse spiral structures. I synthesize spectral energy distributions (SEDs) from the simulations and compare them to fiducial SEDs derived from observed systems. The size distribution of grains in the inner disk can have marked consequences on the near infrared portion of the SED. After being vaporized in a hot midplane region, the

grains do not reform quickly into the size distribution on which most opacity calculations are based. With the original opacities, near infrared emission suppressed relative to observations, with a plausible modification to the opacity, a more realistic SED is obtained. At long wavelengths, insufficient flux is produced and we conclude that the internal heating processes included in our model (due e.g. to gravitational torques) do not provide a large fraction of the thermal energy present in the outer portions of accretion disks.

In chapter 6 (*The Astrophysical Journal* v500, p940 with Roger Angel), I examine the limits which may be placed upon the detection of planets, brown dwarfs and low mass stellar companions using radial velocity measurements. I derive an analytic expression describing the amplitude limits for periodic signals which may be obtained from a set of data of known duration, number of measurements and precision. I have verified the formalism with Monte Carlo experiments and outlined the regions of its validity. I have used the technique to suggest a strategy for continuing large radial velocity searches for low mass companions.

In chapter 7, I outline several problems which may be profitably addressed by building on this work.

CHAPTER 1

HOW WE GOT TO THIS POINT AND WHERE WE'RE GOING

Understanding the character and origin of our solar system and, more generally, of other stars and planetary systems is a problem which has been under study for a large portion of human history. In this introductory chapter I will outline some of the important steps in the development of our understanding of our solar system and of the origin of solar systems in general. I hope that you as a reader finds this as amusing to read as it was amusing for me to write.

Modern records show Greek, Babylonian and Chinese scholars as some of the earliest to make a systematic study of the subject. Due to limited access to their work, similar studies in other parts of the world (e.g. Central America) have contributed to a lesser extent to the current paradigms.¹

Some of the earliest to put forth a model for the solar system were the Pythagoreans, a school founded by the man whose name it bears. The work of this school is unfortunately largely available only through secondhand sources, since they did not generally widely publish their work. They hypothesized a model of a central fire with a spherical earth, the sun, the moon and the stars orbiting around it on circular trajectories. Later Pythagoreans theorized that the earth instead rotated in space (Heraclides, ca. 340 BC). The circumference of the earth was later determined from observations of shadow lengths at different latitudes by Eratosthenes (Eratosthenes ca. 220BC). Also following up the heliocentric theory of the heavens, Aristarchus (ca. 260 BC) determined the size of and distance to the sun and moon.

Eudoxus of Cnidus (ca. 365 BC) proposed what, after a number of modifications, became one of two standard models of the motion of stars through the heavens. In this model, celestial objects orbited the earth on spheres of greater or lesser distance from the earth. Most objects ('the fixed stars') were fixed to an imaginary celestial sphere which rotated around the earth once a day. Five 'stars' which behaved peculiarly were given the special designation 'planets' and were fixed to separate imaginary spheres. The sun and moon were similarly distinguished and given their own spheres.

Due primarily to the efforts of Ptolemy in his landmark treatise on the subject (Ptolemy ca. 150AD), the geocentric model gained favor over the heliocentric models and remained the standard for fifteen centuries. He summarizes and extends the work of many previous astronomers (notably Hipparchus ca. 160 BC, whose work and that of most of his predecessors is largely unavailable), and describes a cosmology in which the earth occupied the center of the

¹In the spirit of referencing original source material, I have done so where possible throughout much of this introduction. In the spirit of obtaining a good historical background of ancient astronomy, I'd recommend Dreyer's *History of Astronomy* or Heath's *Aristarchus of Samos* as excellent introductions to the subject.

universe, celestial objects moved in uniform circular motion around the center, each at a different distance. Smaller circles ('epicycles') were invoked to fix discrepancies between the model and the observations.

A formalism called 'algebra' (al-Khowarizmi ca. 820 AD), suitable for rigorous mathematical models of astronomical observations, was developed and put on a level footing with the geometric mathematics of the Greeks. Many of the geometric constructs of earlier workers (e.g. the Tables of Chords, calculated by various authors) were transformed into the new algebraic form as tables of sines and cosines. In spite of the concurrent studies of astronomy, by the same workers, algebra was not incorporated into the physical models for many more centuries.

Precise observations of the heavens and the redevelopment of the heliocentric model of Aristarchus by Copernicus (Copernicus ca. 1530, 1543) began to overturn the geocentric universe with a heliocentric model in which the earth was one member of a system of objects traveling in circular orbits around the sun. Circular epicycles were still required to reproduce the observed motion but were of smaller size and fewer were required to reproduce the observations.

Developments in instrumentation (Brahe 1598), and observational techniques (Brahe & Kepler 1602) soon resulted in published catalogues (Kepler, Brahe & Eckebrecht 1627) of new, precise astronomical observations of the motions of celestial objects in the solar system over the course of several decades of time. Building on this voluminous database, Kepler (1609, 1619) fit the observations into an empirical framework of laws governing the motion of the planets around the sun. This framework in fact forms the basis of most orbital motion problems today and the 'Keplerian' motion noted throughout this thesis (minus the many astrological implications) is identical to that outlined in Kepler's original works.

Parallel developments in instrumentation (Digges 1571, Lippershey 1608) enabled, by means of a 'telescope', many revolutionary discoveries and observations to be made of the Jovian moons, phases of Venus and Mercury, mountains on the moon (Galilei 1610) and sunspots (Fabricius 1611) which rebutted nearly all of the original criticisms of the Copernican model. Only three criticisms (absence of stellar parallax measurements, the possible presence of an 'aether' and the precession of the orbit of the planet Mercury) remained much longer, being laid to rest only in 1838 (Bessel 1838,1840), 1887 (Michelson and Morley 1887) and 1917 (Einstein 1917), respectively. A review article (Galilei 1632) summarized and compared the so called 'Ptolemaic' and 'Copernican' models and many of the outstanding problems with each and, over the next several decades the Copernican model became the standard.

In the years which followed, Newton (Newton 1687) provided a confirmation of Kepler's empirically derived framework on an entirely theoretical basis. The epicyclic frequency discussed at many points in the following chapters (see esp. ch. 2 and 4) is based upon a solution to orbital motion of celestial bodies made within Newton's theoretical framework. Based upon this same solution, we may now note that had Ptolemaic system allowed for the possibility of elliptical epicycles (specifically with an axis ratio of 2:1) the discrepancies between observations and the Ptolemaic theory would have been much less pronounced and the Copernican model may therefore have been much less readily accepted.

Most of the scientific efforts made until the late 1700's and early 1800's went into describing the physical inventory of the solar system and the character of the motion of the bodies within it. Within the past 200 years, observations have been both precise enough and of a sufficiently diverse nature that a reasonable effort to understand the origin of the solar system and of stars like the sun has been made. With this mathematical and cosmological framework, the development of a theory of the origin of the solar system began to take the shape it holds til this day. Kant (1755) proposed a 'solar nebula hypothesis' wherein the sun and the planets in the solar system began

as a cloud of gas which then proceeded to collapse. Laplace (1796) placed the study of the solar system as a whole onto a solid mathematical framework and outlined a possible theory of how the collapse might take place. Physical conditions under which collapse could occur were outlined by Jeans (Jeans 1902) in which he relates the balance between the self gravity (characterized by the mass density) and internal pressure (characterized by the sound speed) of a cloud.

Observations of stars outside the solar system (Hertzsprung 1911 and independently Russell 1914) showed that a number of differences exist in the apparent color and luminosity of between various stars in the heavens. These differences could be attributed on the one hand, to a ‘main series’ of stars with similar radii but widely differing colors and luminosities, and on the other hand, to other sequences of giant stars with widely ranging radii. Once the sizes and luminosities of stars became known it was apparent that they were emitting prodigious amounts of energy, but the source of the energy was unclear (see e.g. the review of Jeans 1929). Perrin (1919) and later Eddington (1920) proposed that the source of the energy radiating from stars was derived from transmutation of the elements, a theory which over the next several decades was shown to be correct (see e.g. Bethe & Critchfield 1938, Bethe 1939, and the review of Burbidge et al. 1957).

Regardless of their source of energy, stars had to evolve from some other form of matter before they started to undergo any nuclear fusion, and therefore we might hope to observe some stars which are quite young if the evolutionary process is ongoing. Joy (1945, 1949) discovered a new class of stars, which he named ‘T Tauri’ stars after one of the brightest objects in the new class, which were variable in their brightness over time but which were not at all periodic. They also did not fit well into the Hertzsprung/Russell picture of dwarf and giant stars, since they lay some 1–3 magnitudes above the main sequence (Herbig 1952, Walker 1956), which is consistent with a star undergoing gravitational collapse prior to ignition of nuclear fusion. The stars in the class were nearly always associated with dense nebulosity and molecular clouds, leading to the belief that these stars were very young. Further evidence in favor of this hypothesis includes the discoveries that on the one hand the photospheres of this class of stars are very active photospheres (Herbig 1970) and on the other hand that they emit energy far in excess of stellar blackbody emission in the infrared (Mendoza 1966, 1968). Taken together these observations suggest a model of a cool disk slowly losing its orbital energy (the IR emission) and accreting onto the central star (the photospheric activity).

The solar nebula hypothesis and the development of mathematical models of the collapse itself provided a strong impetus for the study of accretion disks, since with the collapse of any realistic cloud of gas there will be some component of angular momentum. Among the first to make a systematic study of disks were the Lindblads, who studied mainly galactic disk systems and developed the theory of spiral structure in a nearly annual series of papers (e.g. Lindblad 1960, 1963) and showed that spiral structure could be explained as a quasi-static phenomenon by the fact that the quantity, $\Omega(r) - \kappa(r)/2$, where $\Omega(r)$ and $\kappa(r)$ are the angular and epicyclic frequencies of matter in the disk, is approximately constant over a large range of radii. This implies that resonant effects may build up the disk into a stable pattern as matter in part of the disk orbiting the star at one radius acts upon matter orbiting at a much different location.

If in fact such accretion disks exist around some stars (and it is now quite evident both from direct and indirect observations that they do—see discussion throughout this work), they must be transient objects, since we see few or no signs of disks around most stars. Lynden-Bell & Pringle (1973) showed that a viscous disk will transport mass radially inward through the disk while angular momentum will be transported radially outward, ultimately ending with nearly all of the disk mass transported into the star and all of the angular momentum transported to infinity. Molecular viscosity however had long since been shown to be far too small to evolve the disk in the available 10^6 – 10^7 yr (von Weizsäcker 1943).

Work by Shakura and Sunyaev (1974) used dimensional arguments to parameterize the magnitude of the viscosity as a function of the sound speed and the scale height of the disk, but this parameterization has little physical basis and has primarily been used as a black box dissipation source. A free parameter, ‘ α ’, combines all of the unknown physical dissipation into a single dimensionless number. In practice, and in the absence of a better model, tuning α to the value which best fits the model to the observations has become the method of choice for many disk models.

For some disks a viscous model is inadequate for a correct understanding of the morphology of the system. Galactic disks, for example, show large spiral shaped density variations. On smaller scales, a similar physical picture may apply to the collapse of the molecular clouds during the star formation process, though direct evidence for such structure is not yet available. Lin & Shu (1964, 1966) theorized that spiral structure could in fact be characterized as density waves and so the formidable mathematical apparatus developed to describe waves could be applied. The development of this density wave theory led at the same time (Toomre 1964) to an extension of the Jean’s criterion for cloud collapse to centrifugally supported disk systems. This condition defines the relationship between the local gas or particle pressure (characterized as a local velocity dispersion of particles or as a sound speed), rotational shear and local self gravity (characterized by the local surface density of mass) under which a disk will become unstable to ring formation and eventual local collapse. In chapter’s 2 and 4, we will study disk systems which are marginally stable according to this criterion and which develop spiral structure which we will compare to theoretical predictions made based on developments of the spiral density wave model of accretion disks.

Without advances in computational hardware (Atanasoff 1940, Eckert et al. 1945, von Neumann 1945) and algorithms for the numerical solution of differential equations (Kutta 1901, Courant, Friedrichs & Lewy 1928, for hydrodynamic equations in particular see e.g. von Neumann & Richtmyer 1950, Godunov 1959, Lucy 1977, Gingold & Monaghan 1977) the loss of one or two dimensional symmetry (ie. planar, spherical or cylindrical symmetry) may have proven insurmountable in attempts to model the behavior of astrophysical systems in general and forming stars or the solar system in particular. The data were becoming precise enough that physical models had to account for more phenomena than could be included in purely analytic (mathematical) methods. However, with these new algorithms and hardware tools and the rate of increase in the density and complexity of electronic components (Moore 1965), the consequent increase in the speed, size and complexity of computational models has been able to keep pace with observed systems (at least somewhat!). The work presented everywhere in this thesis could not have proceeded without the development of such computational resources.

The state of the study of star formation as of about ten years ago is summarized in the review article of Shu, Adams & Lizano (1987). They describe four stages during the formation of stars. The first stage is characterized by the formation of dense cores of gas and dust within molecular clouds. At some point, a core collapses to form a protostar with a disk surrounding it. Later, the star/disk system begins to eject matter via bipolar outflows and continues to accrete matter from the cloud. Finally, accretion and outflow cease, the disk decays and the star evolves onto the main sequence. While this paradigm provides a qualitative picture of the star formation process, many important questions remain.

One example is that this paradigm only models the formation of single stars. Unfortunately, we know that there are lots of stars which are observed to be in binary or even higher order multiples. A survey of one class of such objects (‘spectroscopic binaries’, or binaries whose observed spectral lines are observed to vary periodically and whose motions can be fit to Keplerian orbits) by Duquennoy and Mayor (1991) showed that in fact most stars near the sun are in

multiples. Somehow the theory has to account for these stars as well. More recent observations (Simon et al.1995, Ghez et al.1993, Leinert et al.1993, Reipurth & Zinnecker 1993) have also shown that very young stars are often found in multiple systems. In fact, those observations showed that a higher fraction of young stars are in multiple systems than exist in older stars like those studied by Duquennoy and Mayor.

Another area where understanding is limited is in the evolution of circumstellar disks. How do they form? What is their morphology at different times during the evolution? Do they form spiral density wave structures similar to those seen in galaxies, and do such structures collapse to form binary companions? What mass do such companions have: are they low mass objects like planets or brown dwarfs, or higher mass objects like binary star? The predictions of the α model for the temperature structure of disks during their evolution do not agree with observations. It is also completely inapplicable to a massive disk where spiral structures may develop. Better models must be developed in order to understand these properties of disks.

Still another area of limited understanding is in the formation and evolution of low mass companions like the terrestrial planets and gas giants in the solar system, or of the low mass companions and brown dwarfs recently discovered around other nearby stars. How do these low mass companions form and/or move within the star/disk system?

This thesis continues and builds upon work outlined above (“standing upon the shoulders of giants”—Newton 1675/1676). It is primarily an attempt to better understand the physical processes important during the origin and evolution of solar type stars and of the solar system, the observational consequences of those processes and the limits which can be placed upon detecting certain signatures of already formed systems. This work is organized as a series of published or publishable papers connected by short interludes which describe a little of the background behind the work which follows. The final chapter is an attempt to outline of few of the directions which will be profitable avenues for further research. In the paragraphs below I outline, in a short abstract form, chapter 2 in terms of the improvements beyond previous work and the results which were obtained from this study.

Previous studies of circumstellar disks have provided analyses based on two strategies: (1) analytic or perturbative techniques and (2) numerical simulations of either cloud collapse resulting in a coarsely resolved disk or of already formed, but spatially narrow, tori. Working in collaboration with my advisors Willy Benz and Dave Arnett, as well as Fred Adams at the University of Michigan, I have studied the dynamical evolution of massive circumstellar disks that may form early in the history of young stellar systems using numerical simulations.

In chapter 2, we present a series of two dimensional hydrodynamic simulations of massive disks around protostars. We have used two complementary numerical hydrodynamic methods (the ‘Piecewise Parabolic Method’ and the ‘Smoothed Particle Hydrodynamic’ method) to simulate the growth and evolution of spiral arms within the disks. The simulations using each code are compared to discover differences due to error in the methods used. For this problem, the strengths of the codes overlap only in a limited fashion, but similarities exist in their predictions, including spiral arm pattern speeds and morphological features.

In these calculations, we have studied the evolution of massive circumstellar disks with larger radial extent and over a wider range of parameter space than has been possible before. From the earliest times, their evolution is a strongly dynamic process rather than a smooth progression toward eventual nonlinear behavior. Processes that occur in both the extreme inner and outer radial regions affect the growth of instabilities over the entire disk. Effects important for the global morphology of the system can originate at quite small distances from the star. Therefore, analyses which neglect the inner disk will not model the evolution of the system correctly.

The disks studied here range in mass from $0.05M_*$ to $1.0M_*$ and in initial minimum Toomre Q value from 1.1 to 3.0. We adopt simple power laws for the initial density and temperature in the disk with an isothermal ($\gamma = 1$) equation of state. The disks are locally isothermal. We allow the central star to move freely in response to growing perturbations. The simulations using each code are compared to discover differences due to limitations in the methods used. For this problem, the strengths of the codes overlap only in a limited fashion, but similarities exist in their predictions, including spiral arm pattern speeds and morphological features. Our results represent limiting cases (i.e. systems evolved isothermally) rather than true physical systems.

We show that disks with minimum Toomre stability $Q \lesssim 1.5$ (recall that $Q < 1$ implies instability to the growth of ring-like structures) are dynamically active and spiral structures growing within each disk become distorted, break apart and reform on orbital time scales. A marked change in the character of spiral structure occurs in simulations with differing disk mass. Low mass disks ($M_D \leq 0.2M_*$) form filamentary spiral structures with $\gtrsim 5$ arms. High mass disks form grand design spiral structures with 1–3 arms. Eventual collapse of such structures in more physically realistic models may be responsible for producing some stellar or brown dwarf companions. A detailed picture of their evolution is therefore required to understand the formation of such companions.

In our SPH simulations, disks with initial minimum $Q = 1.5$ or lower break up into proto-binary or proto-planetary clumps. However, these simulations cannot follow the physics important for the flow and must be terminated before the system has completely evolved. At their termination, PPM simulations with similar initial conditions show uneven mass distributions within spiral arms, suggesting that clumping behavior might result if they were carried further. Simulations of tori, for which SPH and PPM are directly comparable, do show clumping in both codes. Concern that the point-like nature of SPH exaggerates clumping, that our representation of the gravitational potential in PPM is too coarse, and that our physics assumptions are too simple, suggest caution in interpretation of the clumping in both the disk and torus simulations.

We calculate approximate growth rates for the spiral patterns and compared the results of our simulations to the predictions of linearized analyses. We examine in particular the SLING mechanism proposed by Adams, Ruden and Shu (1989). They show that a resonance between the motion of the star and a one armed spiral pattern may stimulate growth of the one armed pattern in the outer disk even if other spiral patterns are suppressed. Our simulations show that the one-armed ($m = 1$) spiral arm is not the fastest growing pattern of most disks. Also, due to the dynamic nature of the growth, a resonant growth mechanism such as SLING may be of limited value because pattern speeds and amplitudes display wide, short term variations.

Several qualitative features of the SLING mechanism are reproduced in our simulations. The changeover in behavior between filamentary spiral structures and grand design structures occurs at the disk mass for which the SLING instability is predicted to become active. Approximate growth rates fitted to the spiral patterns present show that the one armed pattern growth rates are similar to those predicted by Adams et al., though they are neither the largest amplitude nor the fastest growing patterns for most systems.

CHAPTER 2

DYNAMICS OF CIRCUMSTELLAR DISKS

Over the past several years a broad paradigm of star formation has been developed (see Shu, Adams & Lizano 1987). First, a cloud of gas and dust collapses and forms a protostar with a surrounding disk. Later the star/disk system ejects matter in outflows as well as continuing to accrete matter from the cloud. Finally, accretion and outflow cease and the star gradually loses its disk and evolves onto the main sequence. While this paradigm provides for a good qualitative picture of the star formation process, many important issues require further work. For example, observations by several groups (Simon *et al.* 1995, Ghez *et al.* 1993, Leinert *et al.* 1993, Reipurth & Zinnecker 1993) show that young stars in many different star forming regions are commonly found in binary or higher order multiple systems, with a broad peak in separation distance at around 30 AU. In addition, many of the higher order multiples show hierarchical characteristics: a distant companion orbiting a close binary for example. In what manner are multiple systems such as these formed?

A variety of studies have been undertaken to model the processes leading to the observed systems. One class of models begins with the collapse of a cloud of matter. These results (Bate *et al.* 1995, Foster & Boss 1996, Boss 1995, Burkert & Bodenheimer 1993, Bonnell & Bastien 1992, Myhill & Kaula 1992) show that both single stars and multiple systems can be formed from the collapse and subsequent fragmentation of rotating, spherical or elongated molecular cloud cores. This class of simulations focus on the collapse phase, but do not follow in detail the dynamics of disks formed from the material with initially higher angular momentum.

In addition, a number of models extended beyond the initial collapse (Bonnell 1994, Pickett *et al.* 1996, Woodward *et al.* 1994) have shown that post-collapse objects can be driven into fragmentation, or into spiral arm and bar formation prior to the development of a Keplerian disk. Laughlin & Bodenheimer (1994) have simulated the evolution of a collapsing cloud in 2D and then followed its late time behavior with a 3D disk simulation. They have found that such a collapse leads to a core plus a long lived, broad torus. The development of $m = 1$ and $m = 2$ spiral patterns may lead to late time fragmentation of the torus (m is the number of arms in the spiral pattern).

As a star-disk or multiple-star-disk system evolves, the dynamics of the disk itself as well as its interaction with the star or binary becomes important in determining the final configuration of the system. Depending on its mass and temperature, a disk may develop spiral density waves and viscous phenomena of varying importance. Each may be capable of processing matter through the disk as well as influencing how the disk eventually decays away as the star evolves onto the main sequence.

A variety of mechanisms for producing of spiral instabilities in disks around single stars have

been suggested. An incomplete list includes the linear perturbation results of Adams, Ruden & Shu (1989; hereafter ARS) who suggest a mechanism ('SLING' – see Shu *et al.* 1990; hereafter STAR) by which a resonance between the star and a one armed ($m=1$) spiral mode may become globally unstable. Both perturbation theory (Papaloizou & Lin 1989) and numerical calculation (Papaloizou & Savonje 1991, Heemskirk *et al.* 1992) have shown another instability mechanism based on the distribution of specific vorticity (termed "vortensity") which can influence evolution in disks and tori. It is driven primarily by wave interactions at corotation and can act either to suppress or amplify spiral waves in the disk, depending on the vortensity gradient there. Another family of instabilities is based upon vortensity gradients at the boundaries of the disk or torus. The SWING amplifier (Goldreich & Lynden-Bell 1965, Julian & Toomre 1966, Goldreich & Tremaine 1978) provides an instability channel whereby low amplitude leading spiral arms unwind and are transformed into much larger amplitude trailing waves. A feedback cycle then creates additional leading waves and the instability grows.

This paper is a continuation of work by two of us (Adams & Benz 1992, hereafter AB92), who began modeling of disks of mass $M_D \gtrsim 0.5M_*$ and observed formation of spiral arms and clumps. We present a series of two dimensional numerical simulations of circumstellar disks with masses between $0.05M_*$ and $1.0M_*$. We attempt to characterize the growth of instabilities and pay particular attention to the existence and effect of the SLING instability. In section 2.1, we outline the numerical methods used and discuss the limitations of each code and their effects on our simulations. In section 2.2, we outline the initial conditions adopted for the disks studied and in section 2.3, we first describe qualitatively the results of our simulations and then begin a quantitative analysis of the pattern growth, the correspondence between two hydrodynamic codes, and the correspondence between linear analyses and hydrodynamic simulations. In Section 2.4, we summarize the results and their significance in the evolution of stars and star systems.

2.1. The Codes

2.1.1. Solving the Hydrodynamic Equations

In order to understand the properties of protostellar disks we have adapted two complementary hydrodynamic codes to the task of simulating such evolution: the Smoothed Particle Hydrodynamic (SPH) method and the Piecewise Parabolic Method (PPM). These codes use very different techniques for solving the equations of hydrodynamics, and it is hoped that, by the use of such widely different techniques, numerical artifacts can be sorted out from true physical evolution. Each code has unique features that allow the simulation of these systems in some regimes not accessible to the other.

The SPH method (see reviews by Benz 1990, Monaghan 1992) uses a procedure by which hydrodynamic quantities and their derivatives are calculated from an interpolation technique over neighboring particles. The interpolation kernel used in our simulations is the standard B-spline kernel with compact support. The smoothing length h is varied over time in a manner such that the number of neighbors is approximately conserved, subject to the condition that a minimum value of $h \sim R_D/1700$ (where R_D is the disk radius) is set to ensure time steps do not become too small. A second order Runge-Kutta-Fehlberg integrator which includes time step control is used to evolve the system in time. Being gridless, the main advantage of the SPH method in our context lies in its ability to follow structure formation anywhere in the disk without the limitations associated with a prescribed grid. The two main disadvantages of the SPH technique are (1) the inherent random noise level associated with the discrete representation of the fluid and (2) the high shear component of the dissipation connected with the mathematical formulation of the artificial viscosity.

We also have adapted the PROMETHEUS hydrodynamic code (Fryxell, Müller & Arnett 1989, 1991) to the problem of evolving disks around protostars. PROMETHEUS is based on the ‘Piecewise Parabolic Method’ (PPM) of Colella & Woodward (1984) in which a high order polynomial interpolation is used to determine cell edge values used in calculating a second order solution to the Riemann shock tube problem at each cell boundary. The interpolation is modified in regions of sharp discontinuities to track shocks and contact discontinuities more closely and retain their sharpness, while a monotonizing condition smoothes out unphysical oscillations. The solution to the one-dimensional Riemann problem is then used to calculate fluxes and advance the solution in time. This code was selected because of its low numerical dissipation and its excellent resolution of discontinuities and shocks.

Both codes incorporate self-gravity using modified versions of the binary tree described in Benz *et al.* (1990) which approximates the gravity of groups of distant particles in a multipole expansion while calculating interactions of nearby particles explicitly. Gravitational forces due to neighbor particles are softened to avoid divergences as particles pass near each other. Due to the organization of the grid, the tree construction can be considerably simplified in the PPM version by substituting a procedure by which adjacent grid cells (modeled as point masses for the purpose of the gravity calculation) or groups of grid cells become progressively higher nodes in the tree. Two simulations run at higher resolution (simulations *pch2* and *pch6* in table 2.2 below) implemented an FFT based solution to Poisson’s equation (Binney & Tremaine 1987, pp. 96ff). Results for a disk simulation at identical resolution showed that the tree and the FFT solutions gave identical dynamical results. However the FFT version proved to be substantially faster. The torus simulations of section 2.3.3, which are more sensitive to resolution, are also more sensitive to the implementation of the Poisson solver. In these cases the simulations using the tree code gave slower pattern growth rates than simulations using the FFT.

It is important to make a distinction between the resolution of the hydrodynamics and that of the representation of the gravitational potential. Just as PPM is well adapted for discontinuities, SPH is well adapted for gravitational clumping. The density reconstruction procedure utilized by PPM contains more structure than is available from the N grid point algorithm used here. Better resolution of the gravitational potential may be possible using densities defined at both the cell centers and at cell interfaces. Further, this grid effectively implies a gravitational softening which is about one cell in size. This algorithm uses only the cell center information, and references below to grid resolution in PPM simulations will imply this fact.

2.1.2. Viscosity in the Codes

Because disk evolution is partially driven by viscosity in the disk, we must look carefully at issues related to numerical viscosity. Except for codes based on a local solution of the Riemann shock problem such as PPM, most methods require implementation of an artificial viscosity to enforce stability and/or improve the shock treatment by the code. In this regard SPH is no exception and our version of the code implements the standard form discussed in Benz (1990). We use bulk and von Neumann-Richtmyer (so called ‘ $\bar{\alpha}$ ’ and ‘ β ’) viscosities to simulate viscous pressures which are linear and quadratic in the velocity divergence. We use the standard values for each of the coefficients, with $\bar{\alpha} = 1$ and $\beta = 2$. We incorporate a switch (see Balsara 1995) which acts to reduce substantially the large undesirable shear component associated with the standard form.

The bulk component of the artificial viscosity $\bar{\alpha}$ in the SPH code can be identified with a kinematic viscosity ν (see Murray 1995) using the relation

$$\nu = \frac{\bar{\alpha} c_s h}{8}, \quad (2.1)$$

where c_s is the sound speed and h is the smoothing length of a particle. It is possible to relate

the coefficient of bulk artificial viscosity $\bar{\alpha}$ to the α -parameter of the standard viscous prescription of accretion disks. We equate the artificial viscosity to the Shakura & Sunyaev (1973) viscosity (defined by $\nu = \alpha c_s H$ and the scale height, H , is defined as $H = c_s/\Omega$, the local sound speed over the angular rotation rate. Solving for α yields

$$\alpha = \frac{f\bar{\alpha}h\Omega}{8c_s}, \quad (2.2)$$

where f is the shear reduction factor discussed in Benz 1990 suitably averaged over particles and time. We caution the reader that the identification of the SPH form of the viscosity is not necessarily equivalent to that of the Shakura and Sunyaev form, especially because of the approximate manner in which the Balsara switch must be taken into account. We estimate equation [2.2] may be valid to a factor of a few but should not be taken as exact.

For a nearly Keplerian disk with a temperature $T \propto r^{-1/2}$ and a roughly linear variation of the smoothing length, h , with radius, we obtain $\alpha \propto r^{-1/4}$. Depending on the temperature constant describing each disk (T_0 , see section 2.2.1), α is of order $\sim 10^{-2}$. Only at small radii ($r \lesssim 2\text{AU}$) and low disk mass (for which T_0 becomes correspondingly small for a specified value of Q_{\min}) does α rise to values in the range $\alpha \sim 0.1 - 1$. These values of α imply that the viscous time scale, $\tau = r^2/\nu$, remains significantly longer than the few orbital time scales we simulate. For most of the disk, the SPH viscosity is small enough not to affect the evolution of the disk significantly. The von Neumann (β) term in the viscosity does not mirror the alpha prescription as the bulk term does. Derived from the assumption that the viscosity is proportional to square of the velocity divergence, its effect is limited to portions of the flow in which shocks occur.

The numerical viscosity inherent to the PPM code is difficult to quantify. The nonlinear nature of the Riemann solver (with the associated PPM ‘switches’ to sharpen discontinuities and enforce monotonicity) renders an artificial viscosity term unnecessary. However, a small numerical viscosity still appears in the code. Porter & Woodward (1994) derive fits for numerical dissipation proportional to the third and fourth powers of $\delta x/\lambda$ where δx is a cell dimension and λ is the wavelength of a disturbance. Thus, large scale disturbances like the spiral arms will experience little dissipation, but small scale motions will be damped more.

2.2. Physical Assumptions and Constraints

Because our simulations involve dimensionless quantities such as the disk/star mass ratio and the Toomre stability parameter Q , the physics itself is scalable to systems of different size. We shall express all quantities in units with values typical of the early stages of protostellar evolution. These units are also comparable (for the most massive disk simulations) to the final dimensions of our own solar system. The star mass will be assumed $M_* = 0.5M_\odot$ and the disk radius $R_D = 50$ AU. Time units are given in either years or the disk orbit period defined by $T_D = 2\pi\sqrt{R_D^3/GM_*}$ which, with the mass and radius given above, is equal to 500 years.

2.2.1. Circumstellar Disk Initial Conditions

The initial conditions for prototype low and high mass disks are summarized graphically in figures 2.1 and 2.2 for our PPM and SPH simulations respectively. We assume that the disks are vertically thin so that two dimensional (r, ϕ) simulations are justified. The variables of interest (density, pressure, etc.) are taken to be vertically integrated quantities. Magnetic fields are neglected in our simulations.

In functional form, the disk mass is initially distributed according to a density power law

$$\Sigma(r) = \Sigma_0 \left[1 + \left(\frac{r}{r_c} \right)^2 \right]^{-\frac{p}{2}}, \quad (2.3)$$

where the power law exponent p is set to $3/2$. As we shall discuss in the following section we found that our PPM simulations implementing the initial density profile of eq. [2.3] became violently dynamic near the inner grid edge and we could not simulate the evolution of the system. Instead, we have chosen to remove matter completely at small radii in our PPM runs by adopting an initial density law which ensures that little matter remains at small radii or interacts with the boundary. This density law takes the form

$$\Sigma(r) = \Sigma_0 \left\{ \frac{[1 - e^{-\left(\frac{r-R_0}{R_c}\right)^2}]}{r} \right\}^p, \quad (2.4)$$

where R_0 is set to the radius of the innermost boundary cell and R_c is set arbitrarily to 6 AU. With this choice, the surface density is substantially reduced near the inner boundary while retaining a nearly pure $r^{-3/2}$ distribution for radii greater than about 10 AU. The temperature is given by a similar power law as

$$T(r) = T_0 \left[1 + \left(\frac{r}{r_c} \right)^2 \right]^{-\frac{q}{2}}, \quad (2.5)$$

with the exponent q set to $1/2$. The softening radius r_c for both power laws is set to $r_c = R_D/50 (=1$ AU).

We choose the value of the temperature power law index based on observed temperature profiles in T Tauri disks (see Beckwith *et al.* 1990; Adams *et al.* 1990). The density power law is much less well constrained, and our choice of $p = 3/2$ is roughly consistent with the infall collapse calculations of Cassen & Moosman (1981). As an additional motivation, this choice of exponents matches the one adopted by ARS and allows a direct comparison with their work.

Σ_0 and T_0 are determined from the disk mass and a choice of the minimum value over the disk of the Toomre stability parameter Q , defined as

$$Q = \frac{\kappa c_s}{\pi G \Sigma}, \quad (2.6)$$

where κ is the local epicyclic frequency. For an ideal gas with an isothermal equation of state (see section 2.2.3), the sound speed is defined as

$$c_s^2 = \frac{kT}{\mu m_p}, \quad (2.7)$$

where the mean molecular weight is μ and we assume the gas is of solar composition.

By definition, the Toomre Q parameter divides the region of phase space for which axisymmetric disturbances (rings) grow exponentially from that in which they are damped. It is derived from the dispersion relation for waves in a disk given by (see Binney & Tremaine 1987)

$$\omega^2 = c_s^2 k^2 - 2\pi G \Sigma |k| + \kappa^2 \quad (2.8)$$

where ω is the complex pattern frequency and k is the wavenumber. Mathematically speaking, if $\omega^2 > 0$ the wave equation from which the dispersion relation is derived will have exponentially

decaying solutions, while if $\omega^2 < 0$ it will have exponentially growing solutions. The line of neutral stability at $\omega = 0$ defines Q . Equation 2.8 then becomes quadratic in the wavenumber k and whose solution yields the condition defined by eq. 2.6.

The temperature and density laws above produce a profile for the instability parameter Q that is nearly flat over the largest portion of the disk, with a steep rise at small radii and a shallow increase towards the outer edge of the disk. The minimum value of Q in the disk is therefore located at $\sim 30 - 40$ AU, depending upon the mass and temperature of a specific disk.

Another common criterion of instability in disks is the X parameter, which is important for so called SWING amplification and is defined by

$$X = \frac{r\kappa^2}{2\pi m G \Sigma}, \quad (2.9)$$

with m the number of spiral arms (the azimuthal wave number). In this instability ‘leading’ spiral waves (i.e. those for which the spiral winds up in the same direction as the orbital motion) unwind and become ‘trailing’ spiral waves, which then are reflected through the origin and the process repeats. Ordinarily, in Keplerian systems where an inner Lindblad resonance exists, the SWING instability is suppressed because the trailing waves reflection instead off of the Lindblad resonance. Nevertheless, we shall examine the value of the X parameter to make certain that contributions to the instability growth from SWING may be neglected. In order for a system to be unstable to SWING amplification, the value of X must be $\lesssim 3$ in the region of interest.

The X parameter shows a similar pattern to that seen for Q , but with a steeper increase at large radii. For most of the disks we study, X is larger than that required to keep the disk stable for the lowest order spiral modes, so that we expect SWING not to contribute to the growth of instabilities. Like the Q and X profiles, the vortensity profile shows a steep increase at small radii. In this case, such an increase may serve to stimulate growth due to the family of instabilities discussed by Papaloizou and Lin (1989). We will discuss this possibility in more detail below.

The star is represented as a point mass, free to move in response to gravitational forces from the surrounding disk. Initially, disk matter is placed on circular orbits around the star, with rotational equilibrium in the disk and radial velocities set to zero. Gravitational and pressure forces are balanced with centrifugal forces such that the rotation curve is given by

$$\Omega^2(r) = \frac{GM_*}{r^3} + \frac{1}{r} \frac{\partial \Psi_D}{\partial r} + \frac{1}{r} \frac{\nabla P}{\Sigma}, \quad (2.10)$$

where the symbols have their usual meanings and Ψ_D , the gravitational potential of the disk, is calculated numerically with the same potential solver utilized in the full hydrodynamic code. The magnitudes of the pressure and gravitational forces are small compared to the stellar term, therefore the disk is nearly Keplerian in character.

2.2.2. The Construction of Circumstellar Accretion Disks, Boundary Conditions and Numerical Resolution

To complete the specification of the initial state of the systems, we must define the conditions at the boundaries of each simulation. The linearized analyses of ARS suggest that the dynamics of an accretion disk will be relatively insensitive to the implementation of the inner boundary condition, becoming active only at distances far from the star. On the other hand, the shape of outer edge of the disk is predicted to be critical for the eventual growth of the SLING instability. In order to search for evidence of the SLING instability we shall implement boundary conditions which may be favorable to its growth.

To ease time step constraints, we set the inner boundary at a greater distance than that which is physically the case for a star/disk boundary. With a grid code, we can define the inner boundary by modeling the inner regions in some steady state approximation or by modifying the density law at small radii (in effect modeling tori) to reduce interactions with the inner boundary. Since ARS predict that the inner regions of the disk will be relatively stable, instabilities are not expected to grow there, given a disk initially in rotational equilibrium. Any boundary condition which does not perturb this equilibrium should be sufficient to describe the inner disk. Since by assumption, the inner disk begins in rotational equilibrium (i.e. with $v_r = 0$), no matter will cross the boundary and a simple reflecting boundary condition will suffice. The reflecting boundary will also serve a second function. The four wave cycle (STAR) important for the amplification of SLING requires a corotation or Q -barrier from which waves can be reflected or refracted during part of the cycle. Until such resonances may develop on their own further out in the disk, the reflecting boundary serves as a surrogate for the actual resonances.

Our PPM simulations showed that for a pure power law for the density (omitting the core radius of eq. [2.3]), the inner regions of the disk are quite dynamic and unstable. After a few orbits, matter in the inner disk moved off its initial circular orbit and began interacting with the boundary. The effect of these interactions is to give a “kick” to the system center of mass as matter reflects off the boundary. In the worst cases, serious computational problems occurred after 20-50 orbits of the inner disk edge and the calculations had to be stopped.

Several prescriptions for avoiding this behavior were attempted without real success. These prescriptions included allowing matter to accrete through the boundary onto the star, attaching the inner disk matter to the star itself, treating the inner disk as a softened point mass at the origin with varying degrees of softening or by treating the inner disk matter as an additional point mass free to move in response to the star and the rest of the disk. In each case results obtained were strongly dependent on the prescription followed. We conclude that the dynamics important for the global behavior of the physical system extend to quite small radii.

With this degree of activity in the inner disk it becomes reasonable to assume that a portion of the inner disk matter becomes depleted by accretion onto the star or ejected in an outflow on short time scales. The inner disk may expand in the z direction and become truly three dimensional as the dynamical effects create dissipation and heating. In light of these ideas, and in order to concentrate our efforts on the large scale features, we have chosen to implement the density law of eq. [2.4] and study a system for which little mass exists close to the star but which retains a power law profile further out. Due to the already artificial nature of the mass distribution at small radii, little physical meaning can be attached to mass accretion rates through the inner boundary, therefore for simplicity we implement reflecting boundary conditions to complete the specification of the inner grid edge.

For our SPH simulations, we define the inner boundary by establishing an accretion radius at a distance from the current position of the star of $R_D/110 (=0.4 \text{ AU})$. This distance is set to be slightly smaller than the initial position of the innermost ring of particles in the disk. The gravitational softening radius for the star is set to the same value. As a particle’s trajectory takes it inside the accretion/softening radius, its mass and momentum are added to the star and it is removed from the calculation. This inner boundary condition does not prove to be as difficult to manage as in our PPM simulations. Even though a great deal of activity occurs in the inner portion of the disk, no particular computational difficulties were experienced. We believe this activity is largely due to crude boundary conditions which obscure the true physical behavior of the system. Particles near the boundary have no neighbor particles further inward to provide pressure support, while accretion of a particle through the boundary implies a sudden loss of pressure support to its neighbors further out. Also, the stellar gravitational softening reduces the

effect of the star on the orbit of each SPH particle there. A small number of particles near the boundary are strongly affected.

Because of our interest in characterizing disk instabilities, especially SLING, we have experimented with several outer boundary conditions as well. In the PPM simulations we have implemented both a reflecting boundary and a boundary condition in which matter falls onto the outer edge of the disk (an “infall” boundary). With the pure reflecting conditions, we imitate the boundary conditions implemented by ARS which have been identified as critical for the SLING instability. With the infall boundary condition, we relax this assumption slightly to allow the disk edge to begin outward expansion or begin to break up if conditions require.

With the infall boundary, the outer disk edge is defined to be initially located at a cell interface several cells inward from the outermost computational cell. We define the disk boundary assuming an isothermal shock, so that the density and radial component of the velocity are determined directly from the shock jump conditions. Since by definition a shock implies that the tangential velocity across the shock is continuous, we know that at the disk edge, R_D , the ϕ component of the infall velocity is the same as the orbit velocity, $R_D\Omega(R_D)$. If we then specify the temperature of the infalling gas as $T = 10$ K, conservation laws for mass, momentum and energy determine the flow from the shock to the outer grid radius. The infall is kept constant throughout the simulation at the values which initially define it. We note in passing that a flow constructed in this manner is quite artificial and may have little relation to flows in real systems. For our simulations, infall provides a mechanism by which the outer edge of the disk can be reasonably well defined.

In our SPH simulations, we adopt a free outer boundary. This choice has the advantage of simplicity in implementation, but suffers because quantities such as the density or pressure are less well defined within about two smoothing lengths of the boundary (see fig 2.2). The result is that over time the surface density at the disk edge spreads radially to a width of ~ 5 AU. The disk edge is no longer defined by a sharp discontinuity, but does remain distinct except for very high Q_{\min} simulations, for which the mass at the outer disk edge is nearly unbound. The sharp outer boundary condition required for SLING to become active is satisfied under these conditions.

At time zero in our SPH simulations we set approximately 8000 equal mass particles on a series of concentric rings with the innermost ring at a radius of $R_D/100$. For our PPM simulations we use an inner to outer radius ratio of 50 and several grid resolutions. Our main series of simulations, with reflecting outer boundary conditions, have a 64×102 cell cylindrical polar (r, ϕ) grid. Two higher resolution simulations are performed with a 100×152 grid, and we have explored the use of an infall boundary at two resolutions of 44×64 and 64×96 . Grid cells are defined to be ‘squares’ in the sense that $\delta r = Cr\delta\phi$ over the entire grid, with C a constant ~ 1 . With the resolution used for our simulations, SPH particle smoothing lengths are less than a few tenths of one AU in the inner portion of the disk up to ~ 1 AU in the outer disk. Grid resolution in the PPM simulations is of order 0.1 AU at the inner grid edge and ~ 2 AU at the outer edge.

The relatively low resolution of our simulations results in part from the large radial extent of the systems we study. Many of the important dynamical processes in a disk occur on orbital time scales in the outer regions of the disk, but the size of a time step (the Courant condition) is derived from the cell size at the inner grid edge, where the cells are the smallest and the velocities are largest. Assuming nearly Keplerian rotation around the star, an inner grid radius at 1 AU, and a moderate resolution of order 150 azimuthal cells, the time step is a few days, while the dynamical time scale of the disk is a few $T_D = 500$ yr. In order to evolve a given simulation to completion, we must integrate over a half a million or more time steps. For ‘high’ resolution simulations of say, 300 or more azimuthal cells, the number is correspondingly increased. With the workstations available, it is not computationally feasible to run a large number of models to

explore the relevant parameter space. A similar problem exists for our SPH simulations.

2.2.3. The Equation of State and Energy Considerations

In each code, a vertically integrated gas pressure is implemented using a single component, ‘isothermal’ ($\gamma = 1$) gas equation of state given by

$$P = \Sigma c_s^2. \quad (2.11)$$

In PROMETHEUS (our version of the PPM algorithm), a truly isothermal equation of state with $\gamma = 1$ is not easily obtained, therefore we use an ‘almost isothermal’ ideal gas with $\gamma = 1.01$ for these simulations.

Each simulation is evolved isothermally, by which we mean that the temperature of each cell, once defined at time zero (by eq. [2.5] and an input value of Q_{\min}), is fixed thereafter. Loss processes such as radiative cooling are assumed to balance local heating processes in the disk. Under this assumption, a packet of matter which moves radially inward or outward, heats or cools according to the prescribed temperature law. Matter which expands or is compressed is heated or cooled according to the same law.

With SPH comes the ability to choose the manner in which one incorporates the isothermal evolution. We may set the temperature of each particle as a function of its distance to the star (Eulerian implementation), or we may keep its temperature fixed no matter where the particle moves (Lagrangian implementation). In most of our simulations, we have chosen to use the Eulerian version. This choice is dictated by consistency, since the isothermal assumption implies that the star must contribute the bulk of the heating, and by the desire to match as closely as possible the PPM calculations.

2.3. Results of Simulations

With the initial conditions outlined above, we have run a series of simulations with both codes in which we vary disk mass but keep a constant minimum Toomre parameter $Q_{\min} = 1.5$. A free outer boundary condition was implemented for each SPH simulation, while one series of PPM simulations was run with a reflecting outer boundary. A second series of PPM simulations used an infall through the outer few cells onto the outer disk edge, which was assumed to be an initially stable isothermal shock. To explore varying stability, we also ran two SPH and one PPM series varying Q_{\min} between 1.1 and a maximum value defined by the condition that the outer edge of the disk remained bound (for disks with high Q_{\min} , pressure forces begin to dominate over gravity). Each simulation was evolved for periods ranging between a small fraction of an orbital period T_D (in the case of very low Q_{\min} runs in which rapid clumping was seen), to several complete orbital periods for runs in which clumping was not observed.

Unless otherwise specified, no explicit initial perturbations have been assumed beyond computational roundoff error. Due to the discrete representation of the fluid variables, this perturbation translates to a noise level of order 10^{-3} in the hydrodynamic quantities for the SPH calculations. The relatively large amplitude of the noise originates from the fact that the hydrodynamic quantities are smoothed using a fixed number of neighbors (see Herant & Woosley 1994). An increase in the number of particles does not necessarily decrease the noise unless the smoothing extends over a larger number of neighbors. Because of its similarity to Monte Carlo methods, the decrease in noise goes as the square root of the number of neighbors, and so decreases slowly with a large increase in computational cost.

For PPM, the noise level can be made as small as machine precision (while double precision is used internal to the code, single precision is used in initialization and dumps, so we obtain $\sim 10^{-7}$). The PPM simulations are terminated at a perturbation amplitude of $\delta\Sigma/\Sigma \sim 20\%$ because matter on elliptical orbits begins to interact strongly with the inner and outer boundaries. SPH simulations on the other hand, are carried out until clumps begin to form (clumping causes the time step to drop drastically and halt the evolution). Highly stable disks, for which clumps do not form, are terminated when no significant additional evolution is anticipated. Each of the SPH simulations run for much of their duration with high amplitude ($\delta\Sigma/\Sigma \sim 100\%$) perturbations. Comparison simulations on a simple test problem (see section 2.3.3 below) were run to high perturbation amplitude using both SPH and PPM in order to confirm the late time behavior of the SPH simulations.

We did not formally introduce a perturbation in our initial conditions, however two conditions provide indirect seeds for perturbations. First, the disk is cut off at an inner radius which, while small, is nonetheless large compared to the stellar radius. This cut off creates a gravitational potential hump at the center, and is equivalent to a strong seed for the $m = 1$ disturbances. As the star moves away from the origin, it is further accelerated by the hump, effectively sliding down the incline. We show in figure 2.3 the gravitational potential near the origin for the disks with the characteristics described above as well as the tori used in our comparison calculations below (section 2.3.3). By following the procedure of Heemskirk *et al.* (1992), who derive an equation of motion for the star including the zeroth order hump term plus first order perturbations, we note that initially the growth rate for a $m = 1$ pattern will be

$$\gamma_1 = \left(\sqrt{\frac{d^2\Psi_D}{dr^2}} \right)_{r=0}. \quad (2.12)$$

Computing numerically the curvature of the hump, we derive a $m = 1$ growth rate due to the hump of $\gamma_1/\Omega_D \sim 5$. Indeed during the very earliest stages of our simulations ($t \lesssim 0.1T_D$), we find a growth rate of this (quite large) magnitude. After the initial transient, growth rates quickly fall to more sedate levels. The contribution to the long term global growth of instability due to this initial perturbation is thought to be a small component of the total.

A second indirect seed of dynamical instability is connected to the fact that the density law has been softened (eq. [2.3]) or modified (eq. [2.4]) in the innermost regions of the disk in order to avoid a singularity at small radii. This density decrease creates a region of high vortensity gradient which excites wave growth (see Papaloizou and Lin 1989). This instability channel also requires a seed, but its proximity to the inner edge, where orbit times are small, coupled with the hump perturbations, make the time scale for its initial excitation quite short.

Features of our simulations are tabulated in Tables 2.1 and 2.2. The first column of each table represents the name of the simulation for identification. The second column defines the resolution (in number of particles or grid size). Initial disk/star mass ratio and minimum Q are given in columns 3 and 4, while total simulation time and spiral features of each simulation fill out the remaining columns.

We illustrate the phenomena seen in our simulations by presenting two representative cases: mass ratios $M_D/M_* = 1.0$ and $M_D/M_* = 0.2$. Both use initial values of $Q_{\min} = 1.5$. These disks represent points near either end of a spectrum of behavior. In section 2.3.2, we show additional models which vary Q_{\min} , demonstrating behavior along another axis in parameter space. We first examine the qualitative nature of the simulations, then examine in detail the structures which form. A comparison of the results of SPH and PPM and limitations imposed by numerical features is discussed in section 2.3.3.

2.3.1. General Observations and Morphology

Spiral arm growth occurs with varying rates and amplitudes. Growth is not smooth or continuous. Frequently arms change shape, stretch, or break off and drift until hit by another passing disturbance. Well developed spiral arms, while subject to irregular change on short time scales, do survive. In figure 2.4, we show a series of snapshots of particle positions in simulation *scv6*, characterized by $M_D/M_* = 1.0$ and an initial minimum $Q_{\min} = 1.5$. Instability first develops in the central regions of the disk, and propagates outward in radius. Even early ($0.5T_D$) in the simulation, variations of density $\delta\Sigma/\bar{\Sigma}$ approach 10-50%; at late times they reach unity.

The dominant patterns are two and three-armed spirals with significant components having other symmetries. At late times we see multiple tails on a single arm, arms unevenly spaced in azimuth, and patterns which have one arm which is significantly stronger than its counterparts. Often such spacing and asymmetry is preceded by the breakup of an arm at its base, and subsequent drift through the disk or capture by another arm. For example, between the $0.94T_D$ and the $1.41T_D$ images, an $m = 2$ structure breaks up, and reforms as an asymmetric $m = 3$ spiral pattern. It then returns to its previous two armed structure by $1.73T_D$.

A comparable series of plots for a PPM simulation (*pch6*) with analogous initial conditions is shown in figure 2.5. The variable plotted is density variation defined by

$$\frac{\Sigma_{ij} - \bar{\Sigma}_i}{\bar{\Sigma}_i}, \quad (2.13)$$

where i and j refer to the grid indices of the r and ϕ coordinates respectively, and $\bar{\Sigma}_i$ is the azimuth average of the surface density at radial grid index i . Only positive variation contours are shown. The linear spacing between one contour and the next higher contour is noted in the upper right hand corner of each plot. The dotted line denotes the disk edge at 50 AU. As in the SPH simulation, instability begins in the inner regions of the disk. Complex structures follow at midtime epochs. Later behavior shows well defined regular spiral patterns, with a mix of several patterns dominated by $m = 2$ and $m = 3$ which dynamically reorganize themselves with time.

The simulations above display a number of similar characteristics, though on a different spatial scale and mass distribution, to the protostellar core/inner disk simulations presented in Pickett *et al.* (1998). In each case, large scale spiral structures grow from marginally stable systems. The instabilities begin their growth in the innermost regions of the system and proceed to involve the entire disk as the simulation proceeds. At late times in both sets of simulations, the spiral arms become azimuthally condensed. A notable difference between our results and theirs, which will be discussed in section 2.3.3 below, is the fact that our simulations exhibit a pattern speed which increases toward the center of the disk. In contrast, Pickett *et al.* report constant pattern speeds.

Initial behavior of our low disk mass runs is similar to those of high mass, with instabilities first becoming apparent in the inner regions of the disk. Evolution at later times differs from that for high mass disks. We see the rapid development of patterns with large numbers of spiral arms, which display a tenuous, filamentary structure not present in higher mass disks. The disk shown in figure 2.6 (simulation *scv2*) has a five armed pattern which predominates, and at late times fragments into multiple clumps from each arm. A region of apparent stability against spiral arm formation becomes apparent in the extreme innermost regions (see also section 2.3.2). Such regions are present to some extent in all of our SPH disks except those which form clumps immediately and are defined by a value of Toomre's Q parameter greater than ~ 2 .

In a low disk mass PPM simulation (*pch2*), shown in figure 2.7, we also find a change in character and an increased number of spiral arms. As in figure 2.5, the instability begins to form

its first spiral structures at amplitudes of 0.01-0.1%. Although the precise number of arms seen does not correspond to that in the SPH run (showing instead the 2-4 armed patterns dominant), the degree of small scale fragmentation in the region around 5-25 AU is similar. We believe that the partial suppression of the high m -number patterns can be attributed to the wavelengths of those patterns approaching the gravitational softening length implied by the grid. This statement is supported by the fact that for the low mass disks ($pch2$ and $pcm2$), the amplitude of the perturbations $\delta\Sigma/\bar{\Sigma}$, is larger in the higher resolution simulation. These simulations do not resolve the small scale structure. Note that the PPM run with $M_D/M_* = 0.1$ ($pcm1$) developed only minimal spiral structure after nearly six full disk orbit periods.

Structures observed in the moderate resolution PPM simulations (runs $pcm1$ - $pcm6$) were qualitatively similar to those observed for our highest resolution runs ($pch2$, $pch6$), although the growth of the low mass/low resolution structures was slower. Growth rates are similar for the low and moderate resolution high mass disks. The simulations may have reached a level of convergence sufficient to resolve the large scale features of the evolution, but further improvement is desirable.

2.3.2. The Effects of Temperature

Two series of SPH simulations were run varying the minimum stability parameter Q , with mass ratios $M_D/M_* = 0.8$ and 0.4 . Other things being equal, high Q implies high temperature in the disk (eq. [2.6]). We vary Q for different simulations between a minimum value of $Q = 1.1$, at which the disk is only marginally stable to ring formation, and a maximum value such that the outer edge of the disk remains bound. For the high mass series, this limit was found at $Q_{\min} = 2.3$, while for the lower mass disks up to $Q_{\min} = 3.0$ were available.

In figure 2.8 we show ‘late time’ behavior of each of the disks in the $M_D/M_* = 0.8$ series ($sqh1$ - $sqh6$). Below an initial value of $Q_{\min} \sim 1.4$, strong instability and clump formation occurs during a few orbit periods of the inner portion of the disk. The outer disk remains largely unaffected during the simulation (which suffers drastic decreases in time step size once clumps form). At moderate Q_{\min} (1.4 to somewhat less than 1.7), instability in the inner regions is slowed to the extent that spiral instabilities involving the entire disk have time to grow. These spiral arms then become filamentary and clump on time scales of one or two T_D . The last few frames in figures 2.4 and 2.6 show such behavior for a disk with $Q_{\min} = 1.5$ and $M_D/M_* = 1.0$ and 0.2 . The portions of the spiral arms at large distances from the central star remain thicker and more diffuse, while the inner regions evolve toward more sharply defined features. As Q_{\min} increases the character of the spiral instabilities changes from narrow, filamentary structures and clumps in the inner disk to thicker arms which develop on disk orbital time scales at higher initial Q_{\min} .

Above initial $Q_{\min} \sim 2.0$, we see only limited asymmetry and spiral structure. However, there is a strong transient epoch in which the centers of mass of the star and the disk orbit each other at large distances (relative to their late time behavior or to other, less stable (lower Q_{\min}) simulations). Simulations have been carried out to more than $4T_D$ for these cases. This resonance gains in strength with increasing Q_{\min} up to the maximum values simulated. Accretion of disk matter onto the star occurs at higher rates in these runs as well. The star makes a hole in which little disk matter remains.

Figure 2.9 shows an example of this transient for simulation $sqh6$. The orbit of the star begins with a slow transient to relatively large distances from the system center of mass (as large as $\sim 0.05R_D$ in the disk shown). In the first $\sim 2T_D$, the star accretes a large fraction initially located in the inner part of the disk. After this time the star settles to a smaller orbit, with occasional fluctuations as it moves in response to disk perturbations, and continues to accrete

from the inner disk. We believe this transient is largely due to the high mass accretion rates with nonaxisymmetric flow. With such fast accretion, the flow of mass onto the star is rapid enough that appreciable angular momentum is swept along as well. A comparable simulation, with the star fixed at the origin, shows nearly as large an accretion rate. We conclude that high accretion drives the stellar migration, rather than the reverse process where the star moves by some other means (caused for example by a torque from the outer disk) into a region of the disk in which high accretion may take place.

Although we find that the accretion rates seen in the most Q -stable disks are higher than low stability disks, it is not clear whether the magnitude of the accretion rates are correct. In SPH the accretion of a particle implies a sudden unphysical loss of pressure support for the neighbors of the accreted particle. As the disk reorganizes itself, additional particles move inward towards the accretion radius. If the mass accretion for all of our disks were to be scaled up or down by a common factor, the transient in figure 2.9 might increase or decrease in magnitude or even disappear. What we can say with certainty is that if a star can accrete matter from the inner disk quickly enough that it loses its pressure support further out, accretion of disk material which has not lost all of its orbital angular momentum can occur, driving the star away from the system center of mass. In the simulations we study here, such a condition occurs when the accretion rate is above $\sim 6 - 8 \times 10^{-5} M_{\odot}/\text{yr}$ for the high mass series and $\sim 2 \times 10^{-5} M_{\odot}/\text{yr}$ for the lower mass series.

Behavior of the lower disk mass series of SPH simulations with varied Q_{\min} is similar. The overall characteristics of the evolution mimic that of the higher mass runs but are ‘stretched’ along the Q axis to higher values of Q_{\min} . Azimuthal condensation of spiral arms is again seen up to initial $Q_{\min} = 1.5$, but the $Q_{\min} = 1.7$ run at this mass ratio appears to be just beyond the critical stability for clumping: many preliminary characteristics of clumping such as well resolved spiral arms and short duration over-density spikes (see below) were evident but no actual formation occurred at the time we stopped the run at $T = 5T_D$. Production of thick arms continues as high as $Q_{\min} = 2.3$ and global star/disk resonances again manifest themselves all the way up to the maximum Q_{\min} values studied. Distinct one armed spiral waves form at $Q_{\min} = 2.0$ for short periods, then lose coherency and fade back into a smooth, global pattern.

One series of PPM simulations was run with varying Q_{\min} . The late time density variation contours for the series are shown in figure 2.10. Because of the low amplitude of the initial noise, these simulations were continued to $\sim 2T_D$ even for the lowest minimum Q values. In the highest stability ($Q_{\min} = 2$) simulation, we find that the strength of the instabilities near the inner boundary dominate the instabilities over the disk as a whole. This instability does not seem to be the same as the transient seen in the SPH runs: it is limited to small radii inside the density maximum, and does not enter the outer disk at all. Because of the boundary behavior noted above, simulation of the disks into epochs having large amplitude variations was possible for only short times. We could not determine if a large transient in the orbits of the centers of mass of the star and the disk developed at late times for these simulations.

At low and moderate Q_{\min} (≤ 1.7), there is a great deal of correspondence between the qualitative results of our SPH and PPM runs. For simulations with moderate initial Q_{\min} ($\sim 1.4 - 1.7$) multiple spiral arm structures develop with the $m = 2$ and $m = 3$ patterns most prominent. The $m = 1$ pattern is present at varying levels as an asymmetric component of the dominant $m = 2$ or 3 patterns.

For the lowest stability simulation, run at $Q_{\min} = 1.1$, density variations up to $\sim 40\%$ are present in the disk and variations within a single spiral arm produce local density maxima within that arm. Continued collapse from large amplitude spiral structure into one or more clumps is not observed, probably because we have not resolved the gravitational potential or the rotational

motion of the matter about a collapsing core to the necessary scale. The evolution of these lowest stability disks (i.e. simulation *pqm1* and *pqm2*) at early times in the simulations are dominated by the growth of the $m = 1$ pattern which, unlike their more stable cousins, is distinct even at the $10^{-5} - 10^{-6}$ level. Later, these patterns tend to break up and reform as $m = 2$ and $m = 3$ patterns.

2.3.3. Spiral Pattern Growth

An important connection of numerical simulations to linear perturbation analyses is to define, if possible, the linearly growing spiral patterns of a system. To do so requires a specification of the growth rates and pattern speeds of the dominant spiral patterns in each system.

We compute the growth rates by first computing the amplitude of spiral patterns by Fourier transforming a set of annuli spanning the disk in the azimuthal coordinate. The amplitude of each Fourier component is then defined as $|A_m| = \ln(|\Sigma_m|/|\Sigma_0|)$, where Σ_m is

$$\Sigma_m = \frac{1}{\pi} \int_{R_i}^{R_o} \int_0^{2\pi} e^{im\phi} \Sigma(r, \phi) r d\phi dr, \quad (2.14)$$

for $m > 0$ and the inner and outer radii of the disk are defined by R_i and R_o . The $m = 0$ term is defined with a normalization of $1/2\pi$. With this normalization, the Σ_0 term is the mass of the disk and the amplitudes, A_m , are dimensionless quantities. The phase angle is then defined from the real and imaginary components of the amplitude

$$\phi_m = \tan^{-1} \left[\frac{Im(\Sigma_m)}{Re(\Sigma_m)} \right]. \quad (2.15)$$

Local amplitudes for each component can also be derived for annuli by neglecting the integration over radius in eq. [2.14]. Each Fourier component is computed about the center of mass of the system.

Assuming strictly linear growth for each Fourier component, we can use least squares techniques to fit a growth rate, γ_m , to each amplitude as a function of time with the equation

$$A_m = \gamma_m t + C_m, \quad (2.16)$$

where C_m is a constant defining the initial amplitude of the component. If we keep track of the number of times, N , a pattern has wound past a phase angle of 2π and add $2\pi N$ to the derived phase at each time, we can derive a pattern speed by a similar fit as

$$\dot{\phi}_m = \frac{\dot{\phi}_m}{m} t + \phi_{m,0}. \quad (2.17)$$

This definition effectively averages over all short term variations (if any) in the pattern speed. A periodogram analysis gives similar results to this fit technique. The frequency with which we produce dumps of the simulation is sufficient to produce accurate pattern speeds over all but the inner $\sim 3 - 5$ AU of our disks (limited by aliasing), and over the full radial extent of the tori (see section 2.3.3).

We may independently derive an additional global growth rate for the $m = 1$ component by noting that it is the only component which can contribute to the motion of the star. All higher order components are symmetric under a rotation smaller than 2π radians (i.e. $2\pi/m$ respectively for each Fourier component) and therefore do not contribute to the motion of the disk center of mass. By fitting the distance between the centers of mass of the star and disk as a function of

time, we find a growth rate independent of the precise geometry of the spiral arms in the disk. In general we find good agreement between this growth rate and the value derived from the above procedure.

The analysis of the pattern growth in disks and tori can proceed at either a local or a global level by either including or excluding the integration over radius in eq. [2.14]. If we derive a growth rate and pattern speed in a succession of narrow rings in the system and compare the values over the entire system, we can readily identify structures which are coherently growing and moving over large temporal and spatial scales. This feature is limited in a global analysis because the integration effectively averages the amplitude and speed of a given pattern over the entire system.

On the other hand, a local analysis can be quite misleading. If we consider a series of concentric narrow rings making up a disk, we must account not only for the growth of instability within any given ring, but also for the transport of already formed instabilities from one ring to another. For example: if some ‘lump’ of matter grows in one ring in the disk, then moves by some process to a second, the amplitude of the Fourier components in each of those rings will be affected: one will exhibit a net loss in amplitude, while the other a net gain. A growth rate based upon amplitudes affected by such processes would no longer represent the physical instability mechanisms present in the disk.

In the analysis that follows, we shall use a local analysis to identify patterns which are growing coherently over large spatial scales, but in order to compare our results to the global analyses of ARS and STAR, we shall utilize globally integrated quantities.

SPH and PPM: A Direct Comparison of Results and Numerics

Each code does well with different aspects of the evolution of disks. For the example of the disks discussed here, the low noise in the PPM calculations allows an accurate growth rate calculation, but with our treatment of boundaries, problems develop as a simulation becomes nonlinear. Matter reflected from the boundaries changes the total momentum of the system to such an extent that its center of mass (exhibited particularly in the position of the star) attempts to move to infinity. Because of its ability to dynamically adapt the available resolution to the interesting parts of the flow and relative sensitivity to boundaries, SPH is able to follow the nonlinear evolution much further. These same features however, forbid simulating a disk with a low density central hole because the steep density gradient near the inner disk edge cannot be adequately resolved at a computationally affordable level. Even for disks without a hole (for which the gravitational softening at the inner boundary blurs the physics and allows the simulation to proceed), the initial noise in SPH (of order 10^{-3}) leaves very little time for random perturbations to organize themselves into ordered global spiral structures while remaining in the linear regime.

Fitting growth rates to the SPH simulations requires much more caution than is required for the PPM runs. The initial noise level is such that only a very short time baseline is available prior to saturation. Typically, we observe a period during which Fourier components grow linearly until reaching a saturation level. This period of linear growth lasts for about one disk orbit T_D or less for SPH and 2–3 T_D for the PPM simulations.

The SPH disk simulations often reach high perturbation amplitudes close to the star before more distant regions of the disk have become active. To compare the two numerical methods and minimize this time scale problem, we have simulated relatively narrow tori. Such tori have a much more restricted dynamic range than a disk, so that the entire system becomes active at once. We

use a torus with an outer to inner radius ratio of $R_i/R_o = 5$ and a $\gamma = 1$ equation of state given by eq. [2.11] with temperature, density and individual particle mass given by a Gaussian function of radius

$$f(r) = f_0 e^{-(\frac{r-r_0}{R_w})^2}, \quad (2.18)$$

where r_0 is defined at the midpoint, $r_0 = (R_i + R_o)/2$, of the torus and $R_w = (r_0 - R_i)/2$, so that the torus extends about three ‘standard deviations’ in either direction from the highest density point (figure 2.11). Each simulation is then evolved isothermally in the same way as is done with our simulations of disks.

With a $\gamma = 1$ equation of state, it is difficult to find toroidal configurations which are initially stable to axisymmetric perturbations (i.e. $Q > 1$ everywhere), except for relatively low mass tori. For a variety of temperature or density laws, either the high density central region will collapse (i.e. the initial Q_{\min} will be less than unity), or the outer edge will be unbound. For our test problem, a ratio of $M_T/M_* = 0.2$ yields a minimum Q of about 1.05 near the center of the torus. As before, the star mass is $M_* = 0.5M_\odot$, the outer torus radius of $R_o = 50$ AU, and thus the outer edge of the torus orbit period is $T_T = T_D = 500$ yr.

Table 2.3 summarizes the characteristics of the simulations. The linear and nonlinear regimes are divided by the condition that the amplitudes of Fourier components other than the dominant pattern (or patterns) reach comparable amplitudes to that dominant pattern, and total perturbations reach $\sim 10\%$.

One SPH and two PPM simulations were run with this toroidal configuration at a resolution of 40×150 cells for the PPM runs and 6998 particles in the SPH run. One PPM simulation with initial random noise amplitude 10^{-3} (comparable to the initial noise in SPH) and one with noise of amplitude 10^{-8} were run. The 10^{-3} noise is input as a random density perturbation in each cell as

$$\Sigma_{ij} = (1 + 10^{-3}(2R - 1)) \Sigma_{ij} \quad (2.19)$$

where i and j refer to the radial and azimuthal grid indices and R is a pseudo-random number between zero and one. The 10^{-8} amplitude noise is derived from truncation error in the initial state, as is done in the disk PPM simulations. Boundary conditions are identical to those used in our disk simulations.

The relatively large amplitude of the noise in the SPH simulations is caused by smoothing over a finite number of neighbors (see Herant and Woosley 1994). Increasing the number of neighbors used in the interpolation has a small effect in decreasing the noise amplitude but at a high computational cost. We have used a varying number of neighbors (depending on local conditions of the run) with a distribution centered near 15–20 neighbors per particle, a number which is standard for two dimensional simulations.

The resolution of features within the torus or disk must inevitably be less accurate in a finitely resolved system than in a physical system. PPM spreads shocks over at least two cells, for example, while further loss of resolution may come from the representation of the gravitational potential. In SPH, resolution is limited by the smoothing length of the particles and the artificial viscosity required to adequately reproduce shocks.

Two additional PPM and two additional SPH simulations of tori have been run to test resolution. One PPM run has 1.5 times the resolution in each dimension (60×225 —roughly doubling the number of cells) and the second twice the resolution (80×300 —quadrupling the number of cells). The SPH simulations increase by a factor of two and a factor of four the number of particles in each simulation. Comparing runs of different resolution is difficult, however, because the power spectrum of the initial perturbations may not be controlled to the limit

required. In an attempt to duplicate the perturbation at low and high resolution, but remain above the uncontrollable level imposed by the grid itself, we have input an initial random noise amplitude of 10^{-3} in each 2×2 block of cells in each of the two higher resolution PPM runs.

We show the evolved configuration of each run in figure 2.12. The time at which each is shown is near the linear regime cut off discussed below. The SPH runs are mapped onto a grid and plotted in the same manner as the PPM runs in order to make the visual comparison as direct as possible. In each of the runs, instability growth is dominated by $m = 2 - 4$ spiral patterns with the higher resolution runs tending to show progressively less of the $m = 4$ pattern and more of the $m = 2$ pattern. The $m = 3$ pattern predominates in each simulation except for the two low resolution PPM runs. The change in morphology in different simulations is probably an artifact of the resolution. As we show for the growth rates below, the lowest resolution simulations are apparently not converged.

In comparison, the results of Laughlin & Różyczka (1996) show a dominance of an $m = 2$ component without a large presence of other patterns. The origin of instabilities in their systems is attributed to the family of vortensity instabilities with corotation exterior to the torus. Different initial conditions seem to be responsible for the $m = 2$ rather than $m = 3$ dominance. Our test simulations use a narrower torus than theirs, with an isothermal rather than adiabatic equation of state. A simulation with an identical initial condition and equation of state compares favorably to their results.

The amplitudes and fits for growth rates for the $m = 3$ spiral pattern at the center of the torus (at $R = 30$ AU) are shown for each simulation in figure 2.13. The fit parameters are derived from only the portion of the curve in which the patterns are growing and little disruption of the large scale structure of the tori has begun. This disruption is characterized by an onset of fragmentation at the inner and outer edges of the torus (SPH) or significant radial distortions in the torus (PPM). We also allow a short period ($\sim 0.1T_D$) prior to the first fitted time point, for some initial transients (e.g. the unphysical ‘ringed’ structure in the SPH initial state) to settle.

The pattern speeds and growth rates for the $m = 1 - 4$ patterns are shown in figure 2.14 for each of the PPM simulations and in figure 2.15 for each of the SPH simulations. The pattern speeds for the $m \geq 2$ patterns for each of the runs agree for both codes over the range of resolution and initial perturbation amplitude. The growth rates from the SPH simulations differ by as much as 50% between runs. For the SPH simulations obtaining a constant rate across each ring in the torus was not possible. For the PPM simulations, the growth rates near the inner and outer boundaries of the tori are reduced due to the fact that perturbations there do not begin to grow until after the denser regions of the torus have been disturbed. A similar effect is found for the pattern speed near the inner edge.

The growth rates for the SPH runs are affected by the high amplitude of perturbations in the initial state and the short time span over which the fit must be derived. Longer lived initial transients caused by the excitation of multiple eigenmodes of the system or by small inhomogeneities in the initial state can cause the amplitude curves to become quite nonlinear in form. The PPM simulations have longer time baselines so such transient effects are less important.

The growth rates for the $m = 4$ pattern in the PPM simulations decrease with increasing resolution, while the $m = 2$ and 3 growth rates are less affected. This fact and the trend towards $m = 2$ and 3 spiral patterns for higher resolution runs suggest that they may be true linearly growing patterns for the system. The change in character with increasing resolution may be due to the fact that the torus begins its life very close to the stability limit, $Q_{\min} = 1.0$. Any inaccuracies in the resolution of the gravitational potential or the mass distribution (hence the pressure) will have their greatest effect in such a circumstance. The SPH simulations show no

comparable effect, but reliable local growth rates can not be obtained for those simulations.

Late in each simulation the tori collapse into several condensed objects, but the details of the collapse vary. Not all of the spiral arms present during the growth of structure condense into separate objects. In many cases the spiral arms break up and/or merge as clumps begin to form. Figure 2.16 shows snapshots of each of the runs at the time at which the spiral arms begin to collapse. Each simulation is halted at this point because of the influence of the boundaries on the simulation and because we did not properly simulate the physics important in the collapsed objects. The structures which develop resemble the simulations discussed by Christodoulou & Narayan (1993) because the tori tend to deform radially as instabilities grow. With both codes the torus becomes so distorted radially that a line of condensations forms from the torus matter which has moved outwards.

We now summarize the similarities and differences between the results of each code.

Each code produces instabilities which grow in the tori as they evolve forward in time. The instabilities produced are multi-armed spiral structures which, at the end of each simulation, have begun to radially distort the torus and collapse into clumps. In both codes predominantly 2–4 armed spiral structures are produced. The high resolution simulations each produce 2 and 3 armed structures while low resolution simulations (apparently incompletely converged), produce predominantly 3 and 4 armed structures.

The initial state of an SPH simulation begins with random noise of amplitude $\sim 10^{-3}$ above or below an ‘ideal’ initial value. Near the boundaries, where particles are not distributed evenly with respect to each other, additional differences from an ideal initial state are present. PPM can begin with noise in the initial state as small as machine precision for any given simulation.

The differences between one code and the other can be attributed to several effects. First, perturbations in the initial state may trigger more than one true eigenmode of the system which, taken together, cause more or less observed growth in a given simulation with respect to another. Because the noise input for each code arises from such different sources, the stimulated pattern growth may therefore initially have a much different character. This growth rate variation is exhibited predominantly by the amplitude of a given pattern ‘waving’ above and below its true linear growth curve and, in essence, constitutes an error estimate for a calculated growth rate. The PPM simulations, for which the growth rates are calculated over longer time baselines and with a smaller initial noise amplitude per Fourier component are not nearly as strongly affected by such effects. We estimate errors of 10–20% in the growth rates due to this effect in the PPM simulations and perhaps an additional 20–40% in the SPH runs because of their very short time baseline. Pattern speeds do not seem to be as strongly affected by these transient effects.

The adaptive nature of the resolution and high noise in SPH causes small scale filamentary structures to become active and develop more quickly than in our counterpart PPM simulations, which are limited to the resolution of the fixed grid. SPH will tend toward developing grainy and filamentary structures quickly, perhaps to a larger extent than is physically the case.

Because the grid boundaries are far away from the main concentration of mass in the torus, they have only a small effect until late in any given simulation. Such is not true for the disk simulations using the PPM code so those simulations cannot be carried out far into the nonlinear regime due to the growing influence of the boundaries at late times. The physics important for the global dynamical evolution of the disk ranges over a dynamic range larger than we are able to simulate. The state at which the PPM runs must be terminated (with 10–20% perturbations) are qualitatively quite similar to those of the SPH runs over most of their duration. It may be that for the disks we discuss below, the PPM runs are representative of the linear regime, while the

SPH simulations are our only representation of the late time nonlinear behavior of the system.

Pattern Growth in Disks

With a clearer understanding of the numerical properties of our codes on a test problem, we return now to the study of disks. Due to the high initial noise of the SPH runs and large radial extent of the disks we study, saturation at small radii often occurs well before the entire disk has become involved in the instability. Because of this noise we do not believe growth rates calculated from these simulations are reliable for any Fourier component except the globally integrated $m = 1$ pattern (for which we have the behavior of the centers of mass of star and disk), and we limit discussion of the growth rates in this and the following sections to the PPM simulations.

The qualitative observations of sections 2.3.1 and 2.3.2 have shown that there is rarely a single spiral pattern present in a disk. More quantitative measurements show that growth is present in all Fourier components up to very high order. Such growth does not necessarily imply that actual spiral arms of that order are present in the simulation, but rather that the arms that do exist become more filamentary than pure sinusoids, creating power in higher order Fourier components (a Dirac δ -function will yield power at all wave numbers for example). In order to be more definitive regarding the true morphology of each disk we visually examine each simulation and tabulate the dominant spiral patterns in Tables 2.1 and 2.2.

Which patterns represent linear growth in each of the systems? To begin to answer this question we must fit growth rates and pattern speeds to the various spiral patterns present in each disk and determine which patterns exhibit rates which are constant at differing resolution, across a large portion of the system and over a large time period. In figure 2.17 we show the amplitude of the $m = 2$ and $m = 3$ patterns as a function of time near the middle of the power law portion of the disk and integrated over all radii for our prototype massive disk shown in figure 2.5. Over long periods the growth is essentially linear in character. Over shorter periods it is punctuated by transients which can change the amplitude by up to an order of magnitude. The amplitude variations apparently arise as short-lived structures successively grow and fragment throughout the disk. Time dependence of pattern speeds within the disk will be discussed in section 2.3.3 below.

Radius dependent growth rates and pattern speeds for the $m = 1 - 4$ are shown in figure 2.18 for two different grid resolutions. The growth rates and pattern speeds are similar at both resolutions, suggesting that the simulations may have resolved the physical processes important in this disk. The growth rates for the $m \geq 2$ patterns are nearly constant with radius but the pattern speeds derived are not at all constant with radius; they decrease as a steep function of the distance from the central star.

Low mass disks show a marked absence of the dominant low order ($m = 1 - 3$) spiral patterns so common among higher mass disks. Typically, the amplitudes and growth rates of all Fourier components are comparable. We plot the growth rates and pattern speeds for the same patterns ($m = 1 - 4$) as above for our prototype low mass disk in figure 2.19. We again find that the pattern speeds are steeply decreasing functions of the radius. We also find that the growth rates do not exhibit the same values for different grid resolutions. This fact suggests that the low mass disks have not fully converged at the grid resolution used in our simulations. The systematic trend towards faster growth in the higher resolution simulation indicates that the small scale features which dominate the morphology of this system may be somewhat inhibited by the resolution of the gravitational potential and the hydrodynamic quantities on the grid. Much higher resolution simulations are required to be able to fully resolve the features important for disks of mass less

than $\sim 0.2M_*$ than are required for more massive systems.

With simulations of varying stability we would ordinarily expect larger Q values to lead to slower instability growth. Similarly, we expect that smaller Q values should imply more rapid growth of instability. In fact, as discussed in section 2.3.2, both extremes lead to rapid instability growth, but of different character.

Although it begins with an extreme initial condition, the simulation *pmq5* (with $Q_{\min} = 2.0$, $M_D/M_* = 0.8$) shows an interesting example of the limiting behavior displayed in a highly stable disk ($Q \gg 1$ everywhere) with a turnover in its density profile near the central star. We show the $m = 1$ and $m = 2$ pattern amplitudes at two locations in the disk and integrated globally in figure 2.20. In this simulation, rather than being suppressed, the amplitude of the instabilities begins to grow quickly in a region limited to the innermost portion of the disk. Further out in the disk much slower growth occurs. The development of such instabilities in disk systems cannot be attributed to a global, linearly growing phenomenon; its localized character and the different behaviors of the amplitude growth at different locations in the system argue against that. It remains unclear to what extent this type of growth happens in real systems, but it seems that with a turn-over in the density law at small radii or the less severe case where the density law flattens (as in our SPH simulations) can lead to increased local instabilities.

It is interesting to note that Pickett *et al.* (1996) report similar behavior (which they refer to as ‘surge’ growth) in several of their more Q -stable simulations. In their work however, the initial mass distribution and rotation curve are somewhat different than in our own work. The fact that similar behavior is observed in simulations of such different character suggests a similar mechanism may be driving the evolution of both sets of simulations.

The lowest stability simulations also show rapid growth of spiral instabilities. In these simulations there are no growth features similar to the ‘hump,’ or sudden rise in amplitude shown in figure 2.20. In general, the qualitative features of the growth are similar to those seen in figures 2.17 and 2.18 but with as much as 50–100% larger growth rates in the case of the lowest stability run (*pmq1*).

The results of our analysis in this section show that in spite of its large amplitude at early times and its continued presence for the duration of the run, our simulations do not show evidence of a pure $m = 1$ pattern. In no case is the $m = 1$ growth rate or pattern speed constant across a large portion of the disk. In contrast to several higher m patterns, the wide variation is true of both the growth rate as well as the pattern speed. Because of the variation of the growth rate and pattern speed we must conclude that a direct connection to the SLING mechanism is not possible. At the high amplitude (late time) phase of evolution shown in the SPH simulations, the $m = 2$ and 3 patterns have become dominant for disks more massive than $M_D/M_* \approx 0.2$, while at the lower amplitudes typical of our PPM runs, $m = 1$ has the largest amplitude, though the pattern itself is ordinarily seen only as asymmetries in higher m structures.

None of the disk simulations we have performed produce pattern speeds for any m pattern which are constant across the entire disk. The growth rates, while ordinarily stable at a single value over the whole system for at least some patterns (see e.g. fig. 2.18), do not reflect the short term behavior of the system as structures fragment or deform over time. In this case the ‘linear growth modes’ of the system, defined as the complex eigenvalue of a system of equations, become difficult to define or to interpret.

Suggestions for the Mechanisms of Instability Growth

In each of our simulations, instabilities are generated in the innermost portions of the disk, eventually impacting the entire system. Such growth occurs in spite of the fact that the inner regions are the most stable as measured by two of the classic stability indicators, namely the Toomre Q criterion and the SWING X parameter. If we are to suggest a mechanism for the instability growth we are limited to mechanisms which can produce instabilities in what are ostensibly highly stable regions.

We have already discussed the possibility that in some cases instabilities may be due to nonaxisymmetric accretion of disk matter onto the star or by accretion of infalling material onto the disk, rather than to dynamical instabilities in the disk itself. In other cases, the vortensity based instabilities of Papaloizou & Lin 1989 (see also Adams & Lin 1993) may provide an answer because they can grow in highly ‘stable’ regions and their growth can be local in nature. They discuss three classes of vortensity instabilities which can exist in a disk: those dependent on vortensity extrema within the disk or at its edge (‘edge modes’), those dependent on resonances (‘resonance modes’), and those which have corotation exterior to the disk (dubbed ‘slow modes’ and studied extensively by Laughlin & Różyczka 1996). Because we find corotation within the disk for most times (though at varying position), we can eliminate the last of these classes from consideration. The remaining two, we believe, are both active at different times and to a greater or lesser extent in the disks we model. At early times, our initial condition (the softened power law or density turn-over at small radii) implies a vortensity extremum near the inner boundary of the disk. This condition may excite an edge mode which over time propagates outward over the density maximum in our PPM simulations via a resonance mode into the disk, exciting global instability channels such as SLING as it propagates into the main disk. We have not established a definite connection between the instabilities in our simulations and the vortensity based instabilities however.

We cannot definitely connect the SLING instability directly to phenomena present in our simulations; see section 2.3.3. We may still perhaps be able to make qualitative connections between phenomena predicted to be important via linear analyses and our results. One example of such phenomena would be growth rates which depend upon the outer boundary condition imposed. Another might be a growth rate which, as a function of disk mass, increases for disks more massive than some critical value, as suggested by the ‘maximum solar nebular mass’ discussed in STAR. Such characteristics would not necessarily be limited to the $m = 1$ pattern but may also exist in $m > 1$ patterns as well.

We do see such characteristics in the variation of the growth rates with respect to the disk/star mass ratio. For each series of PPM simulations varying disk mass, figure 2.21 shows the value of the globally integrated growth rates for the $m = 2$ patterns. Growth rates for other m patterns appear qualitatively similar to those shown. As one expects, growth rates of the highest mass disks are the largest, while instabilities in low mass disks grow much more slowly. In the reflecting boundary runs, a distinct ‘turn on’ mass is evident between $0.2 < M_D/M_* < 0.4$, a value which corresponds to the ‘maximum mass solar nebula’ predicted by the results of STAR. The infall series does not exhibit such a distinct onset, but rather a continuous rise to a plateau which does not flatten out until the mass ratio reaches $M_D/M_* \approx 0.5$.

For low disk masses, the growth rates for each pattern are of order $\gamma_1/\Omega_D = 0.15 - 0.2$. These rates are comparable to the rate attributable to numerical effects. The numerical effects have their origin primarily in the fact that mass interacting with the grid boundaries gives an impulse to the system center of mass, which must be stable in order to determine the amplitude of the $m = 1$ spiral pattern. Higher m patterns are also affected as spiral waves reflect off the grid

boundaries back into the simulation.

For higher mass disks, the outer boundary has a marked influence. As ARS predict, details of the outer radial boundary are an important factor in the growth pattern. The simulations with matter infalling onto the outer disk edge develop spiral structure with growth rates as much as 2-3 times faster than with a purely reflecting boundary. Simulations at two resolutions were run with an infall boundary to test the degree to which numerical effects of the boundary were affecting the growth. Both series show similar growth rates (fig. 2.21).

Importance of Phenomena not Included in Linear Analyses

On short time scales the pattern speeds in our disks can vary by as much as 100%. One example, shown in figure 2.22, is taken from the high mass disk simulation *pch6*. There we show the instantaneous pattern speed for the $m = 2$ pattern near the middle of the disk, as calculated by numerically differencing the pattern phase ϕ_m , at successive output dumps of the simulation. Such variations in time are typical of each pattern in each disk simulation we have performed, and appear in both local and globally integrated pattern speeds. Pattern speeds calculated this way for the torus simulations of section 2.3.3 show much slower variations.

In the case of the $m = 1$ pattern, whose global pattern speed is reflected in the motion of the star, we find that the star occasionally loops back upon its own trajectory and counter-rotates with the disk for a short period. Such a condition is not an uncommon occurrence in systems with disturbances with different orbital (pattern) periods. In our own solar system, for example, the sun's motion about the solar system barycenter was retrograde most recently in 1990, when Jupiter was on the opposite side of the sun from the other three major planets.

The variations seem to arise because of the growth, fragmentation and reformation processes undergone by the spiral arm structures over the course of their evolution. Because the pattern speeds vary, an averaged pattern speed at any location in the disk (via eq. [2.17]) loses meaning and the location of the corotation and Lindblad resonances for each pattern also vary in time. When such variations are occurring, wave analyses, which typically assume stable resonances, may be of limited utility (wave analysis is of course useful in less chaotic circumstances—see, e.g., STAR and Laughlin, Korchagin, & Adams 1996).

The growth of instabilities is not always suppressed as Q increases, but the instabilities do change character; this change is due to the increasing importance of effects not modeled in semi-analytic treatments of disks. For the high Q_{\min} SPH runs, these effects are dominated by the nonaxisymmetric accretion of disk matter onto the star. As the star begins to move from the center of mass of the system (due to ordinary disk processes or the potential hump at the origin), some portion of the accretion becomes nonaxisymmetric. In the warmest disks, as much as 10% or more of the disk is accreted over the life of the simulation. Disk matter accreting onto the star sweeps along some residual angular momentum which is transferred to the star either as spin (an effect we neglect here) or as net angular momentum of the star about the system center of mass. In these cases, the star may gain enough momentum to be driven further away from the center of mass and create power in the $m = 1$ pattern.

In the PPM runs with infall, the instability growth can include a component due to the outer disk edge perturbations. These may be due to infall itself, or to fragmentation of the disk at the boundary. Although the linear analyses of ARS and STAR showed that the conditions at the outer boundary were important for the evolution of the system, they were unable to fully model the effects that the boundary can have on the system (see however Ostriker, Shu, & Adams 1992).

2.3.4. Clump Formation and Characteristics

Returning now to our SPH simulations, in this section we describe several qualitative features of clump formation and evolution in the disks. Due to the unsteady nature of the spiral instability growth and the presence of multiple spiral patterns in the system, each disk sequentially approaches and moves away from conditions in which clump formation is likely. These conditions are most readily apparent in plots of the minimum Q value in the disk and in the maximum over-density in the disk (defined as $\Sigma(r, \phi, t)/\Sigma(r, t = 0)$) with respect to time.

The value of Q is defined rigorously only for an azimuthally symmetric disk. Nevertheless, as an indicator of the most unstable locations in the disk, we examine its value in nonaxisymmetric systems. To calculate its value locally we must first determine the epicyclic frequency at each point in the disk. We use the same procedure by which SPH obtains derivatives of all other hydrodynamic quantities. By definition

$$\kappa^2 = \frac{1}{r^3} \frac{d}{dr} [(r^2 \Omega)^2], \quad (2.20)$$

so the value $d[(r^2 \Omega)^2]/dr$, taken pairwise over each neighbor, is weighted using the SPH kernel. The result is summed to form a local value of the epicyclic frequency.

Plots of maximum over-density and minimum Q are shown in figure 2.23 for our two prototype SPH $Q_{\min} = 1.5$ disks. Each variable is a global extremum. As such, the value of one could be determined from a completely different portion of the disk than the other. However, after only a relatively small fraction of an orbit time T_D , the locations of minimum Q and maximum over-density are close, at a position between about 10 and 30 AU.

After a few orbit periods of the inner disk regions, the over-density rises to about twice its initial value (of unity). A slow secular trend towards stronger spiral arms over the course of the run follows, punctuated by one or more sharp, short-duration episodes of very strong activity in which density locally increases to 5-10 times. Over-density spikes become more and more frequent as the simulations progress, finally leading to clump formation. With the one exception $M_D/M_* = 0.4$, $Q_{\min} = 1.7$ which, as noted in section 2.3.2, appears to lie on the ‘boundary’ between clumping and non-clumping disks, simulations which do not eventually form clumps also do not show these large over-density events. We attribute the origin of the over-density events in our simulations to the growth of spiral instabilities into a high amplitude nonlinear regime. In this regime spiral patterns present constructively interfere with each other or collide with other arms and orphaned arm fragments.

The results of Adams & Watkins (1995; hereafter AW) show that a density enhancement within a disk will lead to collapse if the condition

$$\frac{\Sigma(r, \phi, t)}{\Sigma(r, 0)} > \frac{5}{2}Q \quad (2.21)$$

is met, where Q is the local value (azimuth average) of the Toomre parameter at the location of the density enhancement. For the disks in our study, this expression implies that an over-density factor of 3 or higher must be present in the disk, depending on where in a disk the collapse event occurs. This prediction is supported by our numerical results, which show that disks can survive (i.e. not exhibit collapse) for long periods with over-densities of 2-4, but collapse when over-density spikes of magnitude 6-10 occur.

For all disk masses, the minimum value of Q rapidly falls below its initial value to well below unity. After the initial steep decline, a slower decrease occurs until clumping begins and minimum Q falls to zero. The initial decline occurs most quickly in the highest mass disks, in

which instabilities of any type are most strongly felt. With Q below unity, the disk becomes unstable not only to spiral instabilities but also to ring formation or, in the case of isolated patches, collapse. The collapse is slowed by the effects of rotation within the forming clump.

We can verify that it is rotation which slows the collapse by noting that the effects of the over-density spikes manifest themselves at only the 20-30% level in Q . We also know that the sound speed is constant in the proto-clump (due to our assumption that the disk evolves isothermally), from the definition of Q we know that the rotation of an individual proto-clump (really the shear across the clump, measured by the local value of the epicyclic frequency κ) is the mechanism which inhibits further collapse. Only after spiral arm amplitude has reached sufficient levels to overcome rotation can an irreversible collapse begin.

Clumps condense out of the spiral arms on quite short time scales in even the least massive disks. During and after the initial stages of their formation, we find that the clumps show prograde rotation. No clumps were seen to form in any disk studied whose initial Q_{\min} was greater than 1.5. Clump formation is most common at radii less than $\sim 0.5R_D$ and usually several clumps will form from the same disk (and even within the same spiral arm). Less massive disks form many low mass clumps and higher mass disks form 2-4 higher mass clumps. The mass inside the clumps is of order 1% of the star mass at the time each simulation is ended. It is clear, however, that from the amount of remaining disk that no final mass has been determined.

The clumps form with such vigor in each of these disks because of the strong cooling implied by the isothermal assumption. Any density enhancements like those seen in figure 2.23 instantly lose their pressure support and collapse rather than dispersing. With more realistic cooling, the clumping behavior seen in our results may change. Thus our results are most useful as an indication of the behavior of disk clumping and as indicator of where clumps may be most likely to form in more physically realistic disks.

Figure 2.24 shows a plot of the radius at which each clump formed for each disk in the series. Only in the case of the $M_D/M_* = 0.2$ disk, in which clump formation is prolific in nearly all regions, were any clumps formed at radii greater than $0.5 R_D$. With this exception, we believe the variation in the locations of clump formation in disks of different mass in figure 2.24 to be due more to stochastic effects rather than any physical process. To test this idea we ran a comparison series of simulations (\times 's), utilizing the Lagrangian version of the equation of state. When such an assumption is made, the background noise inherent in the code changes character. No overall structural changes are evident in figure 2.24, but differences in detail are present. Also, for the disk with $M_D/M_* = 0.2$, clumps were not formed at the largest radii. We believe this lack of clumps is due in part to the radial motion of some warmer particles into the outer disk, causing clumping to be suppressed.

The prior results of AB92, in which clumps are seen to form at much larger radii, correspond to a somewhat different initial configuration. In particular, our present results use a much smaller ‘core radius’, r_c , for the density and temperature power laws. The gravitational softening parameter for the star is correspondingly smaller, and no initial perturbations are assumed. These differences conspire to push collapse instabilities to larger radii in the AB92 results, since in their simulations more mass is concentrated at large distances from the star. We believe the present conditions to be more realistic and thus to represent an improvement over the AB92 results.

Initial Orbital Characteristics

Out of the entire sample of newly formed clumps, none have an initial eccentricity much higher than $\epsilon = 0.2$, and most are between zero and 0.1. The low mass companions now being discovered around nearby solar type stars show both small and large values of eccentricity (Mayor *et al.* 1997; Marcy & Butler 1996; Butler & Marcy 1996). Although the clumps in our simulations form only in relatively low eccentricity orbits and are therefore dissimilar to many of those being discovered, considerable evolution of eccentricity can take place between the times corresponding to the end of our simulations and the final morphology of the system (see e.g., Artymowicz 1993, 1994; Goldreich & Tremaine 1980).

2.4. Conclusions

By using two conceptually different hydrodynamic methods (SPH and PPM), we are able to simulate a broader range of problems, but gain a sobering insight into the limitations of these tools. It is striking that PPM indicates violent behavior near the inner boundary (weakly supported by SPH), and that SPH indicates pronounced clumping (weakly supported by PPM). Both methods indicate that instability growth is not a steady progression from low to high amplitude perturbations with a single dominant pattern present throughout. Both methods indicate a marked change in the character of instabilities with disk mass. Low mass disks form many armed filamentary spiral structures while high mass disks form few armed grand design spiral structures.

In this study of the evolution of circumstellar accretion disks, we have found simultaneous growth of global spiral instabilities with multiple Fourier components. Growth of each of the components occurs over the course of a few orbit periods of the disk and a single component rarely dominates the evolution of a disk. As expected, the massive disks are found to be the most unstable, due to self-gravitating instabilities within the disk. Accretion of matter onto the star itself can, in warm disks (i.e. those with high Q_{\min} values), significantly drain matter from the disk time scales similar to the self-gravitating instabilities. Short-term variations in the amplitude of a given component, and strong constructive interference behavior between different components, can produce ‘spikes’ in the surface density. These spikes can eventually grow to such amplitude that gravitational collapse occurs resulting in the production of one or more clumps.

Pattern growth is stimulated at early times by the rapid growth of instabilities at small radii which eventually engulf the entire disk. Steady spiral arm structures are not generally present. Instead, spiral arms progressively grow, fragment and reform as time progresses. In cases where accretion is rapid, power can be produced in an $m = 1$ spiral pattern due to nonaxisymmetric accretion of mass and momentum onto the star. Understanding the dynamics of the inner region is of primary importance for understanding the global morphology of the system.

The gross structure of low and high mass disks are markedly different from each other. High mass disks form large, grand design spiral arms with few arms, while low mass disks form predominantly thin, filamentary multi-armed structures. In almost no case is the $m = 1$ spiral pattern the fastest growing pattern in the disk. Typically a combination of $m = 2 - 4$ patterns in high mass disks or very high order patterns ($m \gtrsim 5$) in low mass disks dominate the morphology. The transition between these behaviors comes at approximately $M_D/M_* = 0.2 - 0.4$. This transition corresponds to the ‘maximum solar nebula’ mass discussed in STAR, above which $m = 1$ modes due to SLING are expected to grow strongly.

It is intriguing to speculate that the collapse processes seen here are responsible for the production of brown dwarf-like companions such as that seen by Nakajima *et al.* (1995) and/or

of planetary companions similar to those recently discovered around several nearby stars (Mayor & Queloz 1995, Marcy & Butler 1996, Gatewood 1996). However, we must emphasize that clump formation in self-gravitating circumstellar disks depends on the ability of the gas to cool efficiently. Our simulations here use a simple isothermal equation of state which favors clump formation. Additional simulations with realistic cooling functions, including radiative transfer effects, must be done in order to clarify this important issue.

We wish to thank the referee, Richard Durisen, for a thorough referee report which improved this paper substantially. Bruce Fryxell provided valuable insights into PPM. Greg Laughlin provided valuable discussion on the tori we use for our comparisons between SPH and PPM. AFN wishes to thank his collaborators for patience in seeing this work through to its completion. This work was supported under the NASA Origins of the Solar Systems program with grants NAGW-3406 and NAGW-2250. FCA is supported by an NSF Young Investigator Award, NASA Grant No. NAG 5-2869, and by funds from the Physics Department at the University of Michigan. DA is supported by NASA NAGW-2798 and NSF ASTRO 94-17346.

Table 2.1. Disk Parameters For SPH Simulations

Name	No. of Particles	M_D/M_*	Q_{\min}	End Time ($T_D=1$)	Dominant ^a Spiral Patterns	Number Clumps
scv0	7997	.05	1.5	3.5	$\gtrsim 12$	6
scv1	7997	.1	1.5	1.6	~ 10	14
scv2	7997	.2	1.5	1.6	5-6	33
scv3	7997	.4	1.5	1.7	3-4	7
scv4	7997	.6	1.5	1.7	2-4	6
scv5	7997	.8	1.5	2.4	1-3	3
scv6	7997	1.	1.5	1.8	1-3	3
sqh1	7997	.8	1.1	0.1	NR	18
sqh2	7997	.8	1.3	.25	NR	11
sqh3	7997	.8	1.4	.35	NR	7
sqh4	7997	.8	1.7	4.2	1-2	0
sqh5	7997	.8	2.0	4.2	1	0
sqh6	7997	.8	2.3	4.2	1	0
sql1	7997	.4	1.1	.15	NR	28
sql2	7997	.4	1.3	0.3	NR	7
sql3	7997	.4	1.4	0.4	4	1
sql4	7997	.4	1.7	5.0	1-3	0
sql5	7997	.4	2.0	4.2	1-2	0
sql6	7997	.4	2.3	4.2	1	0
sql7	7997	.4	2.7	4.2	1	0
sql8	7997	.4	3.0	4.2	1	0

^aWhen only $m=1$ patterns are indicated, actual evolution is apparently an accretion induced transient star/disk oscillation (see figure 2.9) rather than a spiral arm. NR (not resolved): for low stability disks, assignment of specific spiral arm patterns loses meaning due to their rapid breakup.

Three series of runs are represented in this table. The first letter in each name is 's', signifying an SPH simulation. The second, is either 'c' or 'q', signifying constant or varying Q_{\min} , and the third letter signifies that the simulation is a member of a high (h), low (l) or varying (v) disk mass series. Ascending numerical order in each series refers to successive values of either disk mass or Q_{\min} , for each series.

Table 2.2. Disk Parameters for PPM Simulations

Name	Grid Res.	M_D/M_*	Q_{\min}	End Time ($T_D=1$)	Dominant ^a Spiral Patterns	Outer Bndry
pcm1	64×102	0.1	1.5	5.8	NR	Refl.
pcm2	64×102	0.2	1.5	5.0	2-4	Refl.
pcm3	64×102	0.4	1.5	4.0	1-3	Refl.
pcm4	64×102	0.6	1.5	3.75	1-3	Refl.
pcm5	64×102	0.8	1.5	3.0	1-3	Refl.
pcm6	64×102	1.0	1.5	3.0	1-3	Refl.
pch2	100×152	0.2	1.5	5.0	2-4	Refl.
pch6	100×152	1.0	1.5	3.6	1-3	Refl.
pqm1	64×102	0.8	1.1	1.8	1-2	Refl.
pqm2	64×102	0.8	1.3	2.6	1-2	Refl.
pqm3	64×102	0.8	1.4	3.0	1-2	Refl.
pqm4	64×102	0.8	1.7	3.0	1-2	Refl.
pqm5	64×102	0.8	2.0	2.0	1	Refl.
pci2	64×96	0.2	1.5	3.8	3-4	Infall
pci3	64×96	0.5	1.5	2.1	1-3	Infall
pci4	64×96	0.6	1.5	2.0	1.3	Infall
pci6	64×96	1.0	1.5	1.6	1-3	Infall
pcl1	44×64	0.1	1.5	5.6	NR	Infall
pcl2	44×64	0.3	1.5	4.2	1-3	Infall
pcl3	44×64	0.4	1.5	4.2	1-3	Infall
pcl4	44×64	0.5	1.5	2.8	1-2	Infall
pcl5	44×64	0.7	1.5	2.8	1-2	Infall
pcl6	44×64	1.0	1.5	2.0	1-2	Infall

^aNR: not resolved. For some low mass disks, distinct spiral patterns are not possible to distinguish.

Each of these PPM runs begins with ‘p’ to distinguish it from SPH series. The second letter is ‘c’ or ‘q’ signifying a constant or varying Q_{\min} value for each disk in the series. The third letter implies a *low*, *moderate* or *high* resolution simulation. Moderate resolution infall boundary simulations are distinguished from reflecting boundary simulations using an ‘i’ in place of ‘m’. Numbers are successive values of disk mass or Q_{\min} in each series of runs.

Table 2.3. Tori and Disk Results in SPH and PPM

Initial Density Structure	Hydro Method	Linear Regime	Reason/Result	Non-linear Regime	Reason/Result
Disk (eq. 2.3)	PPM	fails	inner boundary	not accessible	...
	SPH	not accessible	short time baseline	succeeds	spiral arm formation and collapse
Disk w/Central Hole (eq. 2.4)	PPM	succeeds	spiral arm growth	short duration only	boundary influence
	SPH	not accessible	short time baseline
Torus (eq. 2.18)	PPM	succeeds	spiral arm growth	succeeds	spiral arm collapse
	SPH	partial success	spiral arm growth	succeeds	spiral arm collapse

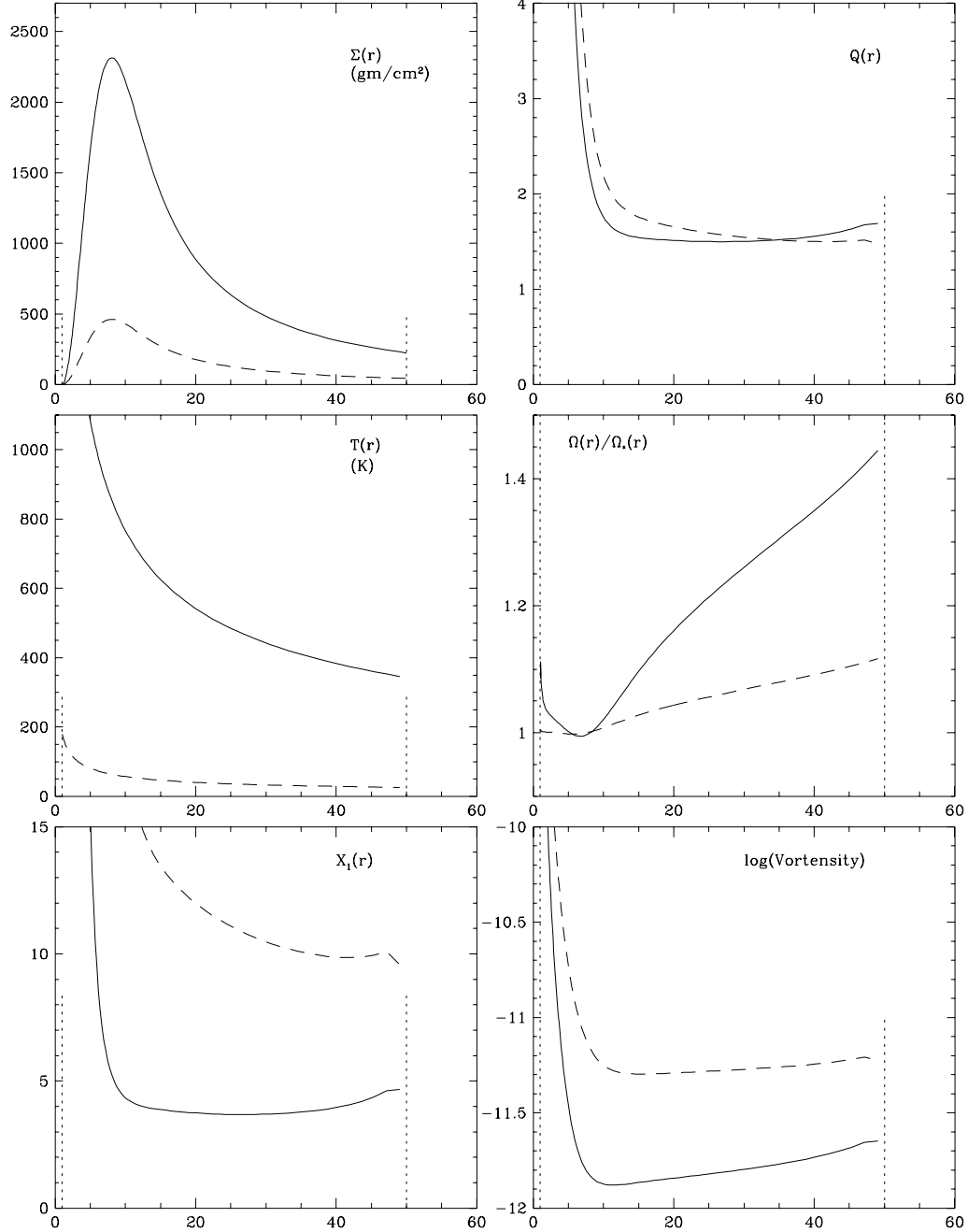


Figure 2.1 A summary of the initial conditions for low (dashed) and high (solid) disk mass PPM simulations (simulations *pch2* and *pch6*). The six panels show surface density Σ , Toomre Q , temperature T , the ratio of the rotation period at radius r with the Keplerian value. We define $\Omega_*(r)$ in the middle right panel as $\Omega_*(r) = \sqrt{GM_*/r^3}$. In the lower left panel, we show the value of the SWING X parameter for the $m = 1$ pattern. Higher order patterns ($m > 1$) are smaller by a factor $1/m$ than the value shown. In the lower right panel, we show the value of the vortensity at each radius.

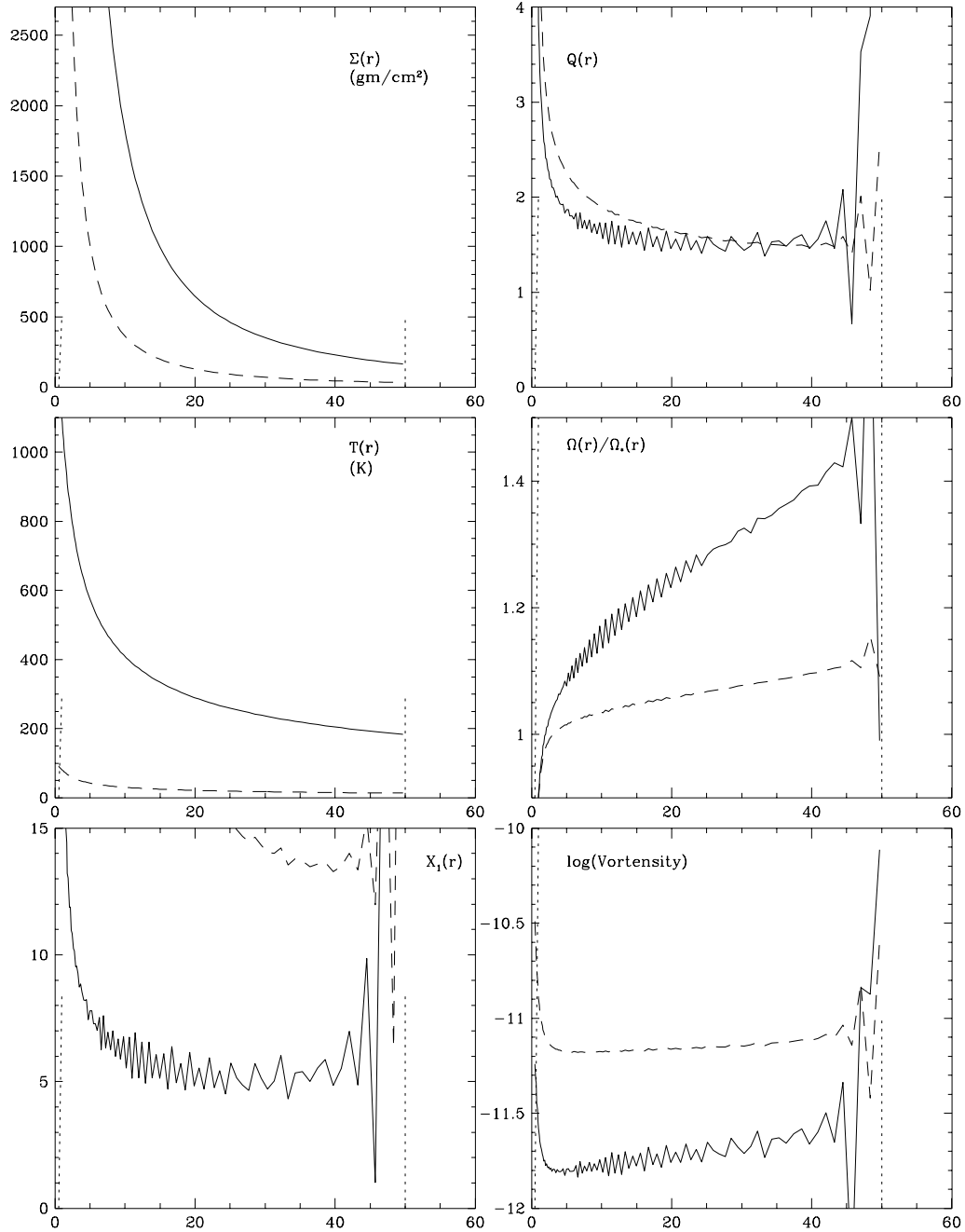


Figure 2.2 A summary of the initial conditions for low (dashed) and high (solid) disk mass SPH simulations (simulations *scv2* and *scv6*). This figure shows the same parameters as shown in figure 2.1.

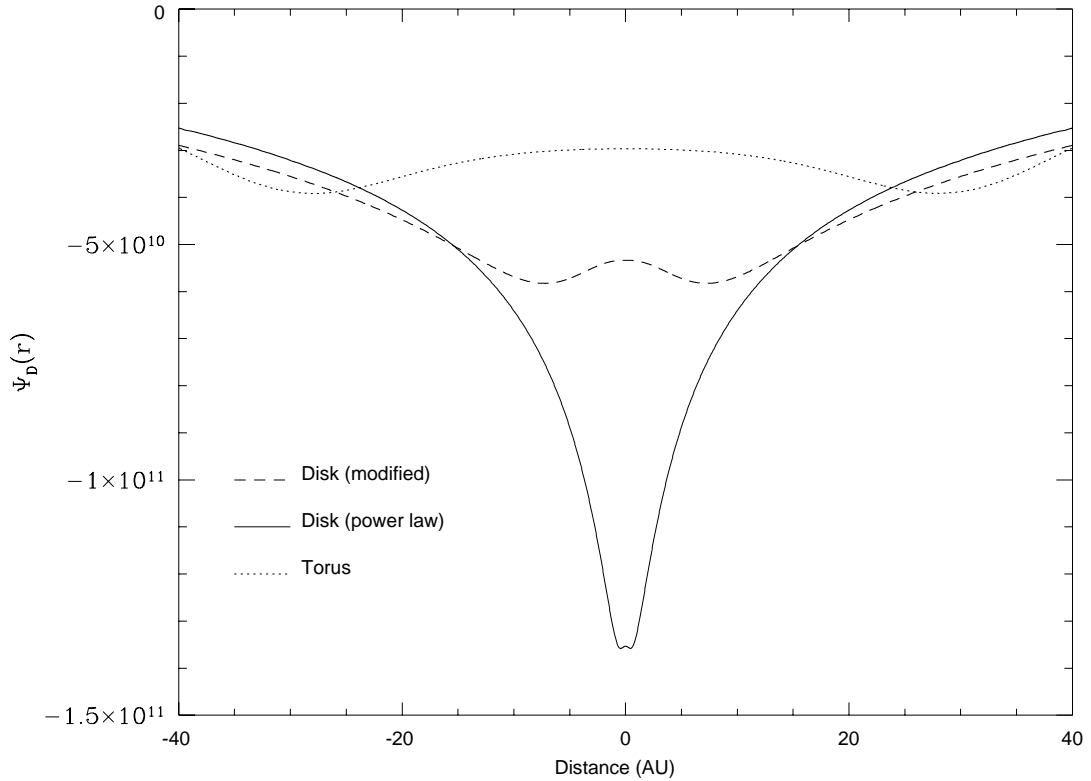


Figure 2.3 The initial gravitational potential due to the disks and tori we study. We show a slice through the origin where the star is initially located. The solid curve represents the gravitational potential due to the pure power law as given by eq. [2.3]. The dashed curve is that due to the modified power law of eq. [2.4], while the dotted curve is that due to a torus as defined in section 2.3.3. The mass in each disk or torus is $M_D/M_* = 0.2$. Each system produces a gravitational potential hump at the origin which seeds the growth of $m = 1$ disturbances in the disk or torus.

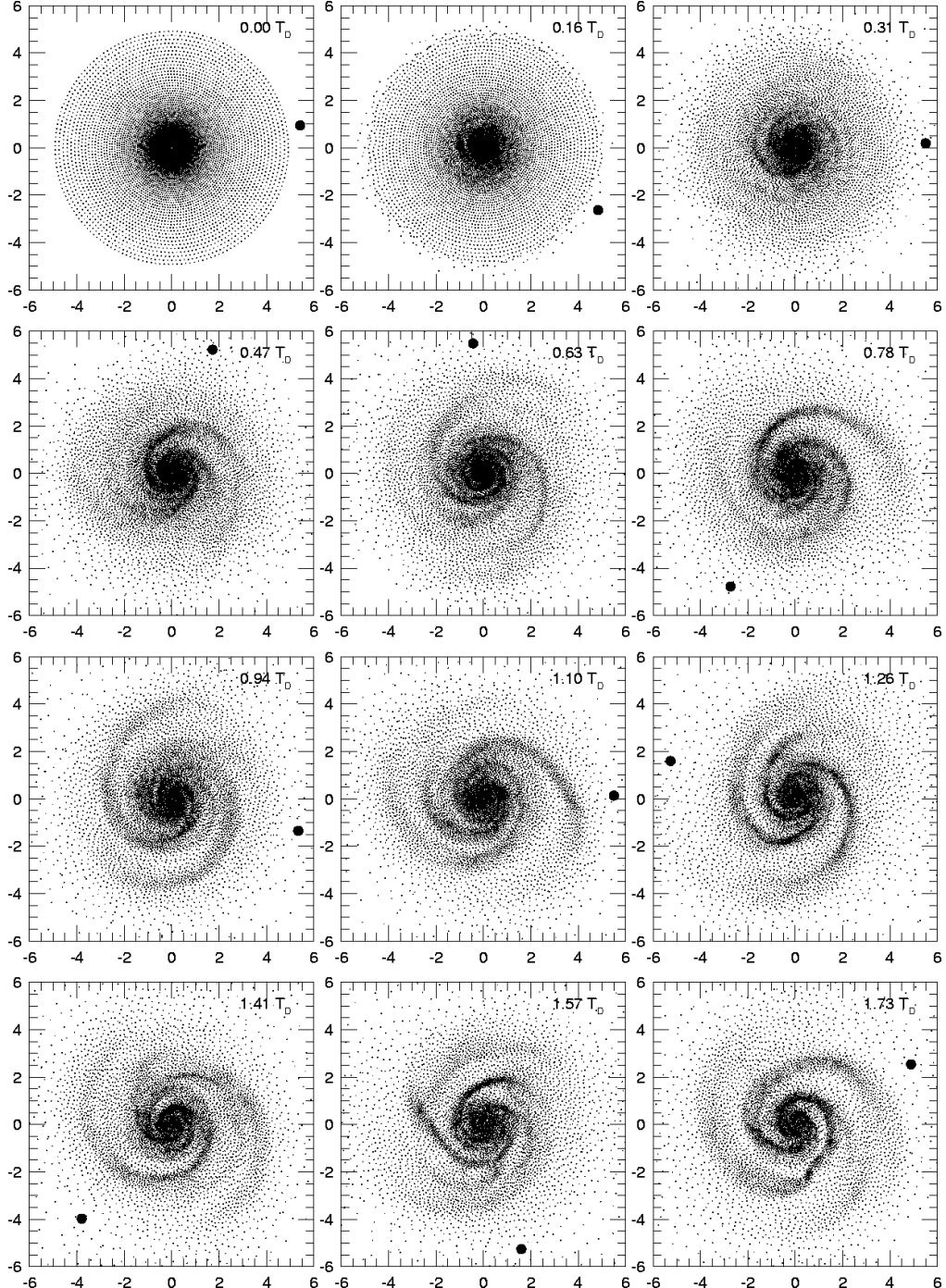


Figure 2.4 A time series mosaic of SPH particle positions for a disk of mass $M_D/M_* = 1.0$ and $Q_{\min} = 1.5$ (simulation *scv6*). Note the strong variation of spiral structure over time. Length units are defined as 1=10 AU and time in units of the disk orbit period T_D . The large, solid dot is the angular position of the star projected out to a distance of 55 AU, just outside the outer disk edge. The final image in this mosaic shows the beginning stages of clump formation as a clump begins to form in the disk at about an azimuth angle of 5 o'clock and radius of $r = 20$ AU. A second clump which initially formed in the other spiral arm is present but difficult to distinguish in the image at 3 o'clock and $r \sim 7$ AU.

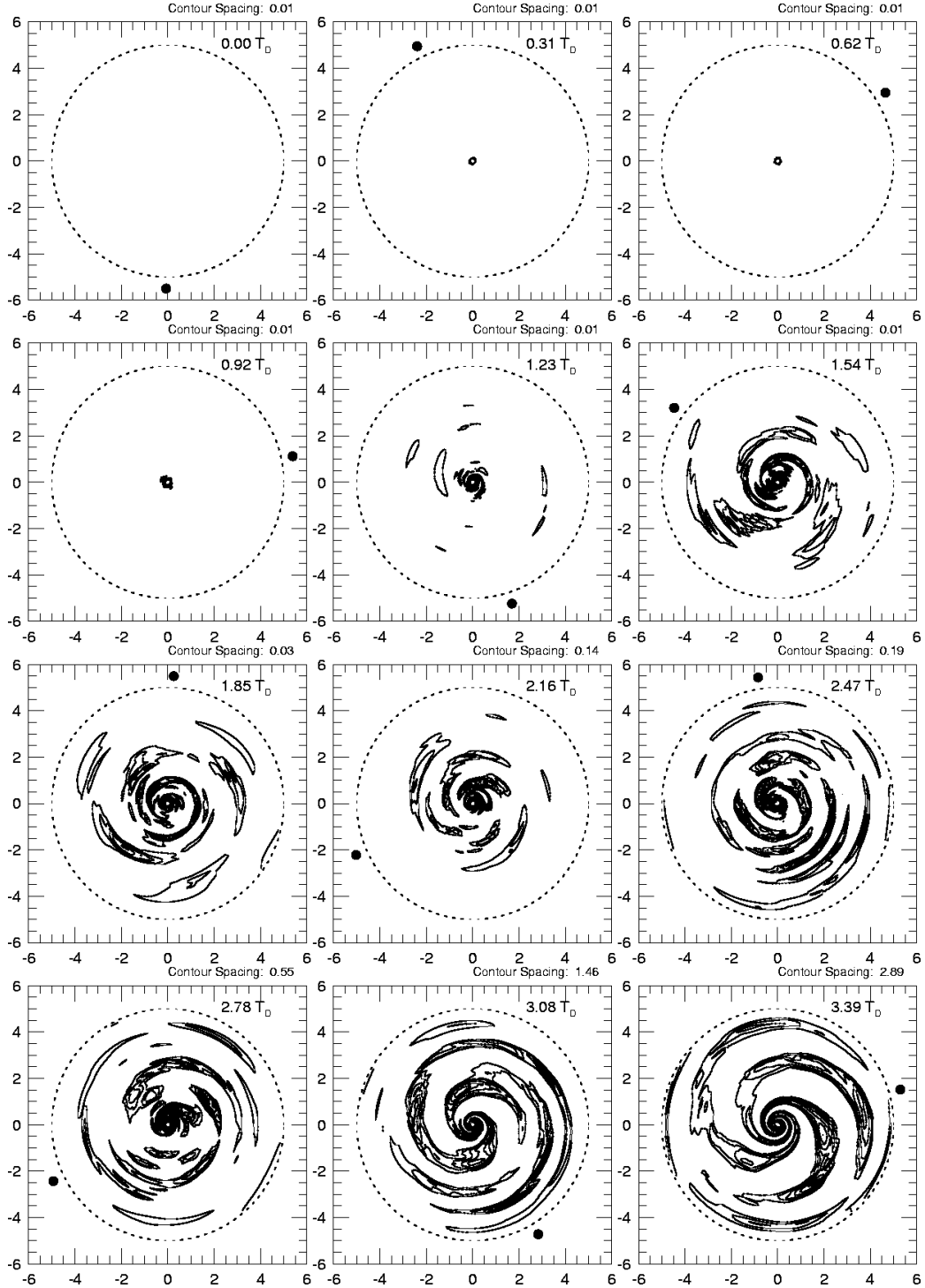


Figure 2.5 Time series of density variation in the disk for a PPM simulation (simulation *pch6*). with the same initial conditions as figure 2.4. Only positive density variations are plotted and the maximum contour is derived only from deviations at radii larger than ~ 7 AU. Contours are linearly spaced and set to a minimum of .01% variation per contour line. Larger variations are implemented as the instability grows. The contour spacing is denoted in the upper right corner of each frame.

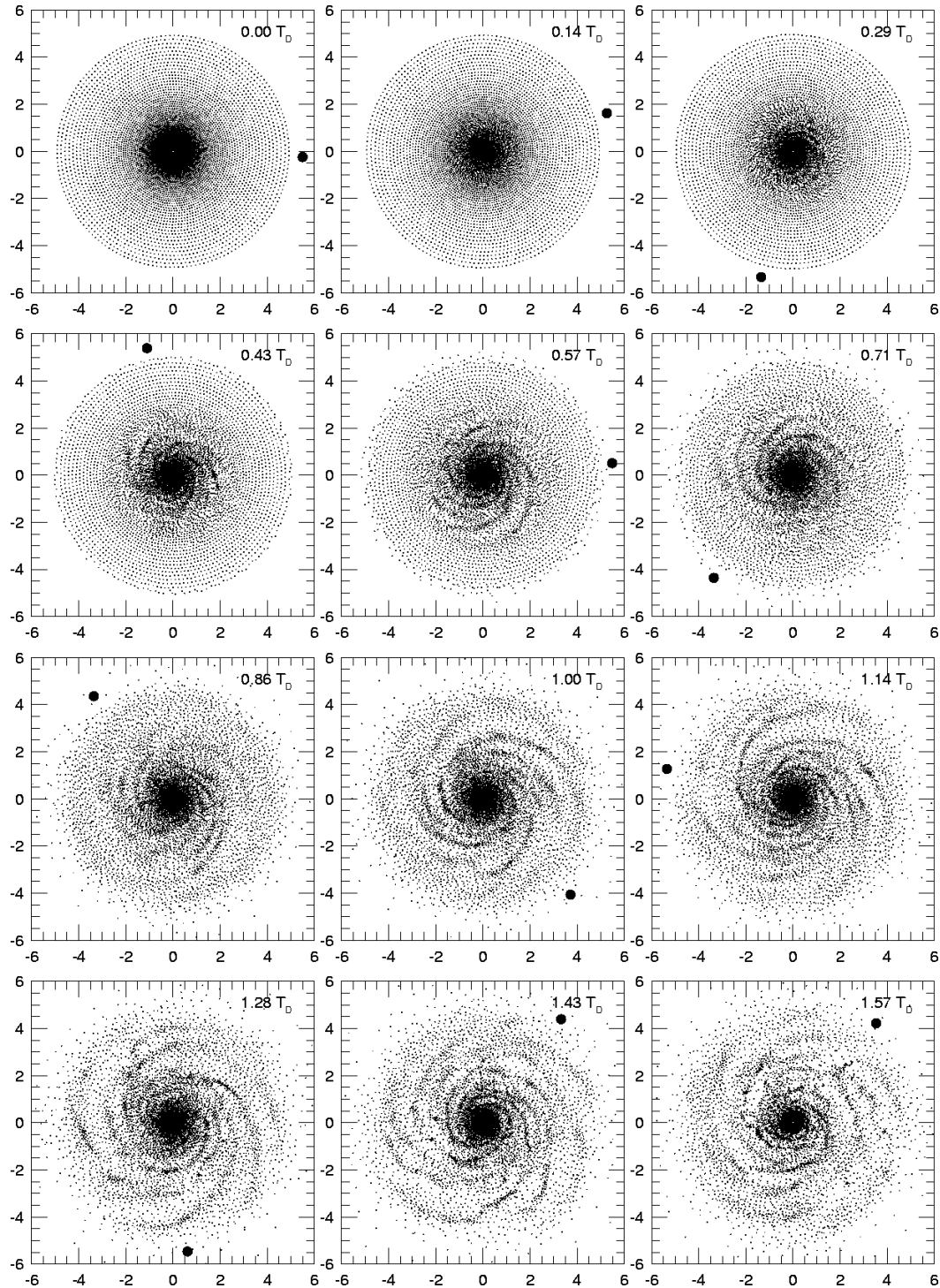


Figure 2.6 Evolution of a disk with $M_D/M_* = 0.2$ and with initial $Q_{\min} = 1.5$ (simulation *scv2*). Note the production of long filamentary spiral arms and the production of multiple clumps at later times.

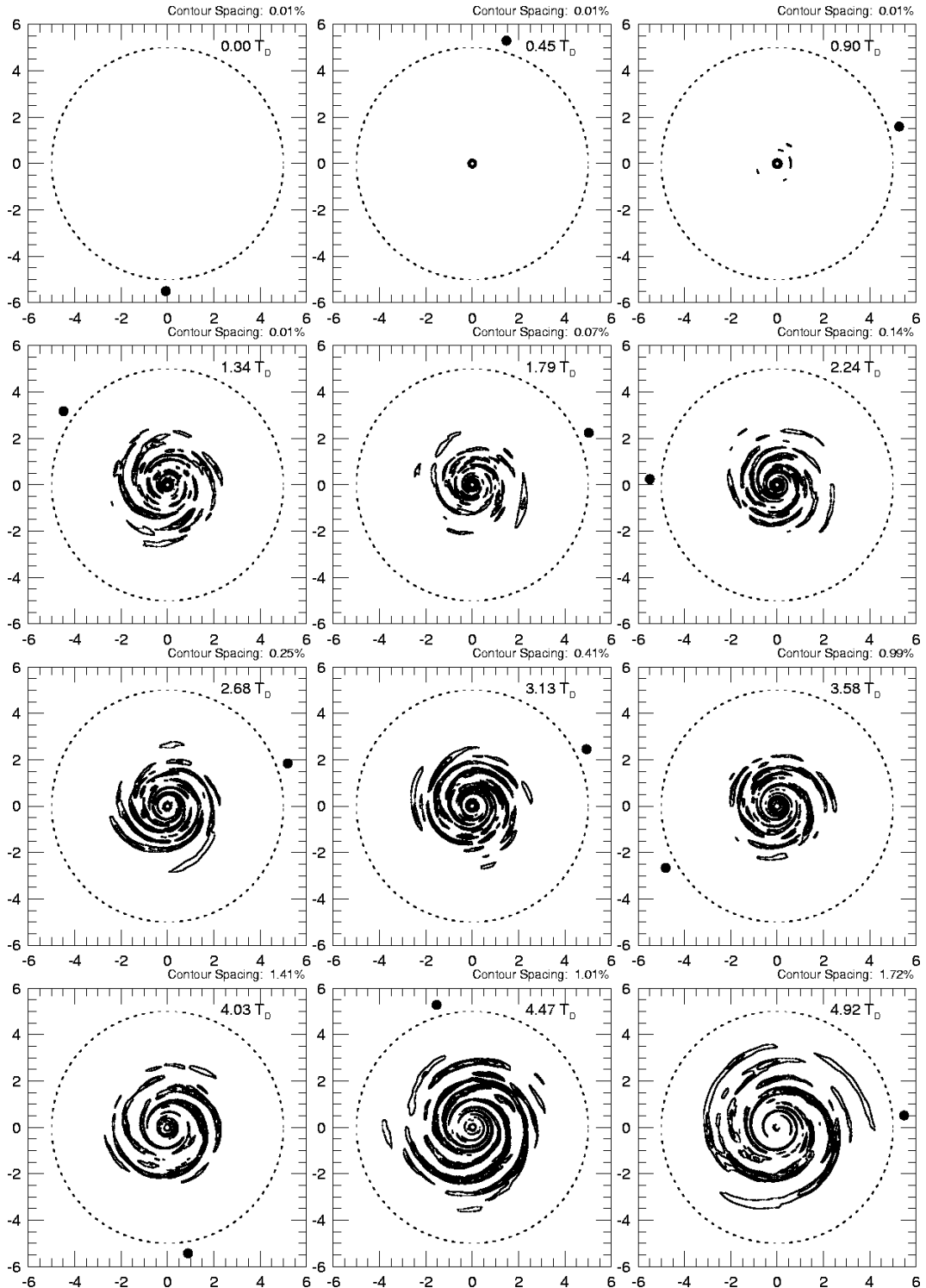


Figure 2.7 The same initial conditions as figure 2.6 with the PPM code (simulation *pch2*). A much longer evolution than figure 2.6 is possible here due to the low initial noise of PPM.

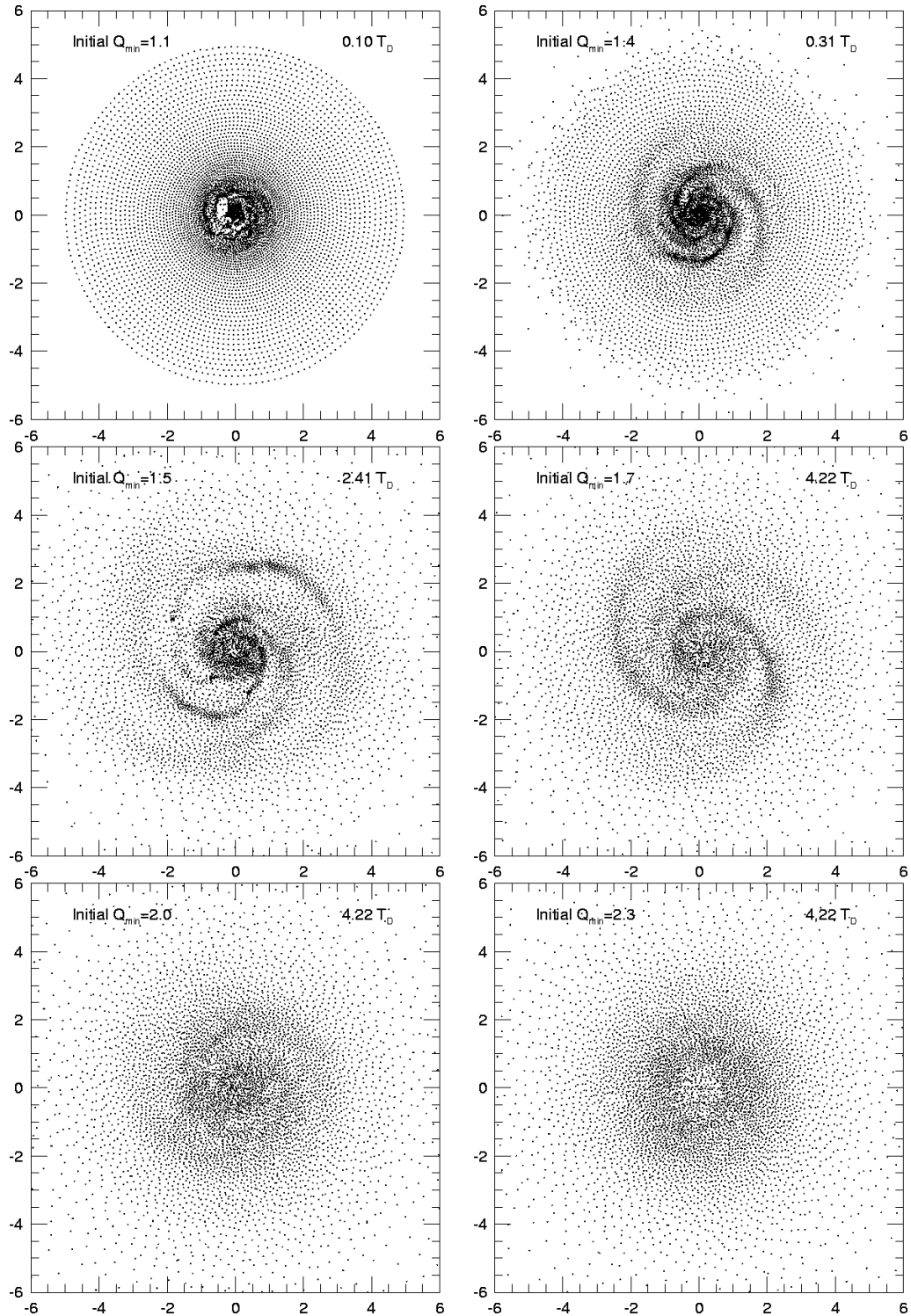


Figure 2.8 Late time snapshots of a series of disk simulations using our SPH code. Each disk has the same disk mass of $M_D/M_* = 0.8$ but varying Q_{\min} (simulations *sqh1*, -3, -4, -5, and -6, as well as *scv5* are shown).

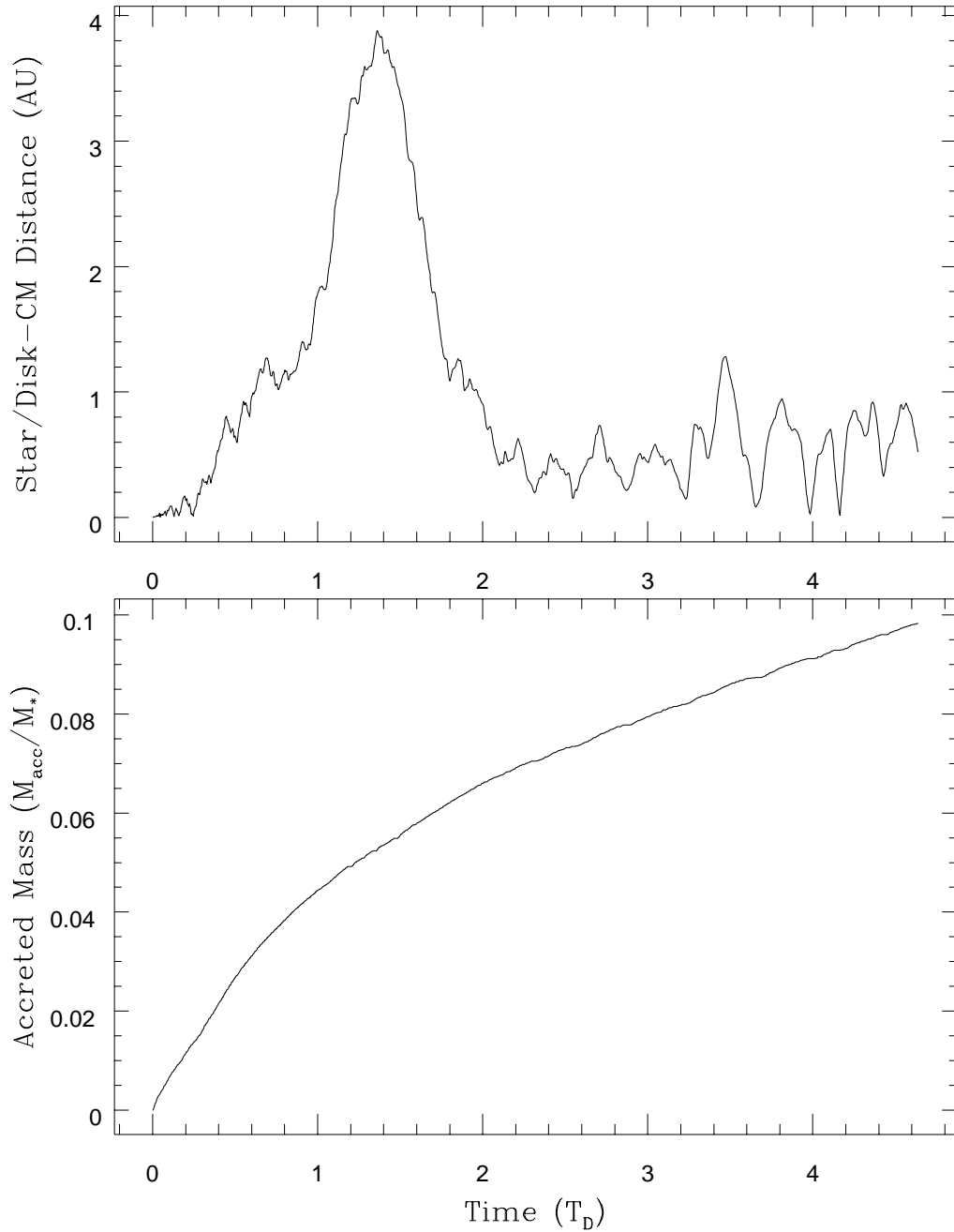


Figure 2.9 The distance between the star and the disk center of mass is shown as a function of time in the top panel here, while the mass accreted by the star is shown in the second. The simulation these data are taken from is *sqh6*, which begins with $M_D/M_* = 0.8$ and an initial minimum Q value of 2.3. With the units assumed for our systems, the mass accretion rate is near $8 \times 10^{-5} M_\odot/\text{yr}$ at its maximum. When accretion begins to drain the inner disk matter and the rate falls sufficiently (in this simulation, to $\sim 3 \times 10^{-5} M_\odot/\text{yr}$), the star falls to the center of the system and returns much of its temporary increase in angular momentum to the disk.

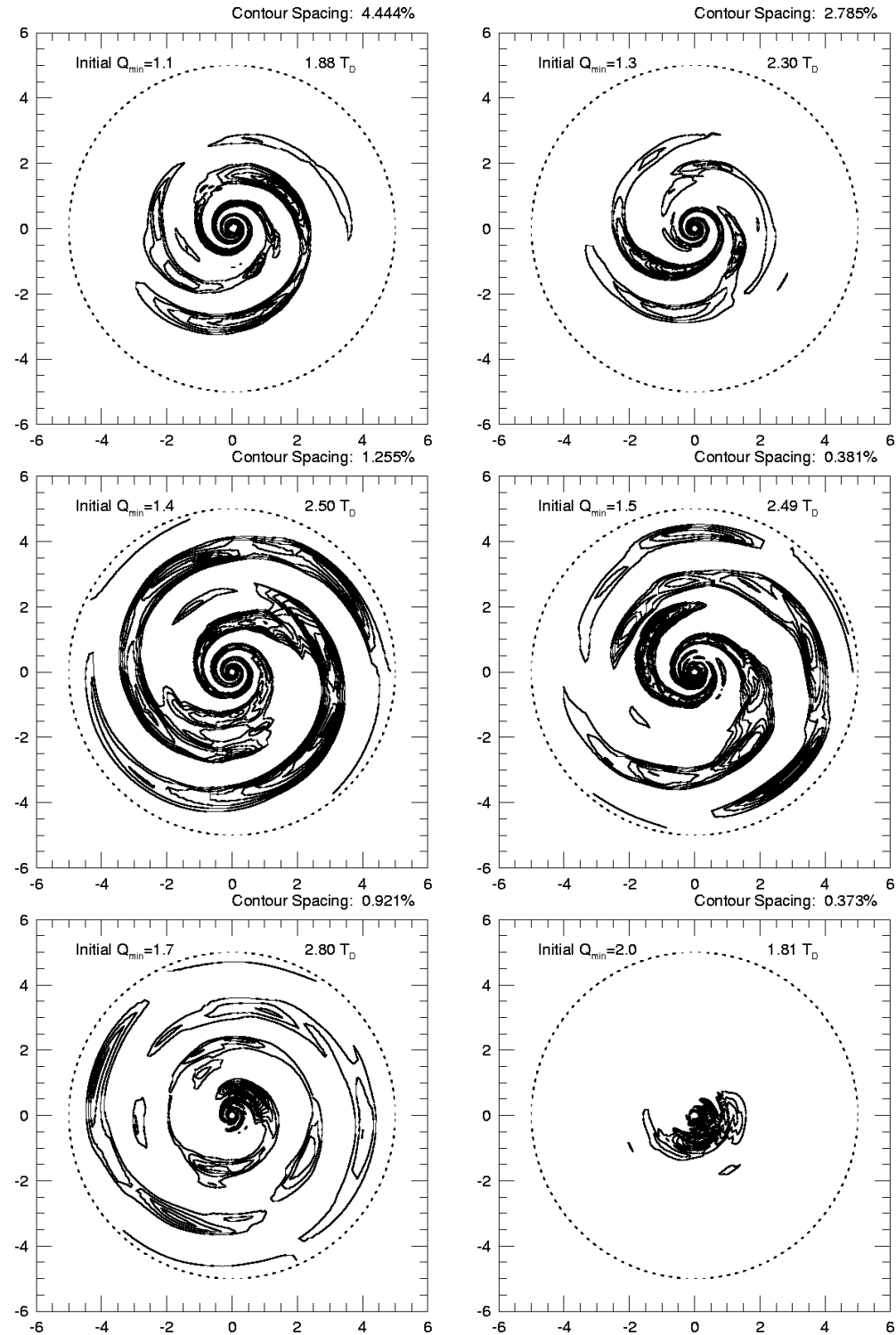


Figure 2.10 Late time snapshots of a series of disk simulations using our PPM code. Each disk has the same disk mass of $M_D/M_* = 0.8$ but varying Q_{\min} (simulations *pqm1-5* as well as *pcm5* are shown).

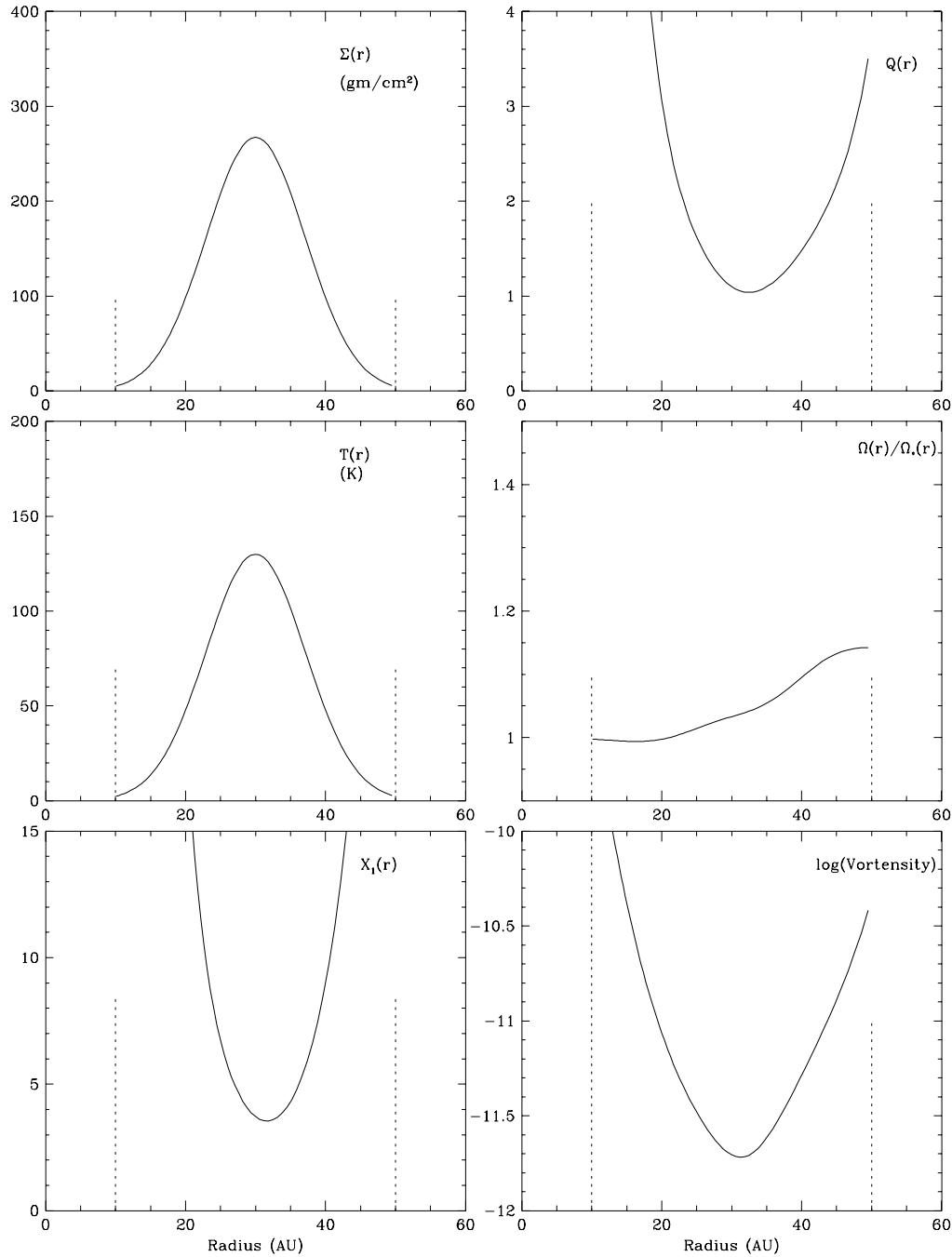


Figure 2.11 Initial conditions for torus simulations. Each frame contains the same variable as in the corresponding frames in figures 2.1 and 2.2.

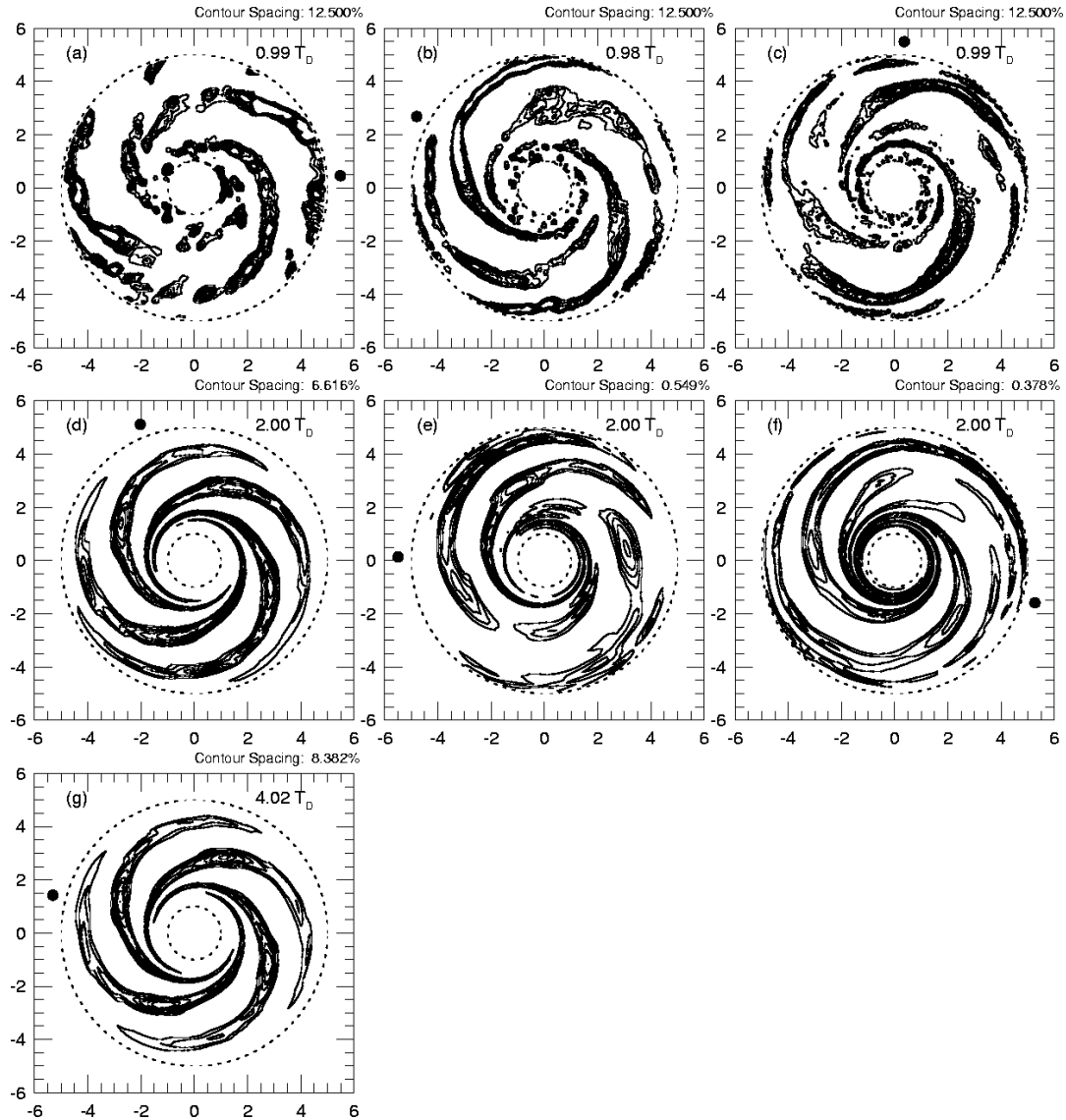


Figure 2.12 Late time snapshots of a torus with identical initial conditions using (a-c) SPH with ~ 7000 , 14000 , and 28000 particles respectively. (d-f) PPM with 10^{-3} amplitude random initial noise at three grid resolutions: 40×150 , 60×225 and 80×300 and (g) PPM simulation with low initial noise (10^{-8}) at 40×150 grid resolution. For comparison purposes, the SPH runs are mapped onto a grid identical to that used for the corresponding PPM runs.

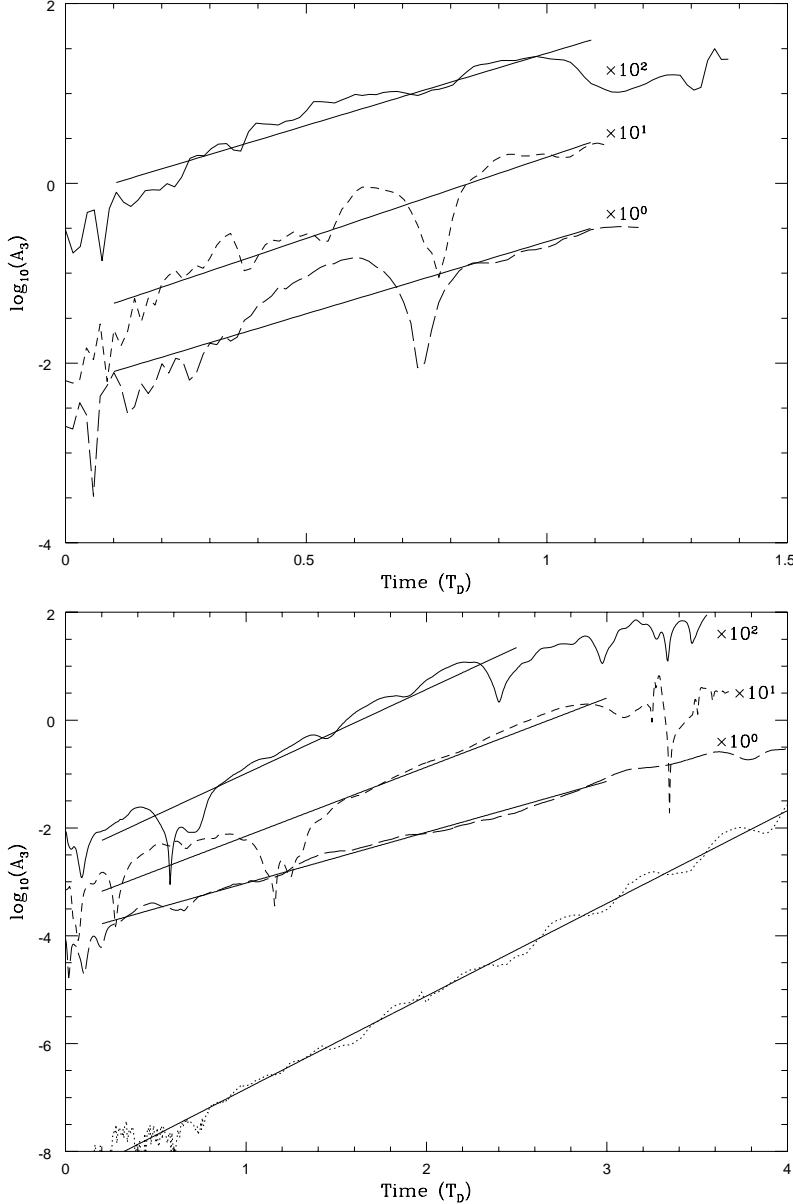


Figure 2.13 Amplitudes and linear best fits for the $m = 3$ pattern at the center of the torus ($R = 30$ AU) for different resolution SPH and PPM simulations. The top panel shows SPH simulations. The lowest resolution (~ 7000 particles) is denoted with a solid curve while double resolution (~ 14000 particles) is denoted with a short dashed curve and the highest resolution (~ 28000 particles) is shown with a long dashed curve. Each of the fits are shown as solid lines. Bottom panel: PPM simulations with the two lowest resolution runs denoted by a solid and dotted line for the 10^{-3} and 10^{-8} amplitude initial noise runs respectively. The short dashed curve represents the middle resolution and the long dashed line represents the highest resolution run. Solid lines denote the best fit curves for each of the runs and displayed only for the times for which the fit was derived. Each of the SPH runs and the PPM runs with 10^{-3} noise are artificially multiplied by a factor of 1, 10 or 100 in order to distinguish between the different runs on the plots.

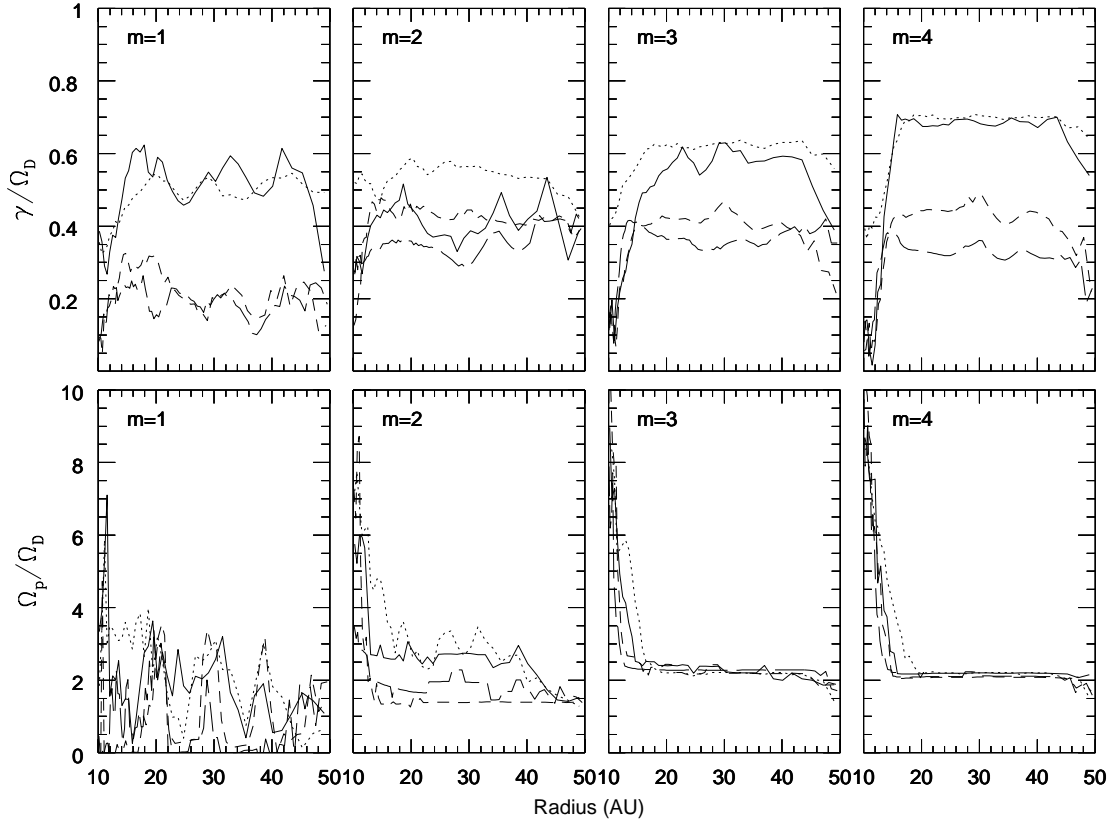


Figure 2.14 Growth rates and pattern speeds for the $m = 1 - 4$ patterns derived from PPM simulations. The increase in the pattern speed at the inner torus edge probably represents a boundary influence and we do not consider it to be significant. Each curve uses the same representation as in figure 2.13 to denote low, moderate and high resolution runs.

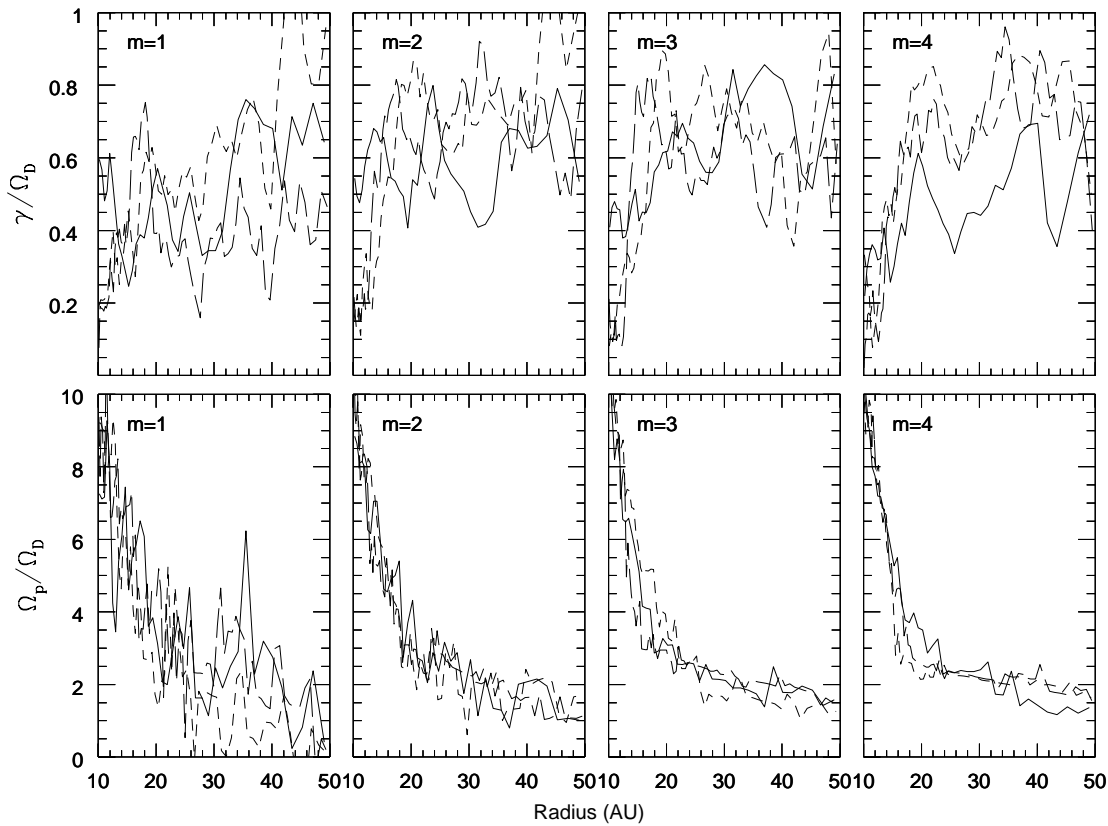


Figure 2.15 Growth rates and pattern speeds for the $m = 1 - 4$ patterns derived from the SPH simulations. Each curve uses the same representation as in figure 2.13 to denote low moderate and high resolution runs.

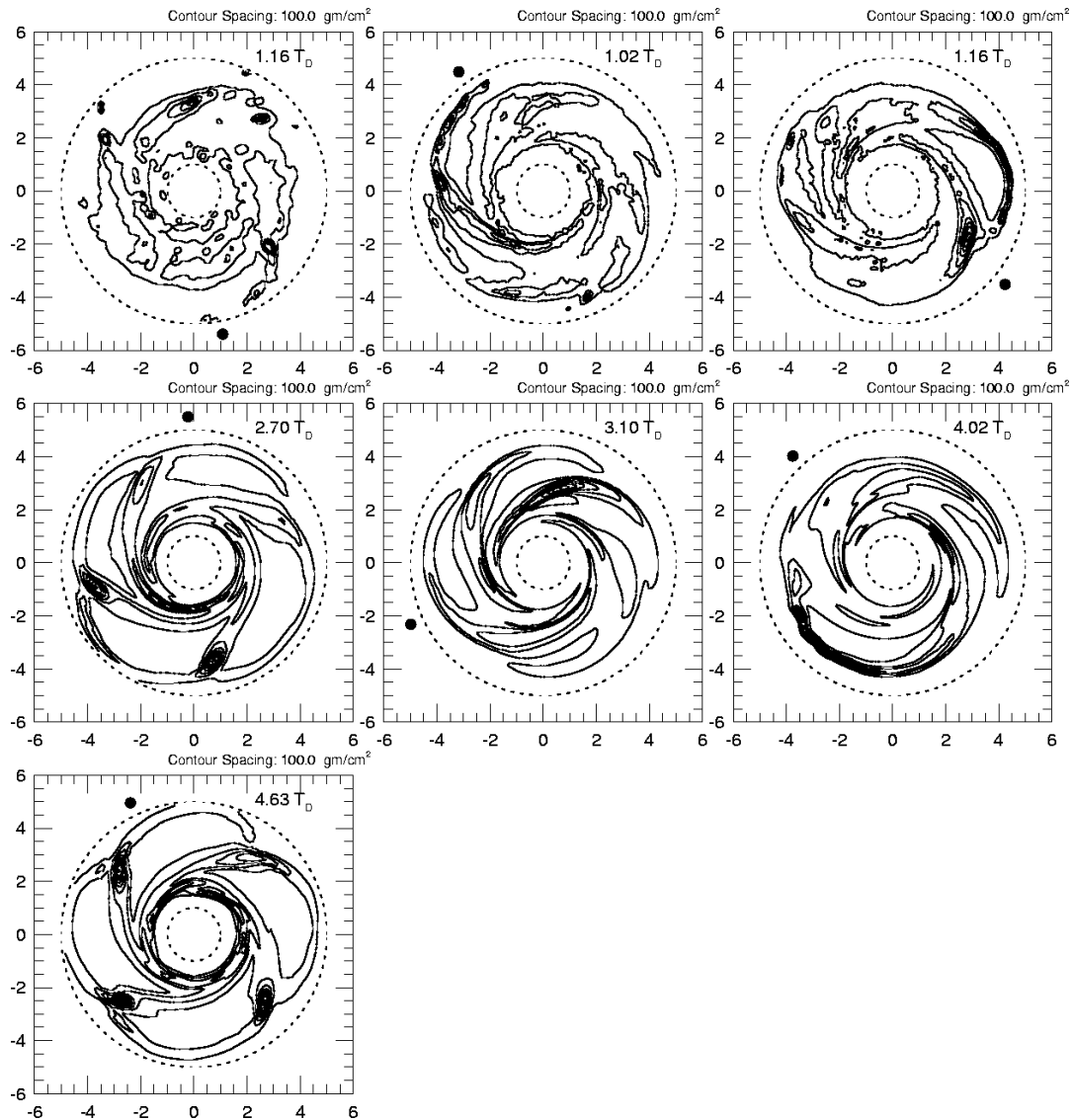


Figure 2.16 Late time snap shots of the same simulations as figure 2.12 above. Here we plot density rather than density variation to accentuate collapse behavior. Contours units are gm/cm^2 and are linearly spaced from 0 gm/cm^2 (not shown) upward with spacing between contours as noted at the upper right of each frame. Because the collapse behavior occurs at a somewhat different time for each of the runs, the plots are not shown at the same time as any other plot. Rather, we show the morphology shortly after collapse begins in each simulation, at whatever time during the simulation that occurred. Each of the SPH runs are mapped onto a grid identical to that used by the corresponding PPM simulation. The dashed curves denoting the inner and outer grid radii therefore have no meaning for these runs.

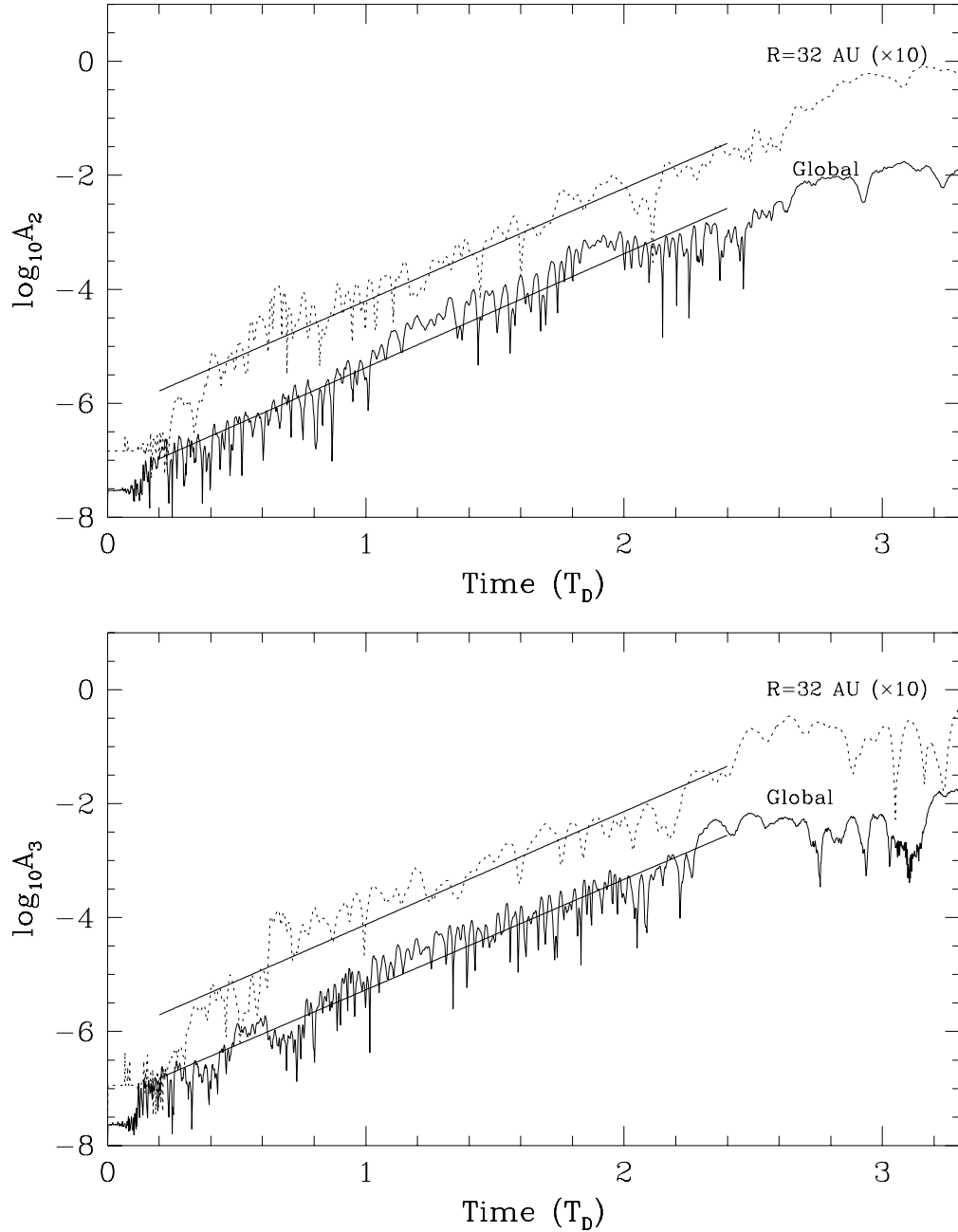


Figure 2.17 The amplitudes and fits for the $m = 2$ (top frame) and $m = 3$ (bottom frame) patterns derived from the simulation shown in figure 2.5. The amplitude ($\times 10$) near the middle of the power law portion of the disk as well as the globally integrated amplitudes for each pattern are shown.

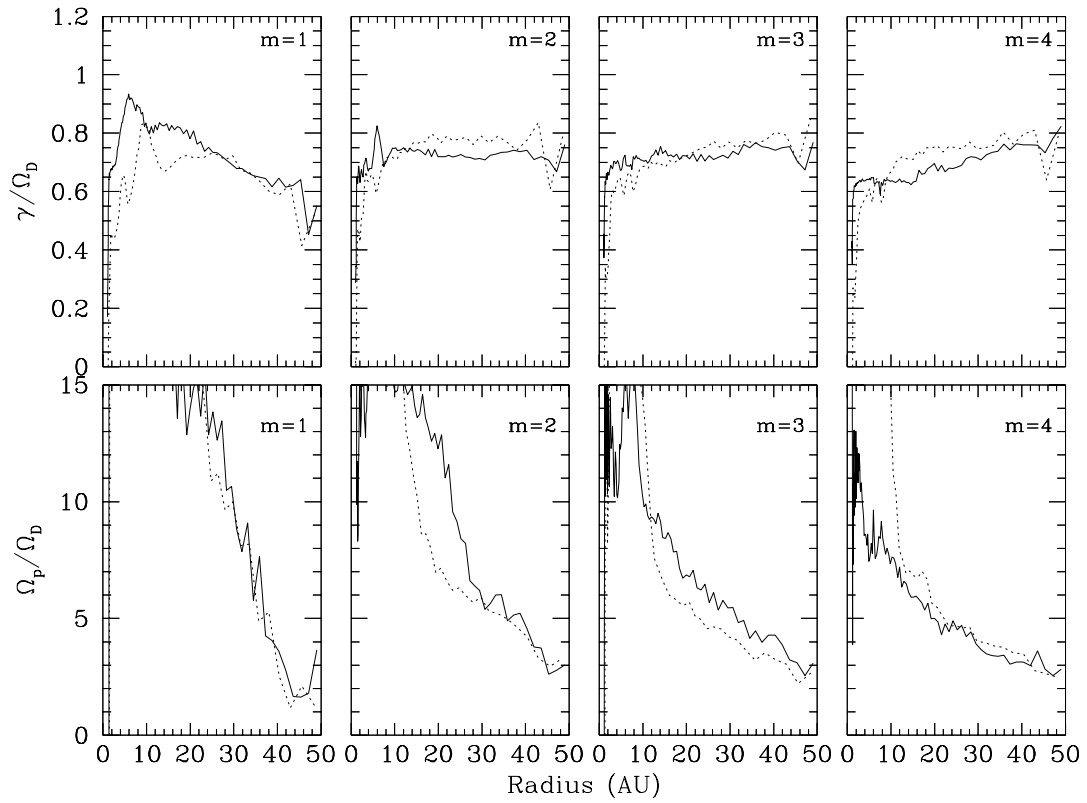


Figure 2.18 The growth rates and pattern speeds for the $m = 1\text{--}4$ spiral arm patterns. The simulation from which these are derived is the same as is shown in figure 2.5. The solid lines represent the moderate resolution simulation $pch6$ while the dotted lines represent results from the lower resolution simulation $pcm6$.

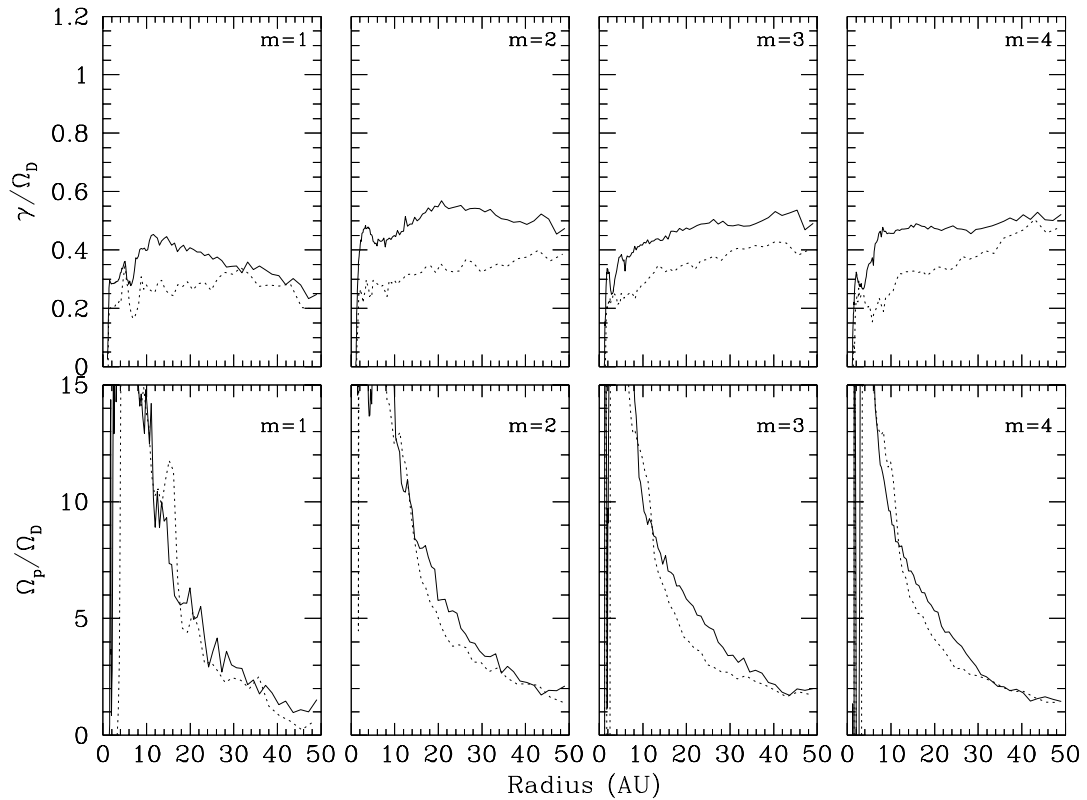


Figure 2.19 The growth rates and pattern speeds for the $m = 1\text{--}4$ spiral arm patterns. The simulation from which these are derived is the same as is shown in figure 2.7. The solid lines represent the moderate resolution simulation *pch2* while the dotted lines represent results from the lower resolution simulation *pcm2*.

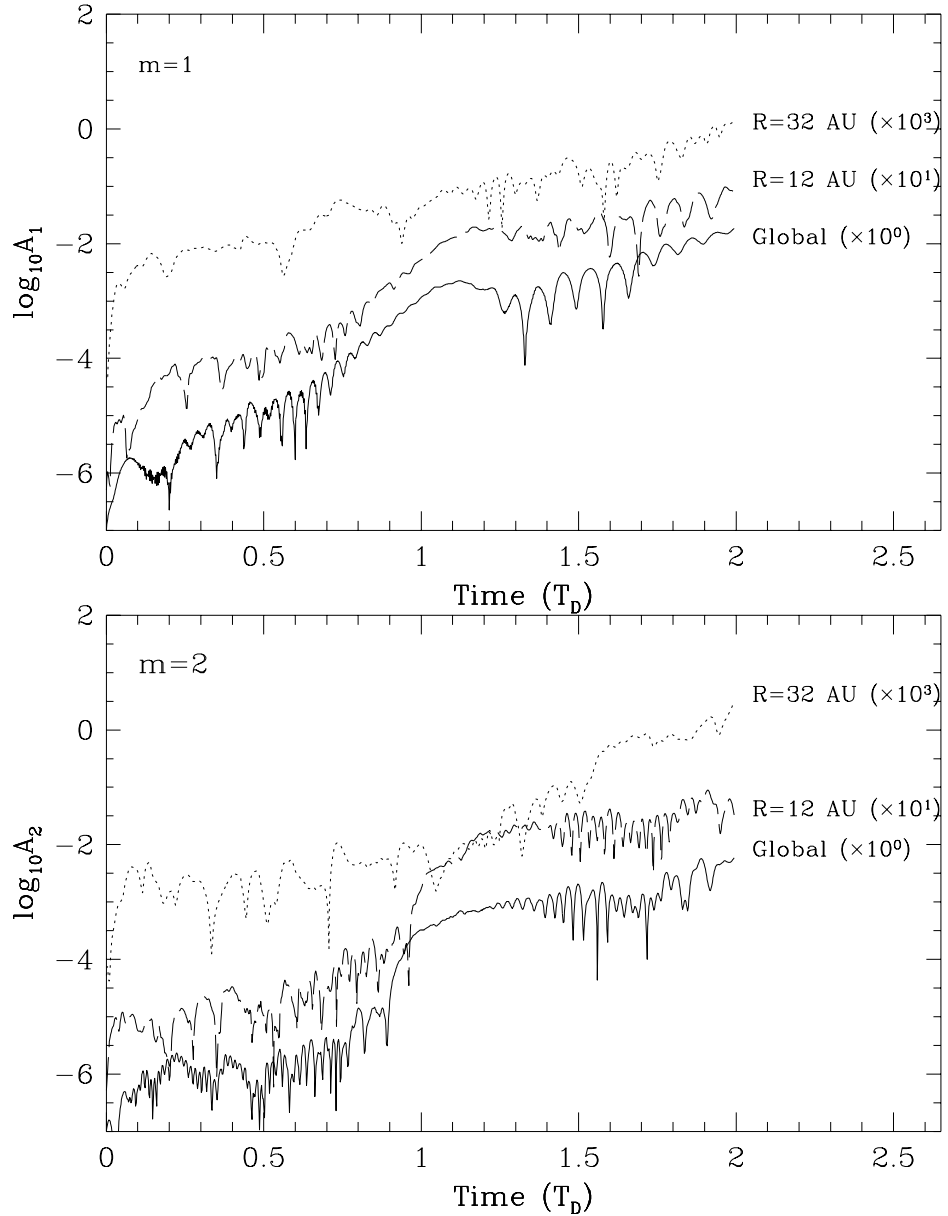


Figure 2.20 Amplitude of the $m = 1$ and $m = 2$ spiral patterns at various locations in the disk simulation *pqm5*. The outer portion of this disk is initially quiescent. The amplitude of the $m = 1$ pattern does begin growing immediately, however near $T_D \sim 1$ it experiences a ‘hump’ in its amplitude as instability propagates towards larger radii. The region near the density maximum ($R \sim 12$ AU) experiences little initial growth in $m > 1$ patterns, but once instabilities enter that region (cf. the lower right panel of figure 2.10) they quickly grow to dominate the instability amplitude over the entire system.

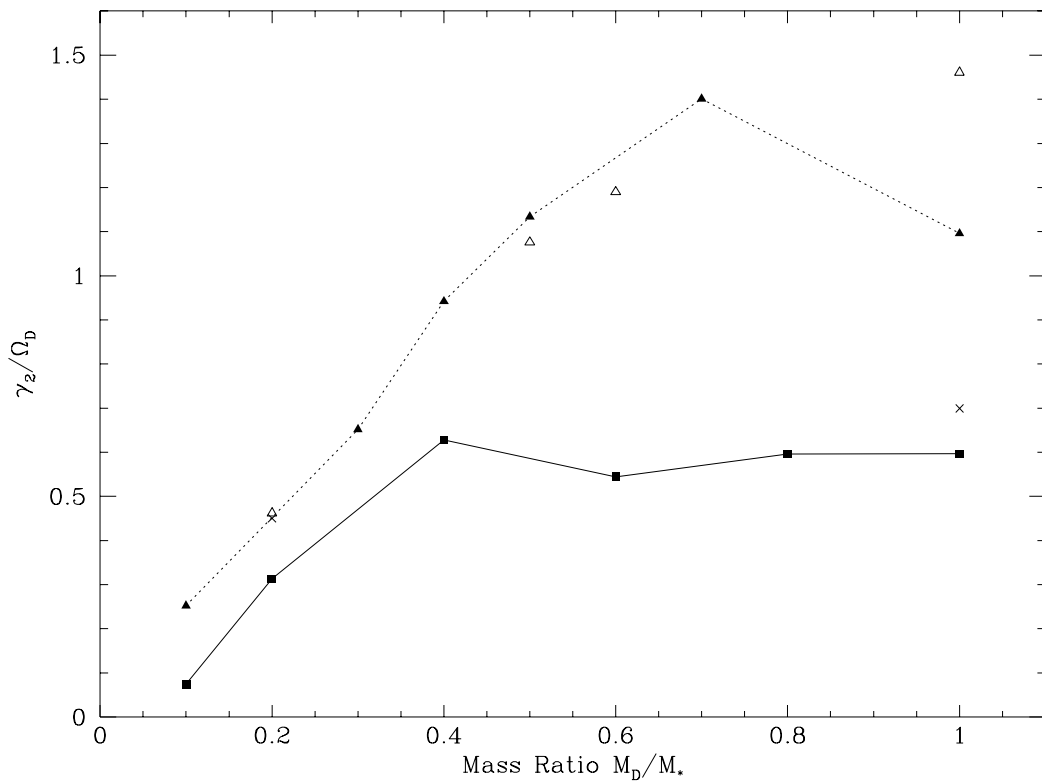


Figure 2.21 Growth rates for the $m = 2$ pattern for PPM simulations using a reflecting outer boundary condition at moderate resolution (solid squares) and at higher resolution (x). A second series of simulations with an infall boundary condition are shown with solid triangles and at higher resolution with open triangles.

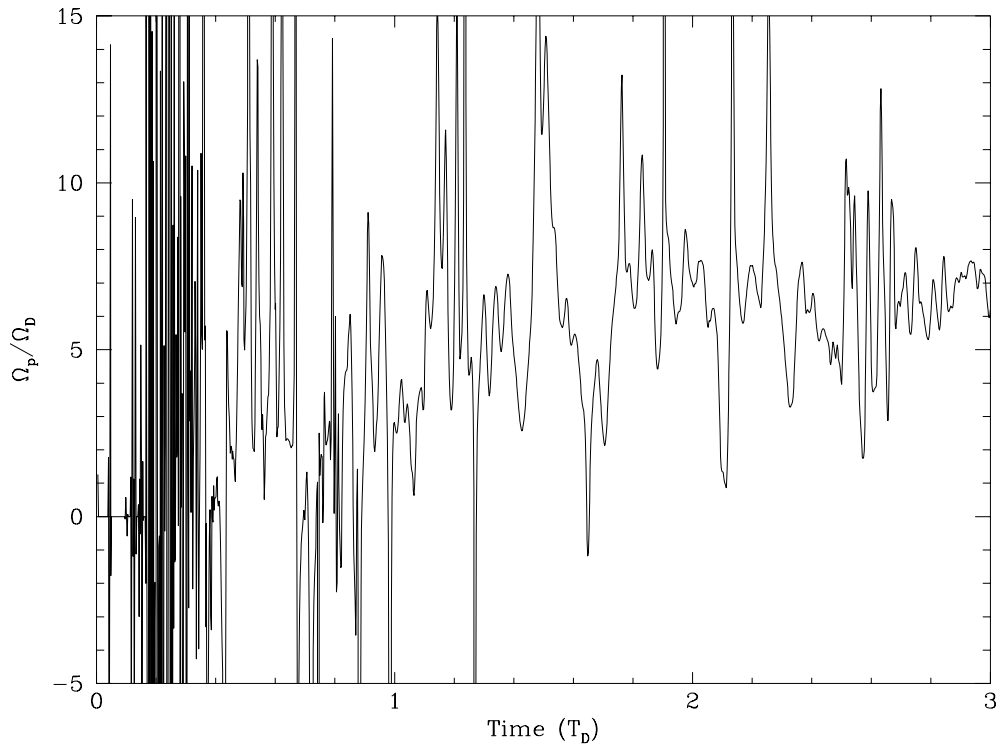


Figure 2.22 Pattern speeds for the $m = 2$ pattern as a function of time for the disk shown in figure 2.5. The pattern speed is for the pattern at a radius $R \approx 32$ AU from the star, which is near the middle of the region where the density is a power law in form.

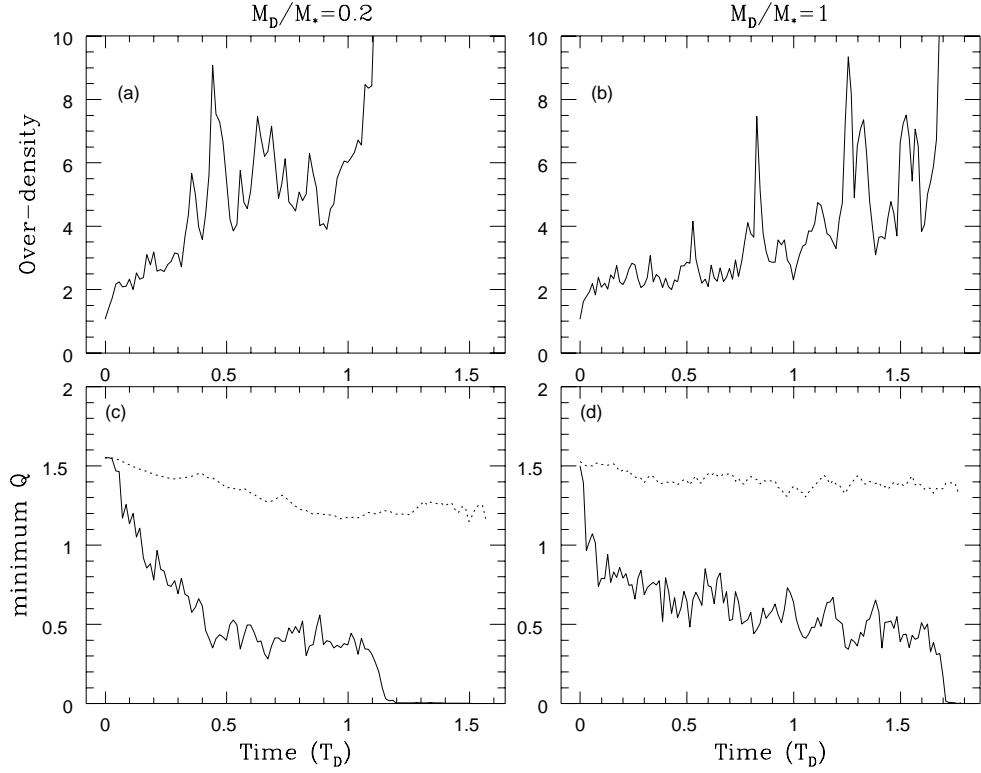


Figure 2.23 Maximum over-density in SPH disks of low (a) and high (b) disk/star mass ratio plotted vs. time (simulations *scv2* and *scv6*). Each disk begins with an initial $Q_{\min} = 1.5$. Upon clumping the over-density assumes values 2-3 orders of magnitude larger than are plotted here and are omitted from these graphs. (c) and (d) show the minimum Q value for the same disks as shown in (a) and (b) with both minimum azimuth average values (dotted line) and local minimum (solid line) values shown.

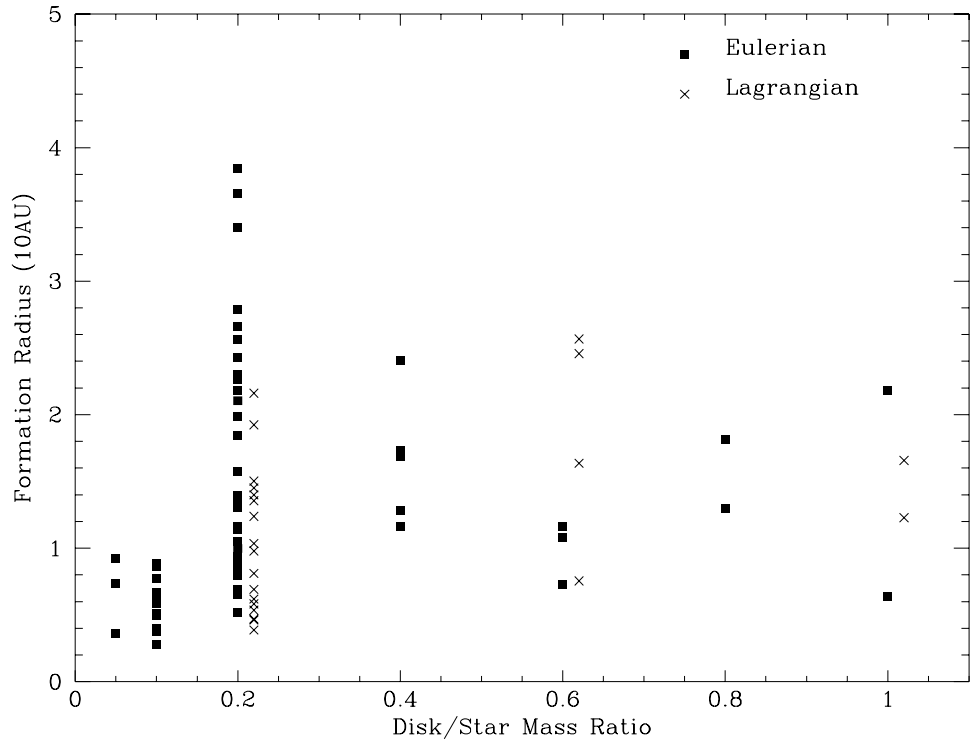


Figure 2.24 Formation radius (in units of 10 AU) for each clump vs. disk mass. Each disk in the series *scv0*-*scv6* begins with an initial minimum Q of 1.5. Clumps form predominantly in the inner half of the disk, with only the $M_D/M_* = 0.2$ disk showing clump formation over the entire range in radius. In the simulations in which more than ~ 10 clumps formed an exact number becomes difficult to determine. Collisions between clumps and fission of a single clump into two (due to accretion of a large amount of angular momentum over a short time) make long term identification of any clump which has undergone a collision or fission event ambiguous and we do not include them here. Filled triangles represent simulations evolved under an Eulerian isothermal assumption (see section 2.2.3) while the crosses (offset from their disk masses slightly to avoid confusion) represent disks with the Lagrangian isothermal assumption.

CHAPTER 3

INTERLUDE ONE

The simulations described in chapter 2 impose a radius dependent temperature profile on the disk which does not vary in time. Other simulations (Boss 1997, Pickett *et al.* 1998) have implemented a similar prescription for both locally isothermal ($\gamma = 1$) and locally adiabatic ($\gamma > 1$) equations of state. In several instances the simulations done here or in their work have resulted in the collapse of part of the disk into one or more clumps, which some have interpreted as forming planetary or stellar companions in the limit of rather strong cooling.

Interpreting the formation of a clump as similar to the formation of a real physical object is premature. The dynamical character of a given simulation can be called into question based on the same grounds. The reason for such strong statements as these are that making the assumption that the temperature structure of the disk is predefined is quite restrictive. It implies that heating and cooling are instantaneous, but act only when the disk varies from its predefined steady state. Any packet of matter moving radially inward or outward heats or cools according to the predefined temperature law, even if no other processes act upon it.

In the following chapter, which is being prepared for publication with W. Benz and T. Ruzmaikina, we have relaxed this temperature law assumption by implementing simple heating and cooling prescriptions. At each time and at each location in the disk, we assume that the disk is locally plane parallel and that the gas is locally adiabatic in its z coordinate. We then calculate the vertical density and temperature structure of the disk and (using opacity tables in the literature) determine the temperature, T_{eff} , at the disk ‘photosphere’ and cool each packet of matter as a blackbody of that temperature. Heating is provided by PdV work, viscous dissipation and shocks which are modeled through the artificial viscosity terms incorporated into the numerical solution of the hydrodynamics. This prescription does not require that any gain or loss in internal energy be immediately restored to the system. Packets of matter are free to radiate their internal energy immediately, travel from one place to another through the disk then radiate, or gain additional energy by further interaction with the disk.

We present a series of 2-dimensional hydrodynamic simulations of marginally self gravitating ($M_D/M_* = 0.2$) disks around protostars using a Smoothed Particle Hydrodynamic (SPH) code. We implement simple and approximate prescriptions for heating via dynamical processes in the disk. Cooling is implemented with a similarly simple radiative cooling prescription which does not assume that local heat dissipation exactly balances local heat generation, however. We find that these simulations produce less distinct spiral structure than isothermally evolved systems, especially in approximately the inner radial third of the disk. These simulations also do not generally produce collapsed objects.

We synthesize spectral energy distributions (SED’s) for our simulations and compare them

to fiducial SED's derived from observed systems. The distribution of grains within the disk and their size distribution can have drastic consequences on the observed SED of a given disk. When grains are vaporized in the midplane of a hot region of the disk, we show that they do not reform quickly into a size distribution similar to that from which most opacity calculations are based. The consequences on the synthesized SED are dramatic. With rapid grain reformation into the original size distribution, the synthesized spectrum of the disk does not contain nearly enough near infrared and optical energy to reproduce observations. With a plausible modification of the opacity, it is possible to reproduce observed SED's at these wavelengths.

Known internal heating processes (PdV work and shocks) are not responsible for generating a large fraction of the thermal energy in the outer part of the disk, though they produce large fraction of the thermal energy at smaller radii. Therefore, gravitational torques, which are responsible for such shocks, cannot transport mass and angular momentum efficiently through the outer disk. Without external heating processes (eg. radiation from a surrounding cloud or from the star) or unspecified internal heating source (e.g. turbulence), the temperatures in the outer part of the disk are very low (only a few degrees Kelvin), resulting in a radial temperature power law fit with an index of $q \sim 1.5$ in the disk midplane and an SED with only a small luminosity at long wavelengths ($> 30 - 50 \mu\text{m}$). The temperature law derived for the disk photosphere is much shallower ($q \sim 1.0$) due to the fact that the disk is optically thick over the inner half of the disk. At distances $\lesssim 10$ AU of the central star, the disk matter becomes heated to such an extent that it expands 'upward' in the z -coordinate, shading the outer part of the disk.

CHAPTER 4

HEATING AND COOLING IN CIRCUMSTELLAR DISKS:
DYNAMICS OF CIRCUMSTELLAR DISKS II

In the early stages of the formation of a star (see the review paper of Shu, Adams & Lizano 1987), a cloud of gas and dust collapses and forms a protostar with a disk surrounding it. Later on, while the accretion from the cloud continues, the star/disk system also begins to eject matter into outflows whose strength varies in time. Finally, accretion and outflow cease and over the next million or so years the star loses its disk and evolves onto the main sequence. A major refinement of this paradigm over the past decade has been to account for the formation of multiple objects from a single collapse. While this picture provides a good qualitative picture of the star formation process, many important issues remain poorly understood.

Once a well developed star/disk system evolves, whether as a single star or a multiple star system, the dynamics of the disk itself as well as its interaction with the star or a possible binary companion become important in determining the system's final configuration. Depending on the mass and temperature of a disk, one may expect spiral density waves and viscous effects to develop and play roles of varying importance. Each may be capable of processing matter through the disk as well as influencing how the disk eventually decays away as the star evolves onto the main sequence.

Until recently the primary observational evidence for circumstellar accretion disks has been the existence of sources with strong infrared excesses which extend from the near infrared to submillimeter and millimeter wavelengths. A number of papers (Adams, Lada & Shu 1987, 1988, Adams, Emerson & Fuller 1990, Beckwith *et al.* 1990—hereafter BSCG, Osterloh & Beckwith 1995) have successfully modeled these excesses assuming a geometrically thin accretion disk with or without additional circumstellar material. Other recent observations (Roddier *et al.* 1996, Close *et al.* 1997) have used adaptive optics to image the disks of several young star systems. Other disk systems (so called 'proplyds') have been observed in the Orion molecular cloud (O'Dell & Wen 1994, McCaughrean & O'Dell 1996) in silhouette against the bright cloud background or through interactions with winds from nearby massive stars.

With these direct and indirect observations it has become clear that disk systems are quite common around young stars. Many efforts to model the dynamical processes involved in their formation (Laughlin & Różyczka 1996, Bonnell & Bate 1997) and evolution (Nelson *et al.* 1998, hereafter Paper I, Boss 1997, Artymowicz & Lubow 1996, Pickett, Durisen & Link 1997) have so far resulted only in a summary of what is possible rather than strong limits on what types of evolution are impossible. Many gaps remain in the understanding of the physical processes important in different regimes and even in the configurations of systems at various points in their history.

Other efforts have been applied to modeling the spectral energy distributions (SED's) of young stellar systems. The SED's of passive disks (i.e. those disks which only reprocess radiation from the central star) have been successfully modeled in recent work by Chiang & Goldreich (1997). Axisymmetric models of a disk and a mixing length approximation for the vertical structure (Bell & Lin 1994, Bell *et al.* 1995, Bell *et al.* 1997) have been used to model the most dynamic properties of disks seen in FU Orionis stars. Time dependent radiative transport calculations (Simonelli, Pollack & McKay 1997, Chick, Pollack & Cassen 1996) have also been incorporated into calculations of the structure of infalling gas and dust. They model the destruction of grains in material falling onto the star/disk system from the surrounding circumstellar cloud and find that under many conditions grains can be partially or totally destroyed prior to their accretion into the star/disk system: heating mechanisms in the cloud and infalling envelope are of comparable effectiveness in heating the grains as in the accretion shock itself.

Paper I showed that in the limit of a disk modeled with a locally isothermal equation of state, spiral arm formation and later collapse into clumps totaling at least a few percent of the disk mass was prevalent in all disks whose minimum initial Toomre stability was $Q_{\min} \lesssim 1.5 - 1.7$. Boss (1997) has concluded that a locally adiabatic equation of state will also produce spiral arm collapse as instabilities grow. Each of these works are limited in the sense that a predefined temperature law is assumed: the gas is locally isothermal or locally adiabatic, but is not globally isothermal or globally adiabatic. In this approximation, any radial motion of gas within the disk causes the parcel of gas to heat or cool, even if no other processes occur to change its state. Compression and shock events are likewise artificially managed. Heating and cooling are instantaneous, but only act when the state of the gas deviates from a predefined 'steady state' value.

We present a series of numerical simulations using Smoothed Particle Hydrodynamics (SPH) modeled under the assumption that the disk is able to heat or cool depending only on local conditions within the disk. Our goal for this work is to understand the dynamical growth characteristics of instabilities in systems with heating and cooling incorporated into the models and to understand which heating and cooling mechanisms are likely to be responsible for which features in the spectral energy distributions of observed systems. In section 4.1, we summarize the initial conditions adopted for the disks studied. In section 4.2, we outline heating and cooling mechanisms included in our study and the numerical method used to determine their magnitude at each point and time in the disk. In section 4.3, we describe the results obtained from our simulations and in sections 4.4 and 4.5, we compare our results to work in the literature and summarize their significance in the context of the evolution of stars and star systems.

4.1. Physical Assumptions

4.1.1. Initial Conditions

The initial conditions used in this work are quite similar to those used in Paper I. We refer the reader to that work for a more complete discussion only summarize them here. At time zero we set equal mass particles on a series of concentric rings extending from the innermost ring at a radius of 0.5 AU to either 50 or 100 AU depending upon the simulation (see table 4.1 below). With the number of particles used, smoothing lengths are less than a few tenths of one AU in the inner portion of the disk and up to ~ 1 AU in the outer disk. The star is modeled as a point mass free to move in response to gravitational forces from the surrounding disk. The gravitational force due to the star is softened with a softening radius of 0.4 AU and particles whose trajectories pass through this radius are absorbed by the star. Magnetic fields are neglected in our simulations.

The disk mass is initially distributed according to a power law:

$$\Sigma(r) = \Sigma_0 \left[1 + \left(\frac{r}{r_c} \right)^2 \right]^{-\frac{p}{2}}, \quad (4.1)$$

while the temperature is given according to a similar law:

$$T(r) = T_0 \left[1 + \left(\frac{r}{r_c} \right)^2 \right]^{-\frac{q}{2}}, \quad (4.2)$$

where the exponents p and q are $3/2$ and $1/2$, respectively, and Σ_0 and T_0 are determined from the disk mass and a choice of the minimum value of Toomre's stability parameter Q over the disk. Q is defined as:

$$Q = \frac{\kappa c_s}{\pi G \Sigma}, \quad (4.3)$$

where κ is the local epicyclic frequency and c_s is the sound speed. The core radius r_c for the power laws is set to $r_c=1\text{AU}$.

Matter is set up on initially circular orbits assuming rotational equilibrium in the disk. Radial velocities are set to zero. Gravitational and pressure forces are balanced by centrifugal forces by setting

$$\Omega^2(r) = \frac{GM_*}{r^3} + \frac{1}{r} \frac{\partial \Psi_D}{\partial r} + \frac{1}{r} \frac{\nabla P}{\Sigma}, \quad (4.4)$$

where Ψ_D is the gravitational potential of the disk and the other symbols have their usual meanings. The magnitudes of the pressure and self gravitational forces are small compared to the stellar term, therefore the disk is nearly Keplerian in character.

4.1.2. The Equation of State

The hydrodynamic equations are solved assuming a vertically integrated gas pressure and a single component, ideal gas equation of state given by:

$$P = (\gamma - 1) \Sigma u \quad (4.5)$$

where γ is the ratio of specific heats, P is the vertically integrated pressure and u is the specific internal energy of the gas. Since we limit the motion of our particles to two dimensions, the effective value of γ is different from that derived from a true three dimensional calculation (see e.g. the discussion of the equations of motion derived for a vertically integrated torus in Goldreich, Goodman & Narayan 1986). For the systems we study, we have taken a simpler approach by assuming that only two translational degrees of freedom exist for each molecule. Helium is included as a monatomic ideal gas and metals are neglected. Coupled with the assumption that the gas is of solar composition, this means the effective value of γ is no longer the well known $\gamma = 5/3$, but rather

$$\gamma \approx 1.53. \quad (4.6)$$

This value includes the contribution of hydrogen with its rotational degrees of freedom active but its vibrational degrees of freedom inactive. This value will be most representative of moderate temperature regions of the disk. In three dimensions, $\gamma \approx 1.42$.

4.2. Thermal Energy Generation and Dissipation

In this work we relax the common practice (see e.g. Paper I, Pickett *et al.* 1998, Boss 1997) of predefining the temperature or adiabatic constant, K , at each location in the disk. Instead, we allow thermal energy to be generated by internal processes and we allow the disk to cool radiatively at a temperature solely dependent upon local conditions at a given time. Thermal energy may be generated in one location in the disk but be dissipated somewhere else if matter moves there, or the disk may heat up or cool down over time in a single location. The disk may therefore equilibrate to the internal energy state that the physical evolution of the system requires.

In our simulations, we only require that the disk be in instantaneous vertical thermal balance in order to determine the vertical structure. We do not require it to be in long term vertical thermal balance. With the latter assumption, the radiative cooling rate at each point is defined to be equal to the local heating rate from internal processes (see e.g. Frank, King & Raine 1992 section 5.4). In some cases, the assumption also includes energy flux radiating onto the disk from outside, so that the radiative cooling rate includes terms due to both internally generated energy and passive reprocessing. Accurate quantification of the relative contributions of each of these terms is critical because by working backwards from observed spectral characteristics of the disk an observer can derive an evolutionary picture of the mass and angular momentum transfer through the system. For example, if radiation emitted by a disk comes entirely from passive reradiation, then no mass or angular momentum transport can occur, since such transport is due to internal dissipation of kinetic energy in the disk. Therefore, if the contributions due to one or more sources of the emitted radiation are incorrectly determined, an evolutionary picture derived from them will be flawed. In the following discussion we outline the physical basis for the heating and cooling processes incorporated into our simulations.

4.2.1. Thermal Energy Generation

Thermal energy in the disk is generated in our simulations from bulk mechanical energy via viscous processes and shocks. In order to concentrate on the physics internal to the disk itself, no contributions to the heating from (for example) either the surrounding molecular cloud or from the central star are included.

We model the energy generation using an artificial viscosity common in many implementations of hydrodynamic codes. Because the balance between thermal energy generation and dissipation are important for both the observed character of the systems as well as their morphology and dynamics, we outline our implementation here. We refer the reader to one of the many discussions already in the literature (e.g. Benz 1990, Monaghan 1992) for a complete treatment.

Most hydrodynamic methods require implementation of an artificial viscosity to enforce stability and/or improve the treatment of shocks by the code. In our simulations we implement viscous pressures which are linear and quadratic in the velocity divergence (the so called ‘bulk’ or ‘ $\bar{\alpha}$ ’¹ and the ‘von Neumann-Richtmyer’ or ‘ β ’ viscosities) to simulate an energy dissipation due to the presence of a viscous pressure of a sum of particle’s j on particle i as

$$\frac{du_i}{dt} = \frac{1}{2} \sum_j m_j \Pi_{ij} (\mathbf{v}_i - \mathbf{v}_j) \cdot \nabla_i W_{ij}, \quad (4.7)$$

where \mathbf{v}_i and \mathbf{v}_j are the velocities of each particle, m_i is the mass of the i th particle and W_{ij} is the

¹Note that we have used the symbol $\bar{\alpha}$ to denote the bulk component of artificial viscosity in order to distinguish it from the Shakura and Sunyaev (1973) turbulent viscosity parameter, α_{SS} .

value of the SPH kernel calculated between the two particles. The factor $1/2$ in eq. 4.7 accounts for half of the kinetic energy dissipation being added to each particle. The viscous pressure, Π_{ij} , is given by

$$\Pi_{ij} = \begin{cases} \frac{-\bar{\alpha}c_{ij}\mu_{ij} + \beta\mu_{ij}^2}{\Sigma_{ij}} & \text{if } (\mathbf{v}_i - \mathbf{v}_j) \cdot (\mathbf{r}_i - \mathbf{r}_j) \leq 0; \\ 0 & \text{otherwise,} \end{cases} \quad (4.8)$$

where \mathbf{r}_i and \mathbf{r}_j are the positions of each particle, c_{ij} is the sound speed and Σ_{ij} is the mean surface density. The velocity divergence μ_{ij} is defined by

$$\mu_{ij} = \frac{h_{ij}(\mathbf{v}_i - \mathbf{v}_j) \cdot (\mathbf{r}_i - \mathbf{r}_j)}{|\mathbf{r}_i - \mathbf{r}_j|^2 + \epsilon h_{ij}^2} \left(\frac{f_i + f_j}{2} \right) \quad (4.9)$$

where ϵ is a small value to prevent numerically infinite divergence as particles come very close and h is the particle's smoothing length.

The f_i and f_j terms are due to Balsara (1995) and are defined by

$$f_i = \frac{|(\nabla \cdot \mathbf{v}_i)|}{|(\nabla \cdot \mathbf{v}_i)| + |(\nabla \times \mathbf{v}_i)| + 0.0001c_i/h_i}. \quad (4.10)$$

Equations 4.7–4.9 are little more than a restatement of the standard form of artificial viscosity for SPH as discussed in Benz (1990). As improvements to the standard formulation, we also incorporate two adaptations which act to minimize the unphysically large shear viscosity present in the standard formulation when used in disk simulations (which arises because the divergence is calculated pairwise between particles rather than as an average over some region in order to more closely model the physical effects of shocks with the code).

First, we modify the velocity divergence from it's usual form by the inclusion of the factors f_i and f_j in eq. 4.9. This factor acts to reduce substantially the large, undesirable shear viscosity which develops in numerical simulations of disks. It is near unity when the flow is strongly compressive, but near zero in shear flows such as are found in disk simulations. For the simulations we have performed we find that typically the reduction due to this term is a factor of three or better. The second improvement is due to Morris and Monaghan (1997). They implement a time dependence to the coefficient $\bar{\alpha}$ which allows it to decay within a few smoothing lengths behind a shock to an equilibrium value much smaller than the normally utilized $\bar{\alpha} = 1$, and grow to larger values in regions where strong compression exists and dissipation is physically appropriate. In our formulation, which includes both the $\bar{\alpha}$ and β terms, we define the ratio $\bar{\alpha}/\beta \equiv 0.5$, but allow their magnitudes to vary in time and space according to the Morris & Monaghan formulation. Thus, except in strongly compressing regions (shocks) where it is required to stabilize the flow, artificial viscosity is minimized.

The origin of the two artificial viscosity terms comes first from the fact that dissipation must be introduced to the system in order to reproduce the hydrodynamic quantities in shocked regions. The β term provides a functional dependence of the viscous coefficient (usually denoted ν) itself on the velocity divergence present in the flow. In this way, the magnitude of the dissipation becomes dependent upon a low order approximation of the discontinuity present in a shock. Without additional correction unphysical oscillations can still develop in the flow, due to the finite differencing in the numerical solution of the hydrodynamic equations. The $\bar{\alpha}$ term is introduced to damp out such phenomena, however in many cases also provides a quite large component of unwanted and unphysical shear viscosity in other regions of the flow. With this in mind we note that, while the von Neumann-Richtmyer term may have some approximate physical basis, its counterpart bulk term can only be considered a necessary nuisance.

Although we must ultimately regard it as a nuisance, since it does not directly model any physical process, with caution we can turn the artificial viscosity into a useful nuisance. We have already identified the von Neumann-Richtmyer term as a low order representative of shock dissipation, and we can make a similar identification of the bulk viscosity as a ‘black box’ source of dissipation in the system in the same manner as is done for the *ad hoc* ‘ α_{SS} ’ model of Shakura & Sunyaev. As we noted in Paper I, there exists a correspondence (Murray 1995, 1996) between the standard α_{SS} form of dissipation and the bulk artificial viscosity implemented in our simulations. In two dimensional simulations the correspondence can be expressed for particle j as

$$\alpha_{SS}^j = \frac{f_j \bar{\alpha}_j h_j \Omega_j}{8c_j} \quad (4.11)$$

where f_j is the Balsara shear reduction coefficient, $\bar{\alpha}_j$ is the bulk viscosity coefficient, Ω is the orbit frequency and c_j is the sound speed of the particle. Defined in this way, α_{SS} is a time and space dependent quantity, in contrast to the usual form in which α_{SS} is constant everywhere or (in a few cases), varies between an ‘on’ and ‘off’ state. This conversion neglects the contribution due to the von Neumann-Richtmyer term and so represents only an incomplete approximation of the magnitude of the dissipation present. It also neglects the time dependence of the viscous coefficients noted above. In the context of attempting to identify the source of the dissipation, this means that if a region experiences repeated compression events or shocks on short time scales, the dissipation would be accounted for as turbulent process rather than as a shock process. Nevertheless, it proves useful as an illustration of where and to what extent thermal energy generation processes are active.

4.2.2. Thermal Energy Dissipation and the Vertical Structure of Accretion Disks

The cooling experienced by a given particle is determined first by calculating the approximate vertical density and temperature (ρ, T) structure of the disk. Then, using these quantities we determine the altitude of the disk photosphere and cool the particle as a blackbody using the calculated photosphere temperature.

In order to calculate $\rho(z)$ and $T(z)$ without a full three dimensional hydrodynamic calculation we make two assumptions about the disk structure. We assume that at each location the disk has some degree of turbulence or convection so that it becomes very nearly adiabatic in the z direction (i.e. that $p = K\rho^\gamma$ with K and γ constant). We also assume that it is locally plane parallel. In this limit, Fukue & Sakamoto (1992) have shown that $\rho(z)$ and $T(z)$ at a known distance from the star are determined by the solution of the second order, ordinary differential equation

$$\frac{d}{dz} \left(\frac{1}{\rho} \frac{d}{dz} (K\rho^\gamma) + \frac{GM_* z}{(r^2 + z^2)^{3/2}} \right) = -4\pi G\rho. \quad (4.12)$$

A known midplane density, ρ_{mid} , the distance from the star, r , the adiabatic constant, K , and the ratio of specific heats, γ , define the conditions which completely specify the solution in the absence of external heating of the disk surface.

In our two dimensional simulations, each SPH particle is uniquely defined at some time by a particular value of internal energy, surface density and distance from the star. These three quantities correspond to the three conditions ρ_{mid} , K and r which specify the structure in z . The distance from the star is, of course, the same for both the SPH and Fukue & Sakamoto specifications. Derivation of the quantities ρ_{mid} and K from the surface density and internal energy must be done by iteration to convergence.

We supply an initial guess for ρ_{mid} and K and solve the differential equation numerically for $\rho(z)$. The z coordinate is discretized with 500 zones and the differential equation is solved

numerically to second order accuracy. Once a tentative solution is reached, we integrate the density ρ over z using the trapezoid rule to derive the surface density of matter defined by the solution. Specific internal energy is obtained by a similar integration over the vertical extent of the disk. The guesses of ρ_{mid} and K are then revised using the downhill simplex method to converge to a self consistent solution. Plots of the density and temperature structure as a function of the altitude, z , are shown for several conditions typical of the disks in our simulations are shown in fig. 4.1.

Implicit in this calculation is the assumption that the gas is adiabatic, i.e. that the gas pressure and density are related by $p = K\rho^\gamma$ and that the heat capacity of the gas, C_V , (and by extension, the ratio of specific heats, γ) is a constant. In fact, this will not be the case in general because, in various temperature regimes, molecular hydrogen will have active rotational or vibrational modes, it may dissociate into atomic form or it may become ionized. As a matter of expediency and in order to retain our prescription for the structure calculation, we have assumed that the rotational states of hydrogen are active, but that the vibrational states are not. Under this assumption and including the contribution due to helium, the effective value for the three dimensional adiabatic exponent of the gas is $\gamma \approx 1.42$.

From the now known (ρ, T) structure we derive the temperature of the disk photosphere by a numerical integration of the optical depth, τ , from $z = \infty$ to the altitude at which the optical depth becomes $\tau = 2/3$

$$\tau = 2/3 = \int_{\infty}^{z_{phot}} \rho(z) \kappa(\rho, T) dz. \quad (4.13)$$

In optically thin regions, for which $\tau < 2/3$ at the midplane, we assume the photosphere temperature is that of the midplane. The photosphere temperature is then tabulated as a function of the three input variables radius, surface density and specific internal energy. At each time we determine the photosphere temperature for each particle from this table and cool the particle as a blackbody at that temperature. The cooling of any particular particle proceeds as

$$\frac{du_i}{dt} = \frac{-2\sigma_R T_{eff}^4}{\Sigma_j} \quad (4.14)$$

where σ_R is the Stefan-Boltzmann constant, u_i and Σ_i are the specific internal energy and surface density of particle i and T_{eff} is it's photospheric temperature. The factor of two accounts for the two surfaces of the disk. On every particle, we enforce the condition that the temperature (both midplane and photosphere) never falls below the 3 K cosmic background temperature.

We use Rosseland mean opacities from tables of Pollack, McKay & Christofferson (1985 hereafter PMC). Opacities for packets of matter above the grain destruction temperature are taken from Alexander & Ferguson (1994). We have chosen not to use the updated opacity models of Pollack *et al.* (1994) in this work. In part this is due to the fact that opacity tables including both ρ and T variation based on this work do not exist (D. Hollenbach, personal communication). As the authors note however, the opacity is only a weak function of density (entering primarily through the change in vaporization temperatures of various volatiles at different densities) and they do produce a figure comparing the new opacity with that of the old for a single value of the density. As we shall note in the sections ahead, it is exactly this vaporization of grains which we find to be an important factor in determining the character of the SED. The functional form derived by Henning & Stognienko (1996) to reproduce the Pollack *et al.* opacity suffers from the same shortcoming. Hence we have chosen to implement the old version of the opacities until such time as new tabulated values become available. In any case, the opacities derived from the new and old works (see their fig. 6) are similar except in the temperature region between 200 and 450 K, where the Pollack *et al.* (1994) derivation exceeds the PMC value by a factor of about

three. The effect on our calculations would be to slightly reduce the photosphere temperature in regions where the differences between the two versions becomes important.

4.2.3. Synthesizing Observations

In order to connect the physical properties of our simulations of accretion disks to observable quantities in real systems we synthesize spectral energy distribution's (SED's) from our simulations. We calculate the SED using the derived black-body temperature of each SPH particle at a particular time. We assume that the disk is viewed pole on and then determine the luminosity of each particle at each frequency as

$$L_\nu^j = \frac{m_j}{\Sigma_j} \pi B_\nu(T_{eff}) \quad (4.15)$$

and of the disk by summing the contributions of all of the particles. In eq. 4.15, m_j is the mass of particle j , Σ_j is it's surface density and B_ν is the Planck function. The area factor is given as m_j/Σ_j in order to avoid ambiguity in the surface area (i.e. the smoothing length and it's overlap with other particles) defined for each particle.

Although we neglect the luminosity of the star as a source of energy input during the calculation, we include it in the post processed SED calculation. We assume the star contributes to the SED as a $1 L_\odot$ blackbody with temperature $T_{eff} = 4000$ K, both values are typical of observed T Tauri stars (see e.g. Osterloh & Beckwith 1995, BSCG, Adams *et al.* 1990). The star's contribution is included primarily to make the visual comparison of our synthetic SED's to observed systems simpler and to provide a constant physically meaningful calibration to the disk emission on the plot. We also neglect the accretion luminosity of particles which are removed from the simulation due to their radial migration inward beyond the defined accretion boundary. We expect these two sources of luminosity to contribute primarily to the optical and UV spectrum, while the disk will contribute primarily at longer wavelengths. Therefore, for our purposes, the disk luminosity will be well separated in frequency from the stellar and accretion luminosities.

4.2.4. Units: The Physical Scale of the System

The introduction of a cooling mechanism requires an introduction of a physical scale to the simulations. We shall assume quantities with values typical of the early stages of protostellar evolution. The star mass will be assumed $M_* = 0.5M_\odot$ and the disk radius of either $R_D = 50$ AU or $R_D = 100$ AU as noted in table 4.1. Time units are given in either years or the disk orbit period defined by $T_D = \frac{2\pi}{\sqrt{GM_*/R_D^3}}$ which, with the stellar mass and disk radii given above is equal to about 500 or 1400 years for disk radii of $R_D = 50$ or 100 AU respectively.

4.3. The Simulations

Paper I showed that the character of disk evolution undergoes a marked change between disk masses of $M_D/M_* = 0.2$ and $M_D/M_* = 0.4$. In this paper, we will concentrate on studies of a disk at the lower edge of this mass boundary. In the following discussion, we present a case in which we simulate the evolution of a disk with a mass ratio of $M_D/M_* = 0.2$ and with an assumed initial minimum Toomre stability of $Q_{min} = 1.5$ under varying physical assumptions. Initial parameters of our simulations are tabulated in table 4.1. The first column of the table represents the name of the simulation for identification. The second column defines the resolution (in number of particles). Initial disk/star mass ratio and minimum Q are given in columns 3 and 4, the assumed opacity modification factor (see section 4.3.2 below) in column 5 and the total

simulation time of each simulation in the remaining column. We examine the qualitative nature of the simulations first, then examine in detail the structures which form and their characteristics.

We have run a series of simulations under three different assumptions about the opacity and therefore the cooling mechanisms which dependent upon it. The first set of simulations proceed under the assumption that gas and grains exist in equilibrium everywhere in the disk and that the grain size distribution is well modeled by the distributions used in opacity calculations in the literature (e.g. PMC, Alexander & Ferguson 1994). Vaporized material, upon entering a region cool enough for it to form grains, does so instantly and in such a way as to reproduce it's original grain size distribution, as defined by PMC. These simulations are denoted by a leading 'a' (100 AU disks) or 'A' (50 AU disks) in the simulation name in table 4.1.

The second set of simulations relaxes the assumption that refractory materials reform into their original size distribution quickly. Instead, we assume that they reform their original distribution more slowly than the overturn time scale for material to be processed through the disk midplane to high altitudes and back again so that their size distribution and therefore their opacities may be modified from their original form. These simulations are denoted with a leading 'B' in table 4.1.

We have also run models of disks under the same 'isothermal evolution' assumption used in Paper I. These simulations are denoted with a leading 'i' or 'I' in Table 4.1. In each case, a capital letter refers to a disk with outer edge at 50 AU while a lower case letter refers to a disk with outer edge at 100 AU. In each case 'lo', 'me' and 'hi' refers to a simulation with low, medium or high resolution as defined in column 2, and with the 'B' simulations we the number 1–5 corresponds to an assumed opacity modification.

4.3.1. Morphology and Spectral Energy Distributions

Using the physical assumptions outlined above and cooling using the 'A' prescription we have completed a series of simulations with initial minimum Toomre $Q = 1.5$. Snapshots of the evolution of simulation *A2me* are shown in figure 4.2 and of its derived SED in figure 4.3. As in our previous isothermally evolved simulations (Paper I) growth of instabilities begins in the inner regions of a disk, engulfing the entire system over the course of about $1 T_D$. Initially, spiral structures develop in the inner disk, but are later suppressed by the heating which occurs there.

The spiral structures which develop throughout the whole disk are multi-armed and change their shape and character over orbital time scales. At times they become somewhat filamentary, but in no case do they become as filamentary as in the isothermally evolved simulations of Paper I. At the end of simulation *a2me* (at $T_D \approx 2.3$) a possible collapse of a spiral arm into a clump is present, however at this point the cooling prescription is unable to determine the vertical structure of the particles near the forming clump. Additional evolution of this simulation becomes impossible and we cannot determine whether collapse would continue or dissipate once again into the background flow. Over the longer time scales available to these simulations a substantial fraction of the matter initially located inside $\sim 5\text{--}10$ AU accretes onto the star. We will discuss this in more detail in section 4.3.7, below.

As was shown in Paper I, SPH is unable to follow low amplitude growth of structure in disks. As a consequence, nearly all of the evolution is carried out in the regime in which the spiral patterns have quite large amplitudes. Short period variation of up a factor of $\sim 3\text{--}5$ occurs in the amplitudes. However, the pattern growth has clearly saturated to the extent that time averages of the amplitudes must be used rather than growth rates to characterize the system. In order to make quantitative comparisons between of the spiral structure of disks evolved under different physical assumptions we therefore examine the saturation amplitudes of various patterns late in

the simulation. We derive the time average of a given pattern as shown in figure 4.4 for the one of the largest amplitude patterns ($m = 4$) produced from an isothermally evolved simulation and the disk shown in figure 4.2. The time averaged amplitudes are shown as functions of radius for the same simulations in figures 4.5 and 4.6.

The averages are taken over the time interval from $T_D = 0.5$ to $T_D = 1.5$ for each simulation. These limits are used in order to ensure than most of the disk has in fact reached it's saturation amplitude (for the beginning limit), but has not evolved long enough to form clumps (in the case of the isothermally evolved runs). The time intervals used for both sets of runs are identical in order to ensure that the comparison can be as close as possible. For example, for the outer part of the disks shown in figure 4.4, it is clear than the cooled simulation reaches it's saturation level well after the isothermally evolved simulation forms clumps and cannot be evolved further. In order to make a fair comparison of the amplitudes we must restrict the averages to the same time window.

Approximately the inner third of the cooled disk shows suppressed pattern amplitudes relative to the isothermally evolved simulation. In Paper I we showed that this region was the region most likely to form collapsed objects in the isothermal evolution limit. With our new series of simulations this conclusion must be revised. No clumps form in this region in these simulations, as they do in the isothermally evolved runs. The maximum amplitude of each pattern is shifted to a larger radius in the cooled simulation vs. the isothermally evolved simulation.

The same shift of large amplitude spiral structure to greater distances from the star is present in disks with outer radii at 100 AU, as shown in figure 4.7 for the cooled simulations $a2lo$, $a2me$ and $a2hi$. These simulations show the same amplitude structure as in the $R_D = 50$ AU disks above. Attempts to compare these results to isothermally evolved simulations were unsuccessful, since such simulations tend to develop clumps on the same physical time scale (750–1000 yr) as with the $R_D = 50$ AU isothermal runs. Evolution of the 100 AU simulations must be terminated before the outer disk has completed even a single orbit.

In part the smaller pattern amplitudes at small radii are a consequence of the less efficient cooling in the present simulations. This relative inefficiency leads to increased temperatures in the central region of the disk relative to the isothermally evolved runs. Higher temperatures imply higher values of the Toomre Q stability parameter and therefore smaller amplitude (or absent) spiral waves. This is true for the inner disk but only to a much smaller degree in the outer part of the disk, where temperatures change from their initial values by only a factor of 20-30% (see section 4.3.7 below). The higher temperatures and Toomre stability do not necessarily imply stability against all perturbations however, since as we shall see shock activity is strongest in the inner disk.

The SED's synthesized from the simulation are shown in figure 4.3. They clearly do not reproduce the observed SED's of T-Tauri stars. Instead they produce a double peaked spectrum with one peak dominated by the assumed 4000 K stellar black body contribution and the other just longward of $10\mu\text{m}$ (~ 3 –400 K). Both the long wavelength end ($> 30\mu\text{m}$) and the near infrared (defined for our purposes as wavelengths from $\sim 1\mu\text{m}$ to $5\mu\text{m}$) portions of the SED are poorly reproduced: insufficient radiation is emitted relative to other wavelength bands.

The long wavelength turnover in the SED's synthesized from our simulations typically occurs near $30\mu\text{m}$ (10^{13} Hz) rather than the ~ 100 – $300\mu\text{m}$ (10^{12} Hz) typical of observed systems. It is also a shallower fall-off towards long wavelengths than is the case for the observations. The simulations with an outer disk radius of 100 AU also suffer from this same deficiency of radiated energy, so we are certain that the effect is not due to modeling a disk of too small a radial extent. Examinations of the photosphere temperature of the particles (see section 4.3.7, below) show that

only a small fraction of the disk radiates at the \sim 20–100 K temperatures required to produce excess in the 30–300 μm wavelength regime. A test simulation identical to *A2me*, but with initial $Q_{\min}=2.5$ so that the initial disk temperatures everywhere are higher, cools over the course of the first $1\text{--}3T_{\text{D}}$ to resemble the conditions in simulation *A2me*.

We do not believe the absence of near IR flux in our simulations is an artifact of the relatively large (0.4 AU) truncation radius of our disk (recall that particles are accreted by the star inside this radius). In part this is because the artificial hole region will already be partially devoid of disk matter, due to the finite size of the boundary region between the inner disk edge and the star. We have verified that the hole is not responsible for flux deficit by running a simulation with a reduced accretion radius of 0.2 AU and found no significant difference in the derived SED.

Primarily, this system does not radiate efficiently in the near IR because of the effect of the large low temperature opacities and the low temperatures implied by our model at high altitudes above the midplane. For any conditions at the midplane of the disk, our vertical structure calculation produces a region which is both cold and sufficiently dense to make the column optically thick at high altitude. Such a condition will accurately model real systems so long as there is sufficient vertical processing of disk matter to retain both a vertically adiabatic structure and a well mixed opacity source, i.e. small grains.

In several regions, our model will break down. At small distances from the star for example, direct stellar illumination of disk material at all altitudes will substantially alter the temperature profile throughout. In this case, the simple vertically adiabatic assumption will break down, perhaps leading to a more uniform vertical temperature structure, since the entire vertical column receives some illumination. This failure mode would lead to higher photosphere temperatures than are obtained in our model. Further, such a temperature structure may produce a radiative zone so that grains begin to settle to the midplane or high altitude corona so that they are destroyed. In each of these cases, the disk would be able to radiate in the near IR more efficiently. However, none of these processes are as yet well enough understood to constrain the present models.

4.3.2. An Attempt to Improve the Cooling Prescription

As is, the cooling prescription in section 4.2.2 fails to reproduce the short wavelength spectrum (near IR) of observed circumstellar disks. This wavelength regime corresponds to the portion of the disk in which the disk midplane temperatures are warm enough to sublimate grains. Our cooling prescription on the other hand, assumes both that the opacity source (grains) is evenly mixed with the gaseous disk material and that the grain size distribution everywhere is not substantially different from that of the interstellar medium distribution used to calculate the Rosseland opacities. Is the failure of our simulations to correctly reproduce observed disk SED's due to the failure of these physical assumptions about the grain physics?

To address the first assumption we note that Weidenschilling (1984) has shown that grains smaller than \sim 0.1–1 cm will be largely entrained in the gas in a turbulent disk and will therefore not settle to the midplane. Because the smaller grains provide the largest contribution to the opacity, we may assume that for the purposes of our model the grains are well mixed.

The second assumption (the size distribution of grains) proves much more difficult to address. Contained within our assumption of a vertically adiabatic disk structure is the fact that the adiabatic condition arises out of a convective or turbulent medium, which acts to smooth any entropy gradients that develop. In such a case, grains entrained in the gas should be processed through the midplane fairly frequently and, if the midplane temperature is hot enough, destroyed. As refractory materials are brought to higher altitudes where temperatures are lower, they will begin to reform into grains. If they reform quickly (compared to their vertical motion) into a

similar size distribution to their original distribution, a narrow boundary region in which grains reform will delineate a hollowed out region within the disk as shown in figure 4.8a.

On the other hand, if grain reformation is slow compared to speed of vertical motion then the region in which the grain size is modified from its original distribution becomes much wider (fig. 4.8b). In this case, calculations assuming one distribution of grains may not determine the true correct opacity, and therefore the cooling will also be incorrectly modeled. Using calculations based upon the coagulation models of Weidenschilling & Ruzmaikina (1994), we demonstrate that in fact this scenario is the case. For a more complete description of the code, see Spaute *et al.* (1991); here we shall merely summarize the model presented there.

The disk is divided into 20 vertical layers and particle aggregates are accounted for as a series of 84 bins spaced logarithmically in grain diameter with each bin $2^{1/3}$ larger than the previous bin. The smallest bin is assumed to contain grains of size $1 \times 10^{-2} \mu\text{m}$. Grains smaller than $1 \times 10^{-2} \mu\text{m}$ are not accounted for and nucleation of grains from the gas phase is likewise neglected. Relative velocities of grains are associated with the turbulence, settling of dust aggregates to the central plane, and radial drift due to gas drag. The turbulent velocity is set to $\sim 260 \text{ m/s}$, equivalent to $\alpha_{SS} \sim 10^{-2}$ (assuming $v_T = \sqrt{\alpha_{SS} c_s}$).

Using the geometric cross section of each grain size, the number density of grains of that size and the relative velocities between grains in different size bins, we compute the number of collisions between all possible pairs of size bins during one time step. The result of these collisions may be coagulation, erosion or total destruction depending upon the relative velocities of the particles and their assumed strength. Collisions resulting in grain coalescence remove aggregates from the smaller bins and change the mean mass of aggregates in the larger bins. If a collision leads instead to erosion or disruption, then the fragments are distributed into appropriate smaller size bins. Vaporization of grains in hot regions is modeled by lowering the grain strength so that any collision causes fragmentation.

The vertical density and temperature structure remain constant throughout the calculations and are computed as outlined by the model in section 4.2.2, with a midplane temperature of 1350 K and a local mass surface density of $\Sigma = 10^3 \text{ gm/cm}^2$ at 1 AU. In the initial state, all of the grains are in the smallest size bin. This initial condition is equivalent to the assumption that at some point in the evolution of a particular column of gas all of the dust has been destroyed and must now reform.

Fig. 4.9 shows snapshots of the grain size distribution at one AU plotted as a function of altitude above the midplane after a short period of evolution. Time step constraints within the coagulation model forbid a very long time evolution of the size distribution, however such long term longer evolution is of limited value because the state of the gas (it's temperature and density) change on these same time scales, making a grain distribution derived from a single (ρ, T) configuration irrelevant physically.

At high altitudes, grains are unable to grow to large sizes in the time shown because of the low densities (which imply low collision cross sections as well) that are found there. The largest size to which grains grow is $\sim 0.02\text{--}0.05 \mu\text{m}$. At moderate altitudes, just above the temperature boundary between grain destruction and reformation occurs, larger grains ($\sim 0.2\text{--}0.3 \mu\text{m}$) can form over this same time interval. At low altitudes near the midplane, grains are unable to grow and remain locked in the smallest size bin available.

The size distribution of grains is quite unlike that of the interstellar medium (ISM), as characterized by Mathis, Rumpl & Nordsieck (1977 hereafter MRN) or Kim, Martin & Hendrys (1994 hereafter KMH), whose work shows a distribution proportional to $a^{-3.5}$. Instead it is

characterized a quantity of grains in the smallest size bin, whose origin is in the partial erosion of larger particles, and an increasing or near flat spectrum near the upper edge of the size distribution with a sharp cutoff. A flat size spectrum such as this is a characteristic feature of the collisional coagulation of grains where little destruction takes place. The flat spectrum forms because larger grains have longer stopping times, encounter more grains and therefore grow faster than their smaller neighbors. A declining power law distribution characterizes destructive processes and is pronounced at lower altitudes. Near the midplane only grains in the smallest size bin exist because the assumed vaporization of grains (modeled in our calculation via grain destruction, which moves grains from larger bins to smaller) is very efficient there.

These differences are important because of the common use of grain distributions similar to those given in MRN and KMH in many opacity calculations. Since the opacity is a function of the size distribution, modifying the distribution from some canonical value will result in differences calculated opacity and, for our model, a difference in the photosphere temperature and cooling experienced by a given column of disk matter.

For example, PMC have shown (see their fig. 5) that a narrow size distribution with an average grain size much less than $1\mu\text{m}$ will produce Rosseland mean opacities which are reduced from their nominal values by a factor of ~ 10 at temperatures above about 150 K and an additional factor of ten above ~ 500 K for very small grains. Frequency dependent opacities calculated for a variety of grain sizes by Miyake & Nakagawa (1993) and by Pollack *et al.* (1994) would seem to contradict this behavior however. They find that for an ensemble of grains of a given size, the frequency dependent opacity rises as the assumed grain size decreases and stays roughly the same for all grain sizes less than $\sim 1\mu\text{m}$.

In fact the two pictures are not contradictory for two reasons. First, the absolute scale of the opacity is dependent upon the temperature due to the different grain species (e.g. ice or silicates) which contribute at colder or warmer temperatures. Miyake and Nakagawa performed their calculations assuming temperatures of 150 K, while Pollack *et al.* (1994), consider higher temperature (750 K) grains and find that the frequency dependent mass opacity is lower by a factor varying between ~ 10 and 100 below that at 100 K in the mid infrared (their fig. 3b). More importantly however, changing the assumed temperature modifies the ratio of the grain size to the wavelength of the dominant radiation. The wavelength/grain size ratio is important because for different radiation temperatures the same grains will require an opacity calculation in quite different limits: either a Raleigh scattering, Mie scattering or geometric optical approximation, with a consequent affect on the opacity.

A reduced opacity implies for our cooling prescription that the photosphere of the disk will be found at a lower altitude and therefore an increased effective radiating temperature will be obtained. Using the nominal tabulated opacities to obtain the location and temperature of the photosphere will therefore underestimate the actual cooling which takes place. Furthermore, due to the higher effective radiating temperatures, the SED will be modified from its previous form as more radiation is emitted at short wavelengths.

We have investigated the effect of a modified grain opacity by adapting our cooling prescription to include an additional assumption. In regions of the disk where the midplane is hot enough to vaporize grains, we assume that the grain opacity is temporarily reduced from its nominal value by a constant multiplicative factor, R , over the entire vertical column of disk matter above and below the midplane. In other regions of the disk we assume the opacity remains unaffected, so that the effective opacity is

$$\kappa_{eff}(\rho, T) = \begin{cases} R\kappa(\rho, T) & \text{if } T_{mid} > T_{crit}, \\ \kappa(\rho, T) & \text{otherwise} \end{cases} \quad (4.16)$$

where T_{crit} is the grain destruction temperature and T_{mid} is the disk midplane temperature. The disk photosphere temperature and altitude are calculated in the same manner as before, with the modified opacity κ_{eff} replacing $\kappa(\rho, T)$ in eq. 4.13 above. The disk photosphere temperature therefore will increase in regions where the midplane temperature is hot enough to destroy grains and remain unaffected elsewhere.

We have performed several simulations varying the amount by which the opacity is modified from the PMC values over the range between $R = 0.001$ and $R = 0.01$. These simulations implement the same initial model as simulation *A2me*. Simulations at our lowest resolution provided inadequate resolution for the inner disk so that the near infrared SED would often be dominated by the contribution of only a few particles. We show time averaged SED's derived from these simulations in fig. 4.10. This figure shows clearly that the near and mid infrared emission from circumstellar disks can be 'turned off' or 'turned on' depending on the extent to which grain reprocessing in the inner disk affects the opacity. At either end of two extremes, too small or too large an opacity, the SED fails to reproduce a flat or shallow spectrum. With too little reduction the SED appears similar to that shown above in figure 4.3 (whose time average is reproduced in the lower right panel of fig. 4.10), while with too much, it appears permanently in an 'outburst' phase in which the $1-5\mu\text{m}$ band is enhanced by as much as a factor of 5–10 over the stellar contribution to the flux. At later times in several of the plots shown (notably the $R = 0.0025$ and the $R = 0.005$) the disk again produces an 'outburst' in the same region of the spectrum as it does in the case with $R = 0.001$. In these instances, the true behavior is episodic and will be discussed more fully in section 4.3.4 below.

Both a frequency dependent radiative transfer code, incorporated into the hydrodynamic calculation at each time step, and a recalculation of the Rosseland opacity for each ρ , T , and grain size distribution accessible to our simulations are beyond the scope of the present work. As a parameterized factor however, we can bracket the difference from the nominal PMC opacities to a factor between 0.001 and 0.01 times the PMC values in regions where the midplane temperature rises above the grain vaporization temperature. Below, we shall implement a 'standard' factor of 0.0075 times the tabulated PMC values in such regions.

It is notable that the values of R which are required to produce $1-5\mu\text{m}$ flux consistent with observations are quite small. In fact, the large modification in the opacity values are not inconsistent with an opacity consisting only of a contribution from gas rather than from both gas and grains. A 'grain free' calculation (D. Alexander: personal communication) of the opacity using the model of Alexander and Ferguson (1994) down to 1000 K produces opacities which are similar in magnitude to our modified values. Coupled with the near and mid infrared time variability present in the simulations, the interpretation we are led to is that in the inner portion of the accretion disk, clouds of grains in small patches of the disk are destroyed and reform, intermittently obscuring the hottest parts of the disk midplane from view. Such an interpretation implies quite naturally the existence of intermittent variability in the near and mid infrared spectra of star/disk systems originating from within the disk rather than from a stellar photosphere. Skrutskie *et al.* (1996) observe such variation on time scales of a few days to a few weeks in the J , H and K bands for several young stellar systems and conclude that, particularly in K band, such variations are likely due to processes in the accretion disk.

4.3.3. Morphology and SED's using modified opacities

The results of a simulation with an identical initial condition, but with the modified cooling prescription 'B' (simulation *B2m4*), are shown in figure 4.11 and the derived SED corresponding to each frame is shown in figure 4.12. The gross morphology of the system as evolved under this modified cooling prescription is quite similar to that produced with the original prescription.

Instabilities begin in the inner regions of the disk and as time progresses, engulf the entire disk, forming filamentary, multi-armed spiral structures. A quantitative measurement of the system morphology as measured by its pattern amplitudes (fig. 4.13) confirms the similar behavior for these simulations. There are no significant differences in the pattern amplitudes apparent.

The similarities are perhaps to be expected since only the inner regions undergo different cooling, however if the inner regions of the disk are truly responsible for dynamical behavior further out, the modifications might create a different pattern of evolution throughout the entire disk. Since no such differences are evident, we may conclude that although the instability growth begins in the inner most regions of the disk, its character at large radii is not strongly dependent on the dynamics of the inner region, at least for the two types of cooling assumptions we have outlined.

In both of the simulations shown in figures 4.2 and 4.11 it appears that a substantial ‘hole’ forms towards the middle of the disk as time progresses. The resulting structure at first glance appears more torus-like than disk-like. As we show in section 4.3.7 however, the surface density only flattens out at small radii rather than evolving towards a true torus, in which the inner region is devoid of material.

In spite of the small differences in the system morphology, the derived SED’s show a marked difference from those produced using the original cooling prescription. In the present case, the SED exhibits a rising (toward higher frequencies) spectrum between $\sim 30\text{--}50\mu\text{m}$ ($\sim 10^{13}\text{ Hz}$) and $\sim 1\mu\text{m}$ (a few $\times 10^{14}\text{ Hz}$), then falls off at the highest frequencies where only the star contributes significantly to the flux. It is also variable in time, with each of the panels in this time mosaic of the SED’s being somewhat different from the others. The variations are concentrated in the near IR region of the disk, for which the calculated midplane temperatures are high enough to invoke the modified cooling.

As before with our ‘A’ cooling prescription, the disk does not emit sufficient flux at low frequencies ($< 10^{13}\text{ Hz}$), since the modifications in section 4.3.2 affect only the hottest portion of the disk. The temperature at the disk photosphere lies above the values required to produce the $30\text{--}100\mu\text{m}$ flux when grain destruction has begun to affect the radiating temperature, or below them, where the matter contributes only minimally to the SED.

4.3.4. Variation of the SED’s with time

We concluded in section 4.3.2 that the time averaged SED in the near and mid IR is strongly dependent upon the microphysics of the dust grain size distribution and its effect upon the opacity, but that our model could only bracket the magnitude of the modification required to accurately reproduce the time averaged spectrum. The instantaneous emitted spectrum synthesized from our simulations is variable in near and mid infrared wavelengths. In fig. 4.14 we plot the emitted power, νF_ν , at 2, 25 and $100\mu\text{m}$ as well as the total luminosity of the disk as a function of time for each of three resolutions for our ‘A’ simulations and our highest resolution ‘B’ simulation (The right hand panels will be discussed in section 4.3.6 below). With the ‘A’ cooling model only small variations in time are present: no short term variations larger than 10% are present at any wavelength and short term variations at longer wavelengths are smaller, less than 1% at $100\mu\text{m}$. At $2\mu\text{m}$, no contribution from the disk is present; the flux is completely dominated by the assumed constant 4000 K black body contribution of the star.

At all resolutions (after an initial transient) there is a slow systematic trend towards smaller emitted fluxes. This decay is due to mass depletion from the inner disk, which occurs more rapidly than it is replaced by matter migrating from further out. As the amount of mass present decreases, the inner disk becomes less dynamically active and consequently less energy

is dissipated as heat and radiation. A systematic difference in the disk luminosity calculated for each simulation is apparently due to the decrease in the amount of dissipation present at higher resolution. Variations in the flux also decrease with increasing resolution, indicating that variation that is present may be an overestimate.

The ‘B’ cooling simulations show behavior identical to the ‘A’ simulations in the mid and far IR, but exhibit large variations in the near IR. At $2\mu\text{m}$ for example, the variation is about a factor of two or more from peak to peak and the total disk luminosity shows a similar amount of variation. Larger variations are again present for lower resolution simulations, indicating that the variation shown is an upper limit.

In order to see the shorter term structure in the flux variation, we show the same variables as in 4.14, but expanded to show a small slice in time in fig. 4.15. The time scale of the variation in the near and medium infrared is similar to the orbital time scales of the inner disk, which is truncated at 0.4 AU in our simulations. At some times, only the assumed stellar component of the flux contributes to the flux, while at others, the flux is dominated by the disk contribution. The variations have no well defined periodicity. Variations occur over periods of less than a year and over periods of as long as ten years. Qualitatively, we can understand the dynamical origin the variation by noting that heating processes such as shocks do not occur at regular intervals as the disk evolves, but rather occur sporadically as spiral arm structures or other inhomogeneities in the disk interact and dissipate orbital energy as heat.

The magnitude of the flux variations present in our simulations must be considered upper limits rather than a definitive prediction for two reasons. First, the variations are a function of the resolution of the simulations, decreasing as resolution increases. We cannot be certain of the amplitude at which variations become independent of resolution. Second, we have not quantitatively determined the effects of the grain vaporization, reformation and size evolution on the opacity. A more detailed understanding of how these variables affect the opacity is required before spectral energy distributions of circumstellar disks can be self consistently incorporated into multi-dimensional models such as ours.

On the other hand, the time scales of the variations will be more reliable because such effects are dominated by the dynamical times of the inner disk. Shorter term variations than appear in our simulations may also occur since our disks were truncated at a relatively large distance from the star.

4.3.5. Variation of the Dissipation with Resolution

In our higher resolution runs, the temperatures are lower than in lower resolution runs and the SED’s synthesized have a systematically smaller amount of infrared excess and total luminosity. This difference is due to the correspondingly lower numerical dissipation possible at high resolution as shown in fig 4.16. Because the purely compressional dissipation (i.e. shocks) is better resolved at higher resolution, we expect that as the resolution increases the shock dissipation term will more closely model the physical dissipation present in shocks and purely numerical dissipation will decrease elsewhere in the flow. Therefore until a set of simulations converges to a well defined amount of dissipation which is not a function of resolution, the dissipation which is present will represent an upper limit on that present in a real system.

Ideally, the contribution of unidentified sources of dissipation to the energy output of the system would be negligible. In such a case, specification of known dissipation mechanisms and the known passive heating mechanisms in the model assumptions would specify the observable appearance of the system. In our models this ideal can only be approached, rather than definitely specified. We have previously identified the bulk viscosity term in eq. 4.8 with the Shakura &

Sunyaev α_{SS} , which models ‘black box’ viscosity. Since our resolution is finite, this black box source of dissipation is non-zero and we approximate it’s contribution to the dissipation (via eq. 4.11) to be of order 2×10^{-3} between 10 and 50 AU for the highest resolution simulations we have run (see fig. 4.16).

Although we cannot assign a physical origin to the bulk viscosity term, we still can constrain the magnitude of other, known sources of thermal energy generation by comparing their computed contribution to those of our bulk term. In our simulations, the ratio between the shock and turbulent energy dissipation mechanisms varies, with higher resolution producing less shock dissipation relative to lower resolution runs. At progressively higher resolution, both the ratio and the absolute magnitude of the dissipation decrease and we conclude that we have not fully resolved the hydrodynamics important for energy generation in the system. Including the contributions in our simulations from both the $\bar{\alpha}$ and β viscous dissipation sources as a conservative estimate, we can conclude that gravitational torques produce large scale shocks which dissipate kinetic energy at a rate no greater than an equivalent α_{SS} dissipation of $\alpha_{SS} \sim 2 - 5 \times 10^{-3}$.

4.3.6. The Origin of Thermal Energy Generation

With the understanding that the artificial viscosity incorporated into our simulations approximately models the underlying physical dissipation of kinetic energy present in the disk, we proceed to calculate the magnitude and origin of the thermal energy generated in different portions of the system. We have previously identified the bulk ($\bar{\alpha}$) viscosity with turbulence (in eq. 4.11) and the von Neumann-Richtmyer (β) viscosity as representative of shocks. We can therefore estimate the thermal energy generation present in our simulations in terms of the Shakura & Sunyaev viscous disk picture using eq. 4.11 and by quantifying the relative magnitude of the two dissipative terms. The goal for this section is to understand which physical processes are responsible (and just as importantly which are not responsible) for the luminosity produced by observed young star/disk systems and to understand the shape of their SED’s. We attempt to minimize all other sources of parameterized or unknown thermal energy generation mechanisms. Of particular interest will be to understand the origin of so called ‘flat’ or shallow spectrum sources which may be representative of more massive disk systems like those in our study.

The azimuth averaged value of the viscous parameter, α_{SS} , derived from our simulations is shown in figure 4.16. Its value in any δr of the disk is of order a few $\times 10^{-3}$. Both the ‘A’ and ‘B’ simulations show identical viscous dissipation rates, so only the ‘B’ results are shown. We also plot the ratio of the dissipation due to the turbulent and shock artificial viscosities and find that over the largest portion of the disk, the magnitudes of each are within a factor of two. The total budget of thermal energy generation from dissipation of large scale gas motions averaged over azimuth is therefore within a factor of a few of that provided by an α_{SS} formulation.

In the innermost portion of the disk, the dissipation attributed to shocks becomes as much as a factor of 2–3 larger than that attributed to turbulence. Also, the value of the viscous coefficient $\bar{\alpha}$ itself is never able to relax to its lowest value in this region, which indicates repeated strongly compressive events, and leads (by eq. 4.11) to an artificial increase in the derived Shakura & Sunyaev viscous coefficient, α_{SS} , which should be attributed instead to the shock dissipation as noted in section 4.2.1.

Taking these two phenomena in isolation one would initially be led to believe that shocks dominate the dissipation in the inner 5–10 AU of the disk. It is not clear that this is the case however because in this same region, and within only a few ten’s of orbits, mass accretion onto the central star begins to reduce the density (see section 4.3.7 below). Since SPH resolves the flow using particles of finite mass, lower mass density in a given region implies fewer particles

and higher numerical dissipation and an ambiguity in the interpretation of its physical origin. Notably, higher resolution simulations produce progressively more centrally peaked dissipations (fig. 4.16), which means that the region in which shock dissipation may be important is limited to a smaller portion of the disk near the star. The derived value of the turbulent dissipation at all three resolutions reaches $\alpha_{SS} \approx 10^{-2}$ at the inner edge, suggesting that this value is fairly well resolved. At early times, for which little mass transport has yet occurred and the structures developing in the inner disk are best resolved, the conclusion that shock dissipation is a strong contributor to the thermal energy generation remains.

In our moderate and high resolution runs the luminosity derived from the simulations (figure 4.14 and 4.15) in general underestimates that from observed systems (e.g. BSCG), especially those thought to be younger systems for which large disk masses are more likely (Adams *et al.* 1990). Simulations at all resolutions underestimate the flux at long wavelengths corresponding to colder regions of the disk distant from the star. The luminosity and the SED characteristics reflect the temperature profile produced by our simulations. In section 4.3.7 below we will show that the temperatures produced by our simulations in the outer disk are quite low, so that very little radiation is emitted, even at long wavelengths. In fact, the SED contains only very small contribution from the outer disk at all; it contributes chiefly in the shallow slope of the SED below 10^{13} Hz. The effect on the integrated luminosity is that only a few percent of emitted flux in our simulations comes from the outer disk.

Two additional questions remain before firm conclusions about the physical interpretation of our simulations can be made. First, we need to be certain that modeling the dissipation of kinetic energy into heat using artificial viscosities gives an reasonably accurate representation of the true thermal energy generation rate. Second, we need to be certain that the assumed disk geometry does not play a large role in the details of the synthesized SED. For example, if the assumed disk radius is doubled, so that the total disk surface area radiating at, say 10–30 K, is increased by a factor of approximately four, will sufficient long wavelength flux be produced?

In order to investigate the first question more completely, we have performed a simulation similar to *B2h3* with the time variation of the viscous coefficients discussed in section 4.2.1 turned off and the viscous coefficients set to $\bar{\alpha} = 1$ and $\beta = 2$. This simulation is denoted *H2h3* in table 4.1. Effectively, this change will increase the global rate of thermal energy generation because we find that the time dependent viscous coefficients for each particle ($\bar{\alpha}_i(t)$) fall well below the value of unity assumed in simulation *H2h3*. The time dependent fluxes are shown in the right hand panels of figure 4.14. The total luminosity is increased by the viscosity modification but the increase comes only from short wavelengths regime representative of the inner disk. The transient in the flux at short wavelengths over the first 2–3 T_D comes from the initially high density in the inner disk, its effect on dynamical activity and therefore also thermal energy generation. With the increased heating, a single heating event will heat a given column of matter to higher temperatures than otherwise, leading to a correspondingly increased flux from that column as it cools.

After the initial transient settles, the near and mid IR flux are increased in magnitude to that of the ‘B’ simulation by only $\sim 5\%$ —barely large enough to be detectable on the plot. The long wavelength flux also increases by only $\sim 5\%$ relative to the ‘B’ simulation. In both simulation *B2h3* and *H2h3*, little thermal energy is produced in the outer disk. More significantly, figure 4.17 shows that the long wavelength turnoff does not shift further into the far IR or submillimeter region. It remains instead near 10^{13} Hz ($\sim 30\mu\text{m}$). The insufficient long wavelength flux in each of the simulations leads to the conclusion that indeed internal heating mechanisms (due to identifiable sources such as shocks) incorporated into our model are an upper limit to the heating from these mechanisms present in real systems.

To test the second question we examined the differences in the long wavelength end of the SED's generated from our 50 AU disks (simulations *A2lo*, *A2me* and *A2hi*) with those generated from 100 AU disks (simulations *a2lo*, *a2me* and *a2hi*). Time averaged SED's for each of the simulations care shown in fig 4.17. Looking specifically at the long wavelength flux behavior, in which dust destruction is unimportant, we find no significant differences between shape of the SED seen in one or the other simulation.

As we will show below, the temperatures in the outer part of the disks are lower than are determined from observations (Adams *et al.* 1990 for example determine temperatures at the outer disk edge of order 15–25 K). In many parts of the disk, they are in fact also lower than those observed for the molecular clouds in which the disks reside (see e.g. Walker, Adams & Lada 1990). We can conclude from the low temperatures and the corresponding long wavelength flux deficit that heating of the disk due to identifiable internal processes (e.g. large scale shocks) in our simulations is insufficient to heat the outer disk to the ‘right’ temperature, i.e. temperatures warm enough to produce SED's from our models which are similar to observed systems. This conclusion implies an upper limit on the amount of mass and angular momentum transport due to gravitational torques, since such torques are ultimately responsible for the growth and evolution of the spiral structures in which the shocks occur. In the inner disk, the picture is not as clear. At early times, shocks produced by gravitational torques there are capable of producing sufficient thermal energy to power the near infrared SED in our simulations. The question which remains for future consideration is whether the surface density and temperature initial conditions assumed in our work, especially given the immediate activity in the inner disk, are in fact similar to those produced by real systems.

If additional (as yet unidentified) sources of internal dissipation exist for the part of the disk at $\gtrsim 10$ AU from the star then additional heating will occur there and the matter will become warmer, the radial temperature gradient will become shallower, and the outer disk will radiate at the higher temperatures required to reproduce observed systems. These processes might come from either phenomena intrinsic to the disk itself, such as magnetic fields, or from three dimensional turbulence not modeled in our calculations.

On the other hand, it may be the case that rather than being internally heated, the outer portion of accretion disks are externally heated, for example by accretion of additional material onto the disk or by radiative heating from the surrounding cloud. If in fact the mechanisms for heating the outer disk are external (i.e. they do not originate in an as yet unspecified internal hydrodynamic or magneto-hydrodynamic turbulent dissipation), then any models which reproduce observed SED's via internal dissipative heating alone will incorrectly model the mass and momentum transport which depends on such dissipation. We have not attempted to model such effects in this work, in part because of the radiative transport approximations we have implemented (i.e. Rosseland mean opacities) preclude a reliable determination of the magnitude of such radiative heating processes in optically thin regimes.

4.3.7. Density, Temperature and Scale Height Structure

Using the structure model from section 4.2.2 we can derive physical disk parameters such as the gas temperature and the disk scale height, as well as the directly available mass density as functions of distance from the star.

The azimuth averaged temperature profiles late in the evolution of the disks shown in figures 4.2 and 4.11 are shown in figure 4.18. Overall, the midplane temperature shows several distinct regions which individually appear as power laws for suitably small radius ranges, however a single power law for the whole range of radii provides only a poor fit to the temperature structure. In

the innermost portion (~ 1 AU) of both sets of simulations, the radial photospheric temperature structure is nearly a flat function of radius. Due to the increased efficiency of cooling when the opacity is modified, the ‘B’ disk midplane temperature profile flattens out in the inner ~ 1 AU so that the temperature lies 2-300 K below that of the ‘A’ disk. Between 1 and 10 AU the midplane temperature decreases roughly according to an r^{-1} power law, but further out (between 10 and 20 AU) the midplane temperature becomes much steeper as the disk transitions from an optically thick to optically thin regime. Beyond 20 AU the disk becomes optically thin to its own radiation so that the midplane and photosphere temperatures are the same.

The photosphere temperature follows a single power law much more closely over its radial range, with the exception of the inner few AU where the temperature again becomes flatter than in rest of the disk. The ‘A’ and ‘B’ cooling prescriptions have profiles which are quite similar to each other. The differences which exist are in the azimuthal variation of the temperature. In regions where the midplane is hot and the modified cooling procedure comes into play, the rms photosphere temperature is nearly as large as the temperature itself, indicating many short lived opacity holes during which hot material near the midplane becomes visible to the surrounding space.

We have fitted the temperature profiles to a power law whose exponent is a free parameter and plotted the resulting exponent as a function of time in figure 4.19. After an initial transient as the disk becomes active the power law at the midplane of the disk is $\propto r^{-3/2}$, while the power law at the disk photosphere is $\propto r^{-1}$. Both of these coefficients compare quite unfavorably to those derived from the models of BSCG, who fit observed SED’s with a model consisting of a disk with a power law temperature profile. In their work, exponents in the range $0.5 < q < 0.75$ were determined. In our simulations, the both temperature profile and the SED are available directly. The differences are due to the lack of heating in the outer disk discussed in section 4.3.6, this leads to insufficient flux at long wavelengths to reproduce observations like those modeled by BSCG.

The result of the activity and increased dissipation (i.e. larger than purely α_{SS} model dissipation) in the inner disk noted in section 4.3.6 is that the inner disk becomes depleted of much of its initial complement of mass (see fig. 4.20) as the orbital energy of the gas is dissipated first as heat and then as radiation. This behavior is true of every simulation we study, both early in a simulation when activity is greatest and later when the density distribution in the inner disk becomes much flatter. Effectively, the surface density profile develops a much larger core radius (r_c in eq. 4.1) than it initially has. Initially, the accretion rate onto the star occurs at a rate of a few $\times 10^{-6} M_\odot/yr$. As this inner region becomes evacuated, the mass accretion rate falls by a factor of ~ 3 . The new core radius is approximately $r_c \approx 10$ AU, but its exact value is dependent upon the dynamics, the initial condition (i.e. the initial core radius and assumed $r^{-3/2}$ power law) and the magnitude of the dissipation. Due to the combined effects of the viscous and gravitational torques a portion of the mass is driven further from the star than in the initial configuration. We defer additional studies of the redistribution of mass and angular momentum to a future study.

In addition to the development of the larger core radius, the density structure exhibits another artifact of the apparently unphysical initial condition. The density first rises to a weak local maximum before decreasing with radius as in the initial power law. We believe this maximum is little more than an artifact of our initial condition and should not be considered as a physical manifestation of the disk evolution. Based on each of these phenomena, we conclude that a more physical radial density structure for circumstellar disks will have a shallower profile than the $r^{-3/2}$ profile assumed here.

The vertical structure model outlined in section 4.2.2 can also be used to calculate the vertical scale height at each point in the disk. For the purposes of this work we define the disk scale height, Z_e , at some point in the disk as the altitude above the midplane at which the mass

density, ρ , decreases by a factor of $1/e$ from its midplane value. We find (fig. 4.21) that as our simulations evolve, the disk becomes quite thick at small distances from the star. No differences are apparent between the scale height produced from the different cooling prescriptions. The altitude of the photosphere shows an even more pronounced rise at small radii, extending vertically to $Z_{\text{phot}}/R \approx 0.27$ near 5 AU. Depending on the details of the grain distribution within a vertical column, this local maximum suggests that the outer disk may become shaded from stellar radiation.

Further from the star the scale height Z_e/R stays nearly constant with no flaring present except at the outermost edge. No doubt the vertical structure produced will be dependent upon the temperature profile and will change when a full description of the heating mechanisms are included. We therefore cannot regard the current scale height results as highly significant.

4.4. Comparison to other work

In a series of papers Bell and her collaborators (Bell & Lin 1994, Bell *et al.* 1995, 1997, Turner Bodenheimer & Bell 1997) have developed an evolutionary model for accretion disks based on an α_{SS} model for radial transport and a mixing length theory (MLT) based vertical structure model. In similar work D'Allesio *et al.* (1998a, 1998b) have also developed a '1+1' dimensional model. In the present work, we follow the evolution through a '2+1' dimensional model, including the evolution of matter in both radius and azimuth, but at the expense of simpler vertical structure and radiative transport (sec. 4.2.2). We investigate the dynamical evolution (and consequent thermal energy generation mechanisms) of the disk which can not be addressed in the 1+1D work due to the input assumptions of the α_{SS} disk formulation.

In an α_{SS} model, three input parameters specify the physics of the model. They are the accretion rate, \dot{M} , the magnitude of the viscosity, α_{SS} and the radiative flux impinging upon the disk surface. Together these three parameters specify the amount of active and passive heating experienced by the disk. They also determine the temperature and density structure throughout the disk as functions of time and one space variable (the distance from the star).

In deriving a vertical structure, the above works assume boundary conditions at the $z = \infty$ boundary which include radiative fluxes from the star, disk and molecular cloud and the thermal conditions of the surrounding molecular cloud. In contrast, we assume that the disk exists in isolation (i.e. that these external fluxes are zero) in order to study the effect of dynamical processes internal to the disk itself. We show that known dynamical heating mechanisms such as shocks or PdV work do not provide enough heating by themselves to reproduce observations. Either additional internal heating mechanisms (e.g. dissipation via magnetic fields as in Gammie 1996 or via some other turbulent dissipation mechanism) or energy flux onto the disk from external sources (for example direct illumination of the disk by the star or the surrounding molecular cloud or by illumination of one part of the disk by another) must be accounted for in order to correctly model the disk evolution.

We find that a full multi-dimensional evolution is important for a description of the density structure of the systems described here because the spiral structures typically have amplitudes, $\delta\Sigma/\Sigma$, of order unity. The temperature structure of such systems does not develop such large variations in azimuth. An azimuth averaged temperature law will be accurate to a few percent except in the inner region of the disk where grain destruction becomes important and the hot midplane intermittently becomes exposed to space.

Bell *et al.* (1997) find that with the low disk masses implied by their model (i.e. their input values of the mass flux through the disk, \dot{M} , and the magnitude of the viscosity, α_{SS}),

the structure obtained is actually super adiabatic in z . Our assumption by which the vertical structure was determined was that the structure was vertically adiabatic and contrasts with their MLT calculation that shows a super adiabatic gradient. The effect that a super adiabatic gradient would have on our simulations would be to systematically reduce the temperature of the disk photosphere. In the absence of a full three dimensional calculation of the vertical structure, the exact nature of the gradient remains unknown. However, we believe that the vertically adiabatic assumption in our simulations is justified because we model high mass systems in which the dynamical effects present are likely to create additional turbulence and act to additionally smooth out vertical entropy gradients.

In spite of the differences between the modeling assumptions and procedures utilized in our work and those noted above, the results produced from each are in many cases quite similar. This should perhaps not be too unexpected since we find that shocks are not the dominant source of heating in the disk and our only other source of thermal energy generation is a viscous heating term analogous to the standard α_{SS} model, extended to include limited time and space dependence. Both methods are able to produce SED's which reproduce observed profiles to varying degrees. The temperature and density profiles on which the SED's are based however are quite different. In our work, the inner disk provides nearly all of the flux and is characterized by an essentially flat surface density profile and an r^{-1} temperature law. Only at distances > 10 AU does the surface density begin to fall off steeply. At these radii, the temperatures derived from our models are low enough not to contribute significantly to the flux. As is shown for the 1D case in Turner *et al.*, absorption and reradiation of infrared and microwave photons can heat the outer disk, flatten the temperature profile and provide additional far infrared flux. Such a treatment in our model would require a multi-dimensional frequency dependent radiative transport code, which has not yet been incorporated.

Both in our work and Bell *et al.* (1995), a mechanism by which the disk may vary its energy output (SED) in time is explored. We consider the variation of the opacity due to the destruction and reformation of grains in the inner disk, while they consider variation in the thermal ionization state of gas within a few stellar radii of the star. They are able to produce very large and long term temporal variations typical of FU Orionis outbursts in accretion disk SED's, while we find much smaller variations (factors of ~ 2 or less) which occur over much shorter time scales.

The puffed up inner disk in our work is similar to the 'volcano region' discussed by Turner, Bodenheimer & Bell (1997) in their simulations of the disks of FU Orionis objects. Their models, derived from Bell *et al.* (1997), assume a much lower mass disks than our own, produce a puffed up region which is also much smaller in radial extent than in our work. Neither our model nor theirs depend upon the validity of the thin disk assumption and both indicate that such an approximation may be inappropriate in the inner regions of the disk.

4.5. Concluding Remarks

In this study of the evolution of circumstellar accretion disks, we have found that the growth of multiple armed spiral instabilities is suppressed relative to the growth found in Paper I. In the present simulations spiral arms grow only weakly in the inner half of the disk. Regions more distant from the star are less filamentary than with an isothermal evolution. The spiral structures also do not collapse into clumps as they did in Paper I.

The spiral structures are similar in that they do not persist as stable structures over even a single orbit of the outer disk around the star. The dynamics of the inner region are very important for understanding not only the global morphology of the system as we showed in Paper I, but also its observational appearance as well. Transport, growth and vaporization of dust

vertically within a column of gas can have marked observable consequences for the spectral energy distribution of the system. A correct model of the dynamics and spectral energy distributions of circumstellar disks similar to those studied here must include an accurate description of the full three dimensional spatial distribution of grains and of their size distribution in order to accurately model the opacities and the radiative transfer which depends on them.

The simulations discussed here produce temperature's in the outer disk which are colder than those produced by models of observations. The temperature profile which results produces a power law exponent near $q = 1.5$ at the disk midplane and $q = 1.0$ at the disk photosphere, rather than the α_{SS} model prediction of $q = 0.75$ or the observed $0.5 \lesssim q \lesssim 0.75$. This steep profile produces a spectral energy distribution which, when compared to observed systems, emits insufficient flux at low frequencies ($\lesssim 10^{13}$ Hz or $30\mu\text{m}$). We attribute this primarily to the influence of physical phenomena present in observed systems which are not included in our study. As modeled, our systems do not produce sufficient thermal heating from well defined internal sources such as shocks. Additional heating must be supplied from internal sources such as small scale hydrodynamic or magneto-hydrodynamic turbulence or from external heat sources such as radiative heating effects from the circumstellar cloud or the central star or thermal heating due to accretion of additional infalling matter onto the disk may provide additional thermal energy to the outer disk.

We find that the heating due to large scale shocks within the disk does not contribute a dominant portion of the internal energy present in the disk except perhaps in the inner few AU, where shock dissipation provides a much larger fraction. Further, the magnitude of shock dissipation derived from the global spiral arm structures produced in our simulations is insufficient to power the luminosity of observed circumstellar disks. This indicates that mass and angular momentum transport, which depend on such internal dissipation, may be over estimated in α_{SS} models of accretion disks which assume an greater than $\sim 4 - 5 \times 10^{-3}$. This limit is derived from fig. 4.16 in which the magnitude of shock dissipation is roughly equivalent to the black box α_{SS} dissipation which is $\sim 2 \times 10^{-3}$. This conclusion is limited to systems in which the disk is marginally self gravitating, i.e. $M_D/M_* = 0.2$. Spiral arms in these systems are both filamentary and of high order symmetry ($m \geq 3$). It remains to be determined the role that gravitational torques will play in systems with more massive disks, where the dominant spiral patterns are of low order symmetry ($m \leq 3$). Perhaps in this case more efficient transport is present and a flatter SED profile can be realized.

In both Paper I and in the present work, the assumed $r^{-3/2}$ surface density power law quickly becomes modified in the inner part of the disk as matter either accretes onto the star or migrates to somewhere further out. From these results it seems improbable that such a steep density distribution can occur in nature but the true nature of the density distribution as a function of radius remains to be determined. We can suggest weak limits on the density profile by coupling our results with those of Laughlin & Bodenheimer (1994). In their study, initially toroidal initial configurations (of massive systems) evolve towards power law-like distributions, while our power law initial conditions evolve towards flatter profiles.

We wish to thank Phil Pinto for valuable discussions about radiative transport, Sarah Maddison for valuable discussions about initial conditions for SPH disks and Mike Meyer for several useful conversations about SED's. A conversation with Jim Stone provided additional insight into the role of gravitational torques. This work was supported under the NASA Origins of the Solar System grant NAG5-4380.

Table 4.1. Initial Parameters For Simulations

Name	Number of Particles	M_D/M_*	Q_{\min}	Opacity Factor R	End Time ($T_D=1$)	Disk Radius (AU)
I2lo	16520	.2	1.5	...	1.6	50
A2lo	16520	.2	1.5	...	6.0	50
I2me	33399	.2	1.5	...	1.8	50
A2me	33399	.2	1.5	...	6.0	50
B2m1	33399	.2	1.5	0.001	6.0	50
B2m2	33399	.2	1.5	0.010	6.0	50
B2m3	33399	.2	1.5	0.050	6.0	50
B2m4	33399	.2	1.5	0.075	6.0	50
B2m5	33399	.2	1.5	0.025	6.0	50
I2hi	101016	.2	1.5	...	1.8	50
A2hi	101016	.2	1.5	...	6.0	50
B2h3	101016	.2	1.5	0.050	6.0	50
H2h3	101016	.2	1.5	0.050	6.0	50
a2lo	16182	.2	1.5	...	3.0	100
a2me	33134	.2	1.5	...	2.3	100
a2hi	100971	.2	1.5	...	3.0	100

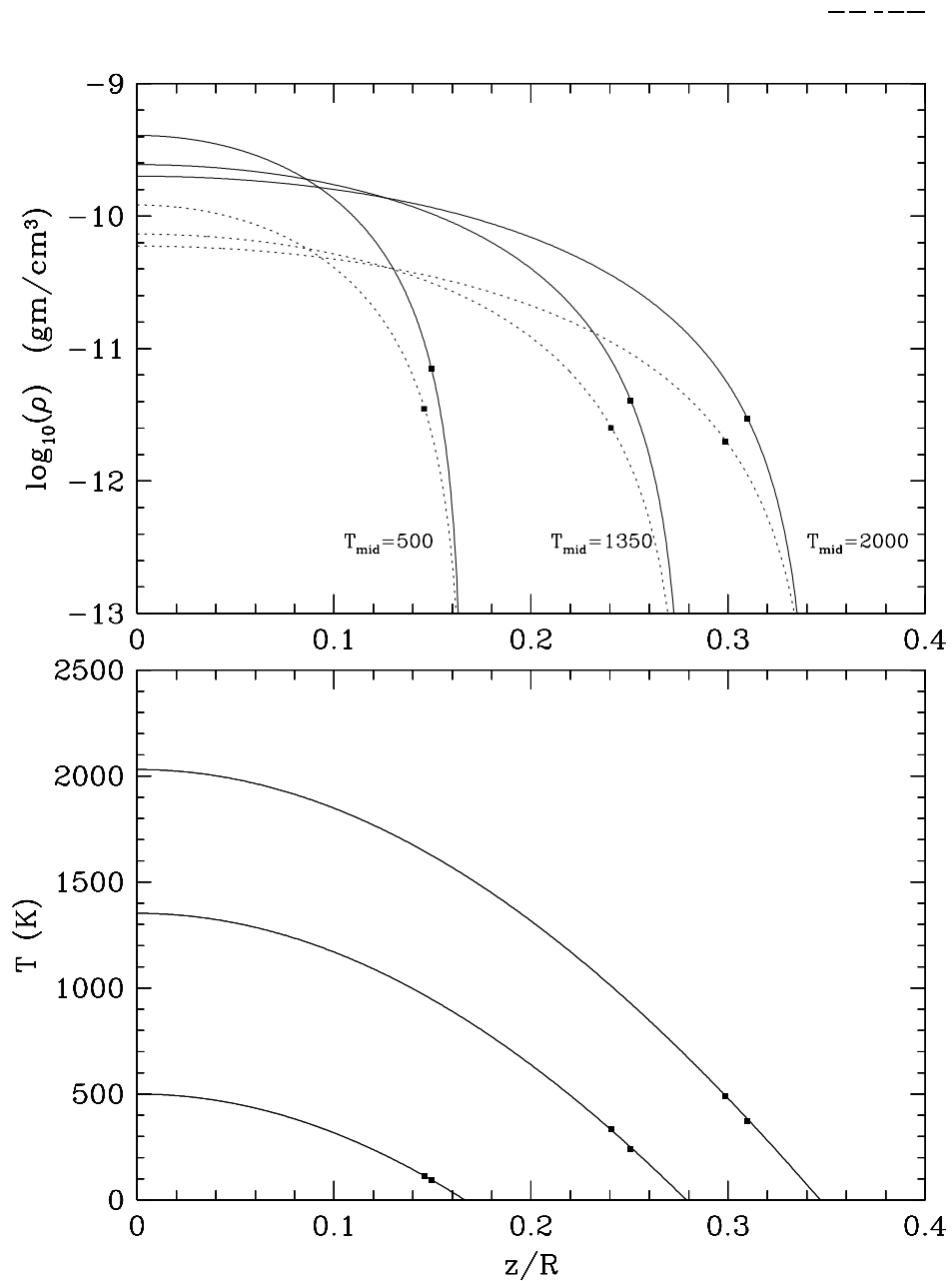


Figure 4.1 Density and temperature structure as a function of altitude above the midplane for conditions typical of our disk simulations at a 1 AU distance from the star. The location of the calculated disk photosphere of the disk are marked with a solid square attached to each curve. The solid curves on the upper frame are typical of the density derived from our simulations of 50 AU disks ($1000 \text{ g}/\text{cm}^2$), while the dotted curves represent the density structure typical of our 100 AU disks ($300 \text{ g}/\text{cm}^2$). Each of the three pairs of curves in the plot show the density structure for an assumed midplane temperature of ~ 2000 K, ~ 1350 K and ~ 500 K as noted. The temperatures, plotted in the lower frame, are in each case, well below, approximately equal to and well above the grain destruction temperature in the disk midplane.

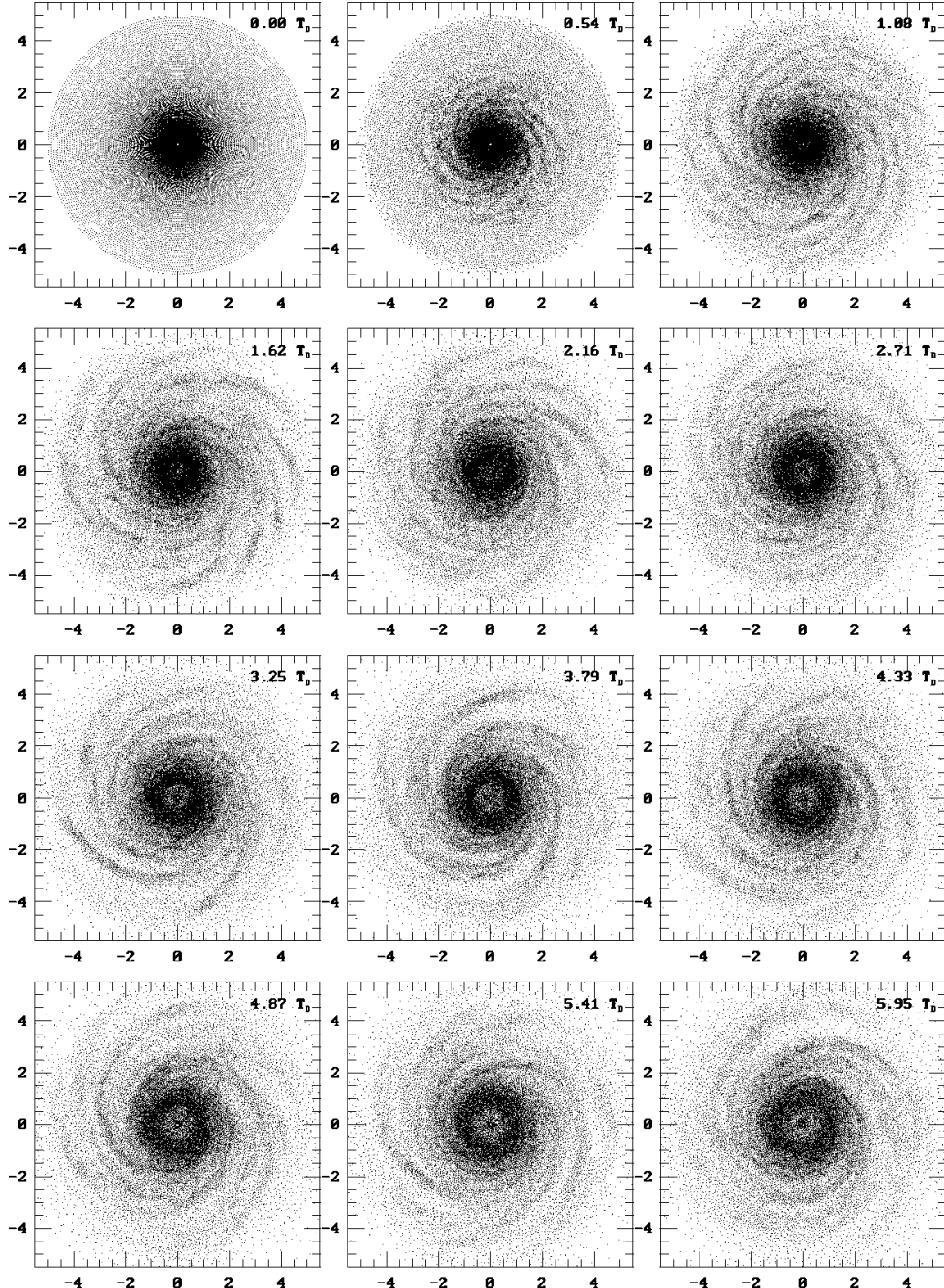


Figure 4.2 A time series of SPH particle positions for a disk of mass $M_D/M_* = 0.2$ and initial minimum $Q_{min} = 1.5$ (simulations $A2me$). Spiral structure varies strongly over time. Length units are defined as 1=10AU and time in units of the disk orbit period $T_D = 2\pi\sqrt{R_D^3/GM_*}$. With the assumed mass of the star of $0.5 M_\odot$ and the radius of the disk of 100 AU, $T_D \approx 1400$ yr.

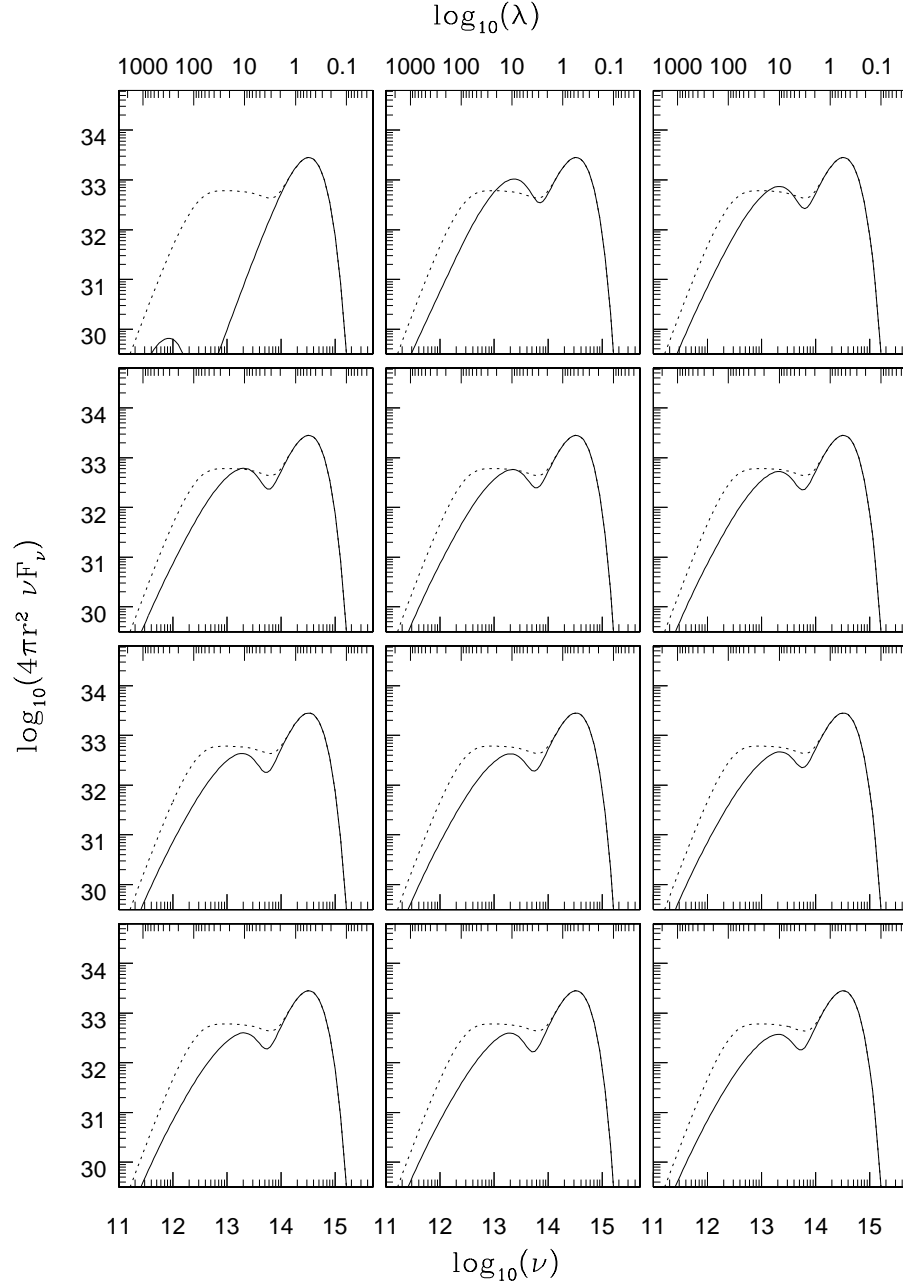


Figure 4.3 Spectral energy distribution's for the disk shown in figure 4.2. Each panel corresponds to the analogous panel in figure 4.2. The dotted line represents the contribution due to the central star, which is assumed to be radiating as a $T_{eff} = 4000$ K black-body with $1 L_\odot$. The horizontal axes of each panel are labeled in frequency (bottom tick marks) and in wavelength (top tick marks). A ‘reference’ SED with the same assumed 4000 K star and with a disk with the same outer radius as assumed in our simulations, with luminosity $L_D = 0.5L_\odot$ and a temperature power law exponent of $q = 0.5$ is shown with a dotted line. The SED’s produced clearly do not reproduce the observed luminosity spectrum around T Tauri stars, producing insufficient flux at both long and short wavelengths.

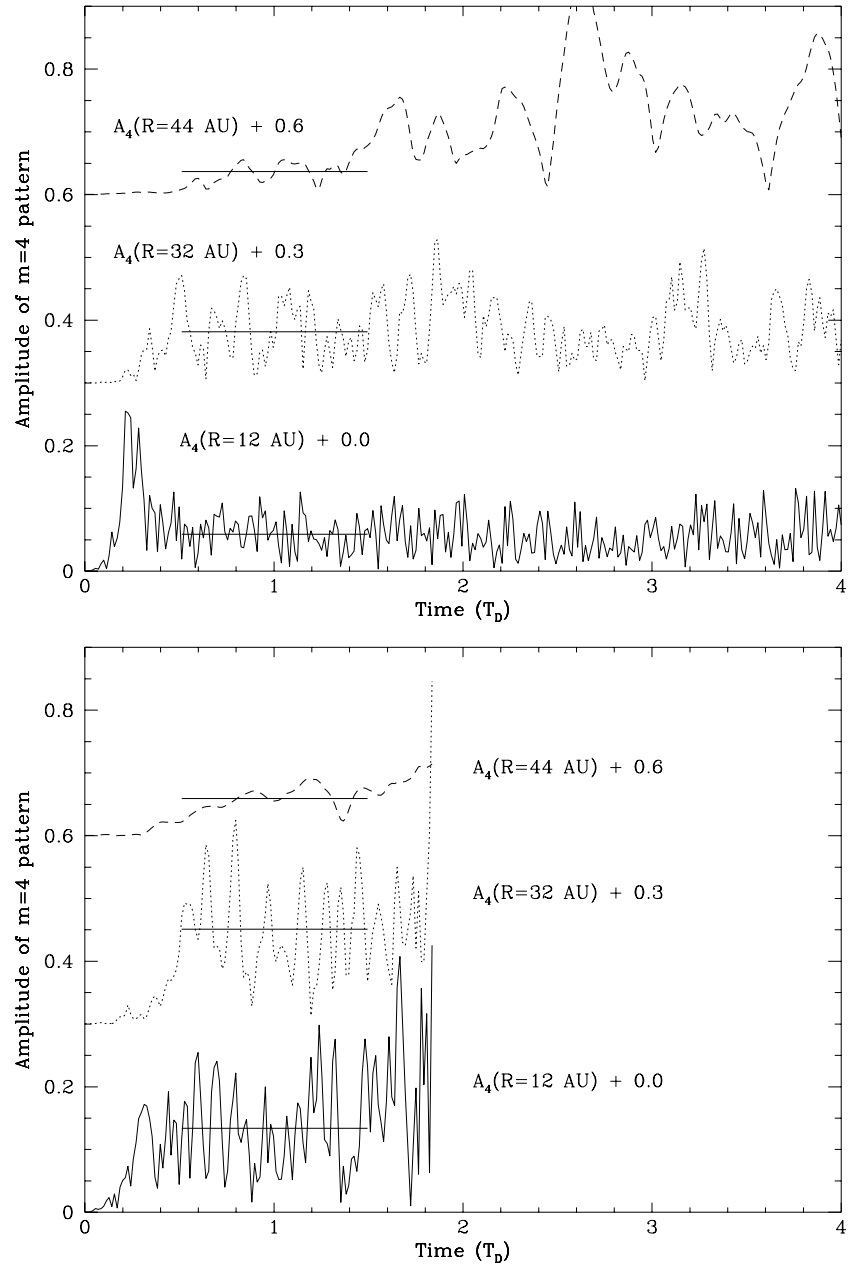


Figure 4.4 The amplitude of the $m = 4$ spiral pattern as a function of time at several distances from the star. The top panel shows the amplitudes derived from the simulation shown in figure 4.2, while the bottom panel shows the isothermally evolved simulation $I2me$. For each curve, the amplitude of the pattern is offset from the origin by the amount noted in order not to confuse the reader. Solid horizontal lines denote the fitted average pattern amplitude and extend over the time span for which the average was calculated.

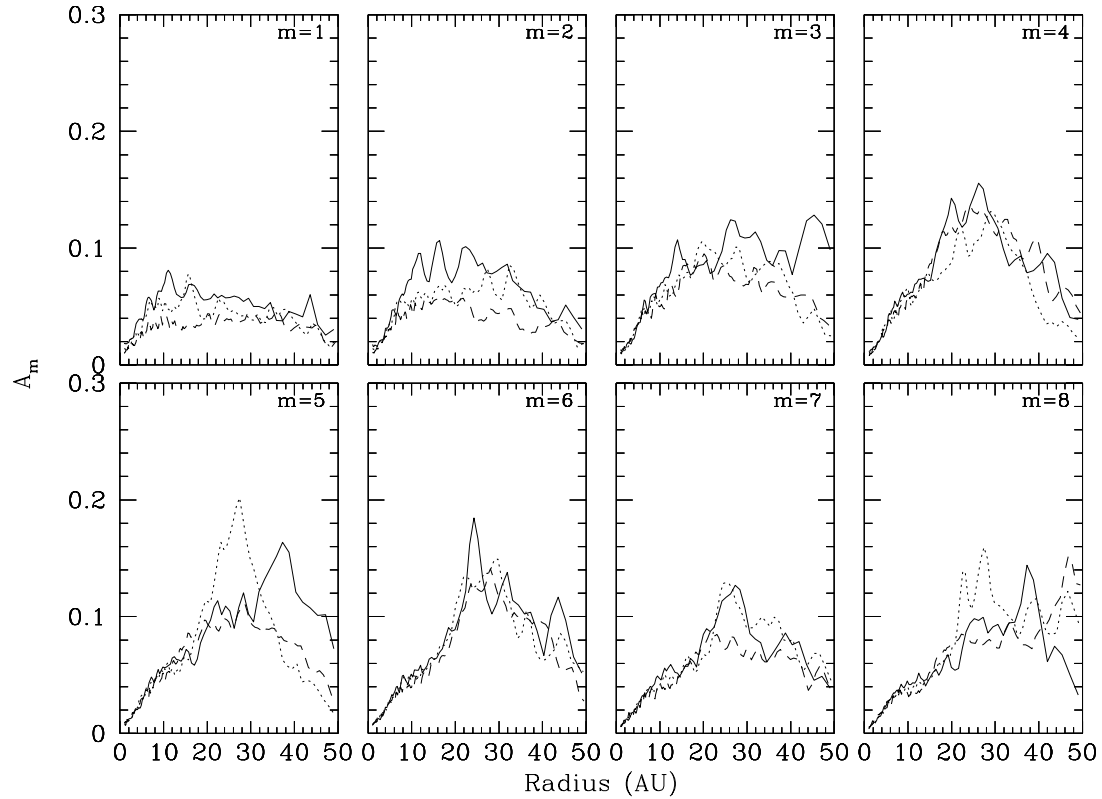


Figure 4.5 The time averaged amplitude of the $m = 1 - 8$ spiral patterns as a function of radius for the disk shown in figure 4.2 as well as its high and low resolution counterparts. The solid line denotes the low resolution run ($A2lo$), while the dotted and dashed lines represent the moderate and high resolution runs, $A2me$ and $A2hi$, respectively.

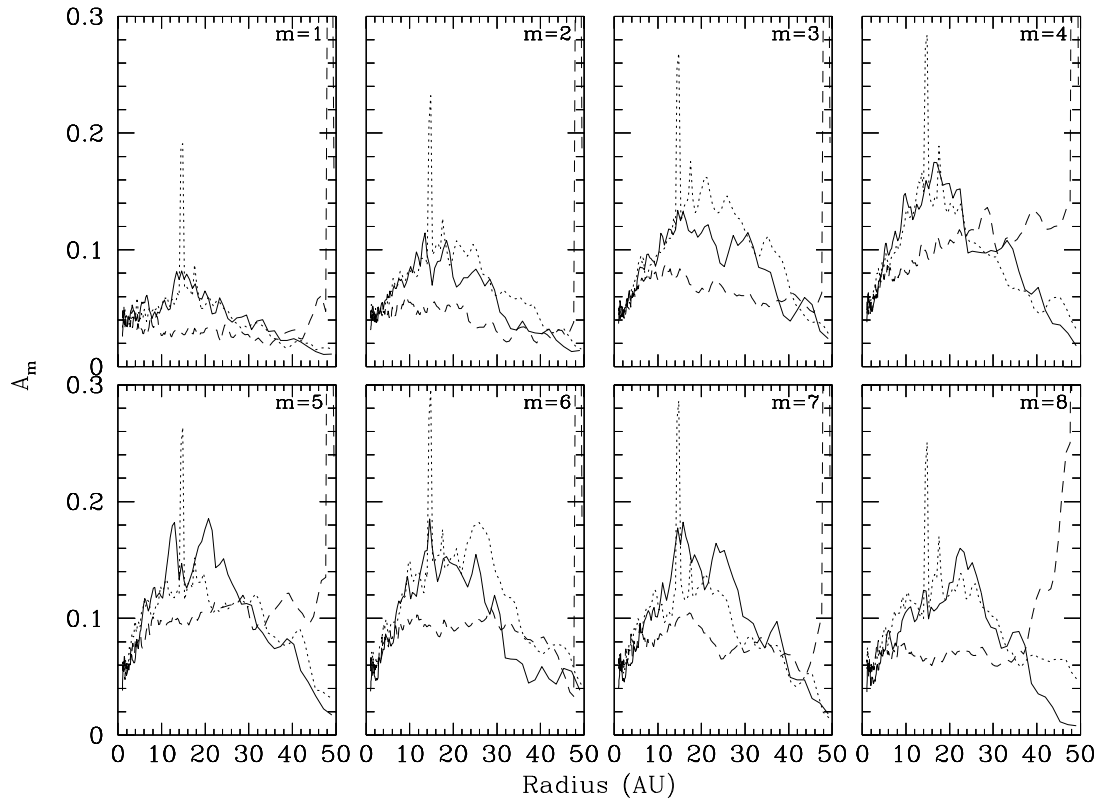


Figure 4.6 The time averaged amplitude of the $m = 1 - 8$ spiral patterns as a function of radius isothermally evolved simulations with the same initial conditions as those shown in figure 4.5. Here again, the solid line denotes the low resolution run (*I2la*), while the dotted and dashed lines represent the moderate and high resolution runs, *I2me* and *I2hi*, respectively. Spike appearing in the plots for the moderate resolution run (at ~ 12 AU) and the high resolution run (near the outer edge) are both artifacts of clumps which formed just prior to the termination of the fit. They should be disregarded in comparisons with figure 4.5.

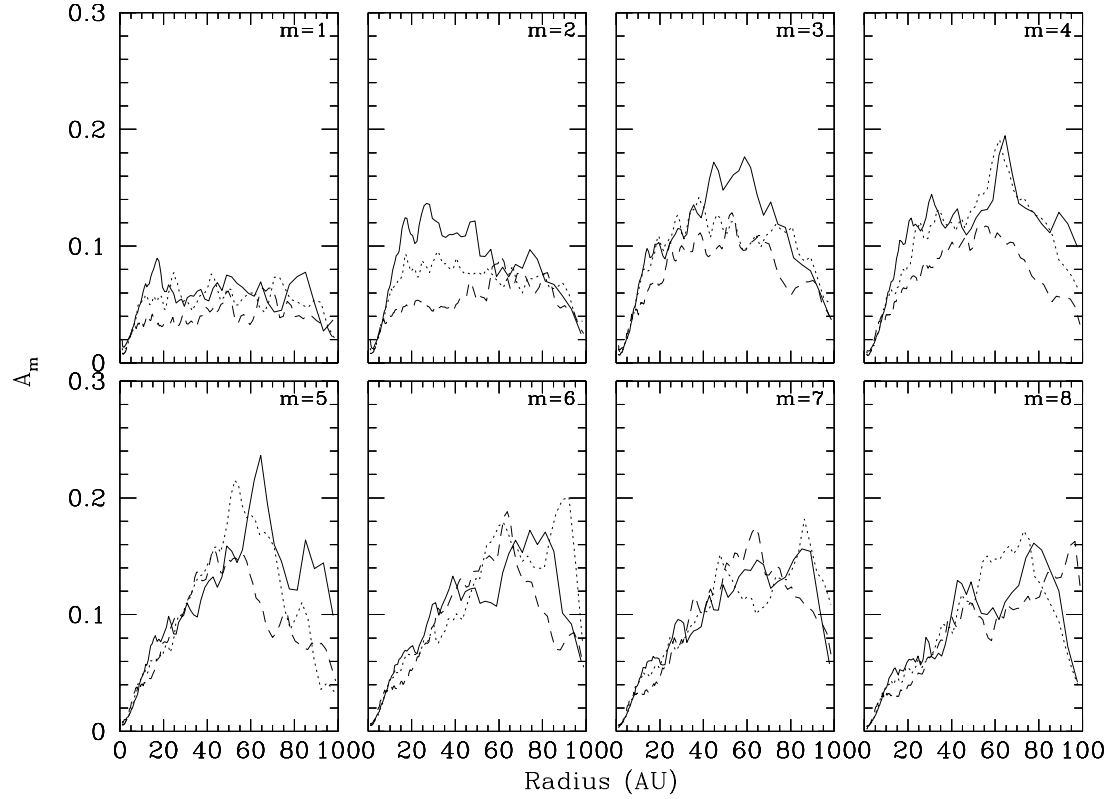


Figure 4.7 The time averaged amplitude of the $m = 1 - 8$ spiral patterns as a function of radius for the $R_D = 100$ AU disks similar to those shown in figure 4.5. The solid line denotes the low resolution run ($a2lo$, while the dotted and dashed lines represent the moderate and high resolution runs, $a2me$ and $a2hi$, respectively. The amplitudes which develop are quite similar to those of the 50 AU disks shown in figure 4.5

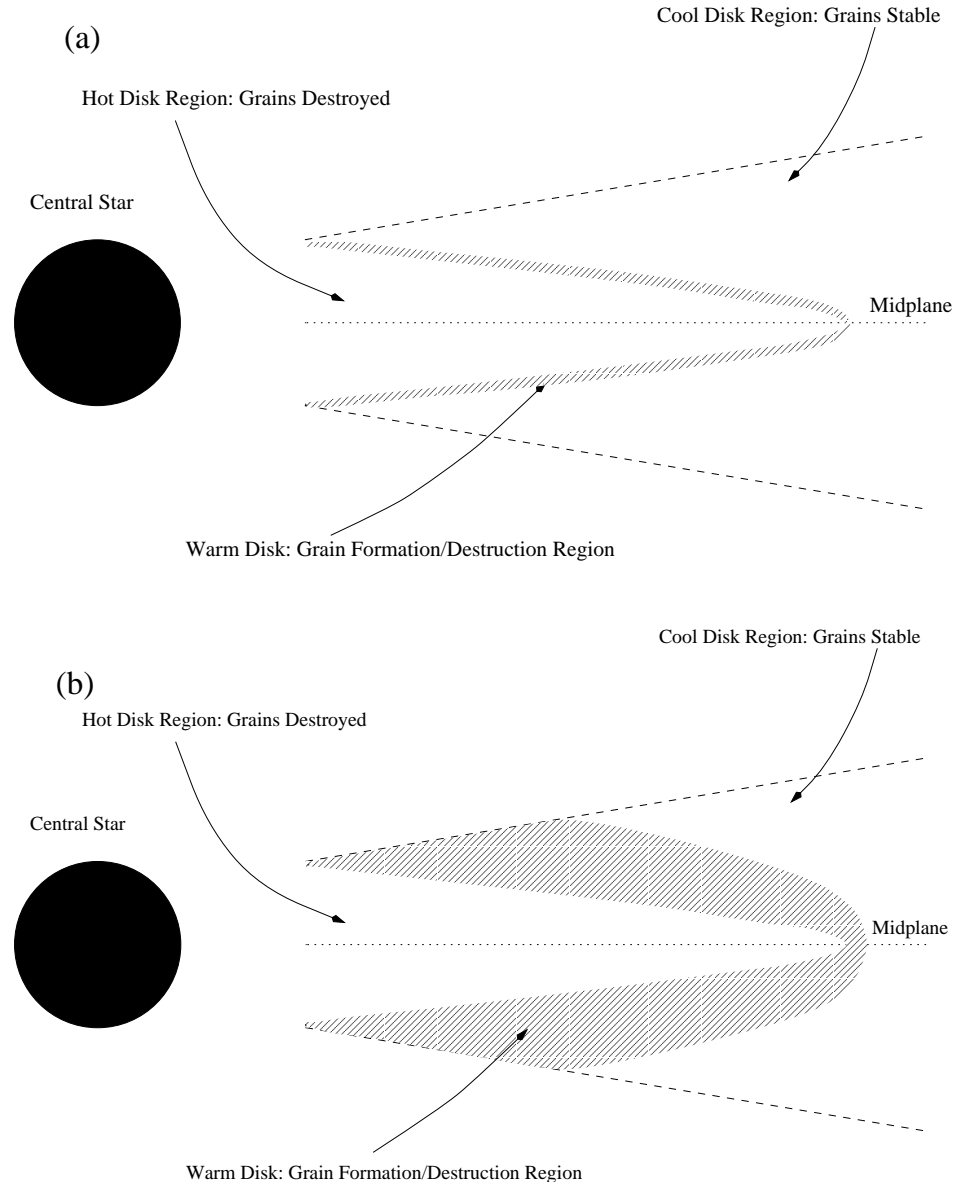


Figure 4.8 (a) A cartoon of the physical conditions of cooling prescription 'a' and implemented for the simulation in figures 4.2 and 4.3. Under this assumption, even if the midplane temperature lies well above the grain destruction temperature, grains embedded in high altitude, cool gas block radiation from the hot midplane matter. (b) the modified condition (cooling prescription 'b') used for the simulation shown in figures 4.11 and 4.12 below. Under this modified assumption, grains are destroyed in the midplane if the temperature is hot enough but reform only slowly at high altitudes. This allows a particular column of gas to become less opaque so that it radiates at a higher effective temperature and cools more quickly.

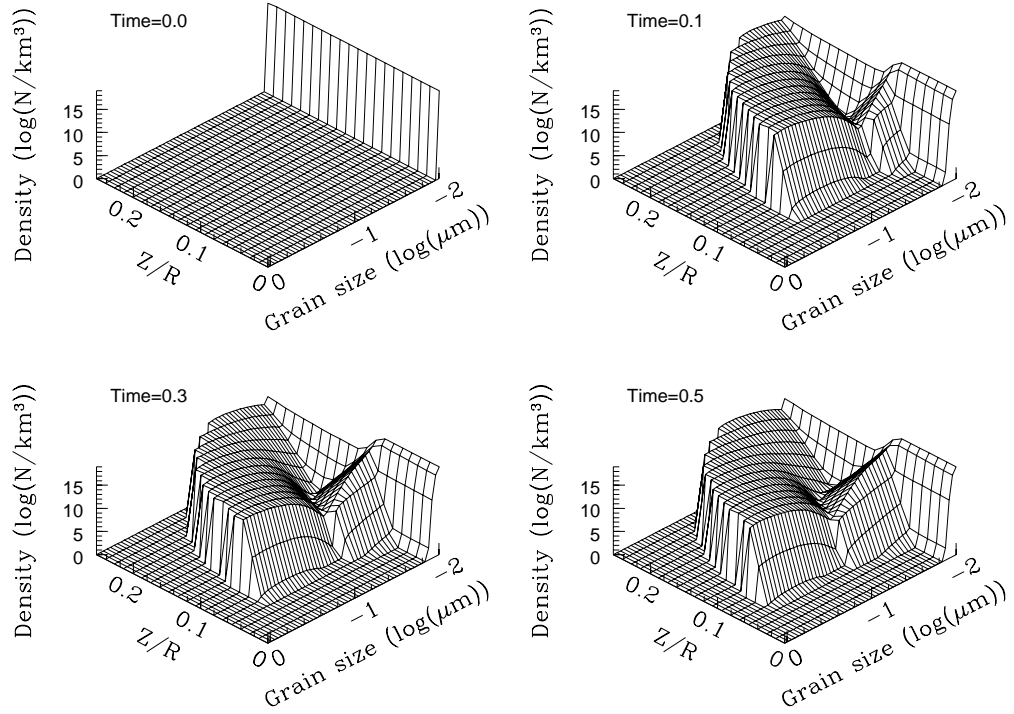


Figure 4.9 The grain size distribution as a function of altitude above the disk midplane. The time units in the upper left of each frame are given in orbit periods at the assumed 1 AU distance from the star ($T = 1 \approx 1.44$ yr). The vertical structure is identical to that shown in figure 4.1 with a surface density of 1000 gm/cm^2 , midplane temperature of 1350 K at a distance of 1 AU from the central star. In the example shown, midplane temperature is above the assumed grain destruction temperature ($T = 1200$ K).

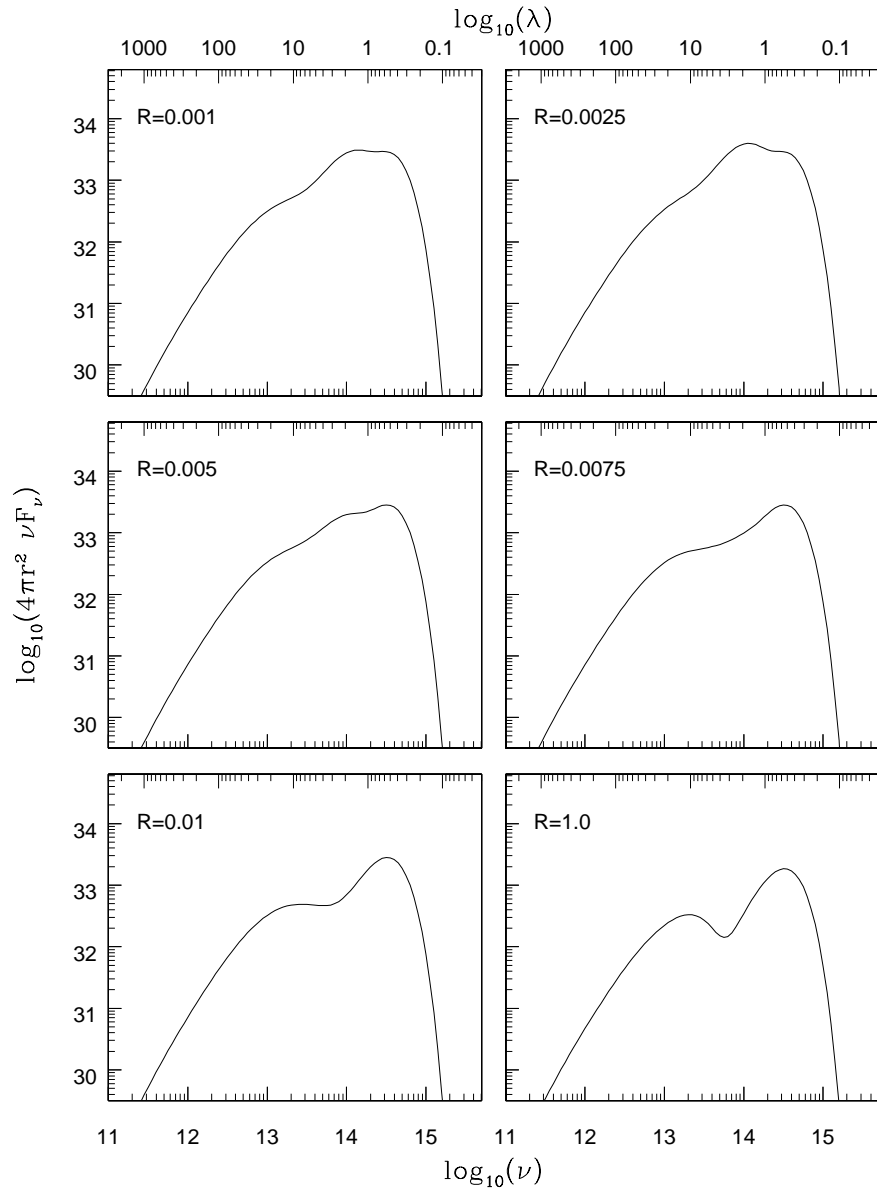


Figure 4.10 Synthesized SED's of simulations with varying modifications in grain opacity. The initial conditions of these simulations are identical to those of simulation *A2me*, but are each carried out under varying physical assumptions. To remove short period time variation, we plot a time averaged SED over the time from $T_D=1$ to $T_D=5$.

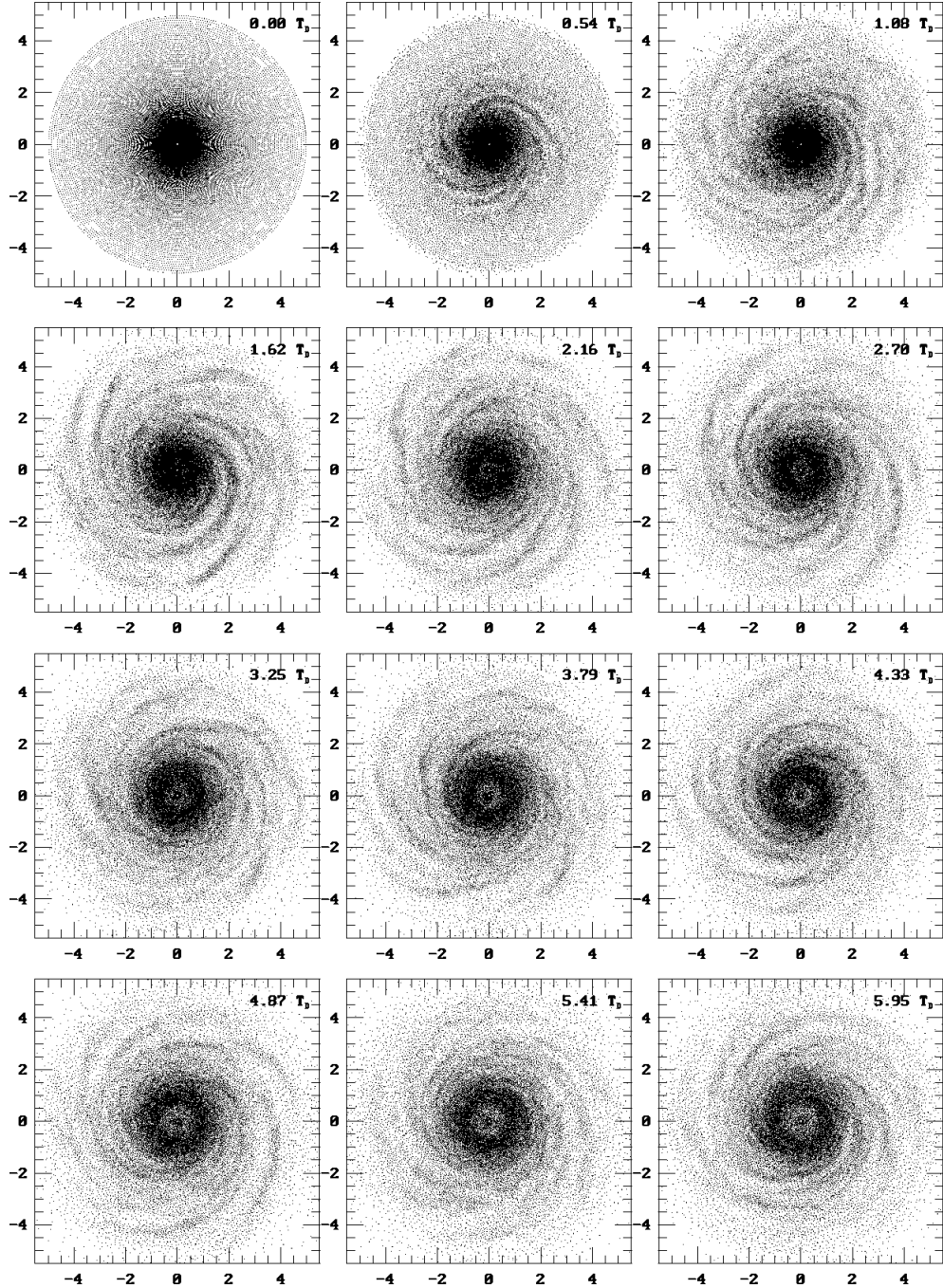


Figure 4.11 A time series mosaic of SPH particle positions for the same initial condition as shown in figure 4.2. The cooling prescription used in this simulation has been revised to include dust destruction over entire vertical columns as shown in figure 4.8b with $R = 0.0075$ (see text). The gross morphology of the structures that develop is quite similar to that shown in figure 4.2, even though the cooling assumptions and gas temperatures in the hottest (inner disk) regions are different.

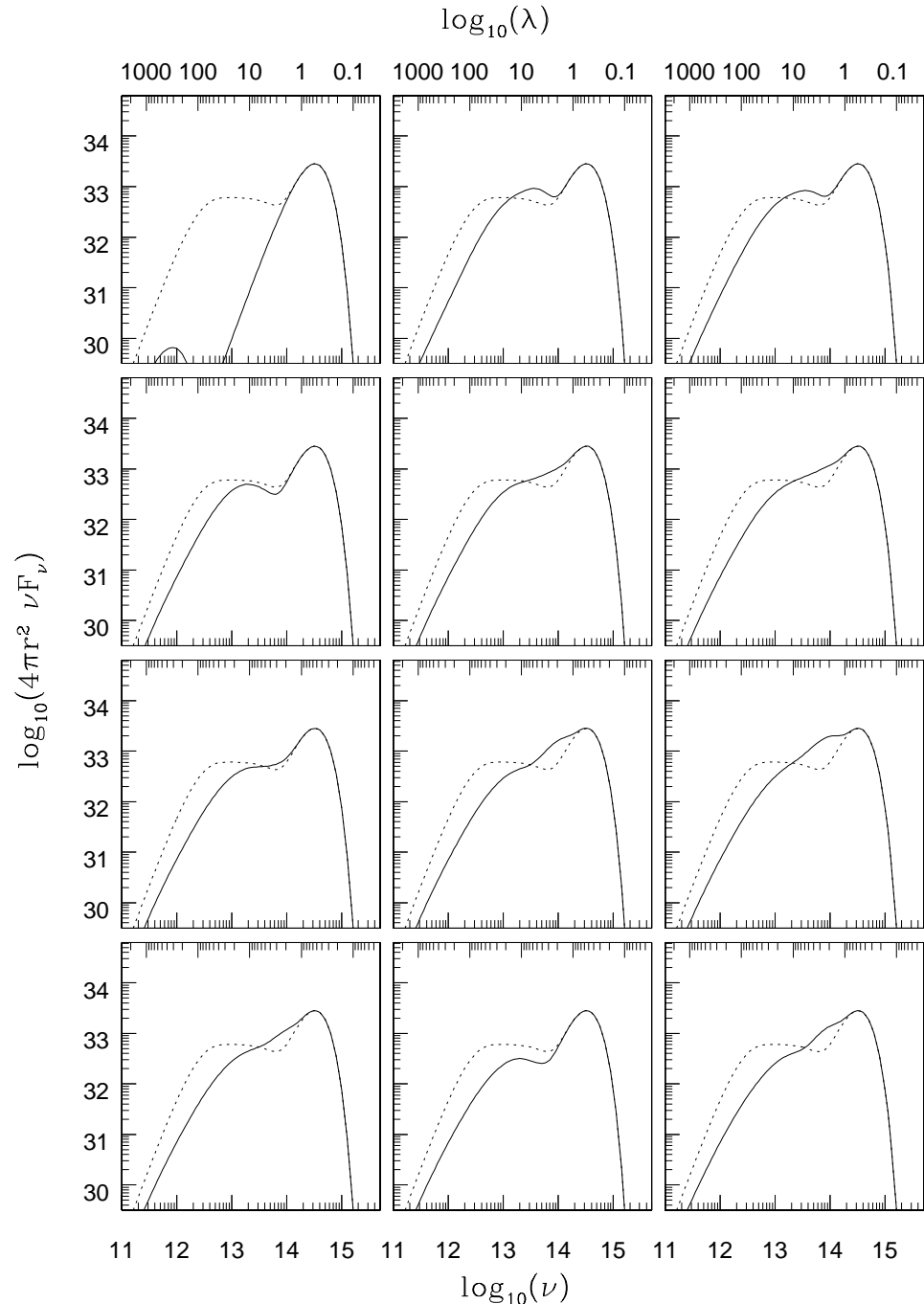


Figure 4.12 SED's for the simulation shown in figure 4.11. Under the modified cooling assumption shown here, a closer correspondence to observed systems is found at near IR wavelengths. Substantial variations in the shape are seen over time scales of a few tens of years to a few hundred years. At some times the contribution of the star is partially masked by emission from the disk, while at others the star contributes nearly all of the short wavelength flux.

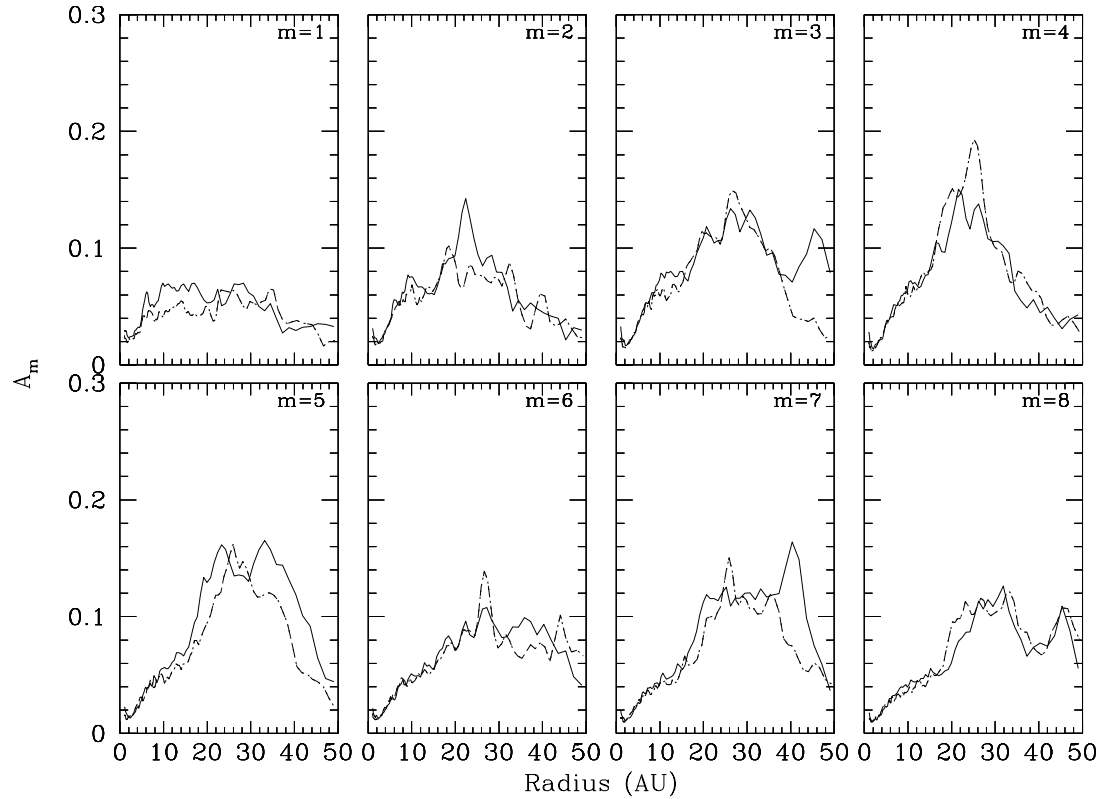


Figure 4.13 The time averaged amplitude of the $m = 1 - 8$ spiral patterns as a function of radius for the disk shown in figure 4.11 as well as its high and low resolution counterparts. The solid line denotes the low resolution run ($B2lo$, while the dotted and dashed lines represent the moderate and high resolution runs, $B2me$ and $B2hi$, respectively.

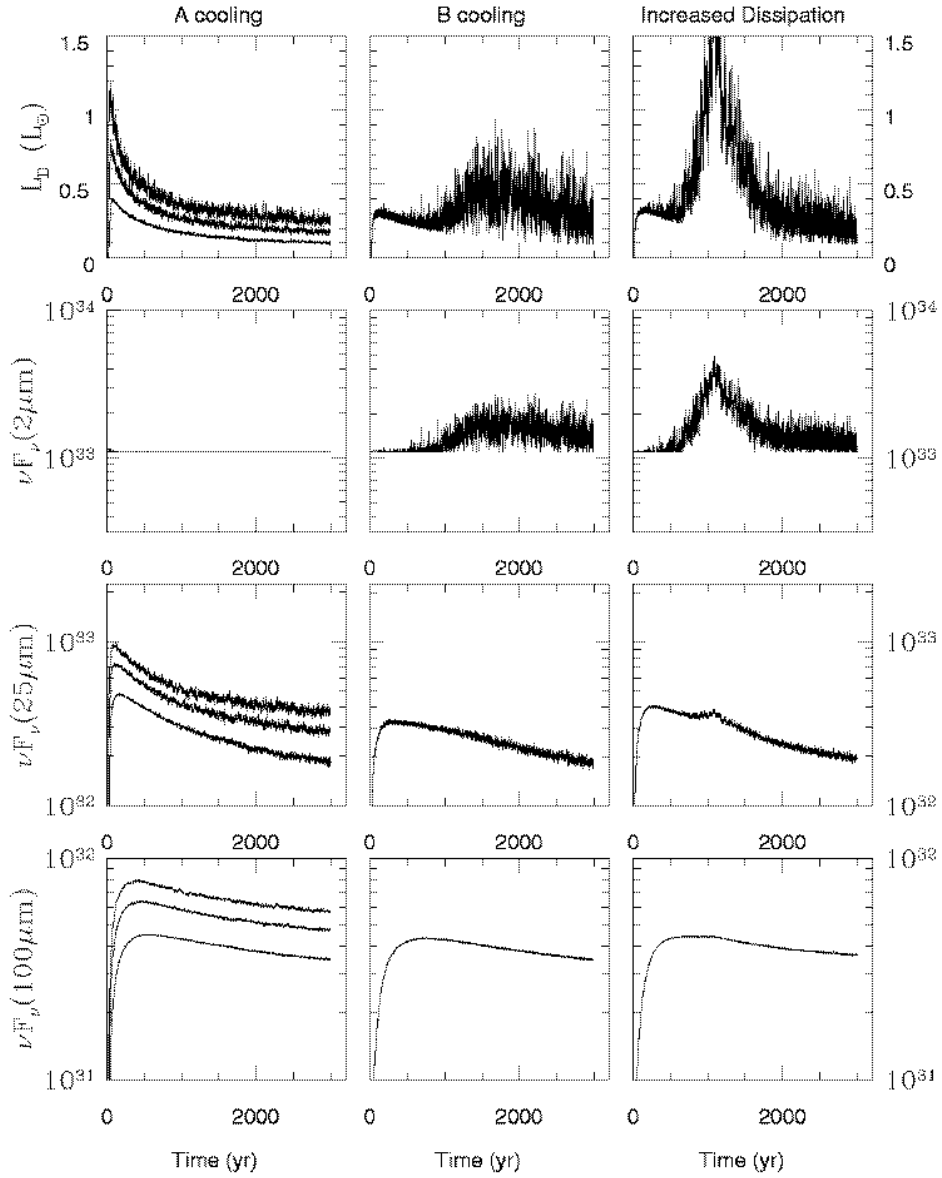


Figure 4.14 The luminosity and emitted power at three wavelengths: $2, 25$ and $100\mu\text{m}$. On the left are simulations $A2lo$, $A2me$ and $A2hi$ and in each panel the top, middle and lower tracks originate from the low, middle and high resolution simulations respectively. The $2\mu\text{m}$ flux consists only of the assumed constant contribution from the stellar photosphere, while the longer wavelengths are dominated by the flux from the disk. The center panels show only simulation $B2h3$. The lower resolution counterparts were suppressed for clarity. The right panels show the results of simulation $H2h3$, for which a higher effective thermal energy generation rate is present.

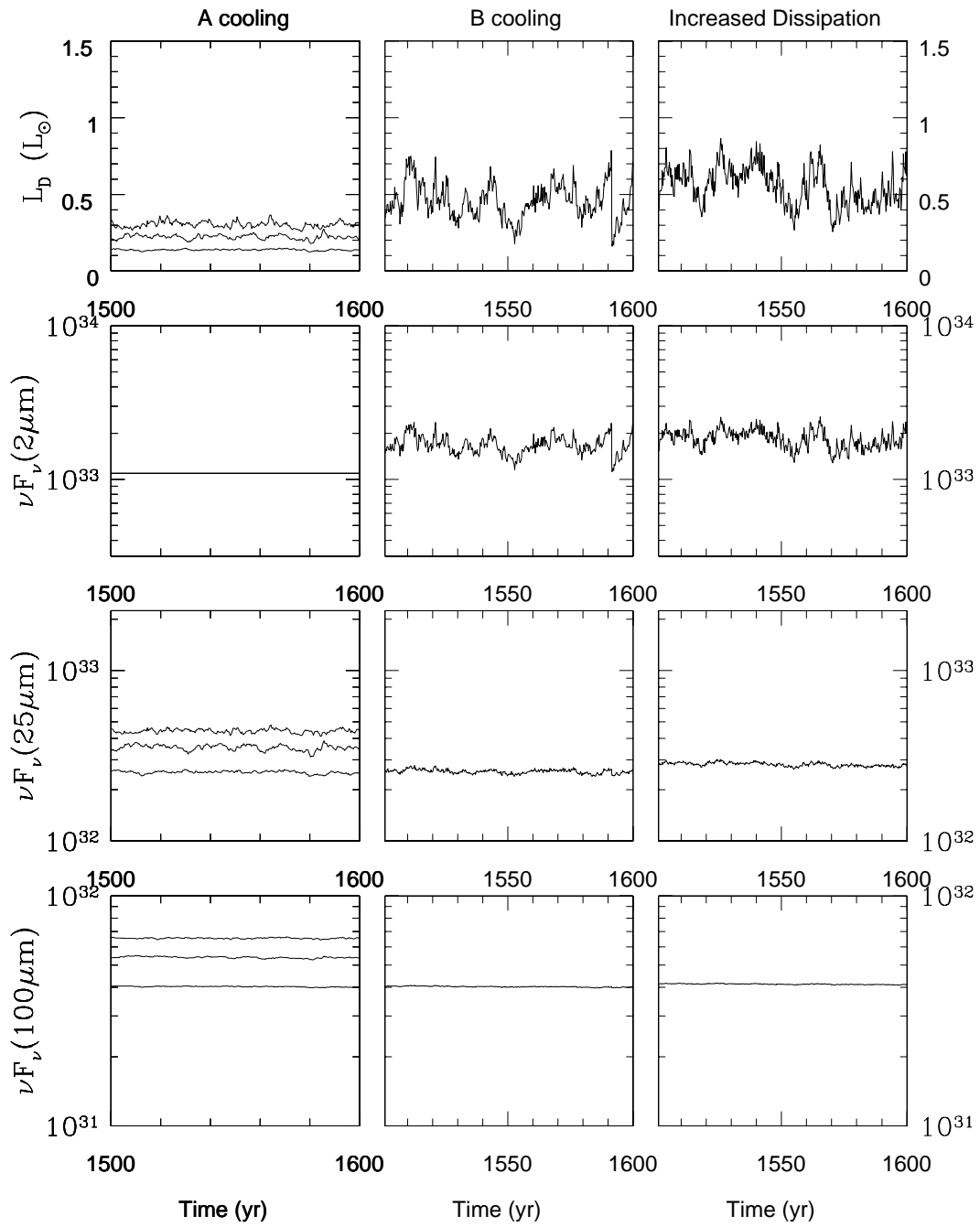


Figure 4.15 The same as figure 4.14 but expanded in time to show the details of the time dependence of the flux.

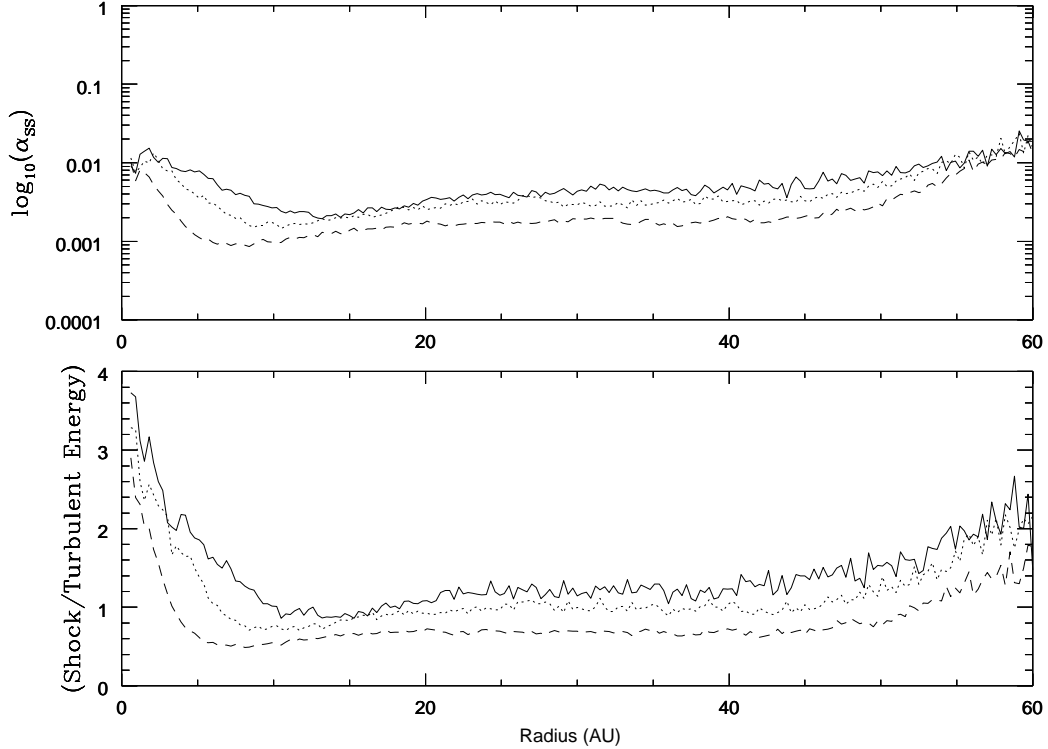


Figure 4.16 Top panel: The azimuth averaged value of α_{ss} near the end of simulations $A2lo$ (solid), $A2me$ (dotted) and $A2hi$ (dashed). Bottom panel: The azimuth averaged value of the ratio of the thermal energy generation rate due to shocks and turbulence. The outer edge of the disk has spread to >60 AU so that values are defined out to the edge of each panel.

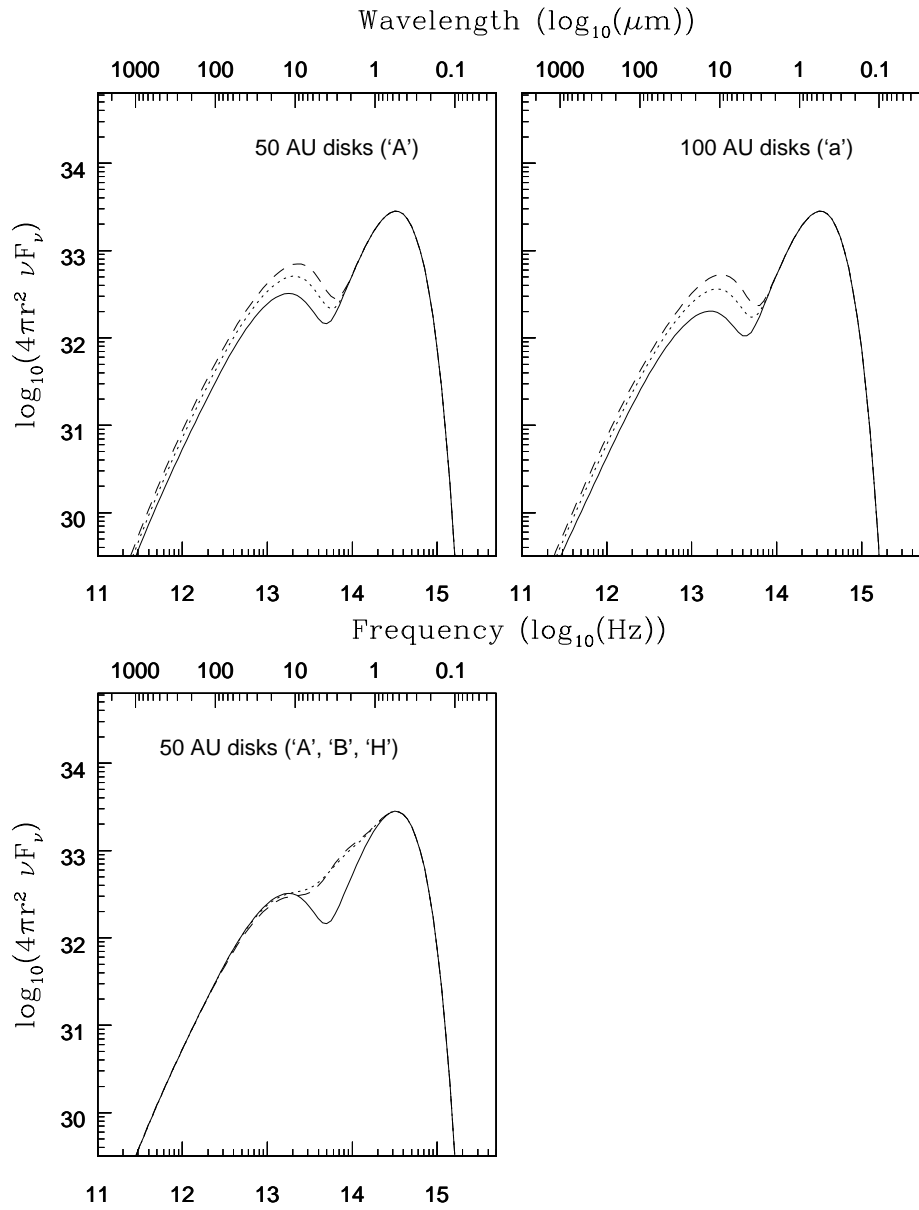


Figure 4.17 Time averaged spectral energy distributions of simulations of different resolution and with assumed disk radii of 50 (top left) or 100 AU (top right). Simulations $A2lo$, $A2me$ and $A2hi$ are designated with dashed, dotted and solid lines respectively. Similar designations define the curves for simulations $a2lo$, $a2me$ and $a2hi$. Little additional long wavelength radiation is produced in the 100 AU disks in spite of the additional surface area. The bottom left panel shows the differences between the SED's produced at high resolution but differing physical assumptions (simulations $A2hi$, $B2h3$ and $H2h3$ with solid, dotted and dashed curves respectively). The time averages are taken between $T_D=1$ and $T_D=5$ except for simulation $H2h3$, which is taken between $T_D=2.5$ and $T_D=6$ in order to reduce the effect of the transient (see fig. 4.14 above).

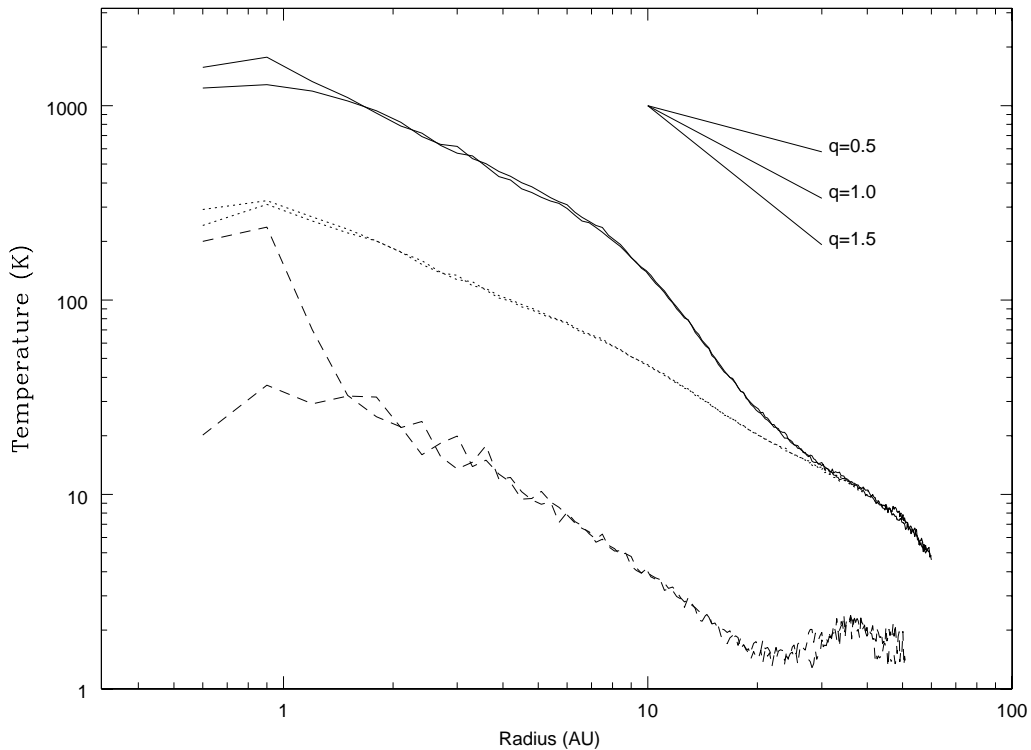


Figure 4.18 The azimuth averaged temperature structure of the disks shown in figures 4.2 and 4.11. The photosphere temperature (dotted), the midplane temperature (solid) and the rms variation of the photosphere temperature in each radial ring (dashed) are shown. Throughout most of the system, the two simulations show near identical temperature structure. In the inner disk, the midplane temperatures for the 'a' simulation differs from that of the 'b' run by about 300 K ('a' is higher than 'b'). The azimuth averaged photosphere temperatures are also quite similar everywhere, however the variation in azimuth in regions where the opacities were modified is of the same magnitude as the temperature itself, suggesting that disk matter becomes transparent intermittently on time scales shorter than a single orbit and as local conditions dictate. The lines drawn in the upper right of the figure represent a power law with index $q = 0.5, 1.0$ and 1.5 respectively.

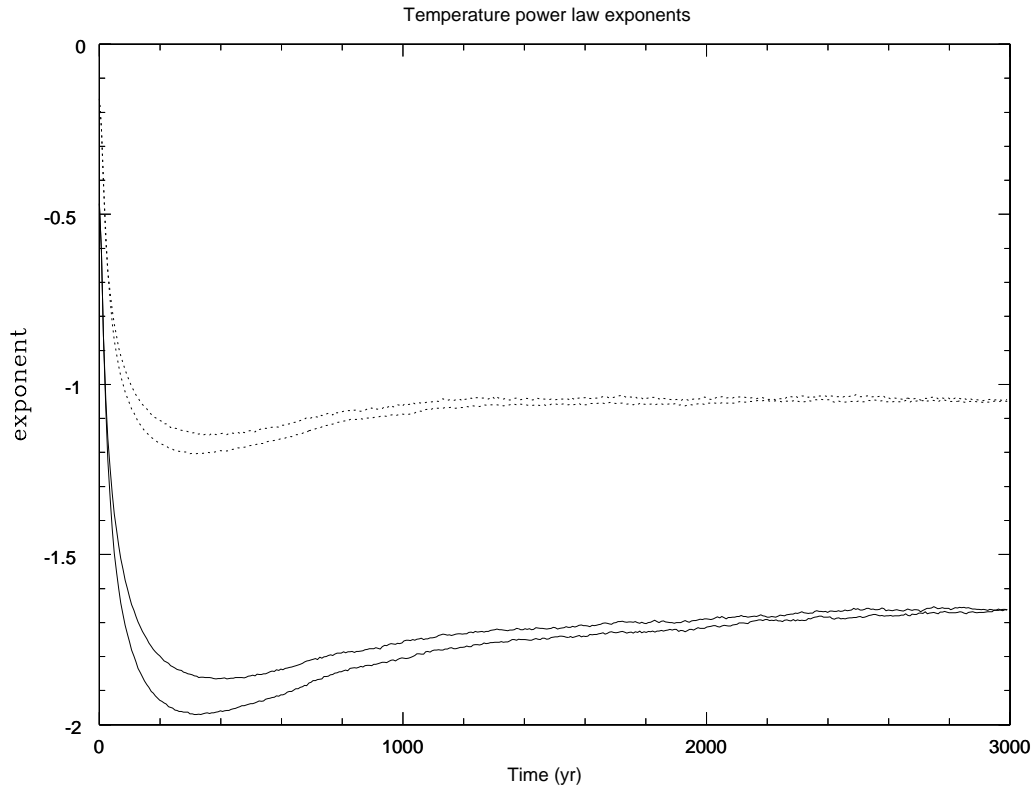


Figure 4.19 The value of the temperature power law index for the simulation shown in figures 4.2 and 4.11 as a function of time. Indices for both the midplane (solid) and the photosphere (dotted) of the disk are shown. Apart from a small difference in the initial transient behavior the fitted exponents for each of the two simulations are identical. The indices for both the midplane and photosphere are far larger than the values ($0.5 \lesssim q \lesssim 0.75$) observed in proto-stellar systems. We believe that the power law index is driven to such large values by the extreme low temperatures in the outer portions of the disk simulation, which are lower than those derived from models of observations.

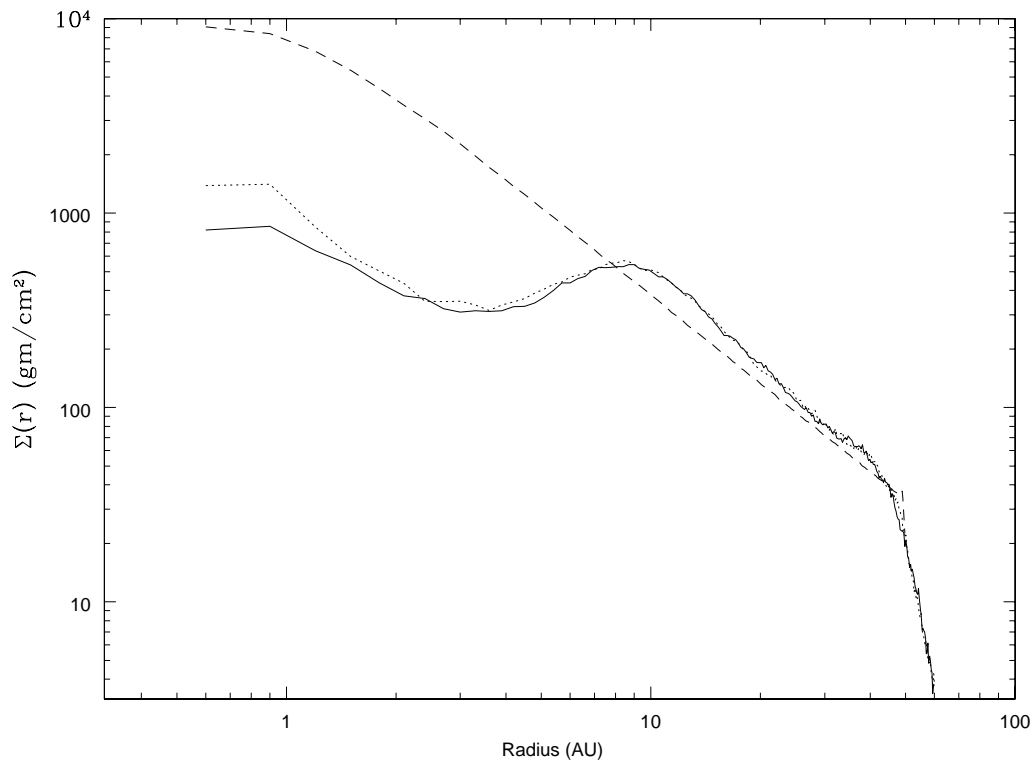


Figure 4.20 Azimuth averaged surface density of the disks in figures 4.2 and 4.11 after evolving $4T_D$ from their initial condition. In both the 'A' (solid line) and 'B' (dotted line) simulations, the inner disk rapidly becomes depleted of matter with respect to the initial profile, which increases as $r^{-3/2}$ all the way to the inner disk edge. The initial profile is shown with a dashed line.

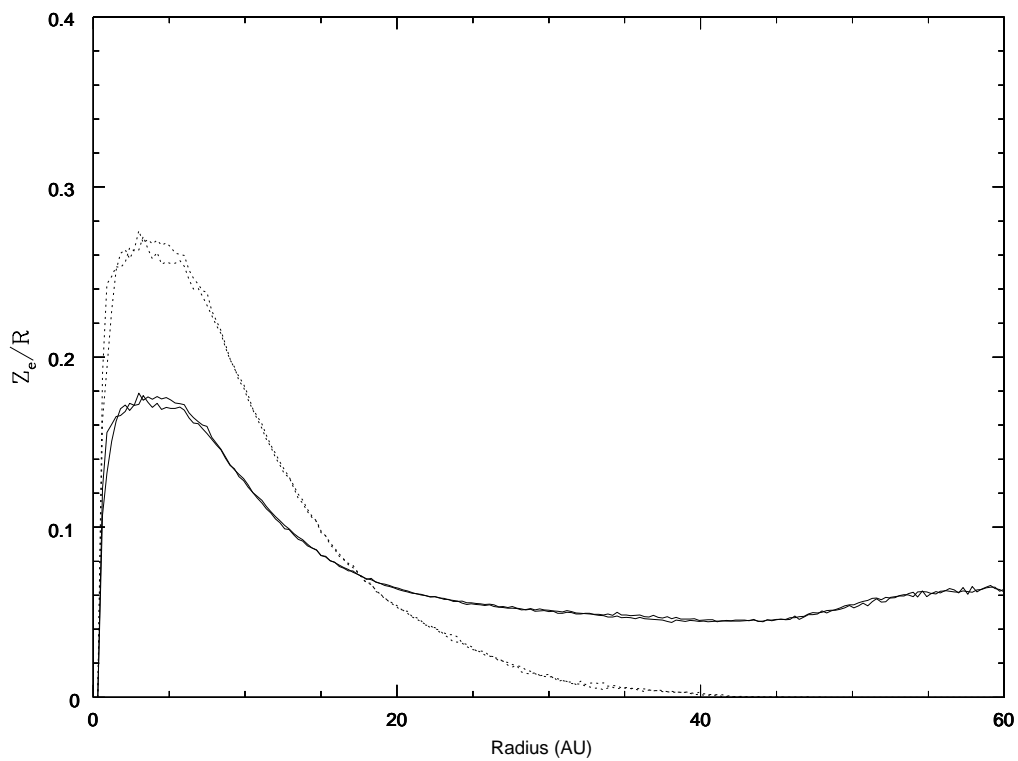


Figure 4.21 Azimuth averaged scale height, Z_e/R (solid), and photosphere altitude, Z_{phot}/R (dotted), of the disks in figures 4.2 and 4.11.

CHAPTER 5

INTERLUDE TWO

Up until this point in my thesis we've discussed objects which are chronologically very young. Circumstellar gas and dust disks, almost by definition, can't exist for very long as steady state or equilibrium objects. As we've shown in chapters 2 and 4, massive disk systems can change their appearance drastically on the scale of only a few thousand years. For lower mass disks, where the effects of self gravity are not significant, the magnitude of the viscosity becomes the limiting factor in how long the system can exist. For any realistic model of what this magnitude actually is, a disk can only live for a few million years or, at the very outside limit, a few tens of million years. As with any generalization though, there are a few cases where it doesn't quite hold true. Of particular interest are the dusty disks around β Pictoris and Vega, which are young stars quite close to the sun.

Another example of where this generalization doesn't hold true is our own solar system. The planets, asteroids, comets and assorted other debris from the formation of the solar system have been in orbit around the sun for more than four and a half billion years. Only a low level of evolution of the various bodies has occurred during that time, relative to that present during the formation of the system. There is also a tiny amount of matter remaining in a roughly spherical distribution (the so called 'zodiacal cloud'), which presumably has as its source various volatilized materials out gassed from comets. In this case, the disk exists only in 'fossil' form, or perhaps more appropriately, a circumstellar disk is an embryonic solar system. Over the first few million years of it's history we expect a disk to evolve into a more or less steady state, but not to go away completely with no trace that it was ever there. It might form clumps which ultimately evolve into planets, brown dwarfs or low mass stellar companion.

Radial velocity measurements have proven a powerful tool for finding planets in short period orbits around other stars. Using such measurements a number of planets and brown dwarfs have now been discovered in orbit around other stars. These detections have renewed interest in the limits which can be placed on the existence of companions by current and future surveys. In collaboration with Roger Angel (Nelson & Angel 1998), I have written the paper which follows in which we discuss some limits which can be placed on one method for detecting such 'fossil' disks around other stars. We have developed a simple, analytic technique to relate the detection limit obtained from a given set of data to its duration, precision and number of measurements. This technique, which is based upon least squares fitting and the periodogram, delineates regions of mass/period parameter space accessible to radial velocity observations of a given quality. We show that until a minimum of 15–20 measurements have been made, it is more efficient to make more low precision measurements than few high precision measurements. For periods longer than the surveys duration we derive an empirical correction to the sensitivity limit predicted by the analytic derivation.

We explore the effects of windowing, and also the sensitivity to periods longer than the total length of observations. We show that current observations are not yet long or accurate enough to make unambiguous detection of planets with the same mass and period as Jupiter. However, if measurements are continued at the current best levels of accuracy (5 m/sec) for a decade, then planets of Jovian mass and brown dwarfs will either be detected or ruled out for orbits with periods less than \sim 15 years.

As specific examples, we outline the performance of our technique on large amplitude and large eccentricity radial velocity signals recently discussed in the literature and we delineate the region explored by the measurements of 14 single stars made over a twelve year period by Walker et al. (1995). Had any of these stars shown motion like that caused by the exo-planets recently detected, it would have been easily detected. The data set interesting limits on the presence of brown dwarfs at orbital radii of \lesssim 5–10 AU. The most significant features in the Walker et al. data are apparent long term velocity trends in 36 UMa and β Vir, consistent with super planets of mass of $2 M_J$ in a 10 year period, or 20 – $30 M_J$ in a 50 year period. If the data are free of long term systematic errors, the probability of just one of the 14 stars showing this signal by chance is about 15%.

We then apply our technique to suggest an effective strategy for new and continuing radial velocity searches. For large surveys beginning now or proposed for the near future the factor most limiting detections is the finite amount of telescope time allocated to the search. Using this constraint, we suggest an observing strategy for future large radial velocity surveys which, if implemented, will allow coverage of the largest range of parameter space with the smallest amount of observing time per star. We suggest that about 10–15 measurements be made of each star in the first two years of the survey, then 2–3 measurements per year thereafter, provided no (or slow) variation is observed. More frequent observations would of course be indicated if such variations were present.

CHAPTER 6

THE RANGE OF MASSES AND PERIODS EXPLORED BY RADIAL VELOCITY SEARCHES FOR PLANETARY COMPANIONS

For nearly two decades most high precision radial velocity surveys of nearby stars were focused on detecting radial velocity variations in stars due to companions with mass and period of Jupiter. The signature would consist of changes in the relative stellar radial velocity with a period of a decade and amplitude of a few tens of meters per second or less, depending on orbital inclination with respect to the solar system. The surprising recent result, triggered by the discovery of 51 Peg B by Mayor & Queloz (1995), has been the finding that as many as 5-10% of solar type stars have companions with mass $< 10M_J$ and with periods less than ~ 3 years. No sub-stellar companions with periods longer than ~ 3 years have so far been detected by radial velocity searches.

Are Jupiter mass companions at longer periods rare, or is it simply the case that current observations do not have the length or sensitivity to see them? Is the theoretical prediction by Boss (1995) correct, that Jovian planets should form preferentially at >4 -5 AU separations from their primary? Our purpose in this paper is to show what we can learn from velocity data of a given duration and accuracy, to help plan continued programs.

The best measurement errors for a series of radial velocity measurements so far published are those of Butler et al. (1996), who observe a magnitude $V = 5$ star and quote an accuracy of 3 m/s for measurements taken over one year. Measurements up until this work have been limited to a lower accuracy standard of about 15 m/s. Several other programs (see section 6.5 for a list of radial velocity search programs currently underway) are planning new or expanded searches with a goal of obtaining measurements with similar accuracy. In light of these efforts, and in expectation of their eventual success in obtaining such accuracy, we shall use 5 m/s as a ‘canonical’ value for the error in many of the examples and the discussion below. Such advances in radial velocity calibration allow accuracy to be relatively free from systematic error. Poissonian photon noise remains as the fundamental limit to accuracy. In this limit, strong constraints can be placed upon the existence of periodic radial velocity signals in a given set of data, given a suitable analysis technique.

Many efforts have been made to determine whether a given set of data contains a signal. Most of those in common use are based upon the periodogram analysis techniques discussed by Scargle (1982). This technique is shown to be equivalent to a least squares fit for the signal at a given period, and he derives an exponential probability distribution of obtaining a false alarm from a given set of data. Horne and Baliunas (1986 hence HB) have refined the technique by showing that this exponential must be normalized to the total variance of the data and derived an empirical expression for the number of independent frequencies available to a set of data. Further

refinements (Irwin et al. 1989, Walker et al. 1995) account for variable weighting of individual data points and correlations between fitted parameters.

Our work represents a different approach in which, rather than dealing with least squares minimization indirectly through a periodogram analysis, we examine the best fits to the data directly and determine their significance. We derive an analytic expression for the probability that a given best fit velocity amplitude is non-random. We first develop analytical expressions relating sensitivity to planetary companions of different masses and periods, given velocity measurements of specified accuracy, duration and number. Motion with periods longer than the duration of observations is detected with reduced sensitivity, and this reduction is explored by Monte Carlo methods. We illustrate our analysis technique by application to the published set of radial velocity data from Walker et al. (1995), the longest time baseline survey so far published, with quoted precision of 15 m/s. Limiting our analysis to the subset of 14 stars which have no known visual binary companion, we obtain quantitative upper limits to companions masses for orbital periods of a few days to periods as long as 100 years. Finally, we suggest a strategy for efficiently implementing a search of a large number of stars for radial velocity signatures due to the presence of a companion.

6.1. Analysis Technique

If a companion of mass M_c exists in a circular orbit with inclination i around its primary M_* , it will perturb the radial velocity of the star as observed from earth by:

$$v(t) = \left(\frac{2\pi G}{PM_*^2} \right)^{1/3} M_c \sin(i) \sin\left(\frac{2\pi t}{P} + \phi\right) \quad (6.1)$$

$$= K \sin\left(\frac{2\pi t}{P} + \phi\right), \quad (6.2)$$

where K is the amplitude of velocity of the companion in a circular orbit around its primary, P is the period of the orbiting companion, G is the gravitational constant and ϕ is an arbitrary phase factor. If an observer can detect the small temporal changes in relative velocity due to a companion, then using fitting or periodogram techniques, it becomes possible to derive a mass (or mass limit) for that companion.

Suppose that velocity data $v(t_i)$ have been obtained in observations extending over time interval P_0 . For a given orbital period, P , we can perform a least squares fit to the data with the equation:

$$v(t) = v_s \sin\left(\frac{2\pi}{P}t\right) + v_c \cos\left(\frac{2\pi}{P}t\right) + \gamma, \quad (6.3)$$

to produce ‘best fit’ values for the components of the motion v_s , v_c and γ . At long periods and with a potential signal whose phase is unknown, the constant offset, γ , allows for the possibility that a companion at a radial velocity extremum (ie. near its maximum or minimum) is properly modeled by the fit function. For shorter periods ($P < P_0$) its inclusion or exclusion has negligible effect so we will focus initially on this domain. Given fitted amplitude coefficients v_s and v_c , a simple trigonometric identity ($K = \sqrt{v_s^2 + v_c^2}$) yields the amplitude of the stellar velocity perturbation due to the companion. From there we identify K with the leading coefficient in equation 6.1 and invert to obtain a ‘best fit’ companion mass:

$$M_c = \frac{K}{\sin(i)} \left(\frac{PM_*^2}{2\pi G} \right)^{1/3}. \quad (6.4)$$

Fitting higher order harmonics would be used to refine the fit and recover information about the orbital eccentricity of a companion.

The orbital inclination remains an unknown parameter in a set of radial velocity data. Statistically speaking however, the average companion mass of a set of systems randomly oriented in space which give amplitude K will be:

$$\langle M_c \rangle = \int_0^{\pi/2} M_c \sin(i) di = \left(\frac{PM_*^2}{2\pi G} \right)^{1/3} \int_0^{\pi/2} \frac{K}{\sin(i)} \sin(i) di \quad (6.5)$$

$$= \frac{\pi}{2} K \left(\frac{PM_*^2}{2\pi G} \right)^{1/3}. \quad (6.6)$$

Thus the average value for a companion mass is $\pi/2$ times the directly derived $M_c \sin(i)$ value. Conversely, a companion with some mass will appear on average a factor of $2/\pi (\approx 0.64)$ less massive than its true value. Very large masses cannot be ruled out but do become increasingly improbable, with the probability that a given mass, M , is exceeded being given by the formula:

$$\mathcal{P}(M_c > M) = 1 - \sqrt{1 - \left(\frac{M_c \sin(i)}{M} \right)^2} \quad (6.7)$$

For example, while values of the companion mass will be greater than twice $M_c \sin(i)$ for 13% of a large sample, the chance of a mass being greater than $10M_c \sin(i)$ are only 0.5%. The true companion mass will exceed $2/\sqrt{3} (\approx 1.15)$ times the measured $M_c \sin(i)$ value in 50% of cases.

6.1.1. Probability of a given velocity amplitude being exceeded by chance

In the absence of an unambiguous detection of a signal at some period, we are faced with the question of whether a particularly large fitted velocity amplitude at some period represents a real detection. Such spikes will occur, because the data are noisy, and the frequency analysis must be taken over a large number of possible periods (from a few days to many years). Adjacent fitted periods may have widely different best fit velocity amplitudes even when the data have no embedded signal. What criterion can we apply to tell if a spectral peak is improbably large compared to these noise spikes? More generally, if the data for a star are analyzed in some way, what is the probability that a given outcome would have occurred by chance? In this section we obtain an analytical expression for the velocity amplitude (and hence companion mass) that will be exceeded by chance, with a given probability and in a given frequency range.

Suppose that in a given set of velocity measurements $v(t_i)$, there is no real signal and that each measurement is drawn from a Gaussian distribution with mean zero and standard deviation σ_p . The data can be fit to eqn. 6.3 to produce coefficients of some amplitude (v_s, v_c) . With no true signal, both v_s and v_c will be normally distributed about zero with standard deviation $\sigma_s = \sigma_c = \sigma$ and the phase of the fitted curve will be uniformly distributed. For a set of n_0 measurements, taken randomly over a time period P_0 , this assumption leads to the expression:

$$\sigma = \sqrt{\frac{2}{n_0}} \sigma_p. \quad (6.8)$$

where factor $\sqrt{2/n_0}$ is derived from the least squares error analysis (see eg. Bevington and Robinson (1992) ch. 7) fitting a periodic signal to random noise.

The probability of any data set with zero expectation value for v_s and v_c to have any particular fit values is:

$$p(v_s, v_c) = \frac{1}{2\pi\sigma_s\sigma_c} e^{\frac{-v_s^2}{2\sigma_s^2}} e^{\frac{-v_c^2}{2\sigma_c^2}} dv_s dv_c. \quad (6.9)$$

which, converted to amplitude and phase gives:

$$p(K', \phi) = \frac{1}{2\pi\sigma^2} e^{-\frac{K'^2}{2\sigma^2}} K' dK' d\phi. \quad (6.10)$$

If we integrate this probability over all ϕ and from zero¹ to some value K , we get the total probability, \mathcal{P} , of a fit with velocity amplitude K or smaller:

$$\mathcal{P} = 1 - e^{-K^2/2\sigma^2}. \quad (6.11)$$

This probability applies to analysis of any single period. In practice we are interested in the probability of a velocity amplitude being exceeded by chance in a range of periods. If we assume that the probability of a given fit at one period is independent of every other period, then for N periods the probability, X , that no fit value exceeding a value K_X will occur is the product of the individual probabilities $X = \mathcal{P}^N$, which to leading order gives

$$X = \left(1 - e^{-K_X^2/2\sigma^2}\right)^N \approx 1 - Ne^{-K_X^2/2\sigma^2}. \quad (6.12)$$

Higher order terms in the right hand equation converge to zero as progressively higher power exponentials. We can invert this equation to derive a limit on the velocity as:

$$K_X = \sqrt{-2\sigma^2 \ln \left(\frac{1-X}{N} \right)} \quad (6.13)$$

which expresses the velocity amplitude which will be exceeded by any of N fits to random data in a given period range with probability $1-X$.

The appropriate number of independent periods is related to the width of peaks in the frequency spectrum given by $df=1/P_0$. To be certain of sampling at a frequency that is close to the peak, we suppose that the sampling is made at frequency intervals $df = 1/(2\pi P_0)$. The number, N , of independent frequencies (or periods) in a given range is then given by:

$$N = 2\pi \left(\frac{f_1 - f_2}{f_0} \right) \quad (6.14)$$

where f_1 and f_2 are the limiting frequencies of the range bounded by periods P_1 and P_2 and $f_0 = 1/P_0$.

Finally, combining eqns 6.8, 6.13 and 6.14 we obtain an expression in terms of the accuracy σ_p , duration P_0 , the number of measurements n_0 and the probability X that a velocity amplitude K will be exceeded in a given frequency range:

$$K_X = 2\sigma_p \sqrt{\frac{1}{n_0} \ln \left(\frac{2\pi P_0 (f_1 - f_2)}{1-X} \right)}. \quad (6.15)$$

The value K_X varies directly with σ_p and varies with the inverse root of n_0 , as we would expect from the central limit theorem. Its sensitivity to the other parameters and our sampling

¹For comparison, the integrated probability for a normal random variable is given by:

$$\mathcal{P} = \frac{1}{\sqrt{2\pi}\sigma} \int_{-K}^K e^{-K'^2/2\sigma^2} dK'.$$

assumptions depends on the details of the survey, but in general we will find that the factor inside the natural logarithm is much greater than 1, so that a factor 2 change in any of the arguments produces only a small fractional change in the value of K_X .

As an example, suppose that a high quality survey were made over a decade, with a total of $n_0 = 50$ observations per star and with rms accuracy, $\sigma_p = 5$ m/s. For a false detection in a one octave range around $P = 4$ days, the velocity amplitude K_X from eqn. 6.15 is 5.2 m/s. At 4 years, the amplitude is 3.9 m/s. If the star's mass is the same as the sun's, then from eqn. 6.4 we find these velocities for 1% false detections will correspond to companions masses $M_c \sin(i)$ of 0.04 and 0.22 Jupiter masses respectively. In practice, if a large number of stars are to be sampled, say 100, and we would want a small probability of a false detection in the sample, say 10%, then we would want to decrease the probability to 10^{-4} per octave per star. In this case, the mass limits increase to 0.047 and 0.28 M_J for each range. The small increase of only some $\sim 25\%$ is due to the fact that the argument of the natural logarithm in eqn. 6.15 is near 20 for this case.

6.2. Monte Carlo Analysis

Eqn 6.15 will fail for periods longer than the span of observations P_0 , under conditions in which the data collection is periodic, or if the total number of observations n_0 is too small. This is because the windowing may imprint its own signature upon the derived best fit parameters and the assumption that random data are fitted with random phase breaks down. We devote this section to a Monte Carlo analysis of synthetic radial velocity data, in order to understand the regimes in which our analysis may fail and the manner of its failure. In this way we can eliminate false detections and establish the validity of a trend in the data consistent with a true periodicity.

For our numerical experiments we assume radial velocity data are gathered for either 6 or 12 years. These data are spaced randomly in time subject to the constraints that data be 'gathered' during the same 6 month period of each year, that they be gathered only during 1/2 of each 29.5 day lunar cycle and that they be gathered only at 'night'. We run a grid of nine Monte Carlo experiments varying the frequency of observation over 1, 5 and 20 observations per year and the precision for each measurement over 5, 15 and 30 m/s.

We set velocities corresponding to the time of each observation using a Gaussian random noise term and the input error as:

$$v_{\text{sim}}(t_i) = Rv_{\text{err}}(t_i) \quad (6.16)$$

with R the random noise term and v_{err} is the error for each point. The value for v_{err} is assigned as noted above. We use the pseudo-random number generator 'ran2' provided by Press et al. (1992) and the rejection method to create Gaussian random numbers. In the analysis that follows, we fit a total of 3000 data sets for the amplitude components v_s , v_c and γ for each star over period ranges from 3 days to 100 years. The boundaries of each period range are defined in table 6.1. We increase each successive fitted period by an amount such that the total number of orbital cycles over the full observation length decreases by $1/2\pi$ (1 radian) as in the analysis above or the period increases by 1/5 year, whichever gives the smaller interval. The chance of any particular outcome is given by the fraction of the synthetic data sets with that outcome.

6.2.1. Confirmation of the Analytical Results

For the subset of experiments with assumed 5 m/s precision, figure 6.1 shows the radial velocity amplitude for each fitted period which is exceeded in 1% of the Monte Carlo trials, ie. there is a 99% probability that a specific period analyzed will not exceed this value. Experiments with higher or lower assumed precision produce limits scaled upward or downward on the plot

but otherwise show the same qualitative features. Also included are the $N = 1$ limits provided directly by eqn. 6.13. In general, the Monte Carlo results confirm the validity of the analytical results above. The difference between $N = 1$ analytic and Monte Carlo results varies about 2%, consistent with statistical fluctuations, except at the assumed windowing periods and at periods longer than P_0 . The analytical prediction for the experiment with the most sparsely taken data (1 measurement per year for 12 years) lies some $\sim 15\%$ below the Monte Carlo result for periods less than 2 years, but agrees to $\sim 2\%$ over the remainder of the valid period regime.

A comparison of the limits provided by the analytical (eqn. 6.15) and Monte Carlo methods for each period range noted in Table 6.1 are also shown in figure 6.1. The assumed windowing periods are masked out of each of the Monte Carlo limits and the results represent limits based on the remaining portion of each range. In general, the Monte Carlo results again confirm the validity of the analytical result to within a few percent, with the exception of the series with only one measurement per year. In that case, the Monte Carlo experiment produces limits which are some 50% or more larger than eqn. 6.15 predicts.

We consider in turn in the sections below the differences between the analytical derivation and the Monte Carlo results due to the long period fall off in sensitivity, due to small numbers of observations, and due to the inherent windowing in the data.

6.2.2. Loss of Sensitivity at Long Periods

The results shown in figure 6.1 show that at periods longer than the 12 year window the sensitivity to a velocity signal drops off in very nearly power law form. In light of this behavior, we adapt an *ad hoc* prescription for the velocity limit using the eqn. 6.15 result at short periods and a power law at longer periods as

$$\hat{K}_X = \begin{cases} K_X & \text{for } P < \beta P_0; \\ K_X \left(\frac{P}{\beta P_0}\right)^\alpha & \text{for } P > \beta P_0; \end{cases} \quad (6.17)$$

We then fit for the free parameters α and β and thereby recover limits for periods much longer than that of the observing window. In this equation, we assume that the value of K_X used for long periods ($P > \beta P_0$) is that defined by the last period range prior to the onset of the fall off. This assumption ensures a smooth joining of the two regimes.

We fit the Monte Carlo results for the constants α and β in eqn. 6.17 for each of the experiments and plot their values in figure 6.2 for both the six and twelve year observing windows studied. The fitted values for the 12 year window are typically:

$$\alpha \approx 1.86$$

with the turn off in sensitivity beginning between

$$1.4 \leq \beta \leq 1.45$$

for the 99% probability curve and similar values for the 99.9% probability curve. A slightly steeper power law exponent ($\alpha \approx 1.92$) is found for a 6 year window. If we err on the side of caution and assume that the turn-off occurs at the *small* end of the range (by setting $\beta = 1.3$, for both the 99% and 99.9% probabilities), then we provide slightly more conservative limits than the best possible based on our Monte Carlo analysis. Under this assumption, we have included in figure 6.1 the long period fits for the velocity limits placed upon the data by eqn. 6.17, and the shorter period limits for 11 period ranges less than 1.3×12 years.

6.2.3. Limits of Sparse Data

When a data set contains only a few measurements, a least squares analysis will depend strongly upon the measured value and placement in time of each measurement. How many data are needed to assure that the random data/random phase assumption is reliable and we are able reproduce the results of equations 6.13 (with N set to unity) or 6.15 (for octave period ranges)? Is there a difference in the number of measurements that must be made if we assume a strategy of taking, say, one or two measurements per year over a long period or taking several measurements per year but over a much shorter baseline?

Taking the first strategy, we assume the data are gathered over a 6 year span with an error in each measurement of 5 m/s. If a star is observed with a frequency of one observation per year, we find (figure 6.3) that the eqn. 6.13 limits with $N = 1$ underestimate the Monte Carlo results by more than a factor of two for periods shorter than 1 year, and by a smaller margin at all periods. The same experiment with a 12 year span shown in figure 6.1 shows a much smaller ($\sim 15\%$) difference. Increasing to three observations per year for 6 years the analytic equation underestimates the limits by $\sim 10\%$, while 5 measurements per year duplicates the analytic results to 5% or better.

For octave sized ranges, the analytical and Monte Carlo results converge somewhat more slowly. Figure 6.1 shows that a single measurement per year over 12 years is sufficient only to provide limits a factor of two higher than would be predicted analytically for periods less than 2 years. When data are gathered at the higher rates shown (5 and 20 obs/yr), the agreement is excellent. An experiment with two measurements per year (not shown), for a total of 24 measurements, is sufficient to recover the analytical form to $\sim 10\%$ in all period bins. With the six year baseline shown in figure 6.3, agreement at the $\sim 20\%$ level is reached if three measurements per year (18 total) are taken.

Taking the second strategy, we assume data are gathered over a two year window. We do not believe we can rely upon octave range limits for such a short data gathering period because of the large effects of windowing, which we discuss below. The long period fall off is similarly affected. We therefore limit our discussion for these experiments to limits for individual periods, shorter than about one year. With a two year data window and a total of 6 measurements (three measurements per year), we again find (figure 6.4) that the Monte Carlo limits exceed those of eqn. 6.13 with $N = 1$ by more than a factor of two. Increasing to 6 measurements per year (12 total), we lose only 15% of the maximum sensitivity for $N = 1$, while 12 measurements per year (24 total) recovers the analytic results with only a $\sim 5\text{-}7\%$ difference.

In order to obtain limits which retain the benefits of a given precision to within 15% at any single period, we find that at least ~ 12 or more observations of a star must be made. This number of observations produces limits a factor of two larger than predicted over octave ranges. To reduce the difference to $\sim 5\%$ for a single period and 15% over octave ranges requires at least 18-20 measurements. Barring windowing effects, these minimum requirements do not seem to depend strongly upon the time span over which the data were gathered, but only upon their accuracy and number.

6.2.4. Windowing

Sensitivity loss of a factor of two or more is present in ‘blind spots’ for any single period near the assumed lunar and annual windowing periods for every experiment performed. There are also double period counterparts and beat periods between the lunar and annual data windows, though lower sensitivity loss is evident there. Day/night windowing effects are not visible in the limits due to their extreme short periodicities. When the data are sparse and the data are gathered over

a short period P_0 , the effects are especially pronounced. Figure 6.4) shows that for a period P_0 of two years, the lunar windowing effects are observable not only at the lunar orbital period, but also at the double, triple and quadruple period aliases. Additionally, fitting for the long period turn-off becomes of little use because the turn-off occurs at a period with lower sensitivity than can be modeled analytically.

Based on these results, we suggest that the limits which can be placed on signals at periods corresponding to a lunar or annual windowing period cannot be reduced beyond a factor of two greater than that given by eqn. 6.13 with N set to unity at a windowing period or a factor of $\sim 3/2$ at one of its double or beat period counterparts.

6.3. Comparison to Periodogram Techniques

To obtain definitive probability that a signal that been detected at some period is nonrandom, nothing less than a full Monte Carlo analysis is adequate. For a large survey which is continually updated as more data are gathered, such analysis is unfeasible because of the considerable commitment of computational facilities to perform a statistically meaningful analysis. Even for the computers of today, a sample of 500 stars might prove unmanageably burdensome. To reduce the effort required per star, either periodogram or fitting techniques such as ours may offer a lower cost alternative. We will now make a comparison of our technique to periodogram techniques in common use.

Each technique is based upon a χ^2 analysis of the data. Indeed, for equally weighted data least squares analysis and periodogram analysis have been shown (Scargle 1982) to be equivalent. The main difference lies in the fact that on the one hand, a periodogram utilizes a normalized measure of the power of the signal at some period while our technique relies directly on the value of the best fit velocity amplitude. Additionally, with the present analysis, we allow the data to be fit with unequal weights, though the amplitude limits derived are based upon only upon equally weighted data.

Let us examine the least squares fitting procedure and, for purposes of illustration, limit ourselves to the case of fitting for only the coefficients v_s and v_c in eqn. 6.3. In this case, the best fit coefficients derived from the χ^2 minimization at some frequency $\omega = 2\pi/P$ for a set of n_0 velocity measurements, v_i , are:

$$v_s = C_{ss} \sum_{i=1}^{n_0} \frac{v(t_i) \sin \omega t_i}{\sigma_i^2} + C_{sc} \sum_{i=1}^{n_0} \frac{v(t_i) \cos \omega t_i}{\sigma_i^2} \quad (6.18)$$

and

$$v_c = C_{cs} \sum_{i=1}^{n_0} \frac{v(t_i) \sin \omega t_i}{\sigma_i^2} + C_{cc} \sum_{i=1}^{n_0} \frac{v(t_i) \cos \omega t_i}{\sigma_i^2} \quad (6.19)$$

where the subscripted C terms are the four components of the covariance matrix used to derive the fit (see for example Press et al. 1992 ch. 15.4 for a discussion). When these terms are combined to form the velocity amplitude K as $K = \sqrt{v_s^2 + v_c^2}$ and data are translated in phase by a value $\tau = \tan^{-1}(v_c/v_s)$ (derived by setting $C_{cs} = C_{sc} = 0$) then, as was shown by Lomb (1976), the square of the best fit velocity amplitude, K^2 , becomes the unnormalized power of the periodogram at that period. With the identification of K^2 with the periodogram power, we note that false alarm probabilities are given in each case is given as an exponential of K^2 , with a normalization given by the variance, σ^2 , of the data.

The use of the velocity amplitude rather than a normalized measure of its square represents an improvement to existing techniques for several reasons. First, a physically meaningful limiting

velocity amplitude (or equivalently, a companion mass $\times \sin(i)$) is explicitly a part of the definition of the probability. A potential weakness of this method is that because it utilizes amplitude as a figure of merit rather than power, its dynamic range is more compressed on a given plot. A single dominant peak will not stand out to nearly the extent that occurs in a periodogram. In spite of this somewhat minor defect, we submit that a best fit amplitude is a far more useful quantity to an observer than is the power.

In sections 6.2.3-6.2.4 we have outlined the regimes for which our analysis is valid and the manner in which it fails for sparse or windowed data and for very long periods. Because of the similar origins of our analysis and periodograms we expect that similar failure modes also apply to periodograms. Hence probabilities derived from sparse data ($n_0 \lesssim 10 - 15$) and at ‘windowed’ periods such as the annual cycle using a periodogram will yield erroneous results. Extensions to standard periodogram techniques (Irwin et al. 1989 and Walker et al. 1995) which explicitly account for unequal statistical weights and correlations between fit parameters may provide more accurate limits than our eqn. 6.15 in such regimes.

Our extensions to long periods explicitly provide limits on the amplitude of the signal (and therefore $M \sin(i)$) possible at any given period at least 10 times as long as the data window. The limits account for the fact that a long period signal may in fact be near an extremum during the time over which most or all of the data were gathered.

Both techniques may be used to determine the probability of a signal being nonrandom for a single period, for a period range or over all independent periods. The Scargle (1982) and HB false alarm probability generates the probabilities, in the ideal case, by requiring a Monte Carlo analysis to specify the number of independent periods, N . Their analysis to determine N is limited to sampling frequencies below the Nyquist limit however. With unevenly sampled data, it is well known that higher frequencies are accessible without aliasing. How far above the Nyquist limit a signal can be detected and how many additional independent frequencies (if any) are required remains unknown.

We also require a specification of the number of independent periods, however our analysis uses a definition of the number of independent periods (not equivalent to the HB definition) based only upon the width of a spectral peak. We make no distinction between potentially aliased spectral peaks at high frequencies and those found at lower frequencies. The excellent correspondence between our analytical formalism and our Monte Carlo analysis for each period range shows that the definition of N made in eqn. 6.14 is reasonable. The functional dependence of the amplitude limit on N is quite weak, going only as $\sqrt{\ln N}$. When N is large, as is the case for the shortest period bins, our definition will yield slightly more conservative (higher) limits than the comparable HB limits, while for longer periods when $N \lesssim 100$, our limits may be somewhat lower.

6.4. Application to Real Data

In this section we apply our analysis technique to data for two stars obtained by Mayor and his collaborators at the Geneva Observatory, data obtained by Marcy et al. (1997) for the star 51 Pegasi, and to the data obtained by Walker et al. (1995) in their 12 year search for extra-solar planets. The Walker et al. radial velocity data are for a set of 21 stars with data taken over a 12 year period from 1980-1992. The data used in our analysis were originally archived at the Astronomical Data Center (URL <http://hypatia.gsfc.nasa.gov/adc.html>) by Walker et al. upon publication of their work. We limit our analysis to the subset of 14 stars for which no visual binary companion is known, shown in Table 6.2. For these stars, no other periodic radial velocity signatures which could obscure a planetary signature are present, and no significant periodicities

attributable to planetary companions were found by the Walker et al. search.

Using equations 6.4 and 6.15 we can derive for any period (or period range) of interest the limit below which random data is fit with probability X to be:

$$M_c = \frac{\hat{K}_X}{\sin(i)} \left(\frac{PM_*^2}{2\pi G} \right)^{1/3} \quad (6.20)$$

where we assume the orbital period, P , is at the midpoint of some range of periods shorter than βP_0 or that $P > \beta P_0$. This mass limit depends upon both the velocity amplitude limit K_X , which changes slowly, and also the period for which we fit the data. The minimum mass detectable by a set of measurements increases only as the cube root of the period at short periods, but for $P > \beta P_0$, this dependence becomes much steeper, increasing faster than P^2 .

Once we have mass or velocity amplitude limits for a set of data, we can define quantities M_{99} and M_{999} via eqn. 6.20 as the mass exceeded by chance by a fit at the 1% and .1% level of probability in each period range. For a sample of radial velocity measurements of say 10 stars observed for 10 years divided up into 10 period ranges, these values are of interest because if there are no true periodicities in the data, we would expect to find by chance one apparent planet with best fit mass $M > M_{99}$, but to find a mass greater than M_{999} with only $\sim 10\%$ probability.

6.4.1. Determining the Measurement Uncertainty

In order to obtain a value of σ_p for use in eqn. 6.15 or 6.20, we assume that no strong periodic signals are present in the data and that each datum is drawn from the same statistical distribution. Then we may use the rms scatter of all the data for a star as an empirical measure of the error, σ_p , for each measurement of that star. For data in which no clear signal is observable, this measurement of the error will give a more reliable estimate of the true value than from internal estimates. In Table 6.2, we show both σ_p as derived directly from the data as well as the average of the internal errors for each star (σ_i) quoted by Walker et al.

6.4.2. Detecting Large Amplitude and Large Eccentricity Signals

In this section we show that our analytic technique is capable of detecting large amplitude signals and signals with high eccentricity. As an initial test we obtained the data for the original discovery of the companion to 51 Pegasi, taken by Mayor and his collaborators at the Geneva Observatory. These data consist of the original 35 measurements as published by Mayor and Queloz (1995) as well as their observations of the star since that time. The total number of observations used in our analysis was 89 radial velocity measurements made over 2.4 years with internal errors of 15 m/s. The value for σ_p was obtained from the rms scatter of all of the velocity measurements and was $\sigma_p = 44.5$ m/s. An independent set of measurements (Marcy et al. 1997) was also used to compare the technique using higher precision data. A total of 116 measurements are characterized by an rms scatter of $\sigma_p = 40.6$ m/s and were gathered over a total time span of 325 days with internal errors of 5 m/s.

We show the results of these two tests in figure 6.5. For each set of measurements, we detect a clear peak in the best fit velocity amplitude at a period $P = 4.23$ days, as expected. For the Mayor and Queloz data, we also detect a number of side lobes peaks which represent the radial velocity signal ‘beating’ against other periodicities in the data such as the 29.5 day lunar cycle (the data were taken predominantly during the same half of each lunar cycle). The Marcy et al. data show one 99% significant peak just shortward of one year. We consider this peak to be an artifact of the short time baseline of their data (less than one year) and do not consider it very significant.

A second 99% significant period is detected at 23.84 days in the Mayor and Queloz data. We have re-analyzed the residuals of the measurements (with the 4.23 day periodicity removed) and found that the peak remains and so cannot be attributed to an alias of 4.23 day periodicity. Is it an artifact of the rotational period of the star itself? We note that the period is roughly in a 2:3 ratio to the observed 37 day rotation period for 51 Peg (Baliunas, Sokoloff & Soon 1996). We suspect that with the incomplete phase coverage for periods near 24 and 37 days, the stellar rotation period may be aliased to the observed 23.84 day period. Only complete phase coverage may be able to determine the origin of this signal.

The independent radial velocity observations of Marcy et al. do not show a similar periodicity and the precision of their measurements is only half the best fit amplitude from the Geneva data. In their work more than 3/4 of the data were gathered in less than two rotation periods of the star. In such a case, it is unclear whether a rotation signature would be observable in Doppler spectroscopy data.

As a second test, we obtained another set of radial velocity data from Mayor. In this case the data were obtained under the condition that the identity of the data and whether they contained a signal not be disclosed until the conclusion of the test. These data consisted of 45 measurements taken with the CORAVEL spectrometer with internal errors of 300 m/s. The data were gathered over \sim 15 years and the value for σ_p obtained from the rms scatter in the velocity measurements and was $\sigma_p = 800$ m/s.

The best fit velocities and the corresponding 99 and 99.9% probability limits for the fits are shown in figure 6.6. In this case, we were unable to detect a significant periodicity in the data except a possible long term signal near 15 yr. The data show no obvious periodicity in the velocities for orbits of \sim 15 yr, but do show that several measurements are some 3–5 σ away from the mean of any other velocity measurements of the star. These data were gathered within 6 days of each other in the fall of 1996.

To test the effect of these data we deleted them from the sample and reapplied our analysis. In this case, the rms scatter was reduced to $\sigma_p = 480$ m/s and n_0 to 40 while the duration of the measurements P_0 remained the same. Figure 6.7 shows the results of this reanalysis. In this case a peak in the best fits for a circular orbit, well above the 99.9% probability curve, becomes visible at 275 days. With the detection of this peak, we concluded our test and obtained the identity of the star from which the observations were taken. The star from which the data were obtained was HD 110833, for which Mayor et al. (1996) published an orbital solution with a best fit companion mass $M \sin(i) = 17 M_J$, a period of $P = 270$ days and an orbital eccentricity $e = 0.7$ using data from both the CORAVEL and ELODIE spectrometers. The difference in the period derived from our analysis and the Mayor et al. fit is due to the inconsistency between the high eccentricity of the companion and assumption made in our analysis that the orbit is circular.

In discussions with M. Mayor and D. Queloz, several issues were brought forward. First, the data from the fall 1996 run may have been faulty due to a combination of several factors, including a slight misfocusing of the telescope or a temperature instability in the spectrometer itself. However, while the measurements in question are unusually distant from the mean of the other measurements for that star, they were gathered during a single periastron passage of the companion and therefore may not contribute as strongly to the detection of the periodicity as they would otherwise. A fit for the set of orbital elements would then yield a higher eccentricity than is truly the case.

This case may therefore expose a degeneracy between results using data derived from a companion which is truly in a highly eccentric orbit and data with possible systematic biases. Our technique is based upon only the lowest order Fourier components of the signal (i.e. a

circular orbit) and does not account for eccentric motion. The fact that so many data (5 of 45 measurements) were so far from the mean and that they were from the same observing run suggests that removing the data from that run from our analysis is justified. Omitting them, we are able to recover a strong periodicity near the best fit period for the orbital solution.

With the results from this section we can be confident that our analytic technique is capable of detecting signals with large amplitude and/or large eccentricity.

6.4.3. Masses from Best Fit Velocities of the Walker et al. Sample, and Analysis of Significance

We have shown that our analytic technique is capable of detecting large amplitude periodicities in radial velocity data. In this section we move to lower amplitude signals and upper limits to companion signatures. For each star in the Walker et al. sample, best fit velocities for periods between 3 days and 100 years were determined by the least squares method using eqn. 6.3. Statistical weights for each datum were taken to be $1/\sigma_i^2$, where σ_i is the quoted internal error for each point as given by Walker et al. Plotted in figure 6.8 are the corresponding companion masses $M_c \sin(i)$ obtained from eqn. 6.4 using the stellar masses from table 6.2. In order to determine the significance of any particular best fit value we compare the best fit mass for some period to the limit provided by our analytical analysis and to Monte Carlo experiments similar to those described in section 6.2 for synthetic data. Each of these limits are shown in figure 6.8.

While as expected from the results of the original analysis of Walker et al., there are no clear cut companion signatures, in several cases the data produce statistically significant fits. We tabulate each of these periods in table 6.3. Are any of these signatures due to the existence of a companion? Stellar processes such as pulsation, rotation or magnetic cycles can affect the measured radial velocity for a star and in many cases it is quite possible to fit such signals with orbital solutions. Early in this century for example (see eg. Jacobsen 1925, 1929), the radial velocity variations of Cepheid variable stars were fit with Keplerian orbits. Although today no one would attribute Cepheid radial velocity variations to a companion, the principle that processes intrinsic to the star must be eliminated from consideration remains if we are to be certain that a given radial velocity detection is definitely due to a companion.

Many of the signals in table 6.3 do in fact correlate with known periodicities due to stellar rotation or magnetic cycles in the star. For example, we find a $>99.9\%$ significant ~ 10 yr period in ϵ Eri and two short period signals (at 11.9 and 52.5 days) with $>99\%$ probability. Walker et al. establish that the 10 year and 52 day peaks are aliases of each other and McMillan et al. 1996 have definitely connected this periodicity to a stellar magnetic cycle. Gray and Baliunas (1995) have observed an 11.1 day periodicity in the Ca H&K S-index with an extensive data set. They comment that subsets of their data taken during different observing seasons produce peaks varying in period from 11 to 20 days. We conclude that we are seeing a comparable effect in the Walker et al. radial velocity data and are in fact detecting the rotational signature of the star.

Further work by the same group (Gray et al. 1996) on the star β Com provides evidence of a magnetic cycle. However their measurements have sufficient duration only to have observed a minimum, and a period is not known. Figure 6.8 shows that for β Com the probability that the best fit velocity amplitude is not random exceeds 99% for periods near 10 years. Assuming a 10 year period, we calculate that the best fit radial velocity curve went through its minimum in 1988/1989, which is coincident with the photometric and Ca H&K minimum observed by Gray et al. (1996). Significantly, the radial velocity minimum is not coincident with the velocity span minimum derived from their line bisector analysis.

The star η Cep shows $>99\%$ significant periodicities at $P = 164$ days and ~ 10 yrs. Walker

et al. have speculated that the 164 day periodicity was due to stellar rotation. No periodicities are detected in line asymmetry to ~ 19 m/s by Gray (1994) with measurements spanning four years. However we find the best fit radial velocity amplitude at each of these periods is only 16 and 13 m/s respectively. If a direct correlation between a radial velocity measurement and a line bisector measurement exists, such signals would be below his detection limit. By analogy to ϵ Eri, we speculate that the 10 year periodicity in η Cep might be linked to a magnetic cycle, but we cannot be certain of its origin.

Other marginal periodicities appear in the data for HR 8832 and θ UMa. Again by analogy to other stars, in this case ϵ Eri and η Cep, we might speculate that these shorter periodicities are due to stellar rotation, however no certainty can be attached to their origin.

We also find that two stars in the subset (36 UMa and β Vir) show best fit minimum masses which, for fitted periods longer than ~ 12 years, rise above the curve for which the best fits are random with 99% and 99.9% probability. Walker et al. find similar trends in these stars but make no firm conclusions based upon their analysis. Are these signals indications of long period companions, or are they also due to stellar effects? We show the data for these stars in figure 6.10, both raw and binned by year. While the raw data show no obvious signals, the binned data, particularly for 36 UMa, show some indication of a partially complete sinusoid. We note that in both cases, the curvature in the velocity trends is of the same sign and the portion of the sinusoid is similar, which suggests a long term calibration error. However, the binned data for all stars taken together shows no such trend so a systematic explanation seems less likely.

6.4.4. A Check by Monte Carlo Analysis

Each of the stars in the Walker et al. sample average 3-5 measurements per year over the 12 year period and, according to the results of section 6.2.3, this number should be sufficient for application of our analytic apparatus. We note however, that implicit in our analytical derivation of mass limits is the assumption that the measurements be at least somewhat regularly distributed. In the case of the Walker et al. data, this is not always the case. The data are irregular on both short time scales (ie. 3 night runs consisting of 1-3 velocity measurements per star per run) and longer time scales, for which more data may be loosely clustered on several year time scales due to changes in observing procedures etc. Because of these irregular sampling patterns fits may be less tightly constrained than a more evenly spaced data set, and the limits provided by our analytic apparatus may become misleading.

Since the Walker et al. data are rather irregular, we examine the effect on our analysis technique by performing a Monte Carlo experiment and comparing the result to our analytic formalism. We create synthetic data sets using a constant value of the error, σ_p , equal to the rms scatter of the observed velocity measurements for each star. This value is input into eqn. 6.16 to derive individual simulated velocity measurements. We use the observation times given by the data itself. We fit the measurements and derive best fit velocity amplitudes (and corresponding $M_c \sin(i)$ values) for periods between 3 days and 100 years. Each synthetic datum used in the fit is weighted with the internal error in that point (quoted by Walker et al.) as $1/\sigma_i(t_i)^2$.

The results of these experiments are shown as the solid histograms in figure 6.8. In general, the agreement between the analytic limits and the Monte Carlo experiments is good. However a small systematic trend towards larger limits for the Monte Carlo experiments is found. Typically the difference is 10% or less, however, in the most extreme case (θ UMa), the limits produced are about 20-30% higher than with the analytic method. This star has the shortest time baseline of any in the sample as well as one of the largest degrees of clumping of any star in the sample, as measured by the ratio of the number of data to the number of runs. A test in which we replace

in eqn. 6.17 the number of data, n_0 with the number of runs recovers the Monte Carlo results for this star quite well. The star ϵ Eri, for which the data are the most highly clumped of any star in the sample, also produces analytic limits lower than reproduced with the Monte Carlo experiment. In this case, replacing n_0 with the number of runs produces limits much larger than the Monte Carlo result, so we cannot recommend such a procedure for general use.

In the case of one star (HR 8832), two measurements were made with a 3-1/2 year separation from any other measurement for that star. This case provides an interesting test in the limit of very irregularly spaced data. We find that the limits derived from the Monte Carlo experiment are quite similar to the analytic result except in the range between about 8 and 12 years, where limits some 20% larger than those derived via eqn. 6.20 are found. The longer period fall-off characteristics are unaffected by the irregularity.

The sensitivity fall off at long periods for each star is similar to that produced in the synthetic data. We show the derived fit values for the power law exponent and the long period turn off in figure 6.9 for the sample of 14 stars. The sharp upturn in limiting velocity at long periods produces a power law exponent which is best fit with values near $\alpha = 1.86$, while the turn-off period, β , is best fit with values near $\beta = 1.45$, but with a larger scatter than is present in the synthetic data. Because the scatter is by its nature rather unpredictable from star to star, we retain the low $\beta = 1.3$ value found for synthetic data when determining limits via eqn. 6.17 or 6.20.

The limits provided by our analytic expression produce upper bounds which are ordinarily $\lesssim 10\%$ different than those produced via Monte Carlo experiments. In the most irregularly spaced data, a difference of up to 20-30% can occasionally be produced. In several cases, the difference results in possibly spurious ‘detections’ of marginal signals by the analytic technique where the Monte Carlo limits do not show that the periodicities are significant. In some of these cases we are able to attribute the detections to physical processes discussed in the literature. In no case do the analytic limits exceed the 99.9% level of probability where the Monte Carlo result did not also show at least a 99% probability. Despite this level of difference, our conclusions about the significance or lack of it for any periods and companion masses for each star in the Walker et al. data remain unchanged. We are confident that this method can be relied upon to obtain probabilities that a given set of data contains a periodic signal.

6.4.5. Sensitivity to Short Period Planets

For the star with the lowest companion mass limits (ϵ Eri), we have also plotted in figure 6.8 several recent planet detections (Mayor and Queloz 1995, Marcy and Butler 1996, Butler and Marcy 1996, Latham et al. 1989, Gatewood 1996, Noyes et al. 1997) and Jupiter. Extra solar planets with combinations of period and mass like those shown would have been readily detected by Walker’s radial velocity measurements. These stars do not have such companions. For most of the stars in the sample, the data are too noisy to have reliably detected a radial velocity signature such as would be predicted for the companion to Lalande 21185, announced by Gatewood (1996) but which remains unconfirmed. Planets such as Jupiter, which would appear at $P = 12$ years with a typical value of $M_c \sin(i) = 0.64M_J$ would not have been reliably detected. The best fit values exceed this period/mass combination in 40% of the sample.

The analysis of Walker et al. sets upper limits to the mass of companions in their sample ($\times \sin(i)$) of $\leq 1M_J$ and $\leq 3M_J$ in periods of less than 1 year and 15 years respectively. In general, our analysis provides limits which are somewhat lower than theirs in both long and short period orbits. For one year periods, we can limit companion $M \sin(i)$ values to $\leq 0.7M_J$ for all but three stars in our subset and $\leq 1.0M_J$ for the rest. In 15 year orbits, our analysis limits

possible $M \sin(i)$ values to $\leq 1.5M_J$ for every star except θ UMa, for which only 6 years of data were gathered. For this star, the limit is $\leq 4.0M_J$. We have also extended range over which companion signatures are constrained to shorter periods than were analyzed in Walker et al. The limits for these extreme short period orbits ($P < 40$ days) correspond to companion masses ($\times \sin(i)$) below $0.4 M_J \sin(i)$.

Under either our own analysis or the original analysis of Walker et al., the companion mass limits derived from the data essentially eliminate brown dwarfs and large Jovian planets with periods $\lesssim 15$ years, barring very unfortunate inclinations. Given the detections of significant periodicities by either our analytic treatment or Monte Carlo experiments, we find more signals present than can be attributed to purely random data. In some cases, such detections may be due to physical mechanisms other than a companion, and we have compared these to known periodicities due to stellar rotation or magnetic cycles, where they have been identified in the literature. In no case do the limits eliminate the possibility of gas giants such as exist in our solar system or low mass brown dwarfs, especially in the period/radius range ≥ 12 yr/5 AU where theory predicts such companions.

6.5. Strategies for Large Radial Velocity Surveys

There are currently six active groups with programs for radial velocity searches at the < 10 -20 m/s level. Three groups began searches at this precision in 1987-88 (Cochran & Hatzes 1994 (Texas), McMillan et al. 1994 (Arizona), Marcy & Butler 1992 (Lick)), while one (Duquennoy & Mayor 1991 (Geneva)) have used lower precision measurements with the CORAVEL spectrometer (~ 300 m/s) to investigate stellar binary companions and have recently built a new spectrometer (ELODIE) to allow $\lesssim 15$ m/s precision measurements to be made. The latest high precision searches (Kürstner et al. 1994 (ESO), Brown et al. 1994 (CfA)) began in 1992 and 1995 with quoted precision of ~ 4 -7 m/s and ~ 10 m/s respectively. Another group (Walker et al. 1995 (UBC)) concluded a 12 year search in 1992. Two others (Mazeh et al. 1996 (CfA), Murdoch et al. 1993 (Mt John NZ)) obtain precision of ~ 500 m/s and ~ 60 m/s respectively.

The recent discoveries of sub-stellar mass companions around other stars have stirred new interest in very large radial velocity surveys. The Geneva group for example, intends to expand their search to ~ 500 stars in the northern hemisphere (ELODIE) and another ~ 800 in the southern hemisphere (CORALIE), and other groups have similar expansions underway. In order to observe as many stars as possible with a finite telescope allocation, such large surveys must necessarily aim toward the most efficient use of the available observing time. The goal of such large surveys might be properly stated as “What fraction of stars have a companion (or a system of companions) and what is the distribution of the masses, periods and eccentricities of those companions?”.

In order to answer this question three criteria must be met. First, an observer must first detect a variation in the radial velocities measured for a star about which a prospective companion orbits. Second, the observer must determine the origin of such variations by fitting a Keplerian orbit and by making additional photometric or spectroscopic observations to constrain effects due to the stellar photosphere. Finally the observer must determine the extent to which the survey is complete: what fraction of stars which were observed may have companion signatures which went undetected over the course of the survey? Based on the analysis in this paper, we can suggest strategies for the most efficient methods of detecting radial velocity signatures and which also provide meaningful upper limits on the amplitudes of undetected signatures.

Let us suppose that the random error for each measurement is dominated by photon noise, ie. that $\sigma_p \propto 1/\sqrt{t}$, where t is the length of a single observation. This should be the case provided

detector read noise is not significant. It follows from eqn. 6.15 that the limiting amplitude, K , is proportional to $1/\sqrt{t_n}$, ie. K depends on the total integration time devoted to a star, t_n , independent of number of observations making up that time. In other words, as long as eqn. 6.15 holds and the total integration time is the same, making many lower precision measurements is equivalent to making fewer high precision measurements. Since constraining additional orbit parameters such as eccentricity is at its most simplistic level an exercise in detecting higher order Fourier components of the signal, this equivalence holds for orbit determinations as well as for detection of a periodic signal. We caution, however that with lower precision data, larger amplitude systematic errors may go undetected. With 15 m/s precision for example, the signal of Jupiter could be completely obscured by a hidden systematic error of amplitude ~ 10 m/s.

From section 6.2, to insure than eqn. 6.15 holds, the number of observations, n_0 , must be at least ~ 12 and preferably as high as 20 in order to constrain octave period ranges. The limits are degraded most severely for periods less than 1–2 years. Longer periods limits are nearly identical to the analytic prediction even for very sparse data (see figures 6.1 and 6.3). This is because with only a few observations of each star, a companion signature could still slip through undetected if by some unfortunate coincidence its radial velocity “zero crossings” corresponded to the times at which the star was observed. For $P \lesssim 1$ year, there are very many independent periods, so that the possibility of any one of them coincidentally undergoing such a zero crossing event is very high. For $P \gtrsim 1$ year, where there are relatively few independent periods, such a condition becomes much more unlikely.

The cost in observing time to obtain useful limits if there are few observations is great. When the data are sparse and eqn. 6.15 breaks down, for example with a total of either $n_0 = 6$ or $n_0 = 12$ observations and the same total integration time, our Monte Carlo simulations show that the limiting amplitude is in fact twice as big for any single period, and ten times as big for octave period ranges. Because 12 much lower precision measurements would identically constrain short period signals as 6 high precision measurements, the increase in sensitivity translates to a reduction factor of 4 or 100 in the amount of observing time required to identically constrain the existence of companion for any single period or over octave ranges in orbits of $\lesssim 2$ years.

As an example of a strategy which addresses this concern, suppose a survey is to observe 500 stars and is to last at least 12 years. Let us also suppose that 1/4 of the use of a telescope is dedicated to the radial velocity measurements, yielding about 400 hours of integration per year to be divided among the stars in the survey. The total number of observations to obtain 12 for each star is 6000. A good “quick look” could be obtained after the first two years if each observations takes $2 \times 400/6000$ hours = 8 minutes.

Butler et al. (1996) report that precision of ~ 3 m/s can be obtained in a 10 minute exposure of a magnitude $V = 5$ star on a 3 meter class telescope. However, in a large survey most stars will be dimmer than $V = 5$, with a practical limiting magnitude between $V = 7$ and $V = 8$, depending on the size of the survey. If the average star is of magnitude $V = 7$, a measurement with 3 m/s precision would nominally require about 60 minutes. With such long duration measurements each star in the program would average less than one observation per year and would make a large, high precision survey unfeasible. In order to complete a large survey at ≤ 5 m/s precision a large allocation of time on an 8–10 m class telescope would be required. If instead we allow reduced precision measurements of ± 10 m/s, using our assumption that the precision is proportional to $1/\sqrt{t}$, a single measurement would require only about 6 minutes on a 3 meter telescope, which would be feasible for a large survey.

For this to be practical without poor observing efficiency, the time from the end of an observation to the beginning of the next on a new star must be short, ideally a minute or less. During this time, the telescope must be slewed to the new star, while the CCD with the exposed

spectrum is read out. Automatic slewing and acquisition would make this quite practical. Also, for a typical spectroscopic CCD with around 3 million pixels, the required read rate of 100 kpixel/sec should be readily achievable at negligible read noise with current devices. A 8 minute cycle time with 6 minutes data acquisition would thus be a reasonable target, and yield 72 minutes of integration for each star, spread through the first two observing seasons.

With this strategy, an observing program should be able to sustain 6 measurements of every star every year that the program is continued. If after two years, variations are detected in some stars, additional measurements of those stars would be possible if constant velocity stars were observed only 1–3 times per year. This compromise has the advantage that limits on companion masses are well constrained by such density of points and orbital solutions, should a star’s velocity later be observed to vary, would also be well constrained. A second advantage is that after the first two years, strong limits on the existence of a companion signal are available for short periods and these limits extend to longer periods incrementally as long as the program is maintained. In contrast, a high precision/sparse observation strategy with say 1-2 measurements per year, will strongly limit short period signatures only after 6 or more years of the program has passed.

As a second example of observing strategy, we consider a search for a Jupiter mass planet with the same 12 year period as Jupiter, around a star with the same mass as the sun, what accuracy measurements are needed over what period to ensure only 1% probability of a false detection for any given star? For sets of observations spanning 6 and 12 years figure 6.11 shows the limiting mass above which a companion would be detected with 99% probability in a given set of data at any single period. A $1 M_J$ companion in a 12 year orbit around a solar twin will have a best fit mass of $\sim 0.64 M_J$ assuming a random inclination. We require via eqn. 6.20, that data be taken with precision ± 5 m/s for 12 years with a single observation per year in order to detect such a companion. Increasing to 5 or 20 observations per year, only 15 or 30 m/s are required, respectively, with the requirement that no hidden systematic errors are also present in the data. For an identical number of measurements per year, a 6 year baseline requires more than 6 times the precision in each measurement to similarly constrain a long period companion, or 36 times the observing time each year. Clearly the cost of impatience is very high.

We would like to thank the referee, Paul Butler, for helpful comments and criticisms in his referee’s report. Alan Irwin also provided helpful criticism of this manuscript. We are grateful to several people for providing the radial velocity data used in this work. Among them are Gordon Walker and Alan Irwin for providing a portion of their radial velocity data prior to publication, Michel Mayor for sharing the data for 51 Peg and HD 110833 and Geoff Marcy for sharing an electronic copy for a second, independent data set for 51 Peg. M. Mayor provided commentary on the results of our analysis and a discussion with Didier Queloz outlined reasons for which the data for HD 110833 may have contained systematic errors in several measurements. W. Benz provided impetus for the section on sensitivity to large signals and Bob McMillan, Adam Burrows, Paul Harding and Heather Morrison provided other helpful discussion. This work was partially supported under NASA Grants NAGW-3406 and NAS7-1260.

Table 6.1.
Period Ranges

3-6d
6-12d
12-24d
24-48d
48-96d
96d-0.5yr
0.5-1yr
1-2 yr
2-4 yr
4-8 yr
8-12 yr
>12 yr

Table 6.2. The Subset of 14 Stars Included in our Analysis

HR	HD	Name	M/M _⊕	σ_i (m/s)	σ_p (m/s)	No. Obs.	No. Runs	Duration (yr)
509	10700	τ Cet	0.87	13	17	68	39	11.7
937	19373	ι Per	1.15	15	18	46	29	10.8
996	20630	κ^1 Cet	0.98	13	20	34	22	10.0
1084	22049	ϵ Eri	0.82	14	16	65	34	11.1
1325	26965	σ^2 Eri	0.84	14	19	42	28	11.0
3775	82328	θ UMa	1.45	24	21	43	23	6.0
4112	90839	36 UMa	1.08	16	21	56	36	10.7
4540	102870	β Vir	1.22	14	26	74	48	11.7
4983	114710	β Com	1.09	16	18	57	40	11.4
5019	115617	61 Vir	0.98	13	18	53	35	11.4
7462	185144	σ Dra	0.85	13	19	56	37	11.5
7602	188512	β Aql	1.30	12	14	59	39	11.4
7957	198149	η Cep	1.36	12	19	58	39	11.2
8832	219134	...	0.79	11	15	32	23	10.6

Table 6.3. Detection of Significant Periodicities

Period range	Star	Period ^a	Companion ^b Mass (M _J)	Probability of Chance Detection in Period Range	
				Analytic	Monte Carlo
3-6d	...				
6-12d	ε Eri	11.9d	0.14	<1%	...
12-24d	...				
24-48d	...				
48-96d	ε Eri	52.5d	0.24	<1%	...
96d-0.5yr	η Cep	164d	0.54	<0.1%	<1%
	HR 8832	165d	0.35	<1%	...
	θ UMa	179d	0.63	<1%	...
0.5-1yr	...				
1-2 yr	...				
2-4 yr	...				
4-8 yr	ε Eri	>7 yr	0.7	<1%	<1%
8-12 yr	ε Eri	10 yr	0.95	<0.1%	<1%
	η Cep	10 yr	1.2	<1%	<1%
	β Com	10 yr	1.05	<1%	...
	36 UMa	10 yr	1.1	<0.1%	<0.1%
>12 yr	36 UMa	15 yr	2.0	<0.1%	<0.1%
		25 yr	5.3	<0.1%	<0.1%
		50 yr	24	<0.1%	<0.1%
	β Vir	15 yr	1.9	<0.1%	<0.1%
		25 yr	5.0	<0.1%	<1%
		50 yr	23	<1%	<1%

^aWe exclude ‘significant’ periods which coincide with known annual or lunar windowing periods

^bBest fit mass assuming that the periodicity is actually due to a companion.

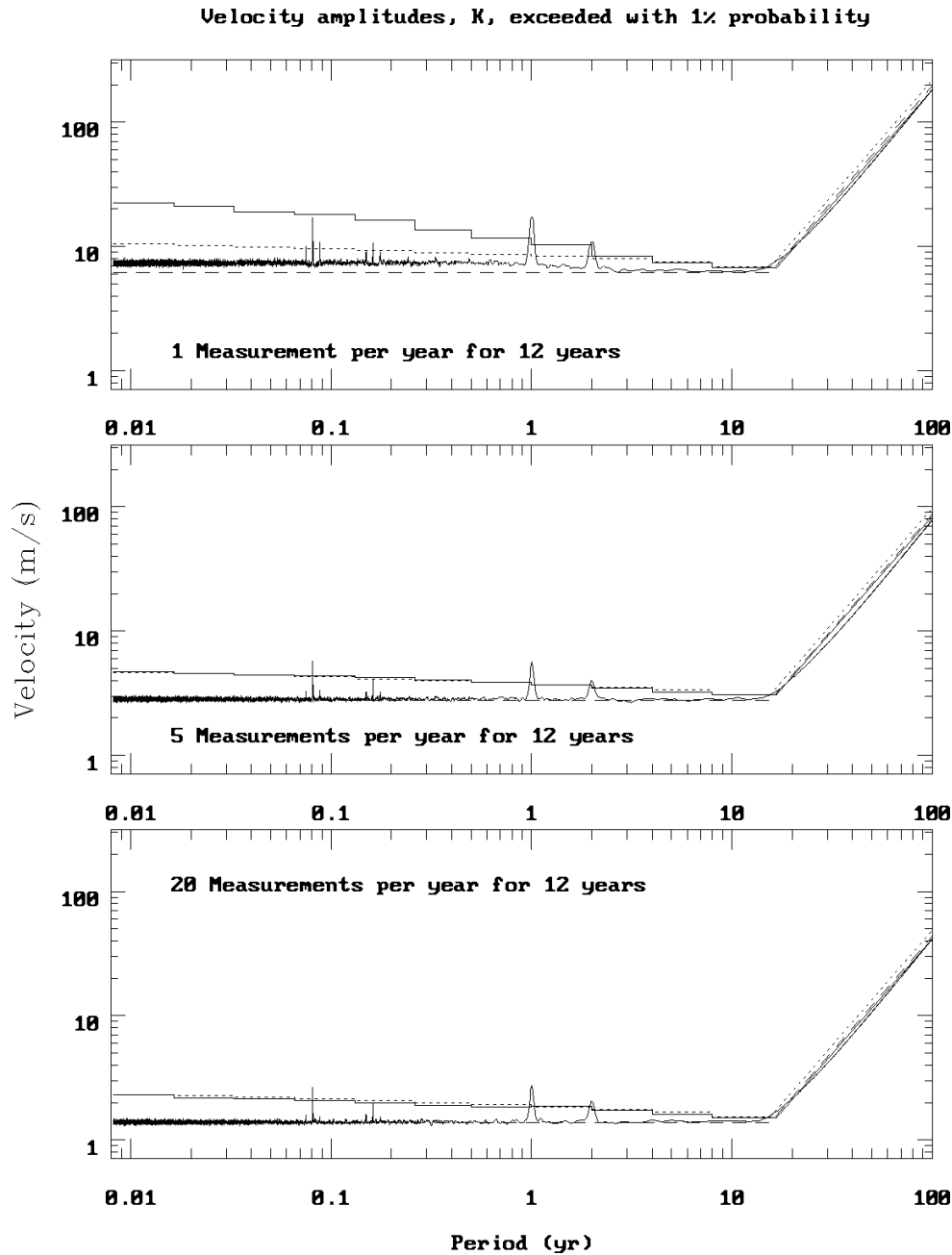


Figure 6.1 Monte Carlo (solid line) and analytic results (dashed line) for the velocity amplitude which, for a given fitted period, is exceeded by chance in 1% of analyses of simulated random data. A second solid line (histogram) shows the Monte Carlo results for the amplitude which is exceeded at any period within a range of approximately one octave, while the dotted histogram line shows the result from our analytic expression, eqn 6.15. For each of the experiments in the bottom two frames (5 and 20 obs./yr), the analytic and Monte Carlo results are indistinguishable. Assumed windowing at the lunar and annual periods as well as their double period counterparts are excluded from the Monte Carlo limits in their respective ranges.

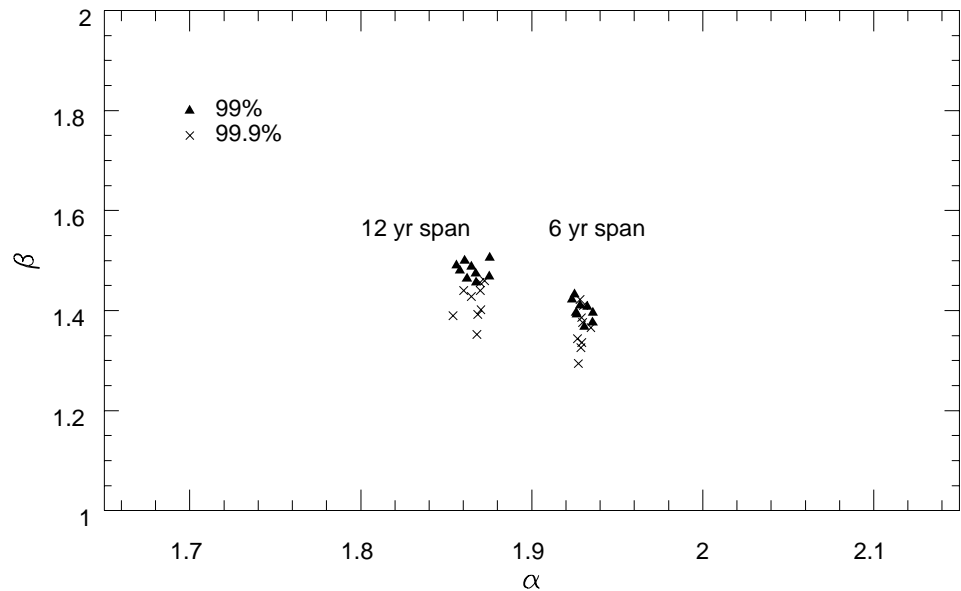


Figure 6.2 Best fit values for the long period sensitivity fall off parameters α and β for the nine Monte Carlo experiments run for both 6 and 12 year baselines.

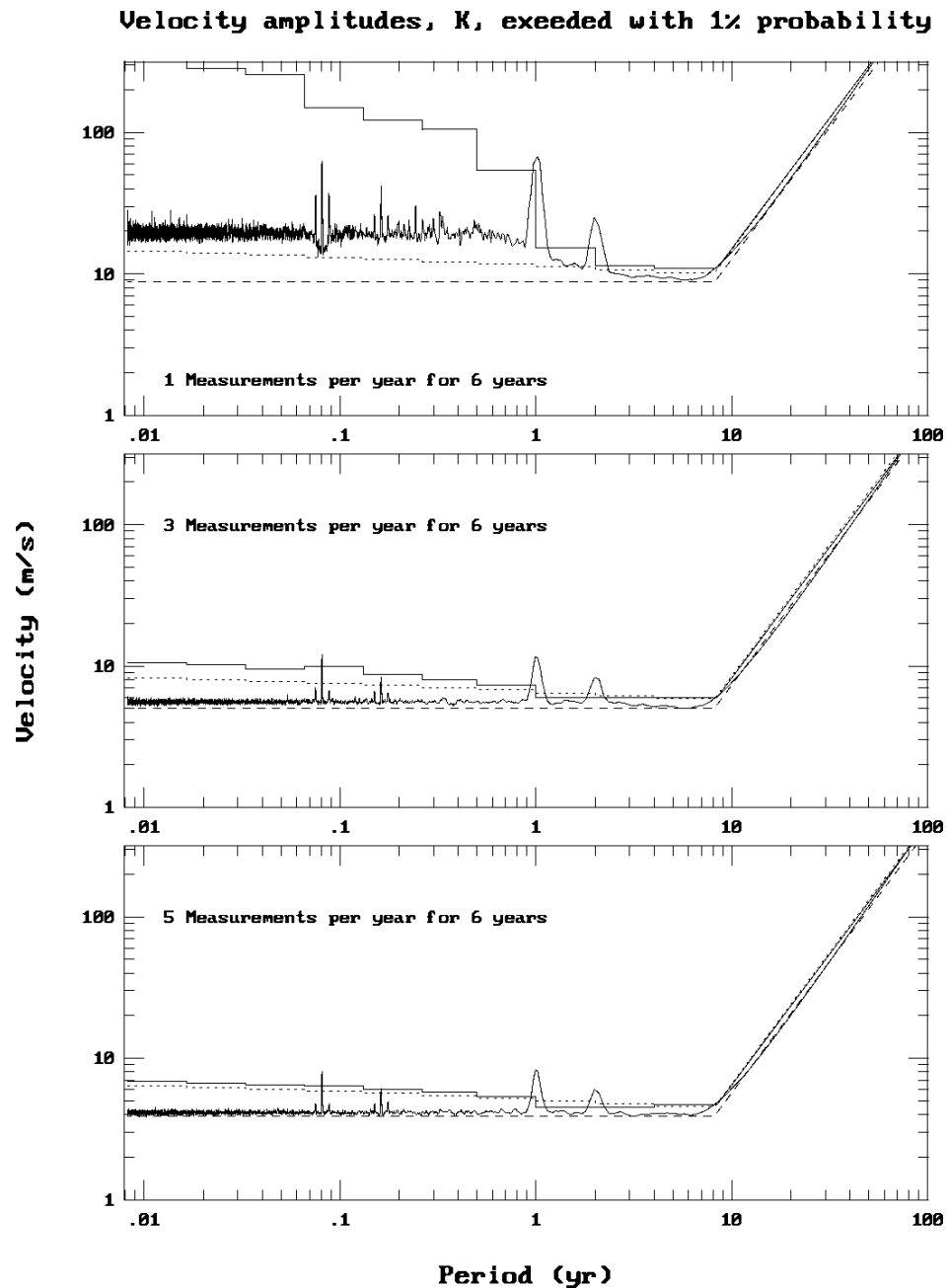


Figure 6.3 Velocity limits given by Monte Carlo simulations (solid), single period ($N=1$) analytic limits (dashed). The histograms represent the Monte Carlo (solid) and analytic (dotted) limits for octave sized ranges. Each of the histogram limits ignore the periods affected by the assumed lunar and annual windowing of the data. A 6 year window is assumed with 1 (top), 3 (middle) and 5 (lower) observations per year.

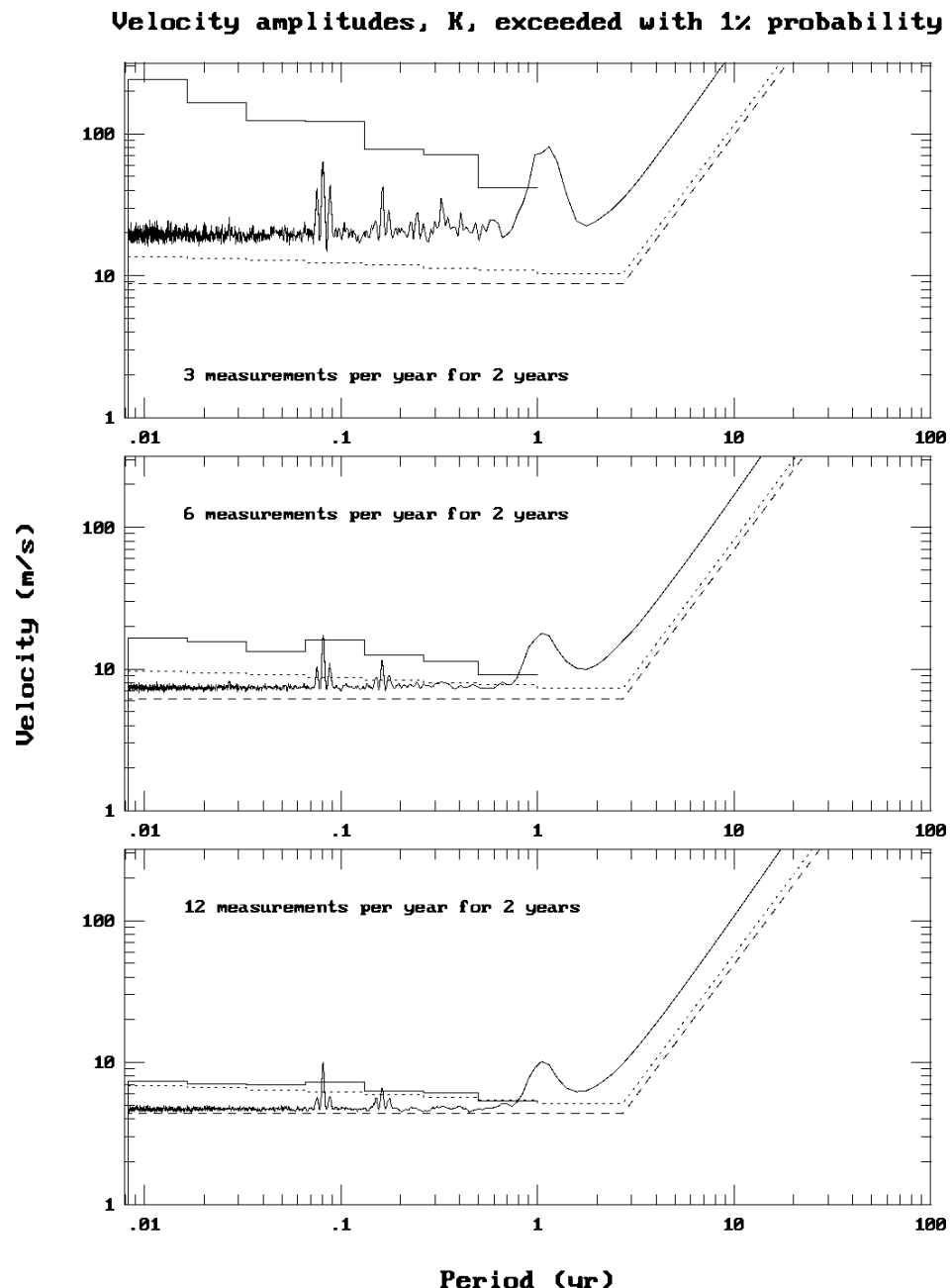


Figure 6.4 Velocity limits given by Monte Carlo simulations (solid), single period ($N=1$) analytic limits (dashed). A 2 year window is assumed with 3 (top), 6 (middle) and 12 (lower) observations per year. As before, histograms represent the Monte Carlo (solid) and analytic (dotted) limits for octave sized ranges and each of the histogram limits ignore the periods affected by the assumed lunar and annual windowing of the data. In this plot however, for periods longer than 1 year the Monte Carlo histogram limits are suppressed.

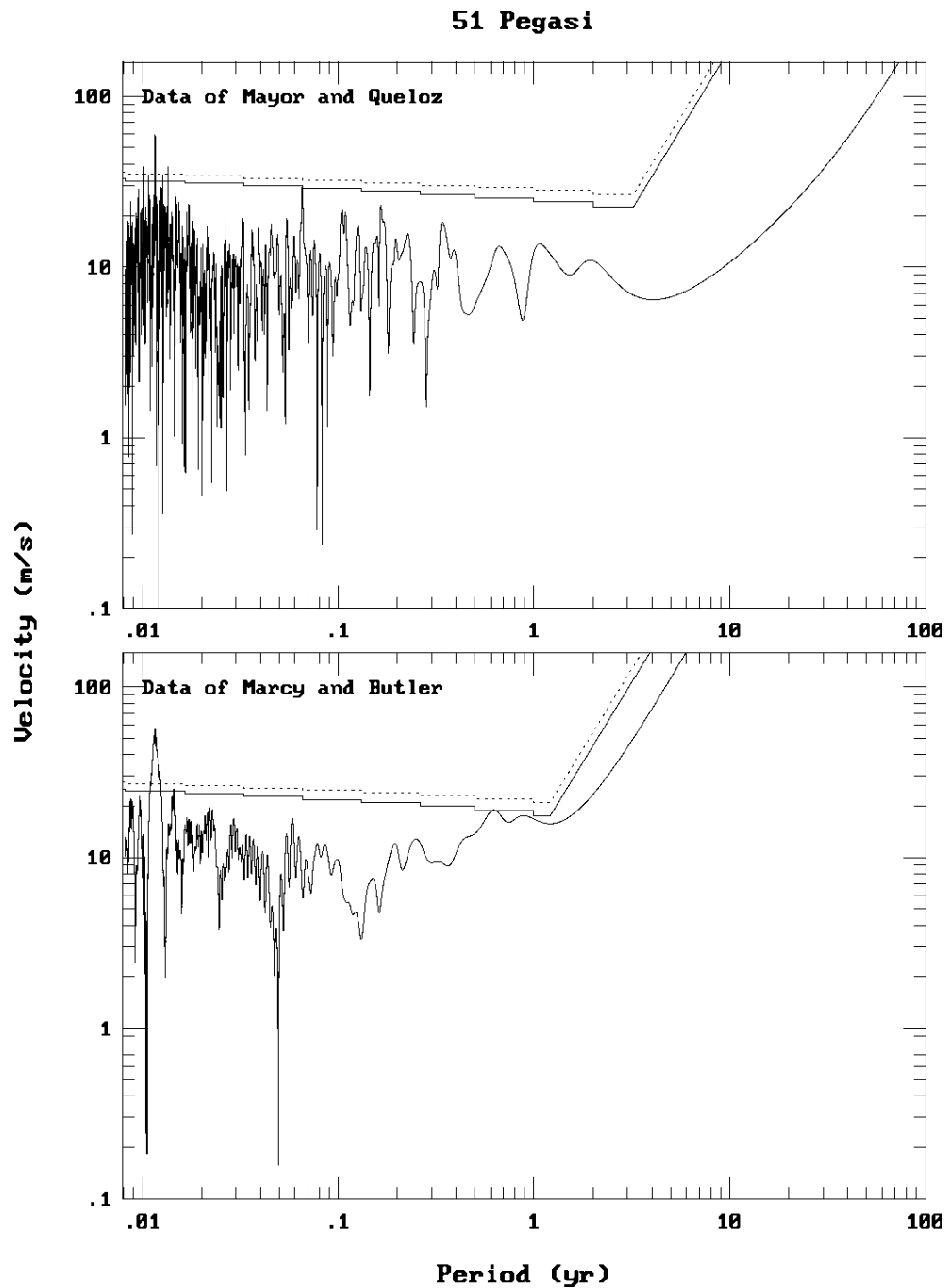


Figure 6.5 Best fit velocities for the star 51 Pegasi. The solid and dotted histograms denote respectively, the limits below which random data would occur with 99 and 99.9% probability.

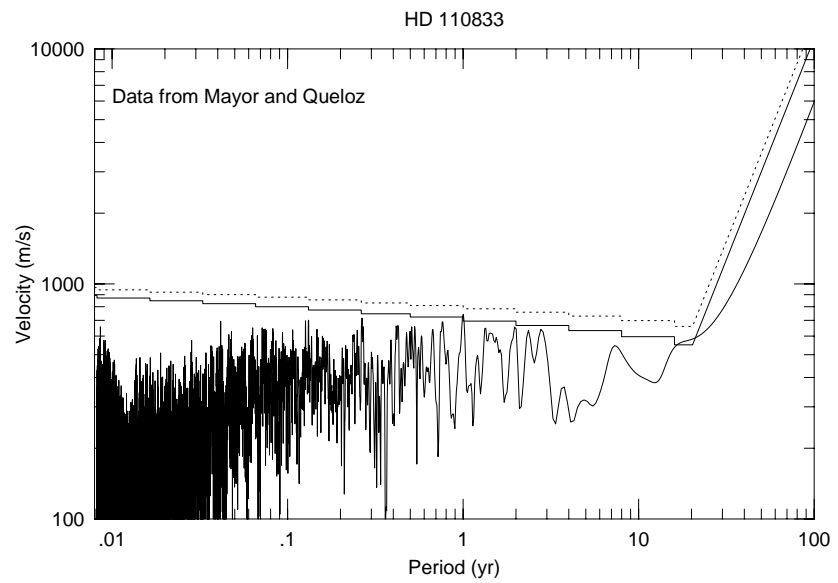


Figure 6.6 Best fit velocities for the data derived from star HD 110833. A 15 year periodicity is apparent in the best fits with >99% probability that it is nonrandom.

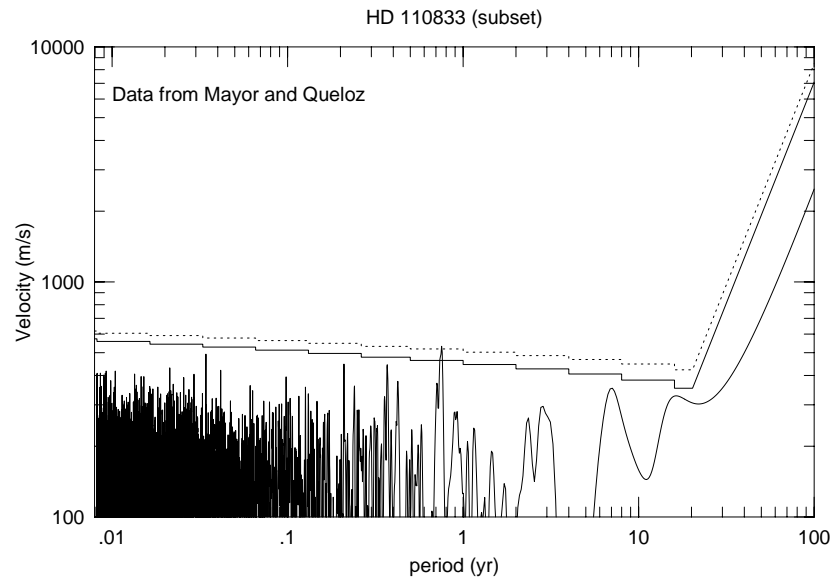


Figure 6.7 Best fit velocities for the the subset of the data from HD 110833 with 5 measurements removed. In this case, a periodicity is present at 275 days with probability $>99.9\%$ that it is non-random.

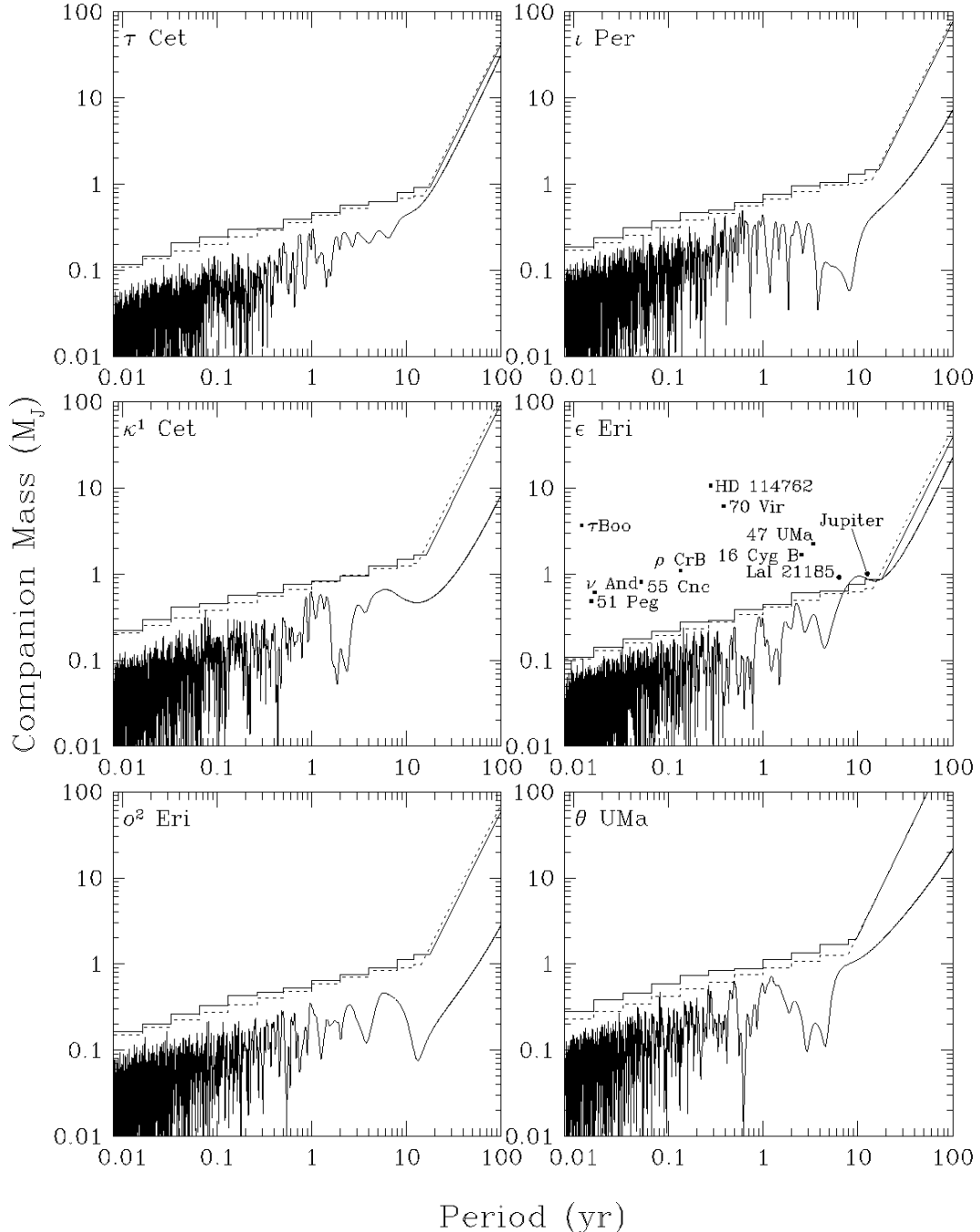


Figure 6.8 Best fit companion masses ($\times \sin(i)$) for each star over a range of periods corresponding to the most sensitive range of the data. The histograms represent the 99% mass limits for each specified period range as given by our analytic formulation (dotted histogram) and based on a Monte Carlo experiment (solid histogram) consisting of 3000 simulated data sets. Also plotted (squares) are the measured $M_c \sin(i)$ values of recent planet detections (see text). Jupiter and the astrometrically detected (but unconfirmed) companion to Lalande 21185, are shown omitting a $\sin(i)$ correction (circles).

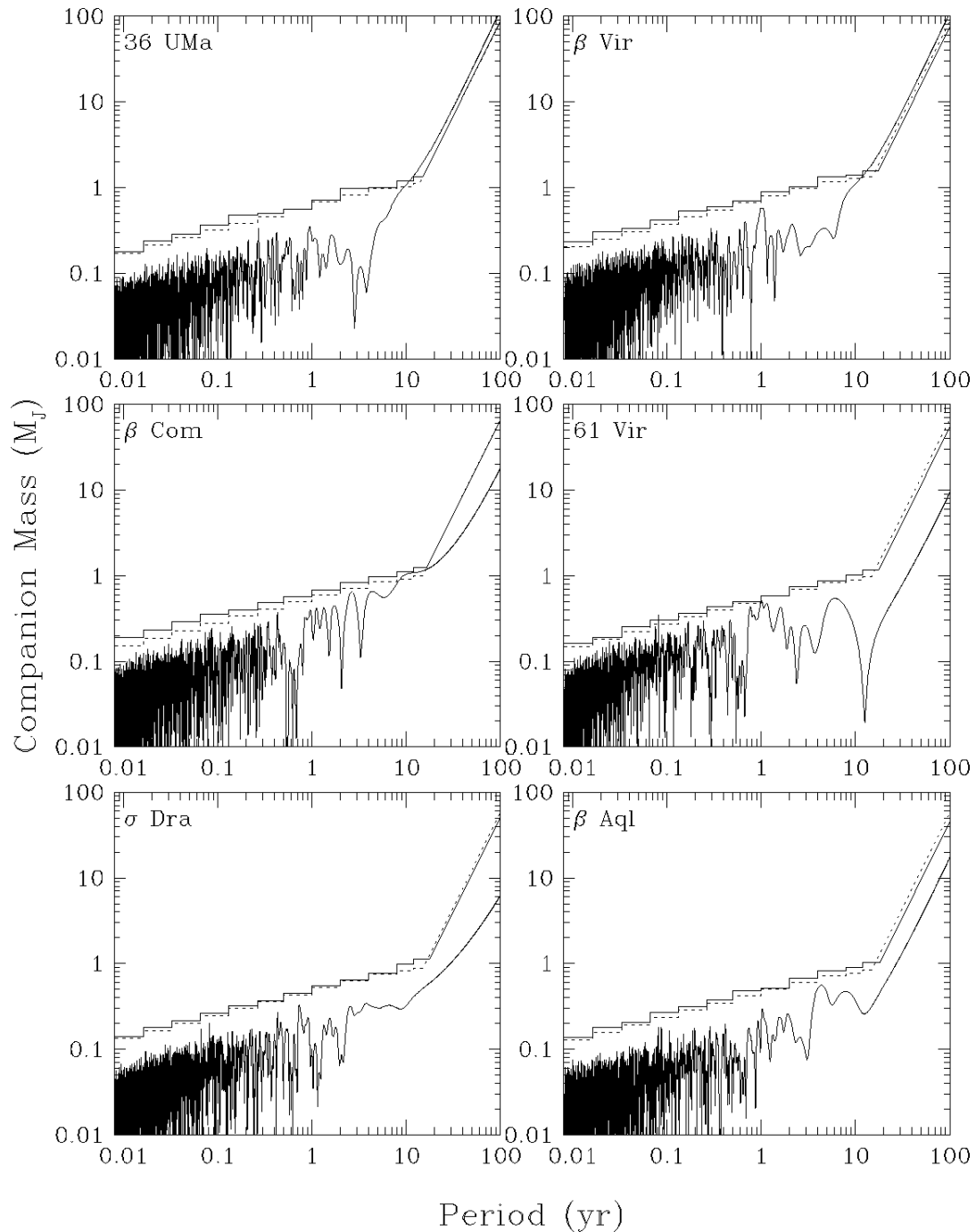


Figure 6.8-continued

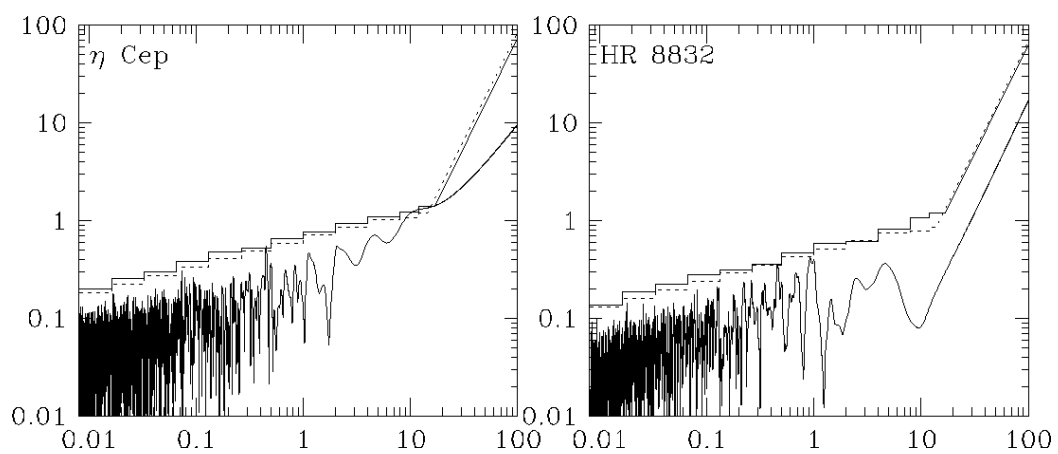


Figure 6.8–continued

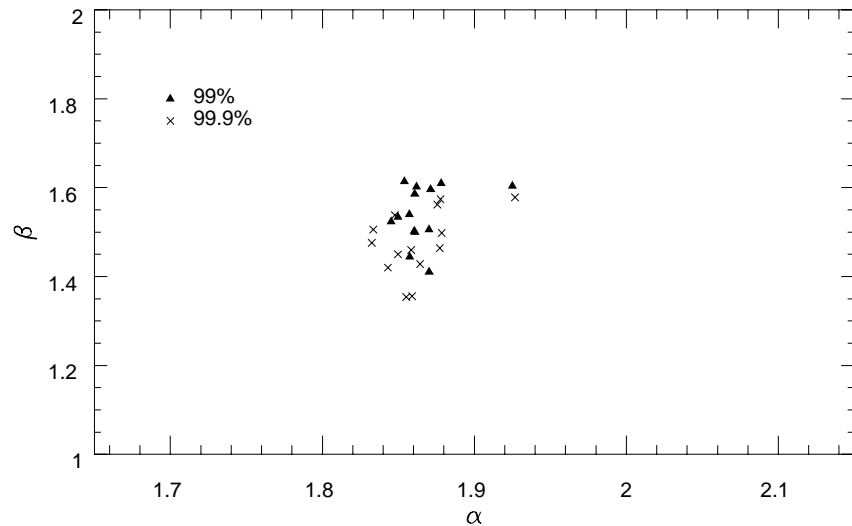


Figure 6.9 Best fit values for the long period sensitivity fall off parameters α and β derived from the data. Values for both 99% (triangles) and 99.9% (\times 's) fall-off are shown. The two points lying to the right of the main group originate from the star θ UMa and are consistent with the Monte Carlo results for a 6 year data span.

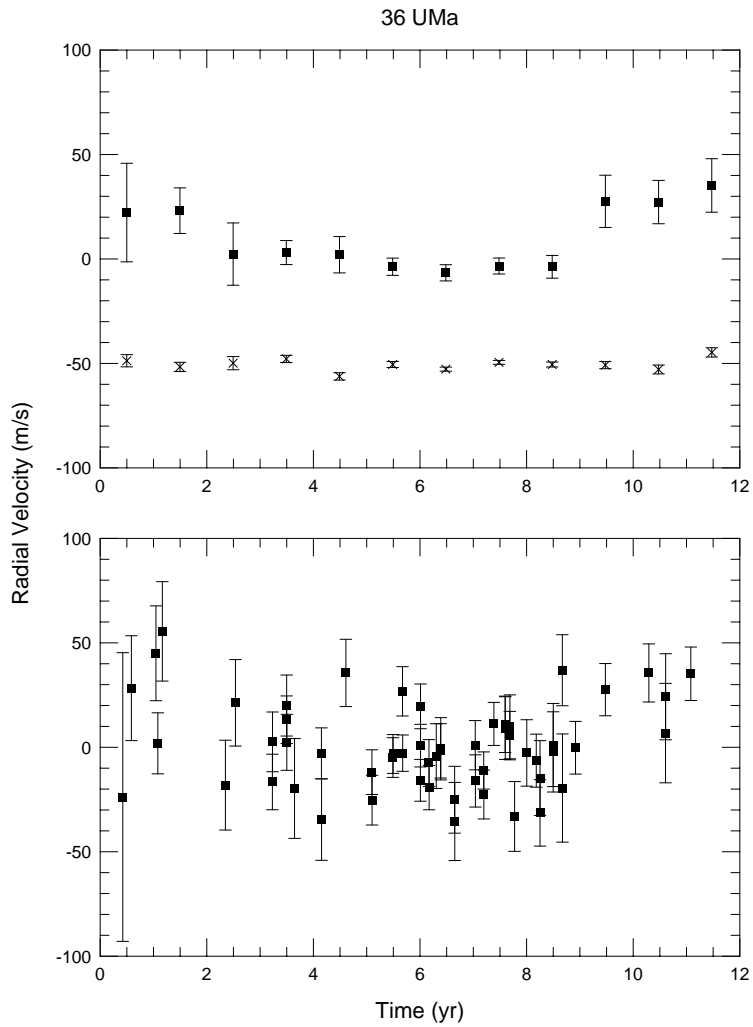


Figure 6.10 Radial velocity data for the stars (a) 36 UMa and (b) β Vir, for which long term trends are observed using both our analysis technique and the Walker et al. analysis. Both the published velocity data and the weighted mean of the velocities for each year are shown. The binned data for the sample of 14 stars taken together is shown offset by -50 m/s. No trend similar to that found in either 36 UMa or β Vir is present, indicating that a systematic error common to all stars is unlikely. Errors are taken from Walker et al. 1995, while the errors in the binned points are derived from the central limit theorem $1/\sqrt{n}$ improvement in the error of a multiply sampled mean.

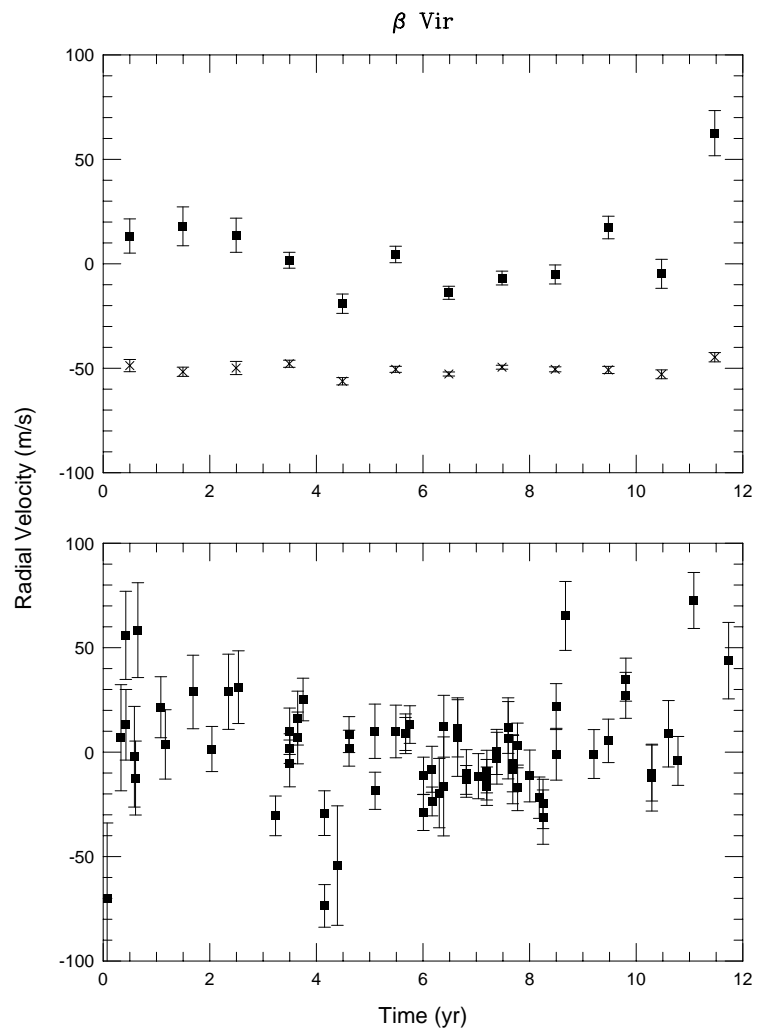


Figure 6.10b

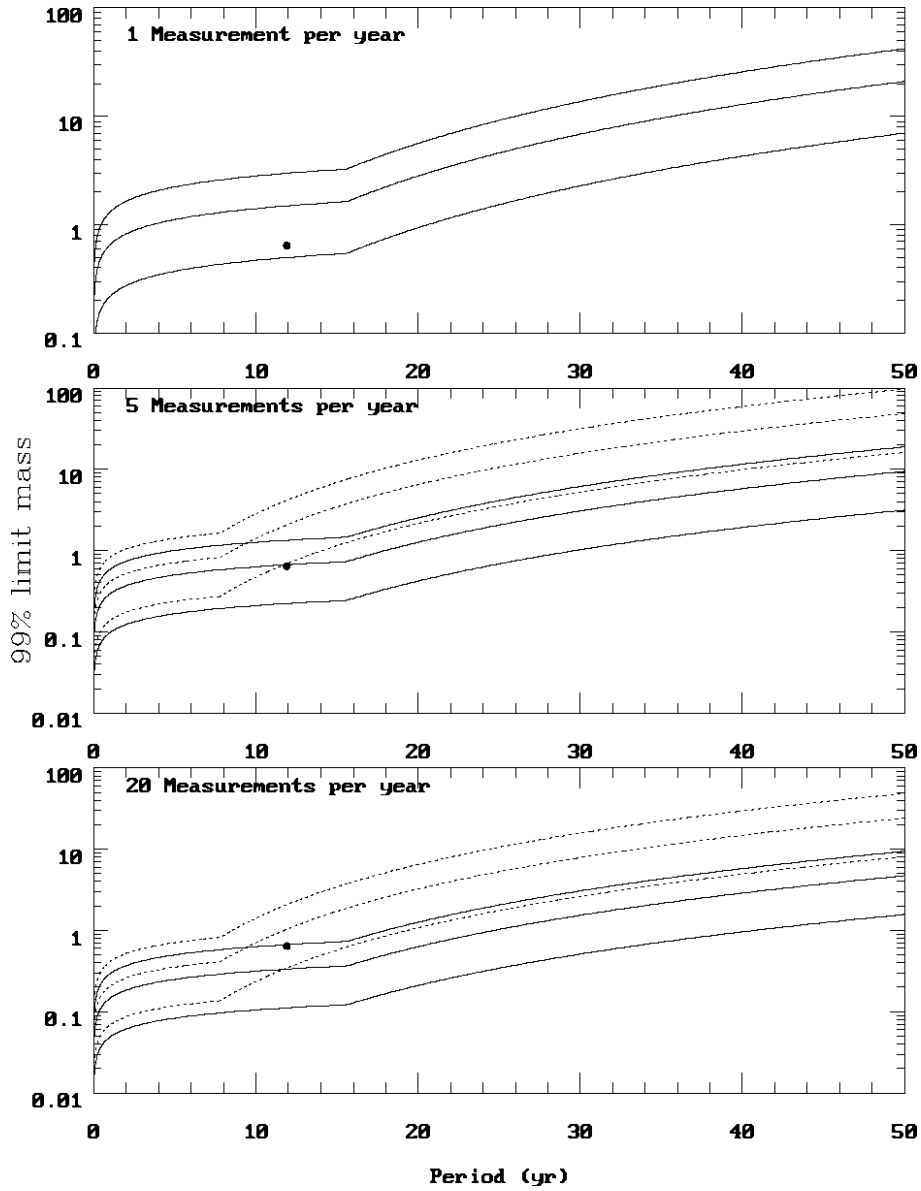


Figure 6.11 Limits above which data of a given quality and duration constrain the mass of companions at the 99% level for any single period. Solid lines represent a 12 year span of data taken with 5, 15 and 30 m/s precision while dotted lines represent a comparable 6 year span. Limits for the 6 year baseline with one only measurement per year are omitted here because they do not correspond to results from Monte Carlo experiments (see section 6.2.3).

CHAPTER 7

CONCLUDING REMARKS AND WHERE WE OUGHT TO GO FROM HERE

Over the past few hundred years, we've developed an extremely detailed understanding of the mechanics and characteristics of objects in our own solar system. Over the past few decades we've started to unravel a few of the problems associated with its formation and origin. The kinds of questions now under study for our own system are not of the type 'what objects are in the solar system and how do they move?' but rather 'what is the internal structure of this or that object, how did it get that way and what is it likely to do in the future?'.

The two thrusts of star formation research: first, to acquire a more complete inventory of the types of solar systems which exist and second, to more completely understand how those systems came to be the way they are now, have each been addressed in this thesis. Our focus has been primarily on understanding the physical processes important during the formation of solar type stars, but we've also focused on the observable signatures of such systems and limits which can be placed on their detection by observers here in our solar system. Working with Willy Benz, Dave Arnett, Fred Adams and Tamara Ruzmaikina, I have numerically simulated the evolution of massive circumstellar disks and analyzed the results for their dynamical and observable spectral characteristics. With Roger Angel, I have outlined the detection limits available to radial velocity searches for low mass (ie. planet or brown dwarf) companions. We then used these limits to suggest an efficient strategy for new or continuing large radial velocity surveys.

Many of the problems which remain require a considerable allocation of resources in numerical computation or telescope instrumentation, so it is important that we address the questions which most efficiently provide answers to our remaining questions. On the theoretical side for example, many of the uncertainties which remain require that no symmetries be assumed which reduce a problem from three to two, or from two to one spatial dimensions. A complete treatment of all three spatial dimensions is required. On the observational side, developing an inventory and understanding of the kinds of systems which exist requires both very high spatial resolution of the sky and very high contrast resolution, in order to detect very faint objects (planets and brown dwarfs) near very bright objects (stars).

The past decade or two has seen a great deal of work attempting to understand the origin of various morphologies of stellar systems. Not much attention has yet been paid to what the systems simulated would actually look like to an observer attempting to detect such objects in some wavelength band. It is not too much of an exaggeration to say that the current state of affairs is one in which we can now make stellar systems of nearly any morphological type (single, binary, multiple etc.) through either cloud collapse or disk evolution. However, several questions about the formation morphology of disk systems and the formation of planetary systems

do remain. Also, the field is nearly wide open in terms of understanding the observational characteristics of simulations of the newly formed systems of all morphologies.

Several of the areas requiring further development which build on the work presented here are (1) to characterize the full inventory of low mass objects which exist in the solar neighborhood and in the galaxy as a whole and similarly, to understand the characteristics of forming systems. Just as importantly, we also require reliable limits on what types of objects and systems are not detected and limits on our sensitivity to detect various classes of objects (2) to understand in detail the initial formation processes of circumstellar disks, from small scales outward, (3) to understand the transport and evolution of ice and dust within the nebula in order to better understand both radiative transfer processes (and the consequent observational characteristics) and the formation of low mass companion objects through agglomeration and (4) to understand the early stages of growth and migration of Jovian companions within disks.

7.1. Taking Inventory: What is Possible Using Various Detection Techniques

In chapter 6, we discussed limits on the detection of low mass companions to nearby stars via a single technique: radial velocity measurements. There are also a variety of other possible techniques which are in various stages of study or implementation, including micro-lensing, astrometry, occultation and direct imaging.

Of the many different techniques that are now or soon will be available, which provides the best chance of detecting companions of other stars, or of detecting low mass objects not orbiting a star? What kind of objects should we expect to detect with one technique or another and what kinds of systematic biases exist for each? How can we know how complete the sample of detected objects is and what kinds of objects are likely to be missed? A study which compares the sensitivities of the various techniques and their systematic ‘blind spots’ would be of great use in establishing the true distribution of low mass objects.

Some of these other techniques have in fact begun to bear fruit, with a variety of low mass objects floating in free space (Hillenbrand 1997, Reid *et al.* 1998, Luhman *et al.* 1998), bound to stellar primaries (Nakajima *et al.* 1996) or even bound to each other (Basri & Martin 1998). Others, such as micro-lensing (Peale 1997) and occultation surveys (Borucki *et al.* 1998), are not yet underway.

Of all of the techniques mentioned, only direct imaging is capable of detecting free floating low mass objects. As marvelous as it is to have a picture of the object you’re looking for, it is also true that direct detection suffers from some systematic biases. Among them are the fact that a substellar mass companion will be orders of magnitude dimmer than its primary. Detection will therefore require quite high angular resolution on the sky in order to make sure that the point spread function of the star on the focal plane of the telescope is small enough to enable the detection of the slight additional flux from the companion.

Other techniques also have biases. For example, it is well known that radial velocity techniques are biased towards detecting companions close to their primary because of the larger reflex velocities imposed on the motion of the star by a close companion. For a similar reason, astrometry is biased toward large companions at large distances from their primary, since a planet in a distant orbit has a larger ‘lever arm’ to perturb the motion of the primary. Both have a systematic bias against detecting companions in large orbits due to the attention span (and in some cases life span) of the observer and/or the apparatus used to make the measurements.

Micro-lensing and occultation searches also suffer from systematic biases. In the case of these two methods, the biases arise because of the large area of sky which must be searched at a very

high rate of observation. For example, occultations of a star by a companion will occur in only a small fraction of stars which have companions (of order a few percent) and will last for only a few hours. Micro-lensing events will undoubtedly prove to be quite limited for detecting individual objects since an event can only be observed once. On the other hand, it may prove to be of great use in establishing larger statistical distributions of objects than can be obtained by any other means.

Given these data on the possibilities of various detection techniques, what is the best strategy for getting a large enough sample of low mass companions of every type (planets, brown dwarfs or low mass stars) around stars near the sun, floating freely in space and in the galaxy as a whole?

7.2. Disk Formation

Circumstellar disks extend over a very large range of radii: from a few R_{\odot} to several hundred AU. They form from the inside out, as higher and higher angular momentum material falls into the system. As we found in the work discussed in chapters 2 and 4, they are notoriously difficult to model due to the vastly disparate time scales involved in their evolution. Because of this problem, numerical simulations of star formation have generally fallen into two general categories: simulations of collapse and simulations of already formed, narrow tori or disks. Only a few collapse calculations have been done which also follow the evolution until a disk forms (eg. Laughlin and Bodenheimer 1994; Boss 1993, 1996). Each of these works resolves the innermost regions on a scale of several AU, which implies that the spatially small, inner disk regions are not important for the evolution of the gross structure of the system. They sacrifice the resolution of the small scale features of the forming disk in favor of understanding the large scale morphology of the system.

We have shown (chapters 2, 4) that the inner regions of already formed disks are in fact very dynamically active and do affect the gross structure of the system. If a spatially large disk (> 50 AU) is to form we must understand how the dynamic inner region can sustain itself while more distant regions form. The small scale features of the collapse from the star outward must be resolved. I suggest a series of numerical simulations modeling the formation of circumstellar disks from this perspective.

Stahler et al. (1994) has extended the work of Cassen and Moosman (1981) to show that as the infall proceeds and the infalling material no longer intersects the stellar surface, three distinct regions form. Each region expands radially as t^3 . Innermost is a Keplerian disk, while in the outer regions the disk is characterized by infalling matter with comparable radial and azimuthal velocities. In between lies a transition region (modeled in their work as a discontinuity) in which the matter loses much of its radial velocity and moves into the Keplerian inner region.

I propose that numerical hydrodynamic techniques like the PPM code discussed in chapter 2 be used to simulate the early evolution of the systems like those studied by Stahler et al. Such a study should investigate several questions not possible to address in their work. In particular, they study only axisymmetric and inviscid systems; each fluid element conserves j_z , the z -component of specific angular momentum. Transport through the disk is provided by accretion of additional low angular momentum material onto the surface of the disk from above and below. They also posit a massive 'fly-wheel' ring in their transition region, which is modeled only as a discontinuity. Such assumptions are unsatisfactory because the forming disk will develop shocks and turbulence and therefore become dynamically unstable. Shock dissipation and the eventual formation of non-axisymmetric structures will play a crucial role in determining the structure and subsequent evolution of this region and of the disk as a whole.

In order to model the dynamics of the forming disk it is likely that three dimensional simulations will be required, at high computational cost. A useful first step can be made if we assume that the collapse originates from a cloud in solid body rotation (see Stahler *et al.* figure 2). Then at any given instant the highest angular momentum material falling onto the disk will come from the equatorial regions of the collapsing cloud. With this assumption, material falling onto the disk from above and below can be neglected and the system can be modeled in only two dimensions (r and ϕ) but still preserve many of the important physical phenomena.

Such a study is a natural outgrowth of this thesis because the dynamically important effects we have described require only small modifications of existing code to address. For example, a number of the simulations performed in chapter 2 assumed an infall onto the outer edge of the disk, so implementation of the infalling cloud matter will be a trivial adaptation of already existing code. Also, because the collapse and disk growth are self similar, modeling the disk formation for the relatively short time scale allowed by a multi-dimensional hydrodynamic scheme will give a good picture of the disk even at much later times.

This study will provide a wealth of information on the properties of a previously unexplored region of parameter space. Several important questions which become accessible with this work are: What is the initial mass distribution in the disk? Is it a power law like that given by the results of Stahler *et al.* and others, or is it flatter/steeper? To what extent can it be fit to a power law at all? What is the form of the transition region and how does it vary in time? What is the character of the boundary layer between the disk and star?

Ultimately, when high resolution three dimensional simulations become computationally feasible, another set of questions can be addressed. For example, what is the origin of the bipolar jets observed to be coming from forming star/disk systems? Undoubtedly magnetic field effects are important in this same region. Some work has already been done (Stone *et al.* 1996, Shu *et al.* 1994a, 1994b, Najita & Shu 1994, Ostriker & Shu 1995, Ouyed & Pudritz 1997a,b) to try and understand what their effects are on the system, but more work is required. An interesting question that bears on both the star/disk boundary layer and the effect of magnetic fields is the question (proposed by Shu *et al.*) of how and whether mass is accreted onto the star through magnetic flux tubes at the interface.

7.3. The Transport and Evolution of Dust in the Disk: Effects on Energy Transport

We have shown (chapter 4) that a correct model of the spectral energy distributions (SED's) of observed systems requires a detailed understanding of the processing of dust within the disk. In the regions of the disk within a few AU from the star, gas may be heated to temperatures above the destruction temperature of dust grains contained in the nebula. We have shown that if dust which is destroyed in the hot midplane of the disk reforms quickly as it is processed to high altitudes, the SED's synthesized from our numerical simulations produce insufficient flux in the near IR ($\sim 1-5 \mu\text{m}$) to reproduce observed systems. On the other hand, if dust reforms on a longer time scale, comparable or longer than the convective overturn time scale so that most of the refractory material is found in the gas phase or in a grain size distribution strongly modified from its original distribution, then we may be able reproduce the SED's of observed systems in the near infrared.

The assumptions underlying our models are that the disk is locally plane parallel and vertically adiabatic at each location in the disk. No true three dimensional calculation of the vertical structure, no self consistent modeling of the transport of dust from low to high altitudes is done and no evolution of the grain size distribution is incorporated into the hydrodynamic calculation. For a complete picture of the evolution all of these effects must be included in the

calculation. Work to study the evolution of turbulence in disks (Cabot 1996, Balbus, Hawley & Stone 1996) for some conditions. However they have not studied its effect on the grains swept along with the gas.

Rather than studying its origin I propose a study of the observational consequences of turbulence. More specifically I propose a study of the processing of disk gas and dust in the vertical coordinate of the disk. Cabot (1996) has shown that full three dimensional simulations may not be required to obtain some information from such a study because the large Keplerian shear quickly removes azimuthal variations. A two dimensional study in r and z may therefore provide many of the physical properties of the disk necessary to model the evolution of the dust and ice present.

This work will require that several species of dust and ice be evolved separately through each simulation. The 'PROMETHEUS' code, which utilizes the PPM hydrodynamic method and which is used in chapter 2, can be easily adapted to this task. In its original implementation, it is used to study the evolution of nuclear species inside supernovae (see eg. Bazan & Arnett 1997). Much of the machinery for multi-species evolution has already been thoroughly tested. Remaining tasks involve adaptation of the code specifically to the problem of ice and dust vaporization and reformation reactions and the specification of the initial state of the system.

The specific simulations I propose should concentrate on modeling the vertical structure of the inner disk where it is warm enough that ice and dust can be vaporized. This region extends outwards from the stellar surface to perhaps 1–2 AU from the star. The outcome of these simulations will lead to a better understanding of the influence of solid material on the transport of energy through the disk and its dissipation into space. It is possible that these simulations of the inner disk may also provide insight into the mechanisms involved in forming a bipolar outflow from the system.

Grain and planetesimal growth processes have been studies for many years, both on small scales and larger scales (Safronov 1969, Weidenschilling 1980, Greenberg *et al.* 1978, Wetherill & Cox 1984, 1985, Greenberg *et al.* 1991, Spaute *et al.* 1992, Tanaka & Ida 1996). The studies outlined in section 7.3 will certainly be able to incorporate many of the results of this work (for example the reaction network physics required to couple grains of different species and size to each other). Most of the work done so far has been in a celestial mechanical framework, with the gas modeled as a 'black box' turbulent fluid with some characteristic velocity. Grains are more or less entrained in the fluid, depending upon their size and collide with each other, break apart or stick at relative velocities defined by the input turbulence assumption.

The calculations I suggest may be able to extend the previous work by relaxing two of the most important of these assumptions. First, the mixing in the previous calculations is assumed to be rather uniform in space: any migration of different sized particles from one place to another is assumed to be mixed instantaneously into the surrounding medium. If instead the grains do not mix well, so that some regions retain grains of whose size distribution is quite different than nearby regions, drastically different grain evolution may result. Secondly, with a hydrodynamic code, the turbulence may be resolved to some extent (depending upon the available computing power), so that relative velocities of grains becomes much better constrained and the dependent collisional properties become more narrowly defined. A solution to these questions will lead to a better understanding of not only the radiative transport processes in disks (through grain absorption and scattering of light), but also of planet formation, through grain growth to larger and larger sizes.

7.4. Migration of Jovian Planets

The classical models for Jovian planet formation (ie. that gaseous disk matter collapses onto a $10-15 M_{\oplus}$ rock/ice core), predict that Jovian planets will form at distances of ~ 5 AU or more from the central star (Boss 1995) due to the condensation of ices at that distance. The detection of low mass companions in orbits very close to their primary (as small as 0.05 AU) has forced theorists to postulate that a companion can form far from its primary, then migrate to its present location. The migration models proposed (see Takeuchi *et al.* 1996 and references therein), have shown that gravitational torques upon the companion by a circumstellar disk are sufficient to change its orbit drastically on a time scale of only a few thousand years. Migration is so efficient that under normal assumptions about the character of a disk, it is far too *easy* for a companion to continue its migration and simply fall into the star.

The migration models proposed have been limited in the sense that they are linear analyses and are one dimensional. They omit effects such as accretion onto the companion, do not take full account of shock dissipation of waves excited in the disk and assume a zero eccentricity orbit.

In (so far) unpublished calculations, I have performed a set of numerical simulations incorporating an already formed companion into a two dimensional (r, ϕ) disk. These calculations show that an already formed Jovian mass companion can form a wide gap in the disk in only a few $\times 10^2$ years. In so doing, it moves inward to nearly half its original orbit radius and then proceeds for the remainder of the simulation on a slow, secular inward evolution. Time step constraints forbid us from following the evolution of the system for the long periods ($\gtrsim 10^4$ yr) necessary to follow the orbital evolution to its conclusion.

The simulations I have performed, although providing interesting results in themselves, begin with an initial condition which is quite artificial. A $\sim 1-2 M_J$ companion would certainly have formed a gap or otherwise modified the mass distribution in the disk. Instead of concentrating on the evolution of the disk once a companion has grown to appreciable size, I suggest simulations modeling the evolution of a low mass core ($\sim 10-30 M_{\oplus}$) as it begins to accrete large amounts of gas from the disk and perhaps carve out a gap.

Three dimensional calculations of Bondi-Hoyle accretion have been done (Ruffert 1997 and references therein) and have shown that accretion proceeds at a rate not unlike the Bondi-Hoyle rate even in flows with transverse velocity gradients. No calculations have been performed in which the accretor lies in a medium undergoing Keplerian shear however. I suggest extending the previous calculations to the problem of an accreting proto-planet. As a first step, these calculations will implement initial conditions including a transverse Keplerian shear but excluding density variations in the r or z directions. This condition is equivalent to simulating the earliest stages of growth, when the proto-planet is only able to affect regions of the disk close to the midplane.

The outcome of these simulations will be to determine the mass and angular momentum accretion rates of the proto-planet as it begins to grow quickly. Comparison of these rates to the rate at which gaps form by gravitational torque processes will provide insight into the eventual final state of the system as a whole. Depending on the outcome of this first round of simulations, it may become of interest to include density gradients in two dimensions. In this case, the question of how large the accretor must be before it first begins to deplete mass from an entire vertical column of the disk. For an accretor of that size, accretion may be reduced due to the loss of material accreting onto the poles of the proto-planet and a gap may form, slowing additional migration through the disk.

REFERENCES

Adams, F.C. & Benz, W., 1992, Gravitational Instabilities in Circumstellar Disks and the Formation of Binary Companions, in Complementary Approaches to Double and Multiple Star Research, IAU Colloquium No. 135, (Provo: Publications of the Astr. Soc. of the Pac.) (AB92)

Adams, F. C., Lada, C. & Shu, F. H., 1987, ApJ, 312, 788

Adams, F. C., Lada, C. & Shu, F. H., 1988, ApJ, 326, 865

Adams, F. C., Emerson, J. P. & Fuller, G. A. 1990, ApJ, 357, 606

Adams, F. C., Ruden, S. P. & Shu, F. H., 1989, ApJ, 347, 959 (ARS)

Adams, F. C. & Lin, D. N. C., 1993, in Protostars and Planets III, ed. Lunine, J. I. and Levy, E. H., Tucson: University of Arizona Press

Adams, F. C. & Watkins, R., 1995, ApJ, 451, 314

Alexander, D. R., Ferguson, J. W., 1994, ApJ, 437, 879

Aristarchus of Samos, ca. 260 BC., On the sizes and distances of the sun and moon. Original publishing data unavailable. Reprinted in Heath, T., 1911, Aristarchus of Samos, The Ancient Copernicus, Oxford: Clarendon Press

al-Khowarizmi, M., ca. 820., Algebra, original publishing information unavailable. Reprinted as Robert of Chester's Latin Translation of the Algebra of al-Khowarizmi with an introduction, critical notes and an English version. Karpinski, L. C., 1915, London: MacMillan & Co.

Artymowicz, P., 1993, ApJ, 419, 166

Artymowicz, P., 1994, ApJ, 423, 581

Artymowicz, P., & Lubow, S. H., 1994, ApJ, 421, 651

Artymowicz, P., & Lubow, S. H., 1996, ApJ, 467, L77

Atanasoff, J. V., 1940, Unpublished memorandum, Reprinted in The Origins of Digital Computers: Selected Papers, Third edition, ed. B. Randell, Springer Verlag, New York, 1982

Balbus, S. A., Hawley, J. F., Stone, J. M., 1996, ApJ, 467, 76

Baliunas, S., Sokoloff, D., Soon, W., 1996 ApJ, 457, L99

Balsara, D., 1995, J. Comp. Phys, 121, 357

Basri, G., Martin, E. L., 1998, in Brown Dwarfs and Extrasolar Planets, Proceedings of a Workshop held in Puerto de la Cruz, Tenerife, Spain, ed. Rebolo, R. & Martin, E. L., Zapatero Osorio, M. R.

Bate, M., Bonnell, I. & Price, N. M., 1996, MNRAS, 277, 362

Bazan, G., Arnett, W. D., 1997, Science, 227, 1359

Beckwith S. V. W., Sargent, A. I., Chini, R. S., & Güsten, R., 1990, AJ, 99, 924 (BSCG)

Bell, K. R., Lin, D. N. C., 1994, ApJ, 427, 987

Bell, K. R., Lin, D. N. C., Hartmann, L. W., Kenyon, S. J., 1995, ApJ, 444, 376

Bell, K. R., Cassen, P. M., Klahr, H. H., Henning, Th., 1997, ApJ, 486, 372

Benz, W., 1990, in The Numerical Modeling of Nonlinear Stellar Pulsations p. 269, J. R. Buchler ed.

Benz, W., Bowers, R. L., Cameron, A. G. W. & Press, W. H. 1990, ApJ, 348, 647

Bessel, F. W., 1838, Astronomische Nachrichten, 365, 366

Bessel, F. W., 1840, Astronomische Nachrichten, 401, 402

Bethe, H. A., Critchfield, C. L., 1938, Phys. Rev. 54, 248

Bethe, H. A., 1939, Phys. Rev. 55, 434

Bevington, P. R., Robinson, D. K., 1992, Data Reduction and Error Analysis for the Physical Sciences, Second Ed., McGraw-Hill, New York

Binney, J., & Tremaine, S., 1987, Galactic Dynamics, Princeton: Princeton University Press

Bonnell, I. & Bastien, P., 1992, ApJ, 401, 654

Bonnell, I. A., Bate, M. R., 1997, MNRAS, 285, 33

Borucki, W. J., Koch, D. G., Lissauer, J. J., Brown, T. M., Jenkins, J. M., Dunham, E. T., 1998, BAAS, 192, 6223

Boss, A.P., 1993, ApJ, 417, 351

Boss, A., 1995, ApJ, 439, 224

Boss, A. P. 1995, Science, 267, 360

Boss, A.P., 1996, ApJ, 469, 906

Boss, A. P., 1997, Science, 276, 1836

Brahe, T., 1598, Astronomiae Instauratae Mechanica, Wandesburgi

Brahe, T., Kepler, J., 1602, Astronomiae instauratae progymnasmata: quarum haec prima pars de restitutione motuum solis et lunae starllarumque inerrantium tractat, et praeterea de admiranda nova stella anno 1572 exorta luculenter agit, Typis inchoata Vraniburgi Daniae, absoluta Pagae Bohemiae.

Brown, T. M., Noyes, R. W., Nisenson, P., Korzennik, S. G., Horner, S., 1994, PASP, 106, 1285

Burbidge, E. M., Burbidge, G. R., Fowler, W. A., Hoyle F., 1957, Rev. Mod. Phys. 29, 547

Burkert, A. & Bodenheimer, P., 1993, MNRAS, 264, 798

Butler, R. P., Marcy, G. W., 1996, ApJ, 464, 153

Butler, R. P., Marcy, G. W., Williams, E., McCarthy, C., Vogt, S., 1996, PASP, 108, 500

Cabot, W., 1996, ApJ465, 874

Cassen, P. M., & Moosman A., 1981, Icarus, 48, 353

Chiang, E. I., & Goldreich, P., 1997, ApJ, 490, 368

Chick, K. M., Pollack, J. B. & Cassen P., 1996, ApJ, 461, 956

Christodoulou, D. & Narayan, R., 1992, ApJ, 388, 451

Close, L. M., Roddier, F., Northcott, M. J. Roddier, C., Graves, J. E., 1997, ApJ, 478, 766

Cochran, W. D., Hatzes, A. P., 1994, Ap&SS, 212, 281

Colella P. & Woodward, P. R., 1984, J. Comp. Phys., 54, 174

Copernicus, N., ca. 1530, preprint: Nicolai Copernici de hypothesibus motuum caelestium a se constitutis commentariolus. Various manuscript copies collated and published 1882: Prowe, L., Nicolaus Coppernicus, Berlin

Copernicus, N., 1543, De revolutionibus orbium coelestium Normbergae: Apud J. Petreium.

Courant, R., Friedrichs, K., Lewy, H., 1928, Math. Ann., 100, 32

D'Alessio, P., Canto, J., Calvet, N., Lizano, S., 1998a, ApJ, 500, 411

D'Alessio, P., Canto, J., Calvet, N., Lizano, S., 1998b, ApJ, In press

Digges, L., 1571, Pantometria (note in preface written by T. Digges), quoted in King, H. C., 1955, The History of the Telescope, Dover: New York

Dreyer, J. L. E., 1953, A History of Astronomy from Thales to Kepler, Dover: New York

Duquennoy, A., & Mayor, M., 1991, A&A, 248, 485

Eckert, J. P., Mauchly, J. W., Goldstine, H. H., Brainerd, J. G., 1945, Description of the ENIAC and Comments on Electronic Digital Computing Machines, Contract W-670-ORD-4926, Moore School of Electrical Engineering, Univ. of Pennsylvania, Phil. PA.

Eddington, A. E., 1920, British Assoc. Reprints, p45 (see also, Jeans (1929) p. 112)

Einstein, A., 1917, Über die spezielle und die allgemeine Relativitätstheorie: Gemeinverständlich, Braunschweig, F. Vieweg

'Ερατοσθένης (Eratosthenes) ca. 220 BC, manuscript unavailable. See Dreyer 1953, p175

Eudoxus of Cnidus, ca. 365 BC., On Speeds, manuscript unavailable. Referenced by Simplicius *Commentary on Aristotle's De Caelo*, ca. 500AD, See footnote in Heath (1981) p320

Fabricius, J., 1611, Phrysii de Maculis in Sole Observatio, Wittenberg

Foster, P. N. & Boss, A. P., 1996, ApJ, 468, 784

Frank, J., King, A. R., Raine, D. J., 1992, Accretion Power in Astrophysics, Second Ed., Cambridge University Press: Cambridge

Fryxell, B. A., Müller, E. & Arnett W. D., 1989, Max Plank Institut für Astrophysik Report #449

Fryxell, B. A., Müller, E. & Arnett W. D., 1991, ApJ, 367, 619

Fukue, J., Sakamoto, C., 1992, PASJ, 44, 553

Galilei, G., 1610, *Siderevs Nvncivs magna: longeqve admirabilia spectacula pandens, suspiciendaque proponens vnicuique præsertim verò philosophis atque astronomis quæ à Galileo Galileo: Patritio Florentino Patauini Gymnasij Publico Mathematico Perspicilli Nuper à se reperti beneficio sunt obseruata in lvnaæfacie, fixis innvmeris lacteo circvlo, stellis nebylosis, apprime verò in qvatvor planetis Circa Iovis, Stellam disparibus interuallis, atque periodis, celeritate mirabili circumuolutis; quos, nemini in hanc vsque diem cognitos, nouissimè Author deprehendit primus: atque Medicea Sidera Nvncvpandos Decrevit. Venetiis: Apud Thomam Baglionum*

Galilei, G., 1632, *Dialogo di Gaileo Galilei Linceo matematico sopraordiario dello stvdio di Pisa, Fiorenza: Per Gio: Batista Landini*

Gammie, C., 1996, ApJ, 457, 355

Gatewood, G., 1996, BAAS, 28, 885

Ghez, A., Neugebauer, G., & Mathews K., 1993, AJ, 106, 2005

Gingold, R. A., Monaghan, J. J., 1977, MNRAS, 181, 375

Godunov, S., 1959, *Matematicheskii Sbornik* 47, 271

Goldreich, P., Lynden-Bell, D., 1965, MNRAS, 130, 125

Goldreich, P., & Tremaine, S., 1978, ApJ, 222, 850

Goldreich, P., & Tremaine, S., 1980, ApJ, 241, 425

Goldreich, P., Goodman, J., Narayan, R., 1986, MNRAS, 221, 339

Gray, D. F., 1994, ApJ, 428, 765

Gray, D. F., Baliunas, S. L., 1995, ApJ, 441, 436

Gray, D. F., Baliunas, S. L., Lockwood, G. W., Skiff, B. A., 1996, ApJ456, 365

Greenberg, R., 1978, Wacker, J. F., Hartmann, W. K., Chapman, C. R., Icarus, 35, 1

Greenberg, R., Bottke, W. F. Carusi, A., Valsecchi, G. B., 1991, Icarus, 94, 98

Heath, T. 1981, *Aristarchus of Samos: The Ancient Copernicus*, Dover: New York

Heemskirk, M. H. M., Papaloizou, J. C. B. & Savonjie, G. J., 1992 A&A, 260, 161

Henning, Th., Stognienko, R., 1996, A&A, 311, 291

Herakleides of Pontus, ca. 340 BCE, reference unavailable, see reference in Dreyer pp. 132.

Herant, M., & Woosley, S. E., 1994, ApJ, 425, 814

Herbig, G., 1952, JRAS Canada, 46, 222

Herbig, G., 1970, Mem. Roy. Soc. Sci. Liege, Series 5, 9, 13

Hertzsprung, E, 1911, Potsdam Observatory Pub., 63

Hillenbrand, L., 1997, AJ, 113, 1733

Horne, J. H., Baliunas, S. L., 1986, ApJ, 302, 757 (HB)

Irwin, A.W., Campbell, B. Morbey, C. L., Walker, G. A. H., Yang, S., 1989, PASP, 101, 147

Jacobsen, T. S., 1925, Lick Observatory Bulletin, 12, 138

Jacobsen, T. S., 1929, Lick Observatory Bulletin, 14, 60

Jeans, J. H., 1902, Phil. Trans. Roy. Soc., 199, 1

Jeans, J. H., 1929, *Astronomy and Cosmogony*, London:Cambridge University Press

Joy, A. H., 1945, ApJ, 102, 168

Joy, A. H., 1949, ApJ, 110, 424

Julian, W. H., Toomre, A., 1966, ApJ, 146, 810

Kant, I., 1755, *Allegemeine Naturgeschichte und Theorie des Himmels, oder, Versuch von der Verhassung und dem mechanischen Ursprunge des ganzen Weltgebäudes nach Newtonischen Grundsätzen abgehandelt*. Konigbserg: J. F. Petersen

Kepler, J., 1609, *Astronomia Nova Αἰτιολογτοσ*, sev, *Physica coelestis: tradita commentariis de motibus stellae Martis, ex observationibus G. V. Thyconis Brahe, jussu & sumptibus Rvdolphi II., plurimum annorum pertinaci studio elaborata Pragæ, Heidelberg: G. Voegelinus*

Kepler, J. 1619, *Harmoices mvndi libri v. qvorvm primus gemetricvs, de figurarum regularium, quae proportiones harmonicas constituant, ortu & demostrationibus, secundus architectonicvs, seu ex geometria figvrata, de figurarum regularium congruentia in plano vel solido, tertius proprie harmonicvs, de prportionum harmonicarum orto ex figuris, Lincii, Austriae: sumptibus G. Tampachii, excudebat I. Plancvs*

Kepler, J., Brahe, T., Eckebrecht, P., 1627, *Tabvlae Rudolphinae, qvibvs astronomicae scientiae, temporum longinquitate collapsae resauratio continetur, Vlmae, Typis J. Saurii*

Kim, S.-H., Martin, P. G., Hendry, P. D., 1994, ApJ422, 164

Kürstner, M., Hatzes, A. P., Cochran, W. D., Pulliam, C. E., Dennerl, K., Döbereiner, S., 1994, *The Messenger*, 76, 51

Kutta, W., 1901 *Z. Math. Physik*, 46, 435

Laplace, S. P., 1796, *Exposition du Système du Monde*, Paris: De l'Imprimerie du Cercle-Social, an 4

Latham, D. W., Mazeh, T., Stefanik, R. P., Mayor, M., Burki, G., 1989, *Nature*, 339, 38

Laughlin, G. & Bodenheimer, P., 1994 ApJ, 436, 335

Laughlin, G., Korchagin, V. & Adams, F. C. 1996, ApJ, 477, 410

Laughlin, G. & Różyczka, M., 1996, ApJ, 456, 279

Leinert, Ch., Zinnecker, H., Weitzel, N., Christou, J., Ridgway, S. T., Jameson, R., Haas, M. & Lenzen, R., 1993, A&A, 278, 129

Lin, C. C., Shu, F. H., 1964, ApJ, 140, 646

Lin, C. C., Shu, F. H., 1966, Proc. Nat. Acad. Sci., 55, 229

Lindblad, P. O., 1960, Stockholm Obs. Ann., 21, 3

Lindblad, B., 1963, Stockholm Obs. Ann., 22, 3

Lippershey, H., 1608, Dutch patent application, reproduced in Moll, G., 1831, Journal Royal Institution, 1, 319

Lomb, N. R., 1976, Ap&SS, 39, 447

Lucy, L., 1977, AJ, 82, 1013L

Luhman, K., Rieke, G. H., Lada, C. J., Lada, E. A., ApJ, In press

Lynden-Bell D. & Pringle, J. E., 1974, MNRAS, 168, 603 (LBP)

Marcy, G. W., Butler, R. P., 1992, PASP, 104, 270

Marcy, G. W., Butler, R. P., 1996, ApJ, 464, 147

Marcy, G. W., Butler, R. P., Williams, E., Bildsten, L., Graham, J. R., Ghez, A. M., Jernigan, J. G., 1996, ApJ, 481, 926

Mathis, J. S., Rumpl, W. & Nordsieck, K. H., 1977, ApJ, 217, 425

Mayor, M., & Queloz, D., 1995, Nature, 378, 355

Mayor, M., Queloz, D., Udry, S., Halbwachs, J.-L., 1997, From Brown Dwarfs to Planets, in Astronomical and Biochemical Origins and Search for Life in the Universe, IAU Colloquium No. 161, (Bologna, Italy: Editrice Compositori).

Mazeh, T., Latham, D. W., Stefanik, R. P., 1996, ApJ, 466, 415

McCaughrean, M. J., O'Dell, C. R., 1996, AJ, 111, 1977

McMillan, R. S., Moore, T. L., Perry, M. L., Smith, P. H., 1994, Ap&SS, 212, 271

McMillan, R. S., Moore, T. L., Perry, M. L., Smith, P. H., 1996, BAAS, 28, 1111

Mendoza, V. E. E., 1966, ApJ, 143, 1010

Mendoza, V. E. E., 1968, ApJ, 151, 977

Michelson, A. A., Morley, E. W., 1887, Phil. Mag., xxiv, 449 (see also: Am. Jour. Sci., 1887, xxxiv, 333 for the same article)

Miyake, K., Nakagawa, Y., 1993, Icarus, 106, 20

Moore, G., 1965, Electronics, 38, Number 8, pp 114-117.

Monaghan, J. J., 1992, ARA&A, 30, 543

Morris, J., Monaghan, J. J., 1997, J. Comp. Phys., 136, 41

Murdoch, K. A., Hearnshaw, J. B., Clark, M., 1993 ApJ, 413, 349

Murray, J., 1995, PhD thesis: Monash University

Murray, J., 1996, MNRAS, 279, 402

Myhill, E. A. & Kaula, W. M., 1992, ApJ, 386, 177

Najita, J. & Shu, F. H., 1994, ApJ429, 808

Nakajima, T., Oppenheimer, B. R., Kulkarni, S. R., Golimowski, D. A., Matthews, K. & Durrance, S. T., 1995, Nature, 378, 463

Nelson, A.F., Angel, J.R.P, 1998, ApJ, 500, 940

Nelson, A.F., Benz, W., Adams, F.C., Arnett, W.D., 1998, ApJ, 502, 342 (Paper I) (see also chapter 2).

Nelson, A. F., Benz, W., Ruzmaikina, T. V., 1998, (in preparation). See also chapter 4.

Newton, I., 1675/1676 Feb 5 letter to R. Hooke, see reproduction in Merton R. K., 1965, On the Shoulders of Giants A Shandean Postscript, New York: The Free Press

Newton, I., 1687, Philosophiae Naturalis Principia Mathematica, Londini: Jussu Societatis Regiae ac Typis Josephi Streater. Prostant Venales apud Sam Smith ad insignia Principis Walliae in Coemiterio D. Pauli, aliasq, nonnullos Bibliopolas

Noyes, R. W., Jha, S., Korzennik, S. G., Krockenberger, M., Nisenson, P., Brown, T. M., Kennelly, E. J., Horner, S. D., ApJ, 483, L111

O'Dell, C. R., Wen, Z., 1994, ApJ, 436, 194

Osterloh, M., Beckwith, S. V. W., 1995, ApJ439, 288

Ostriker, E. C., Shu, F. H., Adams, F. C., 1992, ApJ, 399, 192

Ostriker, E. C. & Shu, F. H., 1995, ApJ, 447, 813

Ouyed, R., Pudritz, R. E., 1997 ApJ, 482, 712

Ouyed, R., Pudritz, R. E., 1997 ApJ, 484, 794

Papaloizou, J. C. B. & Lin, D. N. C., 1989 ApJ, 344, 645

Papaloizou, J. C. B. & Savonje, G. J., 1991, MNRAS, 248, 353

Peale, S., 1997, Icarus, 127, 269

Perrin J., 1919, Annales de Physique, 2, 89

Pickett, B. K., Durisen, R. H., & Davis, G. A., 1996, ApJ, 458, 714

Pickett, B. K., Durisen, R. H., Link, R., 1997, Icarus, 126, 243

Pickett, B. K., Cassen, P., Durisen, R. H., Link, R., 1998, ApJ, 504, 468

Pollack, J. B., McKay, C. P., Christofferson, B. M., 1985, Icarus, 64, 471 (PMC)

Pollack, J. B., Hollenbach, D., Beckwith, S., Simonelli, D. P., Roush, T. & Fong, W., 1994, ApJ, 421, 615

Porter, D. H. & Woodward, P. R., 1994, ApJS, 93, 309

Press, W. H., Teukolsky, S. A., Vetterling, W. T., Flannery, B. P., 1992 Numerical Recipes, Cambridge University Press, Cambridge

Ptolemy C., Great Syntaxis ca. 150, also published under the title Almagest. Original publishing information unavailable. English translation: 1952, Ptolemy, Copernicus, Kepler, Encyclopedia Britannica Inc., Chicago.

Reid, I. N., Kirkpatrick, D., Beichman, C. A., Liebert, J., Burrows, A., Skrutskie, M., 1998, BAAS192, #55.17

Roddier, C., Roddier, F., Northcott, M. J., Graves, J. E., Jim, K., 1996, ApJ, 463, 326

Ruffert, M., 1997, A&A, 317, 793

Russell, H. N., 1913, address to the American Association for Advancement of Science 1913 meeting. Published in Nature 1914, 93, p227, p252, p281

Safronov, V., 1969, Evolution of the Protoplanetary Cloud and Formation of the Earth and the Planets. Nauka, Moscow. NASA Tech. Trans. TTF-677, 1972.

Scargle, J., 1982, ApJ, 263, 835

Shakura, N. J. & Sunyaev, R. A., 1973, A&A, 24, 337

Shu, F. H., Adams, F. C. & Lizano, S., 1987, ARA&A, 25, 23

Shu, F. H., Tremaine, S. Adams, F. C. & Ruden, S. P., 1990 ApJ, 358, 495 (STAR)

Shu, F. H., Najita, J., Ostriker, E. C., Wilkin, F., Ruden, S. & Lizano, S., 1994a, ApJ429, 781

Shu, F. H., Najita, J., Ruden, S. & Lizano, S., 1994b, ApJ429, 797

Simon, M., Ghez, A. M., Leinert, Ch., Cassar, L., Chen, W. P., Howell, R. R., Jameson, R. F., Matthews, K., Neugebauer, G. & Richichi, A., 1995, ApJ, 443, 625

Simonelli, D. P., Pollack, J. B. & McKay, C. P., 1997, Icarus, 125, 261

Skrutskie, M. F., Meyer, M. R., Whalen, D., Hamilton, C., 1996, AJ, 112, 2168

Spaute, D., Weidenschilling, S. J., Davis, D. R., & Marzari, F., 1991, Icarus, 92, 147

Stahler, S.W., Korycansky, D.G., Brothers, M.J., Touma, J., 1994 ApJ, 431, 341

Stone, J. M., Hawley, J. F., Gammie, C. F., Balbus, S. A., 1996, ApJ, 463, 656

Takeuchi, T., Miyama, S.M., Lin, D.N.C., 1996, ApJ, 460, 832

Tanaka, H., Ida, S., 1996, Icarus, 120, 371

Toomre, A., 1964, ApJ, 139, 1217

Turner, N. J. J., Bodenheimer, P. & Bell, K. R., 1997, ApJ, 480, 754 (TBB)

von Neumann, J., 1945, First Draft of a Report on the EDVAC, Contract No. W-670-ORD-492
Moor School of Electrail Engineering, Univ. of Pennsylvania, Extracts reprinted in The
Origins of Digital Computers: Selected Papers, Third edition, ed. B. Randell, Springer
Verlag, New York, 1982

von Neumann, J., Richtmyer, R. D., 1950, J. Appl. Phys., 21, 232

von Weizacker, C. F., 1943, Z. Astrophys., 22, 319

Walker, M. F., 1956, *ApJS*, 2, 365

Walker, C. K., Adams, F. C., Lada, C. J., 1990, *ApJ*, 349, 515

Walker, G. A. H., Walker, A. R., Irwin, A. W., Larson, A. M., Yang, S. L. S., Richardson, D. C., 1995, *Icarus*, 116, 359

Weidenschilling, S. J., 1984, *Icarus*, 60, 553

Weidenschilling, S. J., Ruzmaikina, T. V., 1994, *ApJ*, 430, 713

Wetherill, G. W., Cox, L. P., 1984, *Icarus*, 60, 40

Wetherill, G. W., Cox, L. P., 1985, *Icarus*, 63, 290

Woodward, J. W., Tohline, J. E. & Hachisu, I., 1994, *ApJ*, 420, 247